University of California
Santa Barbara

Enhancing Mechanistic Crystal Growth Models

A dissertation submitted in partial satisfaction
of the requirements for the degree

Doctor of Philosophy
in
Chemical Engineering

by

Carl Jonathan Tilbury

Committee in charge:

Professor Michael F. Doherty, Chair
Professor M. Scott Shell
Professor Michael Gordon
Professor Guillermo C. Bazan

September 2017

The Dissertation of Carl Jonathan Tilbury is approved.

Professor M. Scott Shell

Professor Michael Gordon

Professor Guillermo C. Bazan

Professor Michael F. Doherty, Committee Chair

July 2017

Enhancing Mechanistic Crystal Growth Models

by

Carl Jonathan Tilbury

If you can't model it, you don't understand it.

If you don't understand it, you can't improve it.

Prof. Michael Doherty, at the start of every senior design class

Acknowledgements

I feel extremely fortunate for my journey over the last 5 years, which has been greatly enriched by those around me. I would like to extend a sincere thanks to everyone who has enabled my progress, supported my development and made my time in Santa Barbara enjoyable.

To my family, and particularly my parents, Carolyn and Mark, thanks for your unwavering support. You remain the foundation for my endeavours and I cannot appreciate enough how you have helped me pursue opportunities and been companions throughout.

To my advisor, Mike, it has been an immense privilege to have worked with you and I could not have imagined a better mentor. Thanks for constantly making time and guiding me both intellectually and professionally. I enjoy finding increased clarity each time we meet and hope to continue gaining your pearls of wisdom in the future!

Thanks to my dissertation committee, past and present members of the Doherty group, our departmental staff, and all my other colleagues at UCSB. You have helped me navigate the process and I have immensely benefited from working alongside such a talented group of people. Thanks also to my colleagues at AbbVie for providing me with invaluable industrial experience over the course of my internship.

This work was funded by the National Science Foundation and Eli Lilly; I would like to express gratitude towards both organizations for the financial support that enabled these developments. Thanks also to the coworkers who aided me in production of the five publications on which this dissertation is based, either through performing experiments, KMC simulations, or engaging in stimulating theoretical discussion.

Finally, thanks to all my friends in Santa Barbara and beyond, you continue to brighten up my life and I truly welcome such fantastic company. To my UCSB lacrosse family, it was a great time on the field and remains great off it.

Curriculum Vitæ

Carl Jonathan Tilbury

Education

2017	Ph.D., Chemical Engineering University of California, Santa Barbara
2012	M.Eng. & B.A., Chemical Engineering St. John's College, University of Cambridge

Publications

Carl J. Tilbury, Mark N. Joswiak, Baron Peters and Michael F. Doherty, "Modeling Step Velocities and Edge Surface Structures during Growth of Non-Centrosymmetric Crystals," *Crystal Growth & Design*, **2017**, *17*, 2066-2080.
DOI: 10.1021/acs.cgd.7b00058

Carl J. Tilbury and Michael F. Doherty, "Modeling Layered Crystal Growth at Increasing Supersaturation by Connecting Growth Regimes," *AIChE Journal*, **2017**, *63*, 1338-1352.
DOI: 10.1002/aic.15617

Carl J. Tilbury, Daniel A. Green, William J. Marshall and Michael F. Doherty, "Predicting the Effect of Solvent on the Crystal Habit of Small Organic Molecules," *Crystal Growth & Design*, **2016**, *16*, 2590–2604.
DOI: 10.1021/acs.cgd.5b01660

Jinjin Li, Carl J. Tilbury, Mark N. Joswiak, Baron Peters and Michael F. Doherty, "Rate Expressions for Kink Attachment and Detachment During Crystal Growth," *Crystal Growth & Design*, **2016**, *16*, 3313-3322.
DOI: 10.1021/acs.cgd.6b00292

Jinjin Li, Carl J. Tilbury, Seung Ha Kim and Michael F. Doherty, "A design aid for crystal growth engineering," *Progress in Materials Science*, **2016**, *82*, 1-38.
DOI: 10.1016/j.pmatsci.2016.03.003

External Conference Presentations

Carl J. Tilbury, Mark N. Joswiak, Baron Peters and Michael F. Doherty, "Modeling the Step Velocity of Non-Centrosymmetric Growth Units and Accounting for Stable/Unstable

Layers," American Institute of Chemical Engineers, Annual Meeting, San Francisco CA, November 2016.

Carl J. Tilbury and Michael F. Doherty, "Modeling Layered Crystal Growth at Increasing Supersaturation by Connecting Growth Regimes," 12th International Workshop of the Crystal Growth of Organic Material & 47th Annual British Association of Crystal Growth Conference, Joint Conference, Leeds UK, June 2016.

Carl J. Tilbury and Michael F. Doherty, "Accounting for Interfacial Solvent Effects within a Mechanistic Crystal Growth Model," American Institute of Chemical Engineers, Annual Meeting, Salt Lake City UT, November 2015.

Carl J. Tilbury and Michael F. Doherty, "Modeling layered crystal growth at higher supersaturations: connecting growth regimes," Gordon Research Conference, Crystal Growth & Assembly, Biddeford ME, June 2015.

Carl J. Tilbury and Michael F. Doherty, "Modeling Layered Crystal Growth at Different Supersaturations: Connecting Growth Regimes," American Institute of Chemical Engineers, Annual Meeting, Atlanta GA, November 2014.

Awards and Honors

Heslin Fellowship **2013**

Cunningham Year Prize **2012**

Wright Prize **2009, 2011, 2012**

Townsend Scholarship **2009, 2010, 2011, 2012**

Gaskell Year Prize **2009**

Abstract

Enhancing Mechanistic Crystal Growth Models

by

Carl Jonathan Tilbury

Crystal growth shapes must be optimized with respect to product functionality. Rapid *in silico* calculations of crystal habits, coupled with theoretical understanding of the physical processes that drive them, will enable intelligent navigation across the vast design space of growth conditions. This dissertation focuses on upgrading a multi-scale mechanistic modeling framework to realize such a design aid for systematic shape engineering.

First, underlying kinetic rate expressions for growth unit attachment and detachment are clarified, and the incorporation mechanism is considered. Second, a method for predicting the dominant growth regime operating on each face is introduced, which enables the effect of supersaturation on crystal shape to be accounted for. Third, the effect of solvent on crystal shape is investigated and a practical technique to account for it is detailed. Fourth, a model for the velocity of a step edge with non-centrosymmetric growth units is developed, which can account for complex instability phenomena unique to this general class of crystals. For each model development, predictions are tested against experimental crystal morphologies (or kinetic Monte Carlo simulations for the case of step velocities), to confirm accuracy. Finally, the strategy for overall model execution and automation is detailed.

These developments act to increase predictive accuracy and enable application of mechanistic models to a wider array of systems and growth conditions, while providing insight for rational crystal engineering.

Contents

Chapter 1

Multi-Scale Models of Crystal Growth: An Engineering Design Aid

Reproduced in part with permission from:

Jinjin Li, Carl J. Tilbury, Seung Ha Kim and Michael F. Doherty, "A design aid for crystal growth engineering," *Progress in Materials Science*, **2016**, *82*, 1-38.

DOI: 10.1016/j.pmatsci.2016.03.003.

Summary

This chapter has three major objectives:

1. Present the motivations for engineering crystal shapes and using *in silico* models
2. Explain how mechanistic models offer the greatest potential
3. Outline the developments in this dissertation that enable mechanistic models to achieve their potential and facilitate crystal shape engineering

1.1 Motivations for Shape Engineering and Models

Crystal growth is a fundamental process in nature and is prevalent in industry for synthesis and purification [1–3]. Crystal morphology plays an important role in pharmaceutical manufacture and other practical applications, with different crystal habits (i.e. rods, needles, plates, blocks) possessing different physicochemical characteristics [4–7]. Key applications include:

- *Pharmaceuticals.* Bioavailability is central to pharmaceutical efficacy and can be impacted by the crystal shape [7–9]. Additionally, high-aspect-ratio, needle-shaped crystals are typically undesirable for pharmaceutical applications, where the shape impacts downstream processing such as filtration [10, 11].

- *Electronic materials.* In contrast to pharmaceuticals, high-aspect-ratio crystals may be preferred, to enhance performance of the active layer in devices [12–15].

- *Catalysts.* Activity is typically face-dependent, according to the different types of surface site, so improved catalysts can result with preferential expression of the crystal faces with optimal activity [6].

- *Explosives.* The crystal morphology can alter shock sensitivity [16, 17], which has important implications for storage and safety.

Figure 1.1 demonstrates a variety of crystal habits for pharmaceutical crystals; their faceted nature is evident with well-defined crystallographic planes. Control over the environmental conditions during crystal growth, such as solvent, temperature, supersaturation and the presence of impurities/additives/stabilizers, can enable dramatically different morphologies to be accessed; consequently subsequent processing and end-use functionality are strongly affected. Often an optimal or at least improved morphology

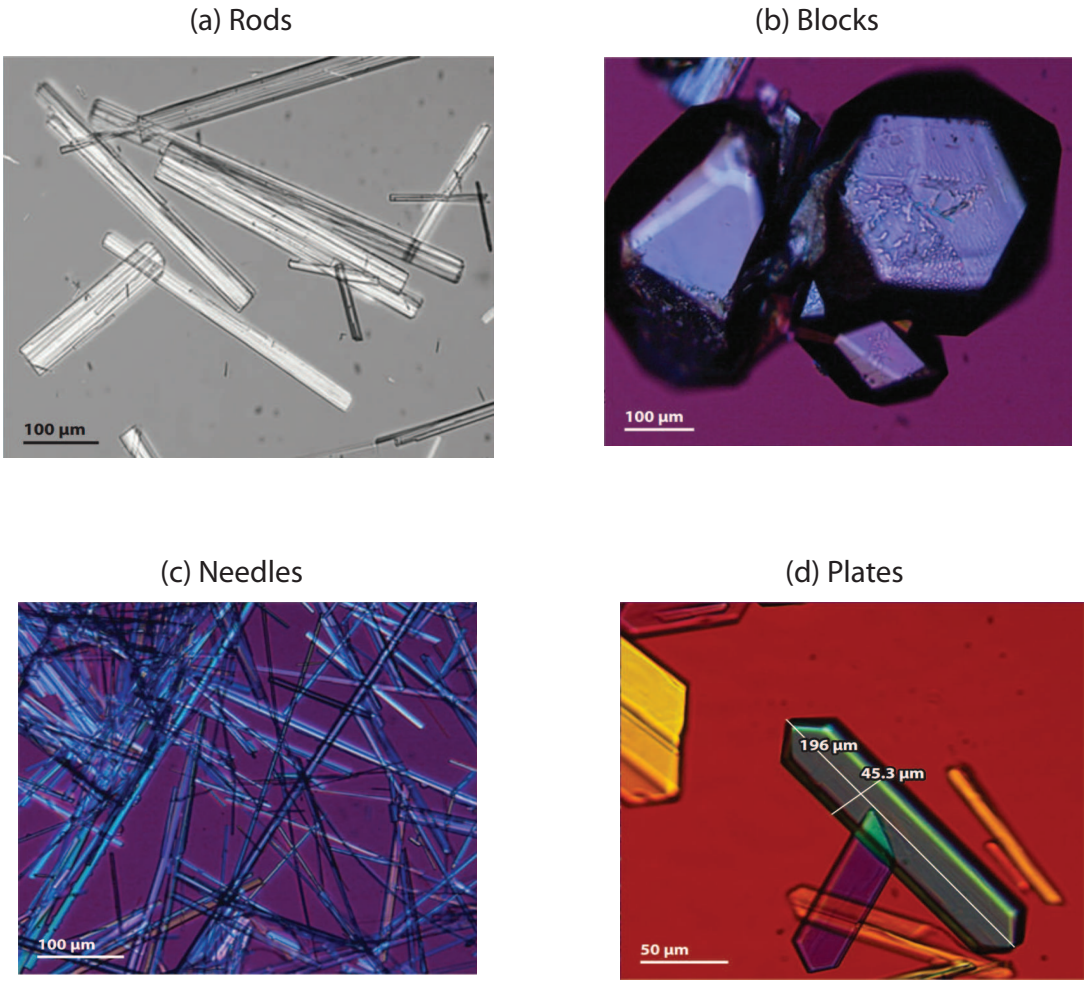

Figure 1.1: Examples of crystal growth shapes under optical microscopy: rods (a), blocks (b), needles (c), plates (d). Image courtesy of N. Variankaval, Merck and Co. (private communication) [1]

can be imagined based on knowledge of the product's function, but the vast design space of growth conditions is difficult to fully explore experimentally.

As understanding of how crystal shapes affect product functionality continues to improve, the ability to synthesize a particular morphology will become even more desirable. Despite much theoretical development, however, scientifically and systematically engineering the shape of crystalline solids remains a challenging task. The typical experimental search for optimal growth conditions [3, 4] is both an inefficient use of limited

resources and not guaranteed to find the optimum form. Accurate and practical *in silico* modeling would offer a powerful tool to enable this shape optimization through a systematic sweep of design conditions that could better target the experimental search [4].

1.2 The Potential of Mechanistic Models

A useful crystal-growth-shape model should have high physicochemical fidelity, so as to capture important effects such as temperature, solvent and supersaturation. To achieve this, our research group has developed [18–20] a multi-scale mechanistic modeling framework based on established theories crystal growth physics. These models have been successfully applied by Koo and co-workers to various crystalline explosives, where accurate morphological predictions have been obtained for 1,3,5-Trinitroperhydro-1,3,5-triazine (RDX) [21], β-Octahydro-1,3,5,7-tetranitro-1,3,5,7-tetrazocine (β-HMX) [22] and 2,2-Dinitroethene-1,1-diamine (DADNE or FOX-7) [23].

Before describing the underlying physics of crystal growth on which this multi-scale mechanistic modeling framework is based, let us first review various non-mechanistic crystal growth models.

1.2.1 Non-Mechanistic Models for Crystal Habit

Gibbs developed the first criteria for describing equilibrium crystal shapes [24], with the underlying principal that the total surface free energy of the fluid-solid interface should be minimized. The work of crystallization can be expressed by the Gibbs-Thomson formula [25]:

$$\Delta G = -\frac{V\Delta\mu}{V_X} + \sum_i \gamma_i A_i \tag{1.1}$$

where the reward for crystallization from a supersaturated solution is based on the chem-

ical potential difference $\Delta\mu$ between a growth unit (e.g., molecule, dimer, ion, cluster, etc.) in the growth environment and in the crystal (V and V_X are the crystal volume and molecular volume, respectively); the penalty is due to surface energies (γ_i) of each facet (having area A_i). The equilibrium shape (i.e., at vanishingly small $\Delta\mu$) corresponds to the minimum in ΔG, which for a fixed crystal size implies:

$$\sum_i \gamma_i \mathrm{d}A_i = 0 \tag{1.2}$$

i.e., the surface free energy is minimized. The shape that solves this problem is given by the famous Wulff construction [3, 25–28]:

$$\frac{\gamma_1}{H_1} = \frac{\gamma_2}{H_2} = \cdots = \frac{\gamma_i}{H_i}. \tag{1.3}$$

H_i is the perpendicular distance of face i from the crystal center, which is, therefore, proportional to its surface energy for the equilibrium shape. This shape ensures that the lowest energy faces are dominantly expressed on the morphology and high surface energy faces can be excluded if their H_i is large enough to produce a plane geometrically beyond where adjacent faces would intersect (i.e., high energy faces lie outside the convex hull). Note that the orientation of each face is fixed based on the crystallography, which determines the angles between planes in forming this construction and also gives rise to the anisotropic γ_i's based on the distinct crystallographic surface structures.

In contrast to fluids, however, solids offer a strong resistance to shape deformation; essentially, there is an activation energy that typically prevents an equilibrium shape being achieved. The barrier to reorganization is reduced with size, leaving nanocrystals as potential candidates to reach their equilibrium shape, but for most crystalline products it is kinetics, instead of thermodynamics alone, that is expected to govern the crystal

morphology. This observation was remarkably noted by Gibbs as a footnote [3, 24], stressing that the kinetically slow-growing faces determine the crystal habit and $\sum_i \gamma_i A_i$ will not usually be minimized.

One can predict the actual (non-equilibrium) crystal habit providing the perpendicular growth rate of each face, G_i, is known. For constant G_i (i.e., in an unchanging growth environment), there exists a steady-state morphology that a crystal will evolve towards regardless of its initial seed shape [29, 30]. This can be calculated using the Frank-Chernov condition [31, 32]:

$$\frac{G_1}{H_1} = \frac{G_2}{H_2} = \cdots = \frac{G_i}{H_i}. \tag{1.4}$$

where H_i is again the perpendicular distance of face i from the crystal center. This is analogous to the Wulff construction with surface energies replaced by growth rates. Therefore, the path to predicting real crystal shapes lies in determining the perpendicular growth rate G_i of each crystallographic face, which via eq 1.4 fixes the relative H_i distances and provides the shape.

BFDH Model

The initial foray into a non-equilibrium model for crystal growth morphology was provided by Bravais, Friedel, Donnay and Harker [33–35] via the now-termed BFDH model. This was the first approach at predicting crystal growth rates, which through the Frank-Chernov condition (eq 1.4) allows one to predict the steady-state crystal morphology. The BFDH model takes the form of a trend between growth rate and crystallographic structure; the perpendicular growth rate G_{hkl} is assumed to be inversely proportional to

the interplanar spacing, d_{hkl}, between successive planes with Miller indices (hkl):

$$G_{hkl} \propto \frac{1}{d_{hkl}} \tag{1.5}$$

This method is solely based on geometrical crystallographic considerations so does not account for any solid-state energetics or modifications from the growth environment. This fixed interplanar spacing for each (hkl) plane can be calculated using the following equations [36]:

$$d_{hkl} = \sqrt{\frac{1}{r_{hkl}}} \tag{1.6}$$

$$\begin{aligned} r_{hkl} =& (1 - \cos^2\alpha - \cos^2\beta - \cos^2\gamma + 2\cos\alpha\cos\beta\cos\gamma)^{-1} \\ & \left[\frac{h^2}{a^2}\sin^2\alpha + \frac{k^2}{b^2}\sin^2\beta + \frac{l^2}{c^2}\sin^2\gamma + \frac{2kl}{bc}(\cos\beta\cos\gamma - \cos\alpha)\right. \\ & \left. + \frac{2lh}{ac}\left(\cos\alpha\cos\gamma - \cos\beta + \frac{2kh}{ab}(\cos\alpha\cos\beta - \cos\gamma)\right)\right] \end{aligned} \tag{1.7}$$

where h, k, l are Miller indices, a, b, c are unit cell dimensions and α, β, γ are the corresponding crystallographic angles. Extinction conditions for the space group should also be considered to select the appropriate Miller indices in each direction, upon which the growth rates are fixed for a crystal system and the morphology can be determined.

The BFDH model is easily implemented since it merely requires knowledge of the crystallography. It is commonly used for this advantage and is built into the commercial software Mercury [37] from the CCDC. While the general trend that faces with large interplanar spacings dominate the crystal habit can be true (best results are obtained for the case of vapor growth [38, 39]), using eq 1.5 to make a quantitative prediction of crystal shape usually fails to match experimentally observed morphologies, particularly for solution-grown crystals [39, 40]. For a given crystallography (i.e., fixed a, b, c, α, β

and γ) it is the Miller indices that determine d_{hkl} via eqs 1.6-1.7; high-Miller-index faces have a small d_{hkl} and are usually not displayed on the steady-state crystal habit due to their commonly high growth rates (a trend that eq 1.5 does predict). A crystal system has only a single shape prediction via the BFDH model (defined by the crystallography) regardless of growth environment, rendering the BFDH model additionally powerless to predict morphological changes as a result of solvent, supersaturation, additives or other imposed growth conditions. Its use should, therefore, be limited to a qualitative prediction of the faces that are likely present for a given crystal; actual shape predictions are ill-advised since the model has no consideration of energetics or surface chemistry effects.

Hartman-Perdok Theory

In 1955, Hartman and Perdok published three landmark papers [41–43] in the science of crystal growth. They established a connection between solid-state interactions and crystal morphology, proposing the concept of periodic bond chains (PBCs) and their use to classify crystal faces.

A periodic bond chain is a repeating array of growth units in a single direction held together by strong inter-growth-unit interactions within the crystal. For organic molecular crystals, these strong interactions usually represent the short bonds within the first co-ordination sphere around a particular growth unit in the lattice [41–44]. As a result of these favorable interactions, on each face crystalline surface structures are typically bounded by the in-plane PBCs (a PBC vector denotes the full translation distance of the chain's repeat unit in the PBC direction). These strong interactions represent bonds formed between growth units during crystallization [41–44] and therefore exclude any intra-growth-unit interactions. More detailed properties of PBCs are presented in Section 6.3.1, alongside our algorithm for PBC determination in complex non-centrosymmetric

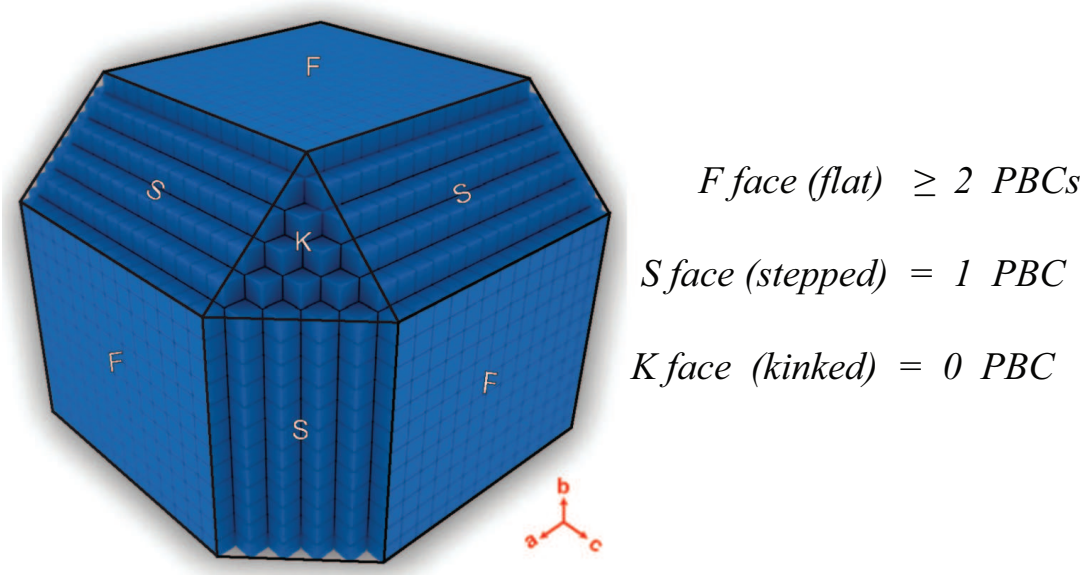

Figure 1.2: F, S and K face classification for a Kossel crystal (cubic growth unit with isotropic interactions). Image adapted and reprinted from Lovette et al. [3] with permission from ACS.

systems.

Hartman and Perdok also introduced a qualitative theory of crystal faces according to their in-plane PBCs, where faces fall into three categories: F (Flat), S (Stepped) and K (Kinked), as shown in Figure 1.2. The dominant faces on the steady-state crystal morphology are slow growing and almost always F faces, which contain two or more PBCs and are, therefore, flat and stable by way of the in-plane growth unit interactions. S faces, containing only one PBC, and K faces, containing no PBCs, have high surface energies (from broken PBCs extending out-of-plane) and usually grow extremely fast.

Attachment Energy (AE) Model

Following the connection between solid-state interactions and characterization of faces, Hartman and Bennema developed [45] the attachment energy (AE) model as a simple method that could predict crystal growth rates relatively well in lieu of a fully

mechanistic model. Since its inception this model has been used extensively to predict crystal shapes [39, 46–50] and remains routinely used today. The underlying principle is that if stronger bonds are formed when a growth unit attaches to a face, then this process will require less time and lead to a faster growth rate [41, 45, 51]:

$$E_m^{att} > E_n^{att} \Rightarrow G_m > G_n \tag{1.8}$$

with m and n being two different faces. The attachment energy for a face (hkl), E_{hkl}^{att}, is defined as the energy per growth unit released upon crystallization of a new slice of thickness d_{hkl}; it includes interactions perpendicular to the terrace alone (equivalently, it represents the average energy to remove a terrace-adsorbed growth unit) [41]. For each plane, the lattice energy (which is constant for the crystal, representing the total lattice interaction energy per growth unit) is divided between this attachment energy (out-of-plane interactions) and the slice energy (in-plane interactions for slice d_{hkl}) [45, 51]:

$$E^{latt} = E_{hkl}^{att} + E_{hkl}^{slice} \tag{1.9}$$

where each energy is usually reported as positive.

While faces with a larger attachment energy have faster growth rates, without a functional form for the relationship between G_{hkl} and E_{hkl}^{att}, no quantitative shape predictions can be made. When using the AE model, therefore, growth rates are typically assumed proportional to attachment energies [52]:

$$G_{hkl} \propto E_{hkl}^{att} \tag{1.10}$$

This assumption has no physical basis and was introduced purely to enable shape predictions by way of the Frank-Chernov condition once attachment energies for each face

have been calculated. Even for simple crystal systems containing high symmetry, mechanistic expressions remain non-linear and do not collapse to eq 1.10. Nonetheless, the approximation can occasionally hold and the AE model usually predicts the correct morphological faces (since low attachment energies lead to low perpendicular growth rates and faces that dominate the morphology).

The AE model is generally an improvement on the BFDH model due to the inclusion of solid-state energetics. Although these interactions, albeit on a more complicated level, do govern the physics of crystal growth, the functional form for the AE model remains arbitrary. As such, the AE model should not be expected to perform well at predicting the crystal shape universally or for complex systems and in particular, the influence of external factors on crystal growth, such as solvent, additives, and supersaturation are not included.

Modified Attachment Energy (MAE) Models

There is growing interest in using modified attachment energy (MAE) models [53–59] to capture effects of the growth environment, such as solvent, supersaturation or additives, which the AE model has no architecture for dealing with. Under MAE approaches, molecular simulations are typically used to model how the growth environment interacts with a crystal face, introducing solvent and/or solute molecules around relevant surface sites and determining resulting energetics (typically binding energies, which are used with E_{hkl}^{att} to create a composite MAE variable). Adopting molecular simulations to study the interface can provide a much more sophisticated picture of the surface chemistry than what is currently able to be incorporated into rapid mechanistic methods (see Chapter 4 later) and much insight can be gained by considering the crystallization process in such detail. Nonetheless, the drawback to using MAE models for shape predictions, beyond the computational expense, is the need to assume or correlate a functional form for the

MAE variable and its relation to face growth rates. Developed MAE models may produce agreement with observed morphologies in certain cases, but with no grounding in mechanistic theories their ability to predict the crystal habit of a general system appears limited.

1.2.2 The Multi-Scale Mechanistic Model of Crystal Growth

Neither the BFDH or AE model is able to provide a high-fidelity description of crystal morphology as a function of the growth environment. MAE approaches are an improvement, but their scope appears limited due to the simplistic functional form that limits generic applicability across all crystal systems and environmental conditions.

A mechanistic approach still determines face growth rates, but instead of obtaining them from a general correlation, our models consider how crystals grow and we develop face-specific parameters describing the relevant processes in detail, across multiple length scales and time scales. Considering the anisotropic face growth rates from a kinetic standpoint is the only way of reliably estimating crystal shapes, as Gibbs himself emphasized [3, 24].

The driving force for crystallization is a chemical potential difference between the solute in its growth environment and in the crystalline lattice. This chemical potential difference can be defined in terms of the supersaturation ratio S [2, 60]:

$$\Delta\mu = kT\ln S \tag{1.11}$$

This supersaturation ratio can be defined as $S = C/C_{sat}$ (or $S = x/x_{sat}$) for solution growth and $S = P/P_{sat}$ for vapor growth. For $S = 1$ the environment is saturated and crystals do not change in size, while growth occurs in the supersaturated state ($S > 1$) and dissolution occurs in the under-saturated state ($S < 1$). Note that eq 1.11 does

not require the solution to be ideal; it assumes only that the activity coefficients of a saturated solution and a supersaturated solution are approximately equal (see Chapter 2 for more detail).

Stable incorporation of growth units into the crystal occurs where multiple bonds can be formed with neighboring growth units in the lattice, which we can determine from PBC theory. Stepped and, particularly, kinked faces are typically those planes with higher Miller indices; they have an extremely high density of these stable incorporation sites. This usually leads to a fast, rough growth mechanism, and these faces do not commonly appear on steady-state morphologies; if they are present, it will result in a high-aspect-ratio needle or platelet shape [3]. The crystal habit is instead bounded by the slower-growing F faces, which typically grow under a layer-by-layer mechanism. Layered growth is amenable to modeling, since it results from the action of polygonal surface structures (spirals, 2D nuclei). These surface structures complete successive face layers through the forward advance of their respective step edges [61]. These steps move due to the successive addition of growth units into the favorable sites for attachment on the step edge: kink sites [1–3,61–65]. If the net rate of incorporation into such sites is positive, in general the step will advance; this net rate depends on the balance of individual growth unit attachment/detachment processes [66].

Figure 1.3 summarizes the structure of this mechanistic approach across multiple scales. Face growth rates are determined from consideration of kink incorporation, the corresponding advance of step edges emanating from a specific surface structure and, finally, how these structures act to complete new face layers. At each scale, multiple types of event/site/structure exist for the specific crystal system (e.g., on a given face there are multiple types of step, on each step there are multiple types of kink, etc.). To model this entire process accurately, the contribution from each category's distinct constituents must be accounted for.

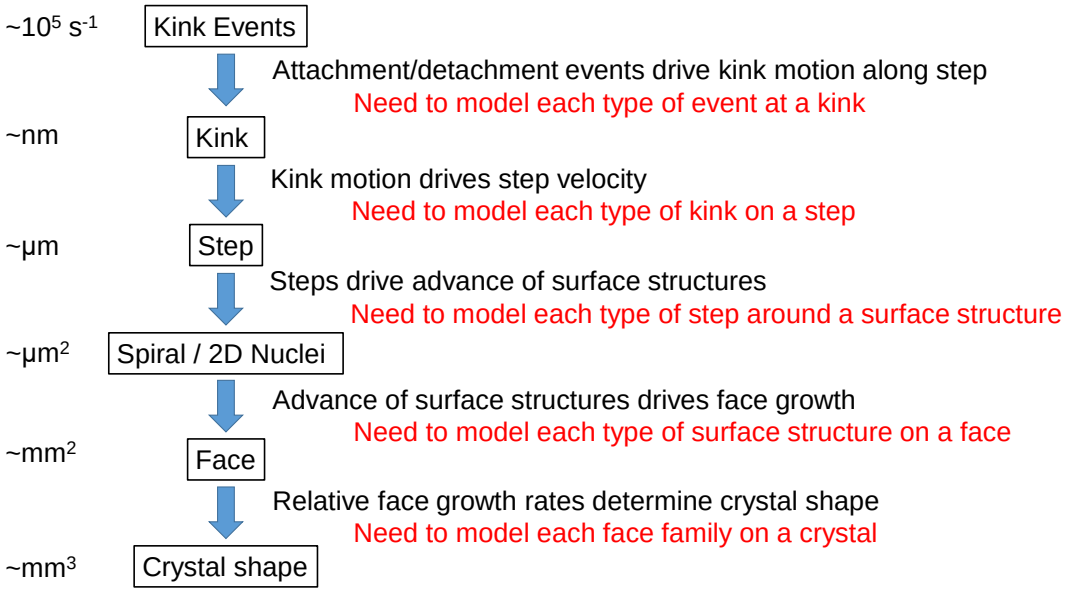

Figure 1.3: The multi-scale mechanistic modeling framework going from molecular events to crystal shapes. Rough scales for each stage are indicated, though these are, of course, highly system specific.

Figure 1.4 shows an example of a step edge on an F face, with kink sites indicated. As can be seen, the forward propagation of a step edge acts to complete the incomplete face layer. Kink sites are renewable upon attachment and furthermore are continually regenerated via thermal roughening [3,61,67,68] (see Figure 1.5 (a) and (b)). Centrosymmetric crystals necessarily have the same kink-site interactions on each edge and face, but for non-centrosymmetric crystals each edge on each face can generally have multiple distinct kink sites containing different sets of interactions. Figure 1.5(c) indicates a tiered array of steps moving across the surface, which is typical of a spiral mechanism; normal growth of the face results from the successive completion of several layers.

Vapor (Sublimation) Growth

In vapor growth, solute particles are provided from a source via sublimation and are deposited directly into the growing crystal. A temperature difference between source

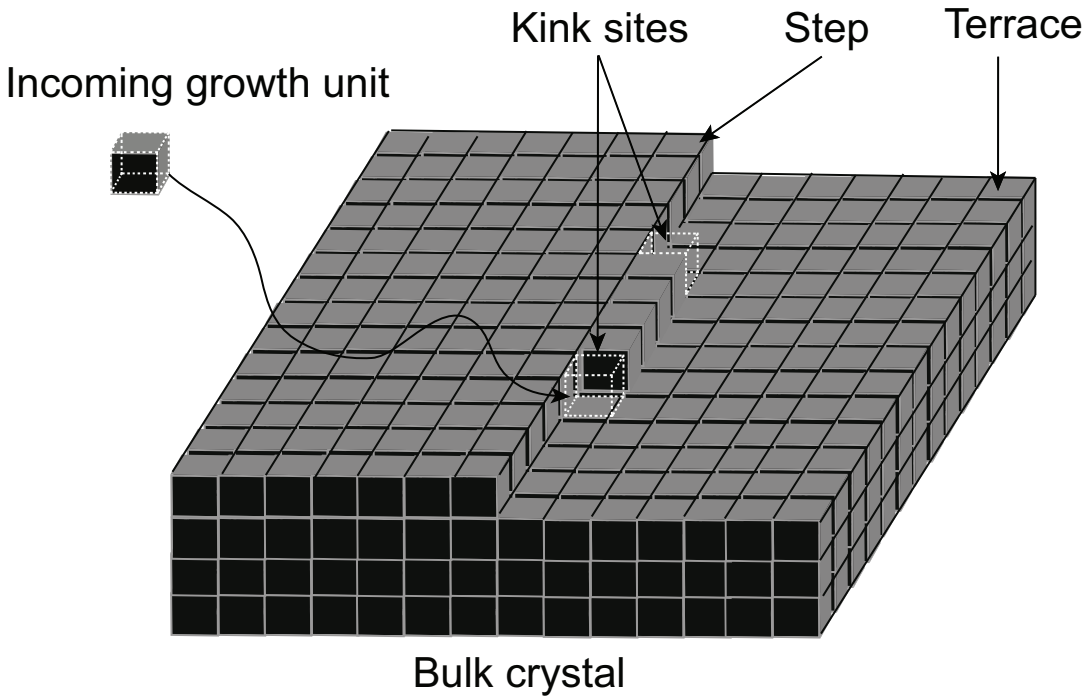

Figure 1.4: Schematic illustration of the surface structure on a faceted crystal with cubic growth units, indicating kink sites, step edge and the terrace. Although not shown here, typically for organic molecular crystals the incorporation process involves sequential adsorption at the terrace and then the step before entering the kink site [1, 61, 69–72]; see Chapters 2 and 4 for more detail.

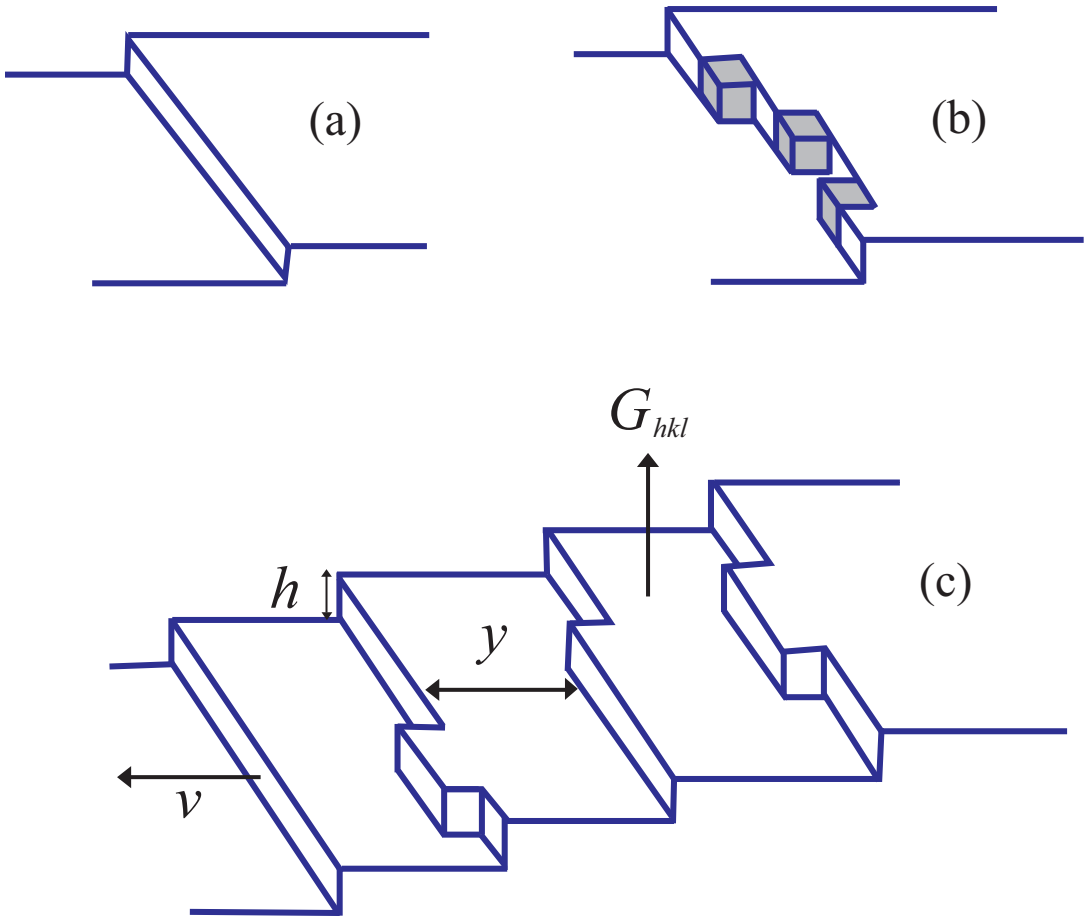

Figure 1.5: At $0K$ the step edge is straight (a), while above $0K$ the propensity for rearrangement via thermal fluctuation leads kinks to exist at all times (b) [3,61,67,68]. (c): The forward velocity, v, of successive steps gives rise to the normal growth rate of the face, G_{hkl}; h is the step height (usually the interplanar spacing d_{hkl}) and y is the inter-step distance. Image adapted and reprinted from Lovette et al. [3] with permission from ACS.

(T_S) and the growing crystal (T_D) is usually used to drive crystallization, which the supersaturation is often expressed as; $S = T_S/T_D$ should not simply be substituted into eq 1.11, however. Features of the vapor growth include the following:

(a) Growth rates can be slow with the small amount of solute vapor impinging on the crystal. This can be useful for facile surface manipulation (e.g., semiconductor manufacture), but is typically inefficient for growing larger crystals [73].

(b) Well-defined facets often form to define the crystal [73]. This can be reasoned through the relatively high surface energies in the absence of favorable solvation effects, which creates a large driving force to crystallize in the most favorable surface structures. Note that this effect is still felt mechanistically even when the Wulff shape is not achieved.

(c) The barrier to attachment is low, consisting primarily of the need to properly orient into the lattice position [60]. Surface diffusion effects are, therefore, expected to be more important than in solution growth, where relatively higher attachment barriers (representing the required desolvation - see below) usually result in a kinetic surface-integration-limited regime.

Solution Growth

The chemical potential driving force in solution is a result of the excess concentration of solute in solution above the saturated concentration. Both the crystal surface and solute growth units in solution are solvated, so following approach of a growth unit to the surface, desolvation must precede attachment. This requirement to desolvate kink and surface represents the principal energetic barrier in solution growth [2,66], which can be significant and often leads to a kinetic regime where the attachment process determines the rate of crystal growth. The various processes taking a growth unit from solution to being attached at the kink site are listed below (see also Figure 1.4) [1,61,69–72]:

(a) Bulk transport (convection/diffusion) from solution to the terrace

(b) Terrace adsorption (partial desolvation)

(c) Surface diffusion across the terrace to a step edge

(d) Edge adsorption (partial desolvation)

(e) Diffusion along the edge to a kink site

(f) Attachment to a kink site (remaining desolvation)

This picture is for an organic molecule; in contrast, inorganic growth units are expected to attach at kink sites directly from solution due to high diffusive barriers on the surface resulting from like-charge repulsion. Coincident with desolvation, the latent heat of crystallization is released and must be transported away, though this is expected to occur on a much faster timescale than the processes described above [70].

The growth rate of a crystal face is limited by the slowest of these processes [70, 74]. For molecular organic crystals growing via a layered mechanism, kink attachment (i.e., surface integration) is expected to be rate-limiting [2]. The density of kink sites on the step is, therefore, an important parameter influencing the growth rate and depends on the strength of intermolecular interactions (discussed later).

Rough Growth

In contrast to layered growth, rough growth occurs when favorable attachment is available across the entire crystal face. This is by definition the case on stepped (S) and particularly kinked (K) faces, which grow under a rough mechanism from any environment. The growth rate of S and K faces are usually significantly higher than F faces due to this increased density of kink sites [3]. Rough growth can also occur on F faces if the environment (e.g., supersaturation, temperature, etc.) is such that attachment is favorable at terrace and step sites in addition to kinks, i.e., a roughening transition has been reached which will destroy any surface structures from layered mechanisms [3, 75].

Under the rough mechanism, crystal growth is expected to be limited by transport of

solute growth units to the surface, instead of attachment kinetics. This bulk transport-limited growth rate, G_{BT}, is then proportional to the concentration driving force between bulk solution (C) and the crystal surface (C_{sat} under fast surface integration) [3, 60]:

$$G_{BT} \propto (C - C_{sat}) \tag{1.12}$$

Crystals under rough growth tend to lose their faceted nature and are instead bounded by high index planes or rounded, non-crystallographic surfaces. This leads to spherulitic shapes, or, in extreme cases of transport-limited growth, fractal and dendritic morphologies [76].

Two-Dimensional (2D) Nucleation-and-Growth

The 2D nucleation-and-growth mechanism was the first model used to describe layered crystal growth [62, 63, 77]. With increasing supersaturation, the 2D nucleation rate increases and the critical size of a 2D nucleus decreases [20], so in the limit of high supersaturation this mechanism essentially represents a rough regime. The critical size of a 2D nucleus can be determined via classical nucleation theory: it is the size beyond which growth is favorable over dissolution [20], which represents a maximum in free energy when considering the volume reward of crystallization (due to the chemical potential difference $\Delta\mu$) against the surface energy penalty.

At low nucleation rates a single 2D nucleus can grow to the face edges and complete the layer before an additional nucleation event (mononuclear growth), while at higher nucleation rates (e.g., higher supersaturation) multiple nuclei form and collectively complete face layers following their subsequent growth across the surface (termed a birth-and-spread regime) [3, 20, 60, 65, 73]. The growth rate under 2D nucleation depends, therefore, on the coverage time.

Earlier models for 2D-nucleation growth regimes rely on simplifying assumptions such as circular nuclei, constant spreading velocities or Kossel growth units [78, 79]. Notable recent models exist for the birth-and-spread regime, considering anisotropic spreading for rectangular [80] and general nucleus shapes [20].

Spiral Growth

The spiral growth mechanism reconciles the discrepancy between observed crystallization at low supersaturation and the extremely slow growth rates expected for 2D nucleation under such an environment. This spiral mechanism was developed by Burton, Cabrera and Frank [61] (BCF) in arguably the most revolutionary paper within the field of crystal growth. Noting that kink sites on steps were critical for growth unit incorporation, they proposed that a screw dislocation could provide a continuous source of steps for a self-sustaining growth mechanism, rather than waiting for 2D nucleation events that would become increasingly scarce at low supersaturations. This explains the dominance of spirals at low supersaturation and accounting for this mechanism is critical to describing the growth of crystals under such conditions. Note the controlled crystallization of APIs often uses a low supersaturation, to ensure good product purity and a uniform, faceted crystal morphology.

Faces of a real crystal are rarely perfect and so screw dislocations exist almost universally, enabling the spiral mechanism to operate for most systems. As growth units attach to the exposed step at the dislocation and lead to its advance across the surface, an adjacent edge appears. There is usually a critical length before this newly exposed edge itself advances, at which point the next adjacent edge appears and the process repeats [18]. Therefore, the emerging edges essentially rotate about the point of the screw dislocation and eventually the original edge reappears one layer higher (corresponding to the interplanar spacing, d_{hkl}, for an elementary step height). Each edge continues its

advance outwards to the face's ends (or upon meeting another step or equivalent boundary), and so the action of the rotating spiral leads to a normal growth rate of the face, with steps continually emerging from the spiral in the edge directions, separated by a regular distance called the inter-step spacing. This process is illustrated in Figure 1.6.

For the BCF spiral mechanism, the growth rate of face (hkl), $G_{S,hkl}$, has been expressed as [3, 18]:

$$G_{S,hkl} = \frac{hv}{y} = \frac{h}{\tau_S} \tag{1.13}$$

where h is the step height (e.g., d_{hkl} or a simple multiple of it), v is the step velocity and y is the inter-step distance (y/v represents the time taken to advance the face a single layer of growth units in the normal direction - see also Figure 1.5(c)). This time y/v is additionally equal to the spiral rotation time, τ_S. With the step height defined for each face based on the crystallographic geometry, the problem of calculating a face's growth rate under the spiral growth mechanism is essentially reduced to finding τ_S.

To determine τ_S, one must consider both the critical length and the step velocity of each spiral side. For kinetically limited growth, which is expected at low supersaturations where the spiral regime operates, one must consider both the density of kink sites on a step as well as the net rate of solute incorporation into each kink site [19]. This net attachment rate is termed the kink rate, and is the balance between attachment and detachment events that can be considered as elementary reactions (see Chapter 2) [64,81].

1.2.3 Molecular Simulations

From a simulation perspective, kinetic Monte Carlo (KMC) algorithms [22, 23, 23, 80, 82–89] and Molecular Dynamics [88, 90–92] have each been utilized in modeling spiral and 2D-nucleation growth mechanisms. A noteworthy example of such an approach is the MONTY algorithm [86, 87], which considers the influence of supersaturation, tem-

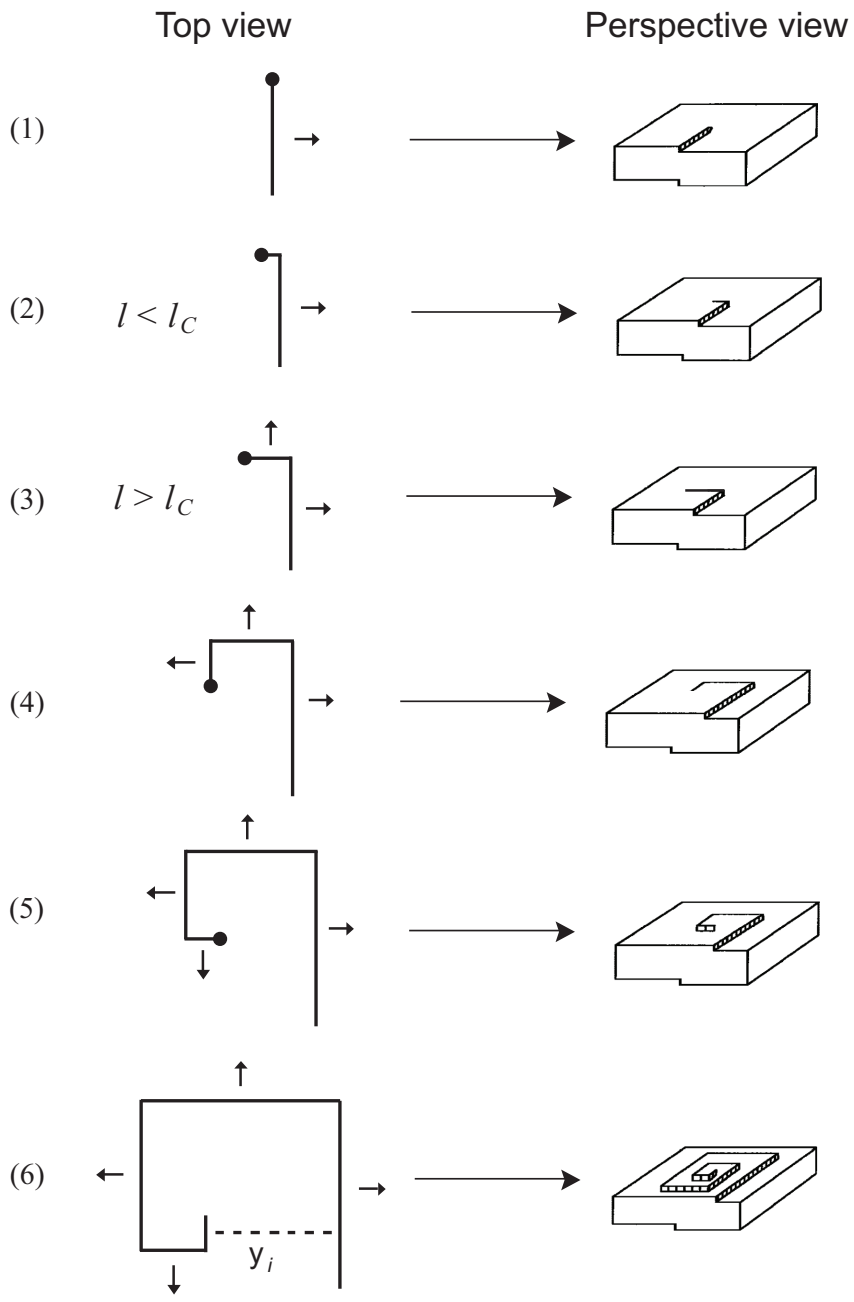

Figure 1.6: The mechanism of spiral growth. The initial dislocation edge advances (1) and exposes the next edge (2), which is stationary while it remains below its critical length, l_C. The newly exposed edge advances (3) once it has surpassed its critical length, due to motion of the preceding step. This process repeats (4), (5), until the original edge reappears one layer higher (6). Image adapted and reprinted from Lovette et al. [3] with permission from ACS.

perature, concentration, and dissolution free energy.

In terms of providing rapid shape predictions for screening purposes, these approaches remain too slow due to the computational expense and the fact that growth mechanisms for each face are common inputs that may have to be determined for each set of tested growth conditions before use. However, such molecular simulations can provide extremely valuable insight to guide model development; indeed, Chapter 5 utilizes KMC simulations to validate a new step velocity model.

1.3 Dissertation Outline: Model Developments

The focus of this dissertation is on the development of mechanistic models and their automation. Not only does a mechanistic approach to *in silico* crystal shape prediction offer greater accuracy, but it enables individual portions of the modeling framework to be systematically upgraded. Figure 1.7 summarizes the focus of each subsequent chapter and which areas of the modeling framework have been addressed. These developments have removed assumptions, increased accuracy and otherwise generalized the modeling applicability to new crystal systems or growth conditions. Figure 1.7 also indicates the top-down and bottom-up modeling strategy. Starting from a crystal, the relevant faces must be determined, then surface structures, steps, kinks and events. Calculating rates at each stage, starting with attachment/detachment events, allows one to progress back up and produce the shape prediction.

1.3.1 Chapter 2: Attachment/Detachment Rate Expressions

The central kinetic processes defining layer-by-layer crystal growth or dissolution are the attachment and detachment rates of growth units at kink sites [2, 3, 66]; the net balance of these activated processes leads to either crystal growth or dissolution. Various

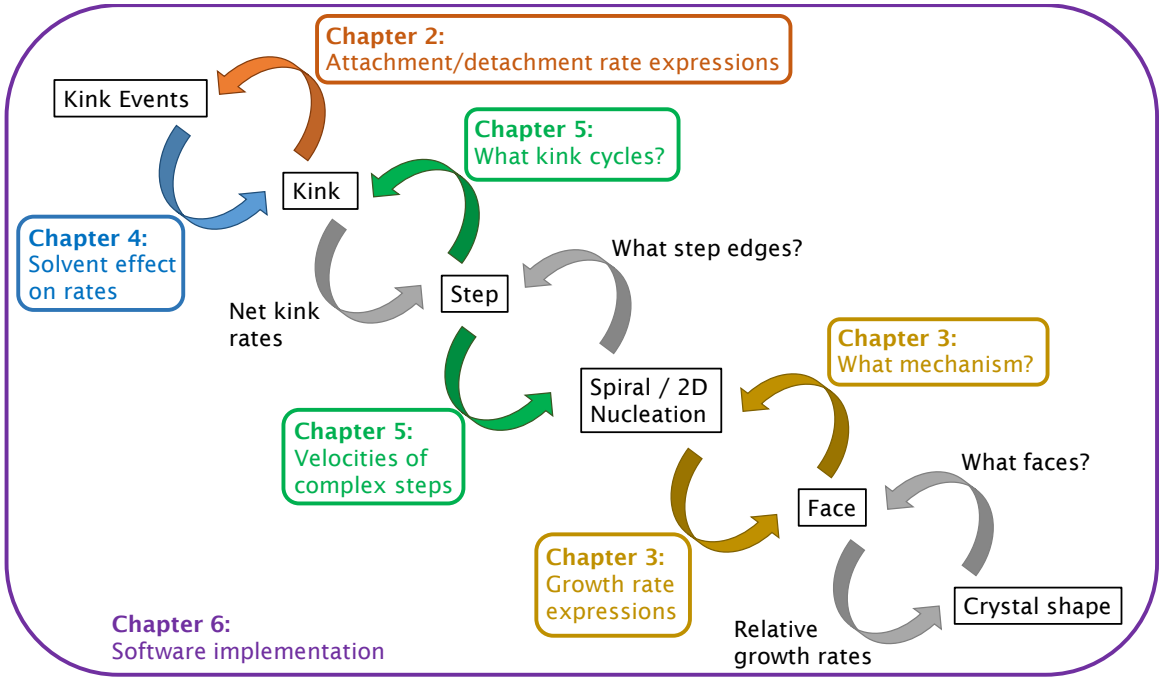

Figure 1.7: The mechanistic modeling approach operates across multiple scales. The focus of each subsequent chapter is indicated.

sets of rate expressions for attachment and detachment processes have been used in the literature, in each case attempting to most appropriately capture the underlying surface chemistry. As these kinetic processes are a pivotal component of mechanistic crystal growth models, it is important that their rate expressions are accurately formulated and self-consistent.

Chapter 2 examines various sets of such rate expressions that have been previously utilized. By applying detailed balance criteria and crystallization thermodynamics, the most appropriate set of rate expressions is identified.

1.3.2 Chapter 3: Connecting Growth Regimes

We have established that under layered crystal growth, steps are generated on F faces as a result of two mechanisms: two-dimensional (2D) nucleation on the surface or screw dislocations (leading to spiral growth). Since both mechanisms are able to

operate concurrently, whichever leads to the fastest normal growth rate will dominate on a face. The dominant mechanism can be different for different faces on the same crystal and depends on both growth conditions and surface interactions (both solid-state and interfacial). At low supersaturation, the spiral growth mechanism with steps emanating from a screw dislocation is dominant [61]. As the supersaturation increases, 2D nuclei form more readily and a 2D-nucleation growth regime can overtake the spiral mechanism. At a sufficiently high supersaturation an F face can also transition to a rough growth regime [3, 75].

Chapter 3 introduces a general mechanistic framework that can predict the dominant growth regime operating on each face at specified crystallization conditions. This model adopts stationary nucleation rate theory to formulate the 2D nucleation rate in terms of face-specific mechanistic parameters that can be readily calculated. To connect layered-growth regimes and calculate crossover supersaturations, growth rate expressions are reformulated in terms of supersaturation-independent parameter groups. This development confers the ability to accurately predict morphological changes resulting from changing supersaturation; principally, face families may grow out of the morphology or the crystal aspect ratio may become supersaturation-dependent. The model is applied to a variety of examples, confirming the predictive capability to account for supersaturation-dependent morphologies.

1.3.3 Chapter 4: Accounting for the Effect of Solvent

Under solution growth, the interfacial chemistry induces an energetic modification that can affect crystal shapes. Accurately predicting this effect is important for crystal engineering, since the solvent is a critical design decision. Essentially, various mechanistic parameters that underpin the overall growth model must be modified from their base

sublimation-growth values.

Chapter 4 details an investigation into pragmatic approaches to accurately calculate the effect of solvent on crystal shapes. This chapter reviews available techniques that can be feasibly integrated into an automated implementation of the modeling framework and identifies the most practical strategy. The necessity of such pragmatic treatment is to retain the potential functionality of an industrial screening step. Sublimation- and solution-growth predictions are compared to experimental results for various systems, isolating the effect of solvent and verifying the accuracy of this proposed technique for interfacial energetic modification.

1.3.4 Chapter 5: Modeling Velocities of Complex Steps

While the typically studied case of a Kossel crystal provides a dramatic reduction in complexity, the model of cubic growth units with isotropic interactions perpendicular to each face is insufficient for real crystal systems. Instead, the anisotropic bonding network and face-dependent geometry must be considered. The easiest class of real crystals to model are centrosymmetric, where inversion centers present within the lattice force interactions to extend equally in opposite directions. Centrosymmetric crystals have kink sites that are half-crystal positions, containing the same set of interactions regardless of the specific edge or face. For centrosymmetric crystals, the kink rates and step velocities have simple expressions that are well established. However, most crystal growth units are non-centrosymmetric, which produces interaction anisotropy within a crystal lattice. This anisotropy generates multiple types of kink sites on each crystal step and repeating patterns of rows with different growth units from the perspective of the lattice interaction environment, even for pure molecular crystals. As a result, unstable edge rows may be generated that dissolve under conditions of crystal growth. A method

to account for edge surface structures, considering such effects, is required to accurately model the step velocity, which is vital for a mechanistic description of crystal growth.

Chapter 5 introduces a model that can handle this complexity and accurately calculate the velocity of a step with non-centrosymmetric growth units. This model accounts for the interdependent effect of various step surface structures, identifying both thermodynamic and kinetic contributions to step row instability. Beyond capturing important non-centrosymmetric phenomena, the developed expressions also collapse to the centrosymmetric formulation under appropriate limits. The increased predictive power of this model is demonstrated by application to various examples of an alternating-row A–B step; the results compare favorably to kinetic Monte Carlo simulations across a wide range of interaction anisotropy.

1.3.5 Chapter 6: Automation and Implementation Strategy

Although mechanistic models of crystal growth enable greater predictive capacity, to achieve significant impact, and actually facilitate rational design of crystalline products, they must be made accessible for industrial uptake.

Chapter 6 summarizes various algorithms and tactics for implementing the presented mechanistic approaches, providing a roadmap to go from crystallography to shape prediction. Specific focus is given to crystals with non-centrosymmetric growth units, which complicate the automation and require careful consideration. The implementation strategy is described within the context of proof-of-concept, academic software called ADDICT (Advanced Design and Development of Industrial Crystallization Technology) that provides an automated execution of the spiral growth model for non-centrosymmetric organic molecules. ADDICT provides a pathway for both current and future state-of-the-art mechanistic models to be automated and transferred to industrial researchers, enabling

next-generation design of crystalline products.

1.3.6 Chapter 7: Conclusion and Future Developments

Chapter 7 reviews the presented advancements to mechanistic models, summarizing how capabilities have been extended. This chapter also identifies areas for improvement and refinement, to further expand the predictive power, applicability and utility of future mechanistic models.

Bibliography

[1] P. Dandekar, Z. B. Kuvadia, and M. F. Doherty. Engineering crystal morphology. *Annu. Rev. Mater. Res.*, 43:359–386, 2013.

[2] P. G. Vekilov. What determines the rate of growth of crystals from solution? *Cryst. Growth Des.*, 7(12):2796–2810, 2007.

[3] M. A. Lovette, A. R. Browning, D. W. Griffin, J. P. Sizemore, R. C. Snyder, and M. F. Doherty. Crystal Shape Engineering. *Ind. Eng. Chem. Res.*, 47(24):9812–9833, 2008.

[4] C. Schmidt and J. Ulrich. Morphology prediction of crystals grown in the presence of impurities and solvents - an evaluation of the state of the art. *J. Cryst. Growth*, 353(1):168–173, 2012.

[5] C. Wu and Y. Xie. Controlling phase and morphology of inorganicnanostructures originated from the internal crystal structure. *Chem. Commun.*, pages 5943–5957, 2009.

[6] H. G. Yang, C. H. Sun, S. Z. Qiao, J. Zou, G. Liu, S. C. Smith, H. M. Cheng, and G. Q. Lu. Anatase TiO_2 single crystals with a large percentage of reactive facets. *Nature*, 453(7195):638–641, 2008.

[7] N. Variankaval, A. S. Cote, and M. F. Doherty. From form to function: crystallization of active pharmaceutical ingredients. *AIChE journal*, 54(7):1682–1688, 2008.

[8] D. Winn and M. F. Doherty. Modeling crystal shapes of organic materials grown from solution. *AIChE J*, 46(7):1348–1367, 2000.

[9] J.-C. Yin, J.-S. Zhou, J. Sun, Y. Qiu, D.-Z. Wei, and Y.-L. Shen. Study of the crystal shape and its influence on the anti-tumor activity of tumor necrosis factor-related apoptosis-inducing ligand (apo2l/trail). *Crystal Research and Technology*, 43(8):888–893, 2008.

[10] M. A. Lovette and M. F. Doherty. Needle-shaped crystals: Causality and solvent selection guidance based on periodic bond chains. *Cryst. Growth Des.*, 13(8):3341–3352, 2013.

[11] N. Panina, R. van de Ven, F. F. B. J. Janssen, H. Meekes, E. Vlieg, and G. Deroover. Study of the needle-like morphologies of two β-phthalocyanines. *Crystal Growth & Design*, 9(2):840–847, 2009.

[12] F. Freitas, V. Sarmento, C. Santilli, and S. Pulcinelli. Controlling the growth of zirconia needles precursor from a liquid crystal template. *Colloids and Surfaces A: Physicochemical and Engineering Aspects*, 353(1):77 – 82, 2010.

[13] G. Giri, S. Park, M. Vosgueritchian, M. M. Shulaker, and Z. Bao. High-mobility, aligned crystalline domains of TIPS-pentacene with metastable polymorphs through lateral confinement of crystal growth. *Adv Mater (Weinheim, Ger)*, 26(3):487–493, 2014.

[14] R. Ruiz, D. Choudhary, B. Nickel, T. Toccoli, K.-C. Chang, A. C. Mayer, P. Clancy, J. M. Blakely, R. L. Headrick, S. Iannotta, and G. G. Malliaras. Pentacene thin film growth. *Chem Mater*, 16(23):4497–4508, 2004.

[15] S. C. B. Mannsfeld, J. Locklin, C. Reese, M. E. Roberts, A. J. Lovinger, and Z. Bao. Probing the anisotropic field-effect mobility of solution-deposited dicyclohexyl-α-quaterthiophene single crystals. *Adv Funct Mater*, 17(10):1617–1622, 2007.

[16] X. Song, Y. Wang, C. An, X. Guo, and F. Li. Dependence of particle morphology and size on the mechanical sensitivity and thermal stability of octahydro-1,3,5,7-tetranitro-1,3,5,7-tetrazocine. *J Hazard Mater*, 159(2-3):222–229, 2008.

[17] H. Chen, L. Li, S. Jin, S. Chen, and Q. Jiao. Effects of additives on ϵ-HNIW crystal morphology and impact sensitivity. *Propellants, Explos, Pyrotech*, 37(1):77–82, 2012.

[18] R. C. Snyder and M. F. Doherty. Predicting crystal growth by spiral motion. *Proc. R. Soc. London, Ser. A*, 465(2104):1145–1171, 2009.

[19] Z. B. Kuvadia and M. F. Doherty. Spiral growth model for faceted crystals of non-centrosymmetric organic molecules grown from solution. *Cryst. Growth Des.*, 11(7):2780–2802, 2011.

[20] M. A. Lovette and M. F. Doherty. Predictive Modeling of Supersaturation-Dependent Crystal Shapes. *Cryst. Growth Des.*, 12(2):656–669, 2012.

[21] H.-M. Shim and K.-K. Koo. Crystal Morphology Prediction of Hexahydro-1,3,5-trinitro-1,3,5-triazine by the Spiral Growth Model. *Cryst. Growth Des.*, 14(4):1802–1810, 2014.

[22] H.-M. Shim and K.-K. Koo. Prediction of growth habit of β-cyclotetramethylene-tetranitramine crystals by the first-principles models. *Cryst. Growth Des.*, 15(8):3983–3991, 2015.

[23] H.-M. Shim, H.-S. Kim, and K.-K. Koo. Molecular modeling on supersaturation-dependent growth habit of 1,1-diamino-2,2-dinitroethylene. *Cryst. Growth Des.*, 15(4):1833–1842, 2015.

[24] J. Gibbs. *The Scientific Papers of J. Willard Gibbs, Vol. 1: Thermodynamics,*. Dover: New York, 1961.

[25] B. Mutaftschiev. *Handbook of Crystal Growth Vol. 1A, Fundamentals-Thermodynamics and Kinetics*, chapter 4: Nucleation Theory, pages 187–247. North Holland, Amsterdam, 1993.

[26] G. Wulff. On the question of speed of growth and dissolution of crystal surfaces. *Z. Kristallogr*, 34:449–530, 1901.

[27] C. Herring. Some theorems on the free energies of crystal surfaces. *Phys. Rev.*, 1951.

[28] R. Kern. *Morphology of Crystals: Part A*, chapter 2: The Equilibrium Form of a Crystal, pages 77–206. Terra Scientific Publishing Co.: Tokyo, 1987.

[29] Y. Zhang and M. F. Doherty. Simultaneous prediction of crystal shape and size for solution crystallization. *AIChE Journal*, 50(9):2101–2112, 2004.

[30] Y. Zhang, J. P. Sizemore, and M. F. Doherty. Shape evolution of 3-dimensional faceted crystals. *AIChE J.*, 52(5):1906–1915, 2006.

[31] F. C. Frank. On the kinematic theory of crystal growth and dissolution processes. In R. H. Doremus, B. W. Roberts, and D. Turnbull, editors, *Growth and Perfection of Crystals*, pages 411–419. New York: Wiley,, 1958.

[32] A. A. Chernov. Crystal growth forms and their kinetic stability. *Kristallografiya*, 8:87–93, 1963.

[33] A. Bravais. *Études Crystallographic*. Paris: Gauthier-Villars,, 1866.

[34] J. D. H. Donnay and D. Harker. A new law of crystal morphology extending the law of Bravais. *Am Mineral*, 22(5):446–467, 1937.

[35] M. G. Friedel. Etudes sur la loi de Bravais. *Bull Soc Franc Miner*, 30:326–455, 1907.

[36] C. Giacovazzo, H. Monaco, G. Artioli, D. Viterbo, M. Milanesio, G. Gilli, P. Gilli, G. Zanotti, and M. Catti. *Fundamentals of crystallography*. Oxford Univeristy Press Inc., New York, third edition edition, 2011.

[37] C. F. Macrae, P. R. Edgington, P. McCabe, E. Pidcock, G. P. Shields, R. Taylor, M. Towler, and J. van de Streek. Mercury: visualization and analysis of crystal structures. *Journal of Applied Crystallography*, 39(3):453–457, 2006.

[38] V. Bisker-Leib and M. F. Doherty. Modeling the crystal shape of polar organic materials: Prediction of urea crystals grown from polar and nonpolar solvents. *Crystal Growth & Design*, 1(6):455–461, 2001.

[39] M. Brunsteiner and S. L. Price. Morphologies of organic crystals: sensitivity of attachment energy predictions to the model intermolecular potential. *Cryst. Growth Des.*, 1(6):447–453, 2001.

[40] C. Lin, N. Gabas, J. Canselier, and G. Pépe. Prediction of the growth morphology of aminoacid crystals in solution: I. α-glycine. *Journal of Crystal Growth*, 191(4):791 – 802, 1998.

[41] P. Hartman and W. G. Perdok. On the relations between structure and morphology of crystals. I. *Acta Crystallogr.*, 1955.

[42] P. Hartman and W. G. Perdok. On the relations between structure and morphology of crystals. II. *Acta Crystallogr*, 1955.

[43] P. Hartman and W. Perdok. On the relations between structure and morphology of crystals. III. *Acta Crystallogr.*, 8(9):525–529, 1955.

[44] M. Frey, J.-C. Genovesio-Taverne, and J. C. Fontecilla-Camps. Application of the periodic bond chain (pbc) theory to the analysis of the molecular packing in protein crystals. *Journal of Crystal Growth*, 90(1):245 – 258, 1988.

[45] P. Hartman and P. Bennema. The attachment energy as a habit controlling factor: I. theoretical considerations. *Journal of Crystal Growth*, 49(1):145–156, 1980.

[46] T. Beyer, G. M. Day, and S. L. Price. The prediction, morphology, and mechanical properties of the polymorphs of paracetamol. *Journal of the American Chemical Society*, 123(21):5086–5094, 2001. PMID: 11457339.

[47] A. T. Anghel, G. M. Day, and S. L. Price. A study of the known and hypothetical crystal structures of pyridine: why are there four molecules in the asymmetric unit cell? *CrystEngComm*, 4:348–355, 2002.

[48] D. S. Coombes, C. R. A. Catlow, J. D. Gale, A. L. Rohl, and S. L. Price. Calculation of attachment energies and relative volume growth rates as an aid to polymorph prediction. *Crystal Growth & Design*, 5(3):879–885, 2005.

[49] E. van der Voort. The morphology of succinic acid crystals: The role of solvent interaction. *Journal of Crystal Growth*, 110(4):662 – 668, 1991.

[50] Z. Wang, P. Jiang, and L. Dang. The morphology prediction of lysozyme crystals deduced from the bfdh law and attachment energy model based on the intermolecular interaction. In *Bioinformatics and Biomedical Engineering (iCBBE), 2010 4th International Conference on*, 2010.

[51] P. Hartman. *Crystal Growth: an Introduction*, chapter Structure and morphology, pages 367–402. North Holland, Amsterdam, 1973.

[52] R. F. P. Grimbergen, H. Meekes, P. Bennema, C. S. Strom, and L. J. P. Vogels. On the Prediction of Crystal Morphology. I. The Hartman–Perdok Theory Revisited. *Acta Crystallographica Section A*, 1998.

[53] E. M. Walker, K. J. Roberts, and S. J. Maginn. A molecular dynamics study of solvent and impurity interaction on the crystal habit surfaces of ϵ-caprolactam. *Langmuir*, 14(19):5620–5630, 1998.

[54] J. J. Lu and J. Ulrich. An improved prediction model of morphological modifications of organic crystals induced by additives. *Cryst Res Technol*, 38(1):63–73, 2003.

[55] R. B. Hammond, K. Pencheva, V. Ramachandran, and K. J. Roberts. Application of grid-based molecular methods for modeling solvent-dependent crystal growth morphology: Aspirin crystallized from aqueous ethanolic solution. *Cryst Growth Des*, 7(9):1571–1574, 2007.

[56] J. Chen and B. L. Trout. Computer-aided solvent selection for improving the morphology of needle-like crystals: A case study of 2,6-dihydroxybenzoic acid. *Cryst Growth Des*, 10(10):4379–4388, 2010.

[57] L. Yang and Y. Dong. Crystal morphology study of N,N'-diacetylchitobiose by molecular dynamics simulation. *Carbohydr Res*, 346(15):2457–2462, 2011.

[58] Q. Yi, J. Chen, Y. Le, J. Wang, C. Xue, and H. Zhao. Crystal structure and habit of dirithromycin acetone solvate: A combined experimental and simulative study. *J Cryst Growth*, 372:193–198, 2013.

[59] E. J. Chan, R. Tejwani, and L. Derdour. Use of molecular simulation in calculating a characteristic relative growth effect curvature to correlate factors influencing crystalline growth and other properties. *Cryst Growth Des*, 15(12):5754–5766, 2015.

[60] I. V. Markov. *Crystal Growth for Beginners: Fundamentals of Nucleation, Growth and Epitaxy.* Singapore: World Scientific,, 2003.

[61] W. K. Burton, N. Cabrera, and F. C. Frank. The growth of crystals and the equilibrium structure of their surfaces. *Philos. Trans. R. Soc., A*, 243:299–358, 1951.

[62] W. Kossel. Zur theorie des kristallwachstums. *Nachr Ges Wiss Goettingen, Math-Phys Kl*, 1927:135–143, 1927.

[63] I. Stranski. Zur theorie des kristallwachstums. *Z Phys Chem*, 136(259):259–278, 1928.

[64] J. Zhang and G. H. Nancollas. Kink density and rate of step movement during growth and dissolution of an ab crystal in a nonstoichiometric solution. *J. Colloid Interface Sci.*, 200(1):131 – 145, 1998.

[65] F. Otalora and J. M. Garcia-Ruiz. Nucleation and growth of the naica giant gypsum crystals. *Chem. Soc. Rev.*, 43:2013–2026, 2014.

[66] A. A. Chernov, L. N. Rashkovich, and J. J. De Yoreo. ABC of kink kinetics and density in a complex solution. *AIP Conf Proc*, 916(1):34–47, 2007.

[67] J. Frenkel. On the surface motion of particles in crystals and the natural roughness of crystalline faces. *J. Phys. (Moscow)*, 9:392–398, 1945.

[68] M. A. Lovette and M. F. Doherty. Multisite models to determine the distribution of kink sites adjacent to low-energy edges. *Phys. Rev. E*, 2012.

[69] D. Elwell and H. J. Scheel. *Crystal Growth from High-Temperature Solutions*. London: Academic Press,, 1975.

[70] T. Kuroda. Growth of a crystal surface with non-uniformity in supersaturation due to laminar flow of solution along the surface. *J Cryst Growth*, 71(1):84–94, 1985.

[71] J. A. Dirksen and T. A. Ring. Fundamentals of crystallization: Kinetic effects on particle size distributions and morphology. *Chem Eng Sci*, 46(10):2389–2427, 1991.

[72] K. Chen and P. G. Vekilov. Evidence for the surface-diffusion mechanism of solution crystallization from molecular-level observations with ferritin. *Phys. Rev. E*, 2002.

[73] M. Uwaha. *Handbook of Crystal Growth, Second Edition, Vol. I, Fundamentals: Thermodynamics and Kinetics, and Transport and Stability*, chapter Chapter 8: Growth kinetics: basics of crystal growth mechanisms, pages 359–399. Elsevier B.V., 2014.

[74] W. R. Wilcox. Transport phenomena in crystal growth from solution. *Progress in Crystal Growth and Characterization of Materials*, 26:153 – 194, 1993.

[75] A. A. Chernov. *Modern Crystallography III: Crystal Growth*, volume 36. Berlin: Springer-Verlag,, 1984.

[76] P. Cubillas and M. W. Anderson. *Zeolites and Catalysis: Synthesis, Reactions, and Applications*, chapter 1: Synthesis Mechanism: Crystal Growth and Nucleation, pages 1–55. Wiley-VCH Verlag GmbH & Co. KGaA, 2010.

[77] M. Volmer. Über gerichtetes kristallwachstum (ordered crystal growth). *Z Phys.*, 9:193–196, 1922.

[78] A. E. Nielsen. *Kinetics of precipitation*. Pergamon Press Ltd. Oxford, 1964.

[79] B. Lewis. The growth of crystals of low supersaturation: I. theory. *Journal of Crystal Growth*, 21(1):29 – 39, 1974.

[80] H. M. Cuppen, H. Meekes, W. J. P. van Enckevort, and E. Vlieg. Birth-and-spread growth on the Kossel and a non-Kossel surface. *J Cryst Growth*, 286(1):188–196, 2006.

[81] A. Chernov, L. Rashkovich, and P. Vekilov. Steps in solution growth: dynamics of kinks, bunching and turbulence. *Journal of Crystal Growth*, 275(12):1 – 18, 2005. Proceedings of the 14th International Conference on Crystal Growth and the 12th International Conference on Vapor Growth and Epitaxy.

[82] G. H. Gilmer and P. Bennema. Simulation of crystal growth with surface diffusion. *J. Appl. Phys.*, 43(4):1347–1360, 1972.

[83] G. Gilmer. Growth on imperfect crystal faces: I. monte-carlo growth rates. *Journal of Crystal Growth*, 36(1):15 – 28, 1976.

[84] H. M. Cuppen, E. van Veenendaal, J. van Suchtelen, W. J. P. van Enckevort, and E. Vlieg. A Monte Carlo study of dislocation growth and etching of crystals. *J Cryst Growth*, 219(12):165–175, 2000.

[85] M. Rak, M. Izdebski, and A. Brozi. Kinetic Monte Carlo study of crystal growth from solution. *Comput Phys Commun*, 138(3):250–263, 2001.

[86] S. X. M. Boerrigter, H. M. Cuppen, R. I. Ristic, J. N. Sherwood, P. Bennema, and H. Meekes. Explanation for the supersaturation-dependent morphology of monoclinic paracetamol. *Cryst Growth Des*, 2(5):357–361, 2002.

[87] S. X. M. Boerrigter, G. P. H. Josten, J. Van De Streek, F. F. A. Hollander, J. Los, H. M. Cuppen, P. Bennema, and H. Meekes. MONTY: Monte Carlo crystal growth on any crystal structure in any crystallographic orientation; application to fats. *J Phys Chem A*, 108(27):5894–5902, 2004.

[88] S. Piana, M. Reyhani, and J. D. Gale. Simulating micrometre-scale crystal growth from solution. *Nature*, 438(7064):70–73, 2005.

[89] M. A. Deij, H. Cuppen, H. M.and Meekes, and E. Vlieg. Steps on surfaces in modeling crystal growth. *Cryst Growth Des*, 7(10):1936–1942, 2007.

[90] F. Falo, A. R. Bishop, P. S. Lomdahl, and B. Horovitz. Langevin molecular dynamics of interfaces: Nucleation versus spiral growth. *Phys. Rev. B*, 1991.

[91] S. Piana and J. D. Gale. Understanding the barriers to crystal growth: Dynamical simulation of the dissolution and growth of urea from aqueous solution. *Journal of the American Chemical Society*, 127(6):1975–1982, 2005. PMID: 15701033.

[92] S. Piana, F. Jones, and J. D. Gale. Assisted desolvation as a key kinetic step for crystal growth. *Journal of the American Chemical Society*, 128(41):13568–13574, 2006. PMID: 17031971.

Chapter 2

Rate Expressions for Kink Attachment and Detachment during Crystal Growth

Reproduced in part with permission from:

Jinjin Li, Carl J. Tilbury, Mark N. Joswiak, Baron Peters and Michael F. Doherty, "Rate Expressions for Kink Attachment and Detachment During Crystal Growth," *Crystal Growth & Design*, **2016**, *16*, 3313-3322.

DOI: 10.1021/acs.cgd.6b00292.

2.1 Introduction

The key underlying kinetic processes during crystal growth or dissolution are the attachment and detachment of growth units (atoms, molecules, ions, etc.) at lattice sites [1]; the balance between the two determines whether crystals grow or dissolve. The sites for attachment and detachment are special locations called kink sites, where growth

units can complete multiple interactions with neighbors in the lattice and adopt the solid-state configuration [2–5]. The importance of kink sites as the locales of crystal growth was first recognized in classic models proposed by Kossel and Stranski, where crystal growth was considered to progress by successive addition of growth units to a kink site until completion of the row (kink sites are renewable since incorporation at one regenerates a new kink site); the addition of a growth unit to this completed row would then reform a kink site and the process could continue [6–8]. In reality this addition of a growth unit to a completed row is seldom necessary, due to the continual creation of kinks from thermally induced step reorganizations [3, 9–11].

At low supersaturations, crystals usually possess well-defined facets that undergo layered growth, where successive layers of the interplanar spacing form as a result of spiral growth or 2D-nucleation mechanisms [2, 3]. Typically, under such conditions, bulk diffusion of growth units to and from the surface is sufficiently fast that the activated process of surface integration at kink sites is rate-determining [3]. Figure 2.1 shows a typical surface structure; the terrace corresponds to flat layers of the crystallographic plane and edges of incomplete layers are called steps. Kinks exist on steps even at equilibrium conditions where no crystal growth or dissolution occurs, as a result of thermal reorganization. The distribution of kink sites on the step can be estimated by considering Boltzmann statistics [9, 11]. An appropriately non-equilibrium formulation has also been developed [12] to predict the steady-state kink density under conditions of growth or dissolution (i.e., when the supersaturation ratio $S \neq 1$).

Modeling layered crystal growth via either a spiral or 2D-nucleation-and-growth mechanism requires the step velocity of each edge (v_i for edge i, see Chapter 3 for face growth rate expressions) [10,15–17]. Initial mechanistic expressions for v_i were formulated [10,18] via a diffusion problem, determining the flux towards each step. More recently, the step velocity on edge i (normal to the step) has been treated [1, 2, 8, 11, 16, 19–23] as limited

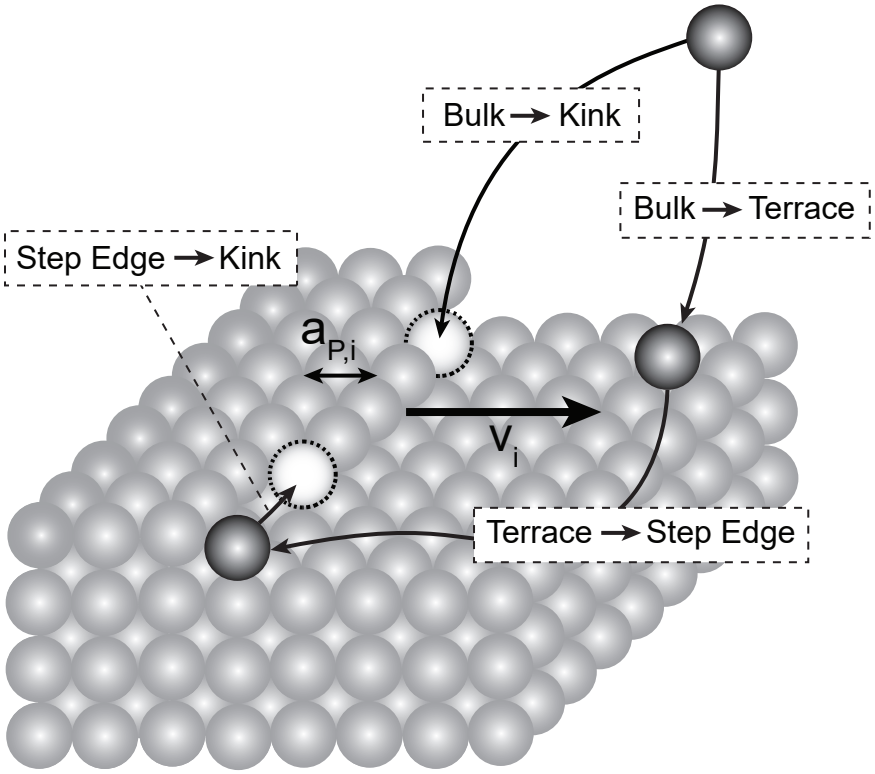

Figure 2.1: Schematic illustration of the surface structure on a faceted crystal with spherical growth units, indicating kink sites (white dashed circles), the step and the terrace. A direct bulk-to-kink incorporation mechanism is indicated alongside a terrace-edge-kink process. Although the latter is expected for organic molecular crystals [4, 10, 13, 14] (see also Chapter 4), both mechanisms have the same driving force and (for adsorption without dissociation) the same dependence on solute concentration in solution. The forward step velocity, v_i, results from successive incorporation events at each kink site, acting to advance the step a distance $a_{P,i}$ (the propagation length for a step monolayer).

by attachment and detachment kinetics,

$$v_i = a_{P,i}\rho_i u_i \tag{2.1}$$

where $a_{P,i}$ is the step propagation length, ρ_i is the kink density (kink sites per step edge site) and u_i is the kink rate (net rate of growth unit addition per kink site). The step propagation length is the magnitude in the edge normal direction (i.e., direction of step motion perpendicular to the step edge) of a vector connecting identical growth units in adjacent layers. For non-centrosymmetric growth units, it may be necessary to consider non-adjacent layers to connect identical growth units and then divide by the number of layers advanced to obtain an average, per-layer $a_{P,i}$. To further analyze eq 2.1, consider that $1/\rho_i$ represents the average number of sites (along the edge) each kink must advance in order to complete a new step row; $1/u_i$ represents the average time for a kink to advance one edge site (via growth unit incorporation). Therefore, the time to complete a new row is $1/(\rho_i u_i)$, which advances the step a distance $a_{P,i}$, justifying the form of eq 2.1 for the step velocity. Equation 2.1 assumes a single kink cycle on the edge; see Chapter 5 for a generalization beyond this, which is important for non-centrosymmetric growth units.

An alternative expression for v_i has also been utilized [1–3, 17–20], which takes the form

$$\begin{aligned} v_i &= \beta_i V_{m,X} C_{sat}(S-1) \\ &= a_{P,i}\rho_i V_{m,X} C_{sat}(S-1)\nu_0 \exp\left(-\frac{\Delta G^{\ddagger}}{kT}\right) \end{aligned} \tag{2.2}$$

$S = C/C_{sat}$ is the supersaturation ratio based on solute concentration, so $(S-1)$ corresponds to the driving force for crystallization; $V_{m,X}$ is the solute molar volume, so

$V_{m,X}C_{sat}$ represents the volume fraction of solute in solution; β_i is termed the step kinetic coefficient and is an edge-dependent proportionality constant (units length/time) producing the step velocity. The step kinetic coefficient can be formulated from TST, [2, 11, 16, 22, 24] Kramers-type barrier crossing, [2, 19, 25] or via a Smoluchowski-Debye incorporation pathway [2, 19]. In each case, β_i can be written in the form

$$\beta_i = a_{P,i}\rho_i\nu_0 \exp\left(-\frac{\Delta G^{\ddagger}}{kT}\right) \tag{2.3}$$

where ν_0 is a frequency factor and $\Delta G^{\ddagger}$ is the height of the attachment free energy barrier. Note that in TST, ν_0 involves kinematic factors, whereas in the Kramer's regime ν_0 involves the diffusion coefficient along the reaction coordinate at the top of the barrier, as well as the barrier curvature. For centrosymmetric growth units and certain rate expressions, eq 2.2 can be derived from eq 2.1.

Thus, the kink rate u_i is a critical quantity required to calculate the step velocity, which enables crystal growth to be modeled mechanistically. To this end, various sets of attachment/detachment rate expressions have been utilized in the literature to determine the kink rate [8, 20, 23, 26, 27], but it is not immediately obvious which expressions most accurately capture the underlying surface chemistry. To address this issue, we consider crystallization thermodynamics and detailed balance criteria to evaluate different sets of rate expressions, which leads us to make specific recommendations for the best rate expressions to use.

2.2 Kink Rate Calculation

Before examining attachment and detachment rate expressions, we first introduce the framework for their incorporation into the kink rate calculation. For crystals with

non-centrosymmetric growth units, kink sites do not generally contain the same set of interactions and are instead specific to that particular 'half-crystal' position; various sites can exist along on an edge. The case of a molecular (or dimeric, but not ionic) growth unit will be considered. The kink rate u_i represents the difference between opposing fluxes: the attachment rate of solute molecules into kink sites (j^+, assumed isotropic – see later) and the detachment rates of solute molecules from kink sites ($j^-_{k,i}$ for kink k on edge i); as successive kink attachments take place in series, these must be weighted by populations of the different kink types (i.e., the relative time spent in each state). Both j^+ and $j^-_{k,i}$ are event frequencies on a per kink site basis, so an appropriate expression for $u_{k,i}$ into kink k on edge i is

$$u_{k,i} = n(j^+ P_{k,i} - j^-_{k+1,i} P_{k+1,i}) \tag{2.4}$$

where $P_{k,i}$ is the probability of a kink existing as type k and n is the number of distinct kink sites for a single direction along the edge (i.e., all 'east' or all 'west' kinks [28]). Note that $P_{k,i}$ should not be confused with ρ_i; $P_{k,i}$ represents the fraction of kinks that exist as type k at steady-state and is determined from kinetics, whereas ρ_i represents the fraction of sites along the step edge that are kink sites (which we estimate from Boltzmann statistics). The prefactor n corresponds to the number of growth units within the repeat unit along the edge, where each growth unit represents distinct molecular orientations and/or interaction sets. This prefactor is necessary to ensure $u_{k,i}$ represents the net number of attaching growth units per kink site, as required by eq 2.1; it was wrongly omitted in our earlier formulations [22, 23, 29] of eq 2.4. For example, the case of $n = 2$ but identical kinetics (i.e., equivalent growth unit interactions), would have $P_k = 0.5$ (since the steady-state probabilities must be identical); the prefactor of $n = 2$ ensures $u_{k,i}$ retains the appropriate per kink site basis from j^+ and $j^-_{k,i}$. The form of eq 2.4

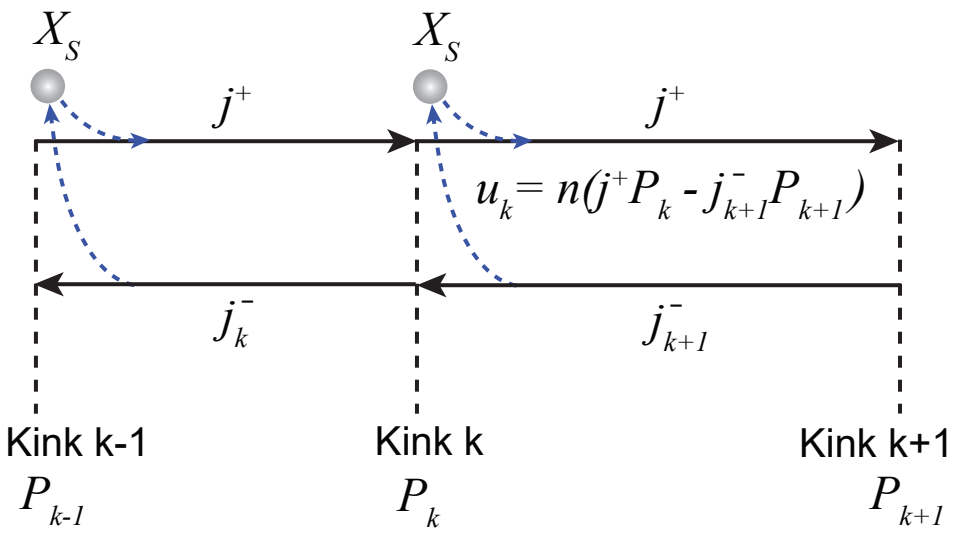

Figure 2.2: The kink rate is the net rate of growth unit incorporation per kink site; it is determined from attachment and detachment rates between kinks k and $k+1$, alongside the probabilities of kinks existing as such types. X_S refers to a growth unit in solution; each transition between adjacent kink sites exchanges a growth unit with the solution.

reflects the net transition rate through the kink site progression, according to the edge periodicity; this is also illustrated in Figure 2.2 (subscript i removed for clarity).

The steady-state master equation (eq 2.5, i subscripts omitted) accounts for each relevant transition into or out of kink k [23].

$$(j^+ + j_k^-)P_k = j^+P_{k-1} + j_{k+1}^-P_{k+1} \tag{2.5}$$

Kink k is created upon attachment to kink $k-1$ or detachment from kink $k+1$, while it is destroyed upon either attachment to or detachment from kink k. At steady-state these rates balance exactly, leading to no change in the kinetic distribution of kinks; as mentioned before, P_k represents the fraction of kinks on the step edge that exist as type k. Note that this probability distribution of kink sites determined from steady-state kinetics ignores thermal reorganization of the step edge, which we expect to occur on a

longer timescale than the individual kinetic processes.

Solving eq 2.5 for j^+P_k and substituting into eq 2.4 yields

$$u_{k,i} = n(j^+P_{k-1,i} - j^-_{k,i}P_{k,i}) = u_{k-1,i} \tag{2.6}$$

By recursion, the steady-state solution of the kink rate is necessarily the same for each kink site within the same cycle; the k subscript can be dropped assuming a single cycle is considered. Solving for the P_k's (using $n-1$ iterations of eq 2.5 and $\sum_{k=1}^{n} P_k = 1$), one obtains the following equations for the kink rate on edge i in terms of the attachment and detachment rates from different kink sites [23]:

$$u_i = n\frac{(j^+)^n - \prod_{k=1}^{n} j^-_{k,i}}{\sum_{r=1}^{n}(j^+)^{n-r}(j^-_i)^{r-1}}, \tag{2.7}$$

$$(j^-_i)^{r-1} = \sum_{k=1}^{n}(j^-_k j^-_{k+1}\cdots j^-_{k+r-2})_i \tag{2.8}$$

A reasonable estimate of an upper bound to n is the number of asymmetric molecules in the unit cell (i.e., $n \leq ZJ$, where Z is the number of asymmetric units within the cell and J is the number of molecules in the asymmetric unit); this allows for an edge that cycles through each molecular orientation within the lattice. Chains where $n > ZJ$ necessitate duplicate instances of a specific orientation within the chain's repeat unit, which seems highly unlikely to produce a 'straight' chain that is favorable to bound crystallization surface structures such as spirals and 2D nuclei. The total number of kink sites is $2n$, considering both east and west orientation directions. The periodic progression of an edge through different kink sites is analogous to the progression around a catalyzed reaction cycle (kink sites could be viewed as catalysts enabling lattice incorporation; they are regenerated upon the attachment of n growth units). Thus, eq 2.7 resembles the

kinetic analysis of catalytic cycles developed by Christiansen and Temkin [30–32] (the prefactor n illustrates that lattice incorporation occurs during each $k \rightarrow k+1$ transition). If a multi-process (terrace $\rightarrow$ edge $\rightarrow$ kink) incorporation mechanism is adopted, only the nearest-neighbor interactions parallel to an edge must be used within the detachment rate $j^-_{k,i}$. Since there exists a cyclic interaction periodicity along the edge, eq 2.7 provides the same kink rate in both the east and west directions for this case.

Multiplying ρ_i (which represents every type of kink) by the kink rate u_i provides the rate at which a new row forms on the step edge, which is converted into a velocity by $a_{P,i}$. Introduction of the prefactor n in eq 2.7 permits it to collapse to the well-known centrosymmetric expression,

$$u = j^+ - j^- \tag{2.9}$$

for both isotropic $j^-_{k,i} = j^-$ cases (i.e., $n > 1$ but $\Delta W_{k,i}$ are all equal) and the case $n = 1$, where the i subscript has been removed since the detachment rate is no longer edge-dependent (due to the symmetry, this is discussed later). For the centrosymmetric case at equilibrium, eq 2.9 requires that $j^+ = j^-$ in order to ensure the net rate of incorporation is zero.

The crystallization environment (e.g., solvent, additives, impurities, counterions, temperature, etc.) can dramatically influence the rates of attachment and detachment, so rate expressions providing an accurate description of reality are important in order to capture these effects and facilitate rational crystal engineering. We subsequently evaluate various rate expressions and summarize our recommendation for the case that best captures the underlying kinetics and thermodynamics.

2.3 Attachment and Detachment Rate Expressions

Figure 2.3 illustrates the activated attachment and detachment directly from bulk solution. State S corresponds to a growth unit in solution, which, along with the kink site, is solvated (the solvent molecules are indicated by the blue V's in Figure 2.3). The transition state ‡ corresponds to partial desolvation between the growth unit and kink site. At state X the surface is re-solvated following growth unit incorporation. Chernov is credited [2] with first considering the growth process as a "reaction" and connecting this incorporation barrier to desolvation under solution growth, which remains the consensus [1, 2, 17, 19, 22, 23, 33]. The reaction coordinate, q, characterizes progress toward incorporating a single growth unit, and it can be comprised of various collective variables, such as distances [34], coordination numbers [35], energy gaps [36], local water density [37] etc. It is assumed that a reaction coordinate exists which yields the free energy profile shown in Figure 2.3, with two basins (S and X) separated by a high free energy barrier ($\Delta G^{\ddagger}$ at state ‡); under equilibrium conditions the free energy difference between S and X becomes zero.

A similar diagram might be constructed for the mechanism of attachment/detachment from sites adjacent to the kink, as depicted in Figure 2.1 (a model for terrace-mediated incorporation is developed in Appendix 2.A). Each process in such a terrace-mediated mechanism will give rate laws that have the same dependence on solute concentration in solution as the direct-from-solution attachment mechanism. The one exception is cases where diffusion on the terrace becomes rate-limiting and zeroth order in solute concentration, due to a fractional coverage of terrace-adsorbed growth units (θ^T) that approaches unity. We assume θ^T is small and, therefore, adopt an effective direct attachment rate expression that is first order in dissolved solute for all subsequent analysis.

Adopting a standard definition of rate constants leads to eqs 2.10 and 2.11 for at-

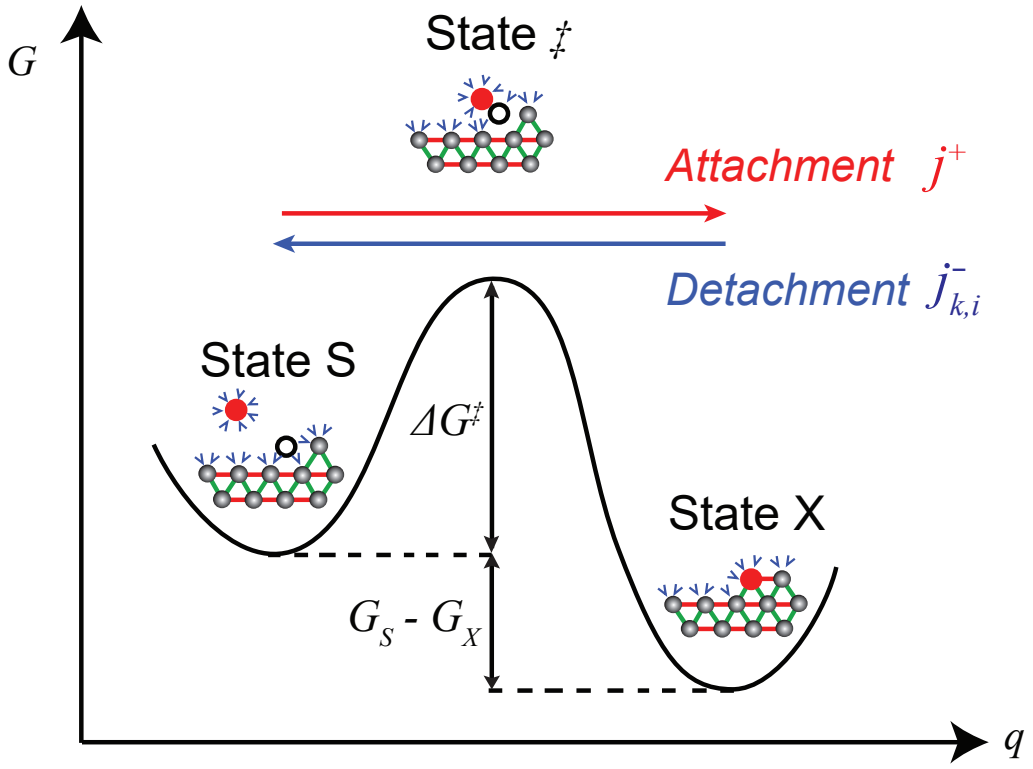

Figure 2.3: Schematic diagram of the detachment (rate $j^-_{k,i}$) and attachment (rate j^+) processes to/from bulk solution and the corresponding free energy profile along the reaction coordinate, q. At state ‡, $\Delta G^‡$ represents the free energy barrier for partial desolvation in the incorporation direction; this is required to progress from state S (growth unit in solution and kink $k-1$ solvated) to state X (growth unit attached forming kink k on step i and surface re-solvated). $G_S - G_X$ is the free energy difference between states S and X, which depends on the supersaturation ($G_S - G_X > 0$ for a supersaturated solution). A simple interpretation of the reaction coordinate q could be a relation to the distance of the growth unit from the kink site. The filled red circles represent the molecule which is attaching to/detaching from the kink site, and the open black circle represents the unoccupied kink site.

tachment and detachment, respectively:

$$k^+ = \nu_0 \exp\left(-\frac{\Delta G^\ddagger}{kT}\right) \tag{2.10}$$

$$k^-_{k,i} = k^+ \exp\left(-\frac{\Delta G^0_{k,i}}{kT}\right) \simeq k^+ \exp\left(-\frac{\Delta W_{k,i}}{kT}\right) \tag{2.11}$$

where a frequency factor ν_0 and energy barrier $\Delta G^\ddagger$ appear, similar to eq 2.2. As indicated previously, for solution growth the barrier $\Delta G^\ddagger$ is expected to result largely from desolvation. For vapor growth, $\Delta G^\ddagger$ is expected [20] to result instead from orientational effects (imposing a small barrier). The additional barrier $\Delta G^0_{k,i}$ in the detachment rate constant represents the standard free energy required to detach a growth unit from a kink-incorporated state. Note that the Δ corresponds to solution–crystal (in lieu of final–initial) as is commonly practiced in describing thermodynamics of crystal growth [2]. Additionally, $\Delta G^0_{k,i}$ is not equal to $G_S - G_X$, in which the difference is entirely due to the supersaturation in solution and vanishes for $x = x_{sat}$ (x is the mole fraction of solute in solution). In a mechanistic approach to morphology predictions, the entropic portion of $\Delta G^0_{k,i}$ is often assumed to be zero [11, 16, 22, 23, 28, 33], in order to facilitate rapid calculations that are useful for guiding experiments. Under such an approach, $\Delta G^0_{k,i}$ is calculated as the energetic detachment work from kink k on edge i, $\Delta W_{k,i}$. This is most justifiable for a solute molecule displacing a single solvent molecule upon attachment, as the reduction in degrees of freedom for the solute can be compensated by the corresponding gain from the freed solvent [2]. This detachment work, $\Delta W_{k,i}$, represents the change in energy between initial and final states (i.e., under the formulation here, the work required to detach from kink to solution). In vapor growth, $\Delta W_{k,i}$ represents the periodic bond chains in the solid-state lattice that must be broken to detach a growth unit. In solution growth, $\Delta W_{k,i}$ must consider the surface energy penalty of the created

faces in the terrace, edge and kink directions, in order to account for the solvent-induced energetic modification of these interfacial energies. See Chapters 4 and 5 for more details (the general expression for $\Delta W_{k,i}$ is given by eq 5.15).

For molecular crystals, to a first approximation k^+ is considered isotropic on each kink on each edge on each face. This enables relative growth rate predictions and the calculation of crystal shapes without the need for accurate estimates of ν_0 and $\Delta G^{\ddagger}$. Calculation of these quantities requires molecular simulations, but the potential number of kink sites for crystal systems with non-centrosymmetric growth units renders this approach somewhat impractical as an engineering tool. This isotropic approximation is most justifiable for centrosymmetric molecules, where the same set of interactions exist on each kink site on each edge on each face. Solvation effects should, therefore, be approximately uniform when considering the transition from solution to crystal. For centrosymmetric growth units the detachment work, $\Delta W_{k,i}$, is also necessarily isotropic due to the same symmetry, leading to a constant value $k^-_{k,i} = k^-$.

Various pairings of rate expressions, j^+ and j^-, for attachment to and detachment from kink sites, respectively, have been employed. To compare each case, we employ thermodynamic relations for a crystal–solution system and discuss kinetic implications in regards to the kink rate. For simplicity, we focus on centrosymmetric growth units first before discussing non-centrosymmetric growth units.

The chemical potentials of the solute in solution (μ_S) and crystal (μ_X) can be written as

$$\mu_S = \mu_S^0 + kT\ln a = \mu_S^0 + kT\ln \gamma x \tag{2.12}$$

$$\mu_X = \mu_X^0 \tag{2.13}$$

where a is the solute's activity in solution; γ is the corresponding activity coefficient

and x is its mole fraction. At equilibrium, $\mu_S(x_{sat}) = \mu_X$; thus, the driving force for crystallization is zero, $\Delta\mu = \mu_S - \mu_X = 0$, which defines the solute solubility mole fraction, x_{sat}. It follows that the equilibrium constant for crystallization is $K_{eq} = a_X/a_{sat} = 1/x_{sat} = k^+/k^-$ (a_X is the crystal activity, which is equal to unity; a_{sat} is the activity of solute in a saturated solution, which is equal to x_{sat} assuming a solution activity coefficient of unity). The rate constants correspond to attachment to and detachment from kink sites because these processes (i) are rate limiting and (ii) do not alter the surface (i.e. no change in surface free energy). Furthermore, the standard Gibbs free energy change (per growth unit exchange between crystal and solution) is $\Delta G^0 = \mu_S^0 - \mu_X = kT \ln K_{eq}$, which can, therefore, be related to solubility: $x_{sat} = e^{-\Delta G^0/kT}$. Note that μ_S^0 is the standard state chemical potential of the solute in solution and also note that ΔG^0 is greater than zero, consistent with $x_{sat} < 1$.

Under conditions of crystal growth, the driving force becomes

$$\frac{\Delta\mu}{kT} = \ln\frac{a}{a_{sat}} = \ln\frac{\gamma x}{\gamma_{sat} x_{sat}} = \ln\frac{\tilde{\gamma} C}{\tilde{\gamma}_{sat} C_{sat}} = \ln S \tag{2.14}$$

The common definitions of supersaturation ratio are $S = x/x_{sat}$ and $S = C/C_{sat}$, which arise from the assumptions that $\gamma = \gamma_{sat}$ and $\tilde{\gamma} = \tilde{\gamma}_{sat}$ (i.e., equal activity coefficients for supersaturated and saturated solutions, which should be appropriate for small x; note that $\tilde{\gamma}$ is the activity coefficient based on solute concentration). In the subsequent analysis we adopt $S = x/x_{sat}$ as our definition of supersaturation. Upon attachment of a growth unit to a kink site, the free energy of the system will decrease by $\Delta\mu$ (no change in the surface free energy). While this change is in terms of the chemical potential of the solute, it also includes changes to the solvent through the definition μ_S. That is, μ_S is the *total* free energy change of the solution upon a differential change in the number of solute molecules in solution.

A good set of rate expressions should follow the aforementioned thermodynamic relations for crystallization. Namely, we expect that $k^-/k^+ = x_{sat}$ and $G_S - G_X = \Delta\mu = kT \ln S$ (G_S and G_X are the free energies of states S and X in Figure 2.3). To test the validity of rate expression sets, we adopt a relationship with the same form as detailed balance that connects attachment and detachment rates under both equilibrium and non-equilibrium conditions; for centrosymmetric growth units this is [1, 21, 38, 39]

$$j^+ \exp\left(-\frac{G_S}{kT}\right) = j^- \exp\left(-\frac{G_X}{kT}\right) \tag{2.15}$$

Note that the rate j^+ is the rate of transition from state S to X (vice versa for j^-) and the probabilities of states S and X are related to their free energies. At equilibrium ($S = 1$), $G_S = G_X$ and $j^+ = j^-$; this is consistent with the kinetics expressed in eq 2.9 and represents both detailed balance and microscopic reversibility. Combining eqs 2.14 and 2.15 ($G_S - G_X = \Delta\mu$) yields a relationship between rate expressions and supersaturation

$$\ln \frac{j^+}{j^-} = \frac{G_S - G_X}{kT} = \ln S \tag{2.16}$$

Various treatments of crystal growth [23,27] have used a simple set of rate expressions:

$$j^+ = k^+ S \tag{2.17}$$

$$j^- = k^- \tag{2.18}$$

In eq 2.17 the attachment process at a kink site is indirectly first order in the mole fraction of solute in solution ($j^+ = (k^+/x_{sat})x$), based on the need for solute growth units to exist in solution if they are to adsorb and eventually incorporate at a kink. However, the detachment process in eq 2.18 is conversely zeroth order, since by definition a molecule that could potentially detach already exists adjacent to each unoccupied

kink site. Equating eqs 2.17 and 2.18 at $S = 1$ leads to $k^+/k^- = 1 \neq 1/x_{sat}$, where the inequality emphasizes that this pair of rate expressions does not agree with the thermodynamic expectation. Additionally, the step velocity should be influenced by solubility [40], which does not result from eqs 2.17 and 2.18. Thus, we do not recommend eqs 2.17 and 2.18 and have not considered this set as a candidate case for further study.

Instead, the rate expressions must include an explicit solute dependence. An attachment rate that is first order in x and a detachment rate that is zeroth order in x is considered in each subsequent case that we investigate. The kink density is accounted for in the step velocity through eq 2.1, removing the need to consider the concentration of kink sites in rate expressions. Note that one could remove the kink density from eq 2.1 and make the attachment rate "bimolecular" (e.g., $j^+ = k^+\rho_i x$) and the detachment rate "monomolecular" (e.g., $j^-_{k,i} = k^-\rho_i$). This provides an alternative view of these processes but results in the same expression for step velocity. It does suggest, however, that k^+ and $k^-_{k,i}$ should actually be considered as second and first order rate constants, respectively, since the rates are essentially multiplied by kink densities within eq 2.1. However, the beauty of rate expressions that use mole fractions is that their rate constants always have units of inverse time, regardless of the reaction "order". This is not true for concentration-based rate expressions.

Next, we discuss three different cases of rate expressions in more detail. We have cast these expressions into "reaction schemes", which are shown in Table 2.1. The significant difference between these cases is how the solvent near the kink site is treated. The inclusion of solvent in the rate expressions has more commonly been interpreted as accounting for the absence of a solute growth unit nearby the kink. We discuss this in more detail for case II rate expressions. While the net reaction for case III is equivalent to case I, it may be important to account for the non-reacting solvent in the rate expressions (there are many cases where rate laws explicitly involve seemingly innocent spectator solvents [41]

or carrier gas species [42]).

Table 2.1: The three descriptions of attachment and detachment rates that we examine. X_S is a crystal growth unit in solution, X_k represents kink site k and W corresponds to the solvent and any solvation-assisting species; x_W is the corresponding mole fraction.

	"Reaction scheme"	j^+	$j^-_{k,i}$
Case I	$X_S + X_k \rightleftarrows X_{k+1}$	$k^+ x_{sat} S$	$k^-_{k,i}$
Case II	$X_S + X_k \rightleftarrows X_{k+1} + W$	$k^+ x_{sat} S$	$k^-_{k,i} x_W$
Case III	$X_S + X_k + W \rightleftarrows X_{k+1} + W$	$k^+ x_{sat} S x_W$	$k^-_{k,i} x_W$

2.3.1 Case I

The next set of expressions are of the form in eq 2.19 and 2.20 and shall be termed case I (note eq 2.19 now contains solubility-dependence).

$$j^{+I} = k^+ x = k^+ x_{sat} S \tag{2.19}$$

$$j^{-I} = k^- \tag{2.20}$$

This form has been presented [8,20] for use in the kink rate, both when state S corresponds to the vapor (under sublimation growth) and when state S corresponds to a terrace-adsorbed growth unit. The adoption of such rate expressions may have been influenced by previous treatments [10, 43] for other processes deemed important to crystal growth (e.g, terrace adsorption/desorption).

Here, the solvent molecules or solvation-assisting species are not considered as reactants in either the forward or reverse reaction. The forward reaction at a kink site (X_k) only requires an approaching growth unit (X_S), while the reverse reaction by definition has a detachable growth unit at the kink site. The resulting reaction is $X_S + X_k \rightleftarrows X_{k+1}$. For this scheme, the attachment rate (j^{+I}, eq 2.19) is, therefore, a first-order reaction

depending on the solute mole fraction in solution $x = x_{sat}S$, with the rate constant k^+ (eq 2.10), which is assumed isotropic as discussed earlier. The detachment rate (j^{-I}, eq 2.20) is instead zeroth order with rate constant k^- (eq 2.11). For these rate expressions, influence of the growth environment resides exclusively within the energy barriers.

In a saturated solution ($S = 1$), a centrosymmetric growth unit requires $j^{+I} = j^{-I}$, which under case I implies $x^I_{sat} = k^-/k^+$, which is in agreement with expectations from thermodynamics. Note that the subsequent relationship between detachment work and solubility is $x^I_{sat} = e^{-\Delta W/kT}$. In practice, the detachment work is computed based on an atomistic force field and bulk interface approximations to account for the solvent; ΔW is then employed to self-consistently determine x_{sat}. The reverse, defining ΔW based on the solubility, is more difficult because x_{sat} for the atomistic force field employed in modeling (i.e., to find periodic bond chains) is almost never known.

We refer to the free energy difference between states S and X (Figure 2.3) as $\Delta G = G_S - G_X$. Using case I rate expressions and x^I_{sat} in eq 2.15 yields $\Delta G^I = kT\ln S$, which agrees with that expected from crystallization thermodynamics (eq 2.16). Using eqs 2.19, 2.20 and x^I_{sat} in eq 2.9 leads to a centrosymmetric kink rate and step velocity of the form:

$$u^I = k^-(S-1) \tag{2.21}$$

$$v_i = a_{P,i}\rho_i u^I = a_{P,i}\rho_i k^-(S-1) \tag{2.22}$$

Note v_i contains the expected $(S-1)$ scaling that appeared in eq 2.2; this dependence has also been experimentally observed [19, 44, 45]. Incorporating eq 2.11 into eq 2.21 produces eq 2.23 (i and k subscripts dropped given the isotropic nature):

$$u^I = k^+\exp\left(-\frac{\Delta W}{kT}\right)(S-1) \tag{2.23}$$

A steady-state kinetic analysis of a multi-process incorporation mechanism is detailed in Appendix 2.A and results in the following kink rate:

$$u^I = k^{+T}\exp\left(-\frac{\Delta W_i^K + \Delta W_i^E + \Delta W^T}{kT}\right)(S-1) \tag{2.24}$$

$$k^{+T} = \nu_0\exp\left(-\frac{\Delta G^{\ddagger T}}{kT}\right) \tag{2.25}$$

where k^{+T} is the rate constant for terrace adsorption. The sum of the terrace, edge and kink detachment work (ΔW^T, ΔW_i^E and ΔW_i^K, respectively) corresponds to the overall crystal-to-solution detachment work, ΔW ($\Delta W_{k,i}$ for non-centrosymmetric growth units). For molecular crystals, the transition state desolvation barrier for terrace adsorption ($\Delta G^{\ddagger T}$) can be assumed isotropic (i.e., the same for each face) in a similar fashion to $\Delta G^{\ddagger}$. Therefore, with k^+ and k^{+T} both being isotropic, relative growth rate predictions using either the solution-to-kink (eq 2.23) or multi-process (terrace adsorption, edge adsorption, kink attachment; eq 2.24) mechanism will be identical.

2.3.2 Case II

An alternative pair of rate expressions (termed case II) has been presented [20, 26] for the kink rate under solution growth

$$j^{+II} = k^+ x = k^+ x_{sat} S \tag{2.26}$$

$$j^{-II} = k^- x_W = k^-(1 - x_{sat} S) \tag{2.27}$$

where x_W is the solvent mole fraction. Case II has been used extensively [11, 16, 22, 33] in recent mechanistic crystal growth modeling. Accounting for the solvent mole fraction ($x_W = 1 - x$) in the detachment rate is designed to represent the requirement of free

space in solution within the region around the kink site. The case II reaction scheme ($X_S + X_k \rightleftarrows X_{k+1} + W$) effectively considers the solvent as a product of the attachment process that becomes liberated from solvating the crystal surfaces.

Equating $j^{+II} = j^{-II}$ at $S = 1$ results in an expression for the centrosymmetric solubility: $x_{sat}^{II} = k^-/(k^+ + k^-)$. This differs from that expected from our thermodynamic analysis. Using case II rate expressions and x_{sat}^{II} in eq 2.15 yields

$$\Delta G^{II} = kT \ln S - kT \ln \frac{x_W}{x_{W,sat}} \tag{2.28}$$

where $x_{W,sat}^{II}$ is the solvent mole fraction at saturation (i.e. $x_{W,sat}^{II} = 1 - x_{sat}^{II}$). The last term in eq 2.28 appears to represent a change in the solvent chemical potential upon growth unit attachment. However, there is no solvent driving force for crystallization; the case II rate expressions do not align with the expected $\Delta G = kT \ln S$.

Interestingly, while case II does not reproduce the required thermodynamic relations, it still yields the same kink rate as case I, eq 2.21, upon using the self-consistent solubility x_{sat}^{II} (this equivalence only holds for centrosymmetric growth units). Note that the solubilities computed with case I and case II expressions are not equivalent, though for most crystals the difference is less than 10% and this difference decreases as ΔW increases.

2.3.3 Case III

Another formulation for the rate expressions is provided by eqs 2.29 and 2.30 (case III). The detachment rate is the same as case II, but now x_W is also included in the attachment rate to involve the solvent in both processes. This represents a reaction scheme where the solvent molecules do not just act as spectators and are necessary to

achieve the correct kinetics: $X_S + X_k + W \rightleftarrows X_{k+1} + W$.

$$j^{+III} = k^+ x x_W = k^+ x_{sat} S(1 - x_{sat} S) \tag{2.29}$$

$$j^{-III} = k^- x_W = k^-(1 - x_{sat} S) \tag{2.30}$$

The expression for centrosymmetric solubility (from $j^{+III} = j^{-III}$ at $S = 1$) is identical to case I: $x_{sat}^{III} = k^-/k^+$. From incorporating case III rate expressions and x_{sat}^{III} into eq 2.15, the involvement of solvent in both processes reduces the free energy change during crystallization to that expected from thermodynamics: $\Delta G^{III} = kT\ln S$. Therefore, cases I and III are equivalent from the perspective of our test criteria. The kink rate for case III is simply $u^{III} = u^I \left(1 - x_{sat}^I S\right)$. This relation is valid for non-centrosymmetric growth units as well (see Appendix 2.B).

Case III is designed to account for a strong effect of solvent molecules acting beyond spectator species (i.e., participating in both attachment and detachment kinetics). Such effects can be captured through mass-action rate law dependence [46] and would be most pronounced in mixed solvent crystallization, where x_W can vary appreciably. Nonetheless, a stronger effect might instead be changing activity coefficients as a result of the multicomponent growth medium. For crystallization from pure solvents (i.e., $x_W \approx 1$), the presented mass-action dependence will have a weak effect and the utility of case III over case I is minimal.

2.4 Discussion of Cases

Each of these three cases of rate expressions portrays slightly different chemistry, as displayed in the "reaction" schemes (Table 2.1). For centrosymmetric growth units the choice of case does not have an impact on relative growth rates or shape predictions (the

kink rates for cases I and II are in fact identical). Thus, for centrosymmetric growth units, the principal source of step velocity anisotropy is the kink density. Steps with high kink energies will have low kink densities and low step velocities, which can lead to low face growth rates, though the entire set of in-plane edges, including their crystallographic orientations, must be considered. For non-centrosymmetric and/or ionic growth units, the choice of case does affect the computed kink rate. Furthermore, the choice of case impacts the attachment rate, even for centrosymmetric growth units, as the computed value of x_{sat} differs. The attachment rate is important for a mechanistic description of 2D nucleation (see Chapter 3); the case-dependent x_{sat} implies that the same supersaturation represents different solution compositions under different cases.

Rate expressions should be selected to form an accurate mechanistic description for non-centrosymmetric and/or ionic growth units (or centrosymmetric growth units under a 2D-nucleation regime). These expressions should obey detailed balance, i.e., predict the correct change in free energy upon kink incorporation. As shown earlier in the text for centrosymmetric growth units, cases I and III obey detailed balance but case II does not (unless a self-consistent, but incorrect, form of x_{sat} is adopted). This is also the case for non-centrosymmetric growth units, which is shown in Appendix 2.B. Although they have significant thermodynamic differences, the calculated kink rates for case I and case II (identical for centrosymmetric growth units) remain similar for non-centrosymmetric growth units. This is shown in Figure 2.4 for a non-centrosymmetric growth unit with $n = 2$. As ΔW_1 and ΔW_2 become more similar the crystal system approaches the centrosymmetric result, where the two cases converge as expected. Note also that the discrepancy between case I and II increases with S and at low supersaturations the kink rates are essentially identical. The overall similarity may be due to the self-consistent determination and use of x_{sat} in each case.

Another notable difference between cases I and II for non-centrosymmetric growth

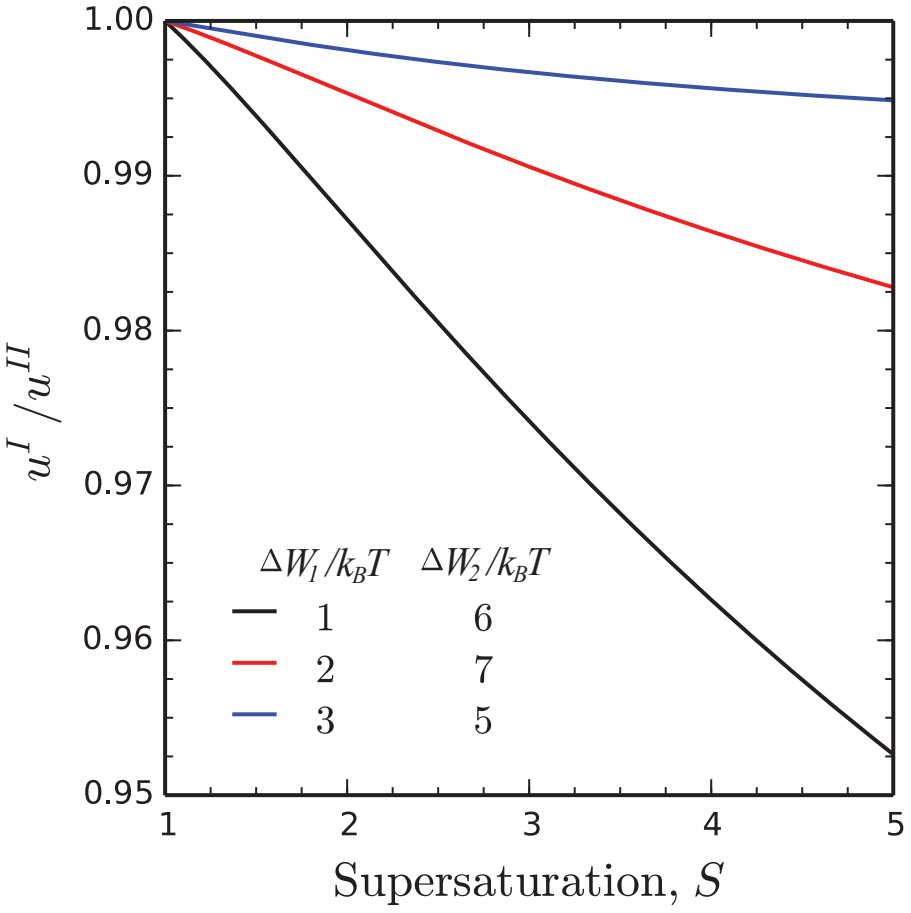

Figure 2.4: Plot of the ratio between case I and II kink rates for a non-centrosymmetric growth unit with two different kink sites ($n = 2$) and various pairs of ΔW_1 and ΔW_2. See Appendix 2.B for the non-centrosymmetric kink rate expressions.

units is in the relation between solubility and the average detachment work per kink site along edge i, $\overline{\Delta W_i} = \sum_{k=1}^{n} \Delta W_{k,i}/n$. Note that n is the number of different kink sites (in a single direction) along the edge and thus the addition of n growth units to an edge does not alter the surface structure.

$$\text{Case I}: \ln x_{sat}^{I} = -\frac{\overline{\Delta W_i}}{kT} \tag{2.31}$$

$$\text{Case II}: \ln \frac{x_{sat}^{II}}{1 - x_{sat}^{II}} = -\frac{\overline{\Delta W_i}}{kT} \tag{2.32}$$

Equations 2.31 and 2.32 (see Appendix 2.B for derivation) display the scaling of solubility with temperature, which, for case I, is in line with the van't Hoff relationship. Both are of the form $\Delta G^0/kT = \ln K_{eq}$; the key difference is that they pertain to different crystallization equilibrium constants:

$$\text{Case I}: K_{eq}^{I} = \frac{1}{x_{sat}^{I}} \tag{2.33}$$

$$\text{Case II}: K_{eq}^{II} = \frac{1 - x_{sat}^{II}}{x_{sat}^{II}} \tag{2.34}$$

The equilibrium constant for case I agrees with our earlier thermodynamic treatment, while case II disagrees.

To summarize, we determined the thermodynamic and kinetic implications of *assuming* different rate expressions (Table 2.1) for attachment to and detachment from kink sites. We found that rate expression sets under cases I and III agreed with crystallization thermodynamics, whereas case II disagreed. From a kinetic viewpoint, cases I and II predict the same kink rate for centrosymmetric crystals (so long as x_{sat} and/or ΔW are determined self-consistently). However, the non-centrosymmetric kink rates for cases I and II are not equivalent, but are approximately identical at low supersaturations. For

sparingly soluble compounds (i.e. large ΔW), case II will collapse to case I.

2.5 Conclusions

Kink sites are the locations where growth units incorporate into the crystal lattice under layered growth mechanisms. The net attachment rate is an important quantity required to calculate the step velocity of a spiral or 2D nucleus edge, which is essential for mechanistic growth shape predictions. In this chapter, three sets of expressions for attachment and detachment processes have been presented, which differ in how to account for the solvent (or absence of a growth unit). The thermodynamic implications of assuming cases I and III agree with crystallization thermodynamics, whereas case II disagrees. Cases I and III account for the solvent in the attachment and detachment process, via the activation barrier (I and III) and as a reactant/product (III only). While it is generally accepted that the solvent impacts $\Delta G^{\ddagger}$, it is unclear if the solvent should be considered as a reactant/product. Cases I and III appear equally valid, but it seems that case III has no practical advantages except where the active solvent molecule is a minor component of the solvent mixture.

For centrosymmetric growth units, it is not necessary to distinguish between cases; relative growth rates (under the spiral mechanism) are unaffected. However, for non-centrosymmetric or ionic growth units the kink rate does depend on which set is adopted, which could potentially affect morphology predictions. It should be noted that cases I and II are nearly identical at low supersaturations or for low kink anisotropy (i.e., low range of $\Delta W_{k,i}$'s) because of conventions for defining solubility and detachment free energy; thus, errors introduced through the use of case II may be insignificant under such conditions. Nonetheless, in addition to the more rigorous agreement of case I with crystallization thermodynamics, which should bestow increased accuracy under more general conditions,

it also presents the advantage of simplicity and so is clearly preferable.

Although we have not discussed the inclusion of additives in these rate laws, they have been shown to have a significant impact on the growth of calcite [47–49], and many other crystals [50, 51], via a variety of mechanisms. For example, additives can assist desolvation and thus alter the energy barrier, $\Delta G^{\ddagger}$. Additionally, the additive–surface interaction may differ significantly from the solvent–surface interaction. The interfacial surface energies should be appropriately modified to account for the work of adhesion from all species in solution. Additives also have the ability to adsorb differently on each crystal face, step or kink as a result of their interaction anisotropies [52], which can affect crystal shapes by modifying the surface chemistry at different locations. Beyond affecting surface energies, additives can have mechanistic effects, such as kink density reduction [18, 53], step pinning [54] and spiral pinning [52, 55]. These effects can potentially have dramatic morphological impacts at low additive concentrations.

Appendices

2.A Microkinetic Growth Unit Incorporation Model

Reproduced in part with permission from Carl J. Tilbury, Daniel A. Green, William J. Marshall and Michael F. Doherty, "Predicting the Effect of Solvent on the Crystal Habit of Small Organic Molecules," *Crystal Growth & Design*, **2016**, *16*, 2590–2604. DOI: 10.1021/acs.cgd.5b01660.

In the presented expression for step velocity (eq 2.1), the kink density, ρ_i, is a dimensionless probability and the kink rate, u_i, has units of inverse time. The kink density accounts for the concentration of kink sites along an edge, whereas the kink rate considers the net frequency of attachment at each site and is identical (at steady-state) for each

kink in the cycle (see eq 2.6). The solution-terrace-edge-kink incorporation mechanism will be considered initially. For a centrosymmetric crystal, the kink rate is:

$$u_i = j_i^{+K} - j_i^{-K} \tag{2.35}$$

where j_i^{+K} and j_i^{-K} are the attachment and detachment fluxes to and from a kink on edge i (from and to an edge site on the step, respectively); these rates must also have units of inverse time.

Terrace and edge adsorption can be considered as reversible, elementary reaction processes. The rate of incorporation at a kink on edge i (j_i^{+K}, eq 2.36) should, therefore, be first order in fractional coverage of edge sites with adsorbed growth units (θ_i^E, which is considered constant for a particular edge since edge diffusion is expected to have a lower energetic barrier and be much faster than attachment/detachment events). The attachment rate constant k_i^{+K} has units of inverse time (from the frequency prefactor ν_0) and contains the transition state barrier $\Delta G_i^{\ddagger K}$ that, under solution growth, represents partial desolvation in the kink direction.

$$j_i^{+K} = k_i^{+K}\theta_i^E = \nu_0 \exp\left(-\frac{\Delta G_i^{\ddagger K}}{kT}\right)\theta_i^E \tag{2.36}$$

The reverse (i.e., detachment) rate (j_i^{-K}, eq 2.37) is a zeroth order process with detachment rate constant k_i^{-K} (units inverse time) that additionally contains the kink detachment work (ΔW_i^K, eq 3.16) as a barrier.

$$j_i^{-K} = k_i^{-K} = \nu_0 \exp\left(-\frac{(\Delta G_i^{\ddagger K} + \Delta W_i^K)}{kT}\right) \tag{2.37}$$

To calculate the kink rate, θ_i^E must be determined. To obtain this, one must first

consider rates for the preceding processes of terrace and edge adsorption and desorption.

The rate of terrace adsorption (j^{+T}, eq 2.38, units inverse time) can be treated as first order in solute mole fraction in solution (x). Excluding kinks, each terrace site is available for adsorption, so there is no need for a fractional terrace coverage term. The terrace adsorption rate constant (k^{+T}, units inverse time) contains the transition state desolvation barrier $\Delta G^{\ddagger T}$, which is now in the terrace direction.

$$j^{+T} = k^{+T}x = \nu_0 \exp\left(-\frac{\Delta G^{\ddagger T}}{kT}\right) x \tag{2.38}$$

The rate of terrace desorption in the vicinity of edge i (j_i^{-T}, eq 2.39) is instead first order in the fractional coverage of terrace sites around edge i with adsorbed growth units (θ_i^T). The terrace desorption rate constant (k^{-T}, units inverse time) additionally contains the terrace detachment work (ΔW^T, eq 3.20) as a barrier.

$$j_i^{-T} = k^{-T}\theta_i^T = \nu_0 \exp\left(-\frac{(\Delta G^{\ddagger T} + \Delta W^T)}{kT}\right) \theta_i^T \tag{2.39}$$

The rate of adsorption to edge i (j_i^{+E}, eq 2.40) is first order in θ_i^T. Again, excluding kinks, each edge site is available for adsorption, so no fractional edge coverage term is included. The edge adsorption rate constant (k_i^{+E}, units inverse time) has a transition state desolvation barrier in the edge direction, $\Delta G_i^{\ddagger E}$.

$$j_i^{+E} = k_i^{+E}\theta_i^T = \nu_0 \exp\left(-\frac{\Delta G_i^{\ddagger E}}{kT}\right) \theta_i^T \tag{2.40}$$

The rate of desorption from edge i (j_i^{-E}, eq 2.41) is first order in the fractional coverage of edge sites on edge i with adsorbed growth units (θ_i^E). The edge desorption rate constant (k_i^{-E}, units inverse time) additionally contains the edge detachment work

(ΔW_i^E, eq 3.19) as a barrier.

$$j_i^{-E} = k_i^{-E}\theta_i^E = \nu_0 \exp\left(-\frac{(\Delta G_i^{\ddagger E} + \Delta W_i^E)}{kT}\right)\theta_i^E \tag{2.41}$$

The kink rate requires the steady-state fractional edge coverage on edge i, $\theta_i^{E,ss}$. Considering how each of the elementary reactions above influence the populations θ_i^E and θ_i^T in the vicinity of a single kink site, the balances shown in eqs 2.42 and 2.43 result. Note that the solute mole fraction in solution, x, is treated as a constant on the timescale of these processes (essentially a large quantity of solution is assumed).

$$\left[\frac{\mathrm{d}\theta_i^E}{\mathrm{d}t} = j_i^{+E} + j_i^{-K} - j_i^{-E} - j_i^{+K}\right]_{\theta_i^{T,ss},\theta_i^{E,ss}} = 0 \tag{2.42}$$

$$\left[\frac{\mathrm{d}\theta_i^T}{\mathrm{d}t} = j^{+T} + j_i^{-E} - j_i^{-T} - j_i^{+E}\right]_{\theta_i^{T,ss},\theta_i^{E,ss}} = 0 \tag{2.43}$$

Substituting eqs 2.36-2.37 and 2.40-2.41 into eq 2.42 and rearranging, we obtain the steady-state fractional terrace coverage:

$$\theta_i^{T,ss} = \frac{\theta_i^{E,ss}(k_i^{-E} + k_i^{+K})}{k_i^{+E}} - \frac{k_i^{-K}}{k_i^{+E}} \tag{2.44}$$

which can be substituted into eq 2.43 together with eqs 2.38-2.41, simplifying to:

$$\theta_i^{E,ss} = \frac{k_i^{+E}k^{+T}x + k_i^{-K}k^{-T} + k_i^{-K}k_i^{+E}}{k_i^{+K}k_i^{+E} + k_i^{+K}k^{-T} + k_i^{-E}k^{-T}} \tag{2.45}$$

Using eqs 2.36, 2.37 and 2.45 in eq 2.35 results in:

$$u_i = \frac{k_i^{+K}k_i^{+E}k^{+T}x - k_i^{-K}k_i^{-E}k^{-T}}{k_i^{+K}k_i^{+E} + k_i^{+K}k^{-T} + k_i^{-E}k^{-T}} \tag{2.46}$$

The mole fraction in solution can be written as $x = Sx_{sat}$ (from $S = x/x_{sat}$). At $S = 1$ ($x = x_{sat}$), the kink rate must be zero to ensure a zero step velocity and no crystal growth or dissolution. Equating $j_i^{+K} = j_i^{-K}$ we obtain:

$$\theta_{sat,i}^{E} = \frac{k_i^{-K}}{k_i^{+K}} \tag{2.47}$$

To ensure a steady-state, $j_i^{+E} = j_i^{-E}$ and $j^{+T} = j_i^{-T}$ must also be true, which leads to:

$$\theta_{sat,i}^{E} = \frac{k_i^{+E}}{k_i^{-E}}\theta_{sat,i}^{T} \tag{2.48}$$

$$\theta_{sat,i}^{T} = \frac{k^{+T}}{k^{-T}}x_{sat} \tag{2.49}$$

Using eqs 2.47-2.49 we obtain:

$$x_{sat} = \frac{k_i^{-K}k_i^{-E}k^{-T}}{k_i^{+K}k_i^{+E}k^{+T}} \tag{2.50}$$

Substituting into eq 2.46:

$$u = (S-1)\frac{k_i^{-K}k_i^{-E}k^{-T}}{k_i^{+K}k_i^{+E} + k_i^{+K}k^{-T} + k_i^{-E}k^{-T}} \tag{2.51}$$

This contains the expected linearity in supersaturation at constant T, which has been experimentally measured [19, 44, 45]. If $\Delta G^{\ddagger T} + \Delta W^{T} > \Delta G_i^{\ddagger E}$ and $\Delta G^{\ddagger T} + \Delta W^{T} + \Delta W_i^{E} > \Delta G_i^{\ddagger K}$, both of which are expected in the absence of extremely anisotropic interactions, then the first term on the denominator dominates, leading to:

$$u = (S-1)\frac{k_i^{-K}k_i^{-E}k^{-T}}{k_i^{+K}k_i^{+E}} \tag{2.52}$$

Upon evaluating rate constants, the kink rate becomes:

$$u_i = (S-1)\exp\left(-\frac{(\Delta W_i^K + \Delta W_i^E + \Delta W^T)}{kT}\right)\nu_0\exp\left(-\frac{\Delta G^{\ddagger T}}{kT}\right) \tag{2.53}$$

which is eq 2.24 in the text.

Considering the solution-terrace-kink mechanism, one can define rates of kink attachment from/detachment to the terrace (j_i^{+KE} and j_i^{-KE}, respectively). The equations become

$$u_i = j_i^{+KE} - j_i^{-KE} \tag{2.54}$$

$$j_i^{+KE} = k_i^{+KE}\theta_i^T \tag{2.55}$$

$$j_i^{-KE} = k_i^{-KE} = k_i^{+KE}\exp\left(-\frac{(\Delta W_i^K + \Delta W_i^E)}{kT}\right) \tag{2.56}$$

$$\left[\frac{\mathrm{d}\theta_i^T}{\mathrm{d}t} = j^{+T} + j_i^{-KE} - j_i^{-T} - j_i^{+KE}\right]_{\theta_i^{T,ss}} = 0 \tag{2.57}$$

Solving for $\theta_i^{T,ss}$, substituting into the expression for u_i and determining an expression for x_{sat} reproduces eq 2.53 (providing $\Delta G^{\ddagger T} + \Delta W^T > \Delta G_i^{\ddagger KE}$). Thus, eq 2.53 inherently describes both terrace-mediated incorporation mechanisms, so should perform adequately regardless of the kink density (see Chapter 4 for further discussion).

Note that an analogous terrace-mediated model for non-centrosymmetric molecules would consider k_i^{-K}, k_i^{-E} and/or k^{-T} values for each different growth unit present, but the centrosymmetric analysis presented here provides the interesting result that only desolvation in the terrace direction (barrier $\Delta G^{\ddagger T}$) is important for the kink rate.

In addition to the kink rate, the 2D nucleation model (Chapter 3) requires an expression for j_i^{+K} alone; which eq 2.58 shows in general form. As described above, the first term in the denominator of eq 2.58 is expected to dominate due to the absence of

detachment work barriers that exist in the other terms. Similarly, this is also expected for the first term in the numerator (note that in forming eq 2.46 the second two terms in the numerator canceled, so such an approximation was unnecessary). Retaining just the dominant first terms and using eq 2.50, the resulting expression for j_i^{+K} is given in eq 2.59.

$$j_i^{+K} = k_i^{+K}\theta_i^{E,ss} = \frac{k_i^{+K}k_i^{+E}k^{+T}x + k_i^{+K}k_i^{-K}k^{-T} + k_i^{+K}k_i^{-K}k_i^{+E}}{k_i^{+K}k_i^{+E} + k_i^{+K}k^{-T} + k_i^{-E}k^{-T}} \tag{2.58}$$

$$j_i^{+K} = k^{+T}Sx_{sat} = S\exp\left(-\frac{(\Delta W_i^K + \Delta W_i^E + \Delta W^T)}{kT}\right)\nu_0\exp\left(-\frac{\Delta G^{\ddagger T}}{kT}\right) \tag{2.59}$$

2.B Extension to Non-Centrosymmetric Growth Units

In this section, we extend our analysis for the rate expressions in Table 2.1 to non-centrosymmetric growth units. Written for this more general case, eq 2.15 becomes:

$$j^+\exp\left(-\frac{G_{S,k,i}}{kT}\right) = j^-_{k+1,i}\exp\left(-\frac{G_{X,k,i}}{kT}\right) \tag{2.60}$$

where $G_{S,k,i}$ is the free energy of state S with kink k exposed and $G_{X,k,i}$ is the free energy of state X following attachment at kink k (which generates the subsequent kink $k+1$ according to the edge periodicity). Rewriting eq 2.60

$$\Delta G_{k,i} = (G_{S,k,i} - G_{X,k,i}) = kT\ln\frac{j^+}{j^-_{k+1,i}} \tag{2.61}$$

Considering addition of n growth units to the edge (i.e., the repeat unit along the edge), defining an aggregate $\Delta_n G_i = \sum_{k=1}^{n}\Delta G_{k,i}$ and noting $j^-_{n+1,i} = j^-_{1,i}$ we obtain:

$$\Delta_n G_i = kT\ln\frac{(j^+)^n}{\prod_{k=1}^{n} j^-_{k,i}} \tag{2.62}$$

2.B.1 Case I

The case I rate expressions for non-centrosymmetric molecules are as follows:

$$j^{+I} = k^{+} x_{sat} S \tag{2.63}$$

$$j_{k,i}^{-I} = k_{k,i}^{-} \tag{2.64}$$

For case I, eq 2.62 becomes :

$$\Delta_n G_i^I = kT \ln \frac{(x_{sat}^I S)^n}{\prod_{k=1}^{n} \exp(-\Delta W_{k,i}/kT)} \tag{2.65}$$

which upon use of eq 2.68 collapses to:

$$\Delta_n G_i^I = nkT \ln S \tag{2.66}$$

Upon substitution of eqs 2.63 and 2.64 into the eq 2.7, the general non-centrosymmetric kink rate expression under case I is:

$$u_i^I = nk^{+} \frac{(x_{sat}^I S)^n - \exp\left(-\sum_{k=1}^{n} \Delta W_{k,i}/kT\right)}{\sum_{r=1}^{n} (x_{sat}^I S)^{n-r} \sum_{k=1}^{n} \exp(-\sum_{j=0}^{r-2} \Delta W_{k+j,i}/kT)} \tag{2.67}$$

For a saturated solution ($S = 1$), the kink rate is zero, leading to the following equation:

$$n \ln x_{sat}^I = -\sum_{k=1}^{n} \Delta W_{k,i}/kT \tag{2.68}$$

Rearranging eq 2.68 provides eq 2.31:

$$\ln x_{sat}^{I} = -\frac{\overline{\sum_{k=1}^{n} \Delta W_{k,i}}}{kT} \equiv -\frac{\overline{\Delta W_i}}{kT} \tag{2.69}$$

2.B.2 Case II

Under case II, the non-centrosymmetric rate expressions become:

$$j^{+II} = k^{+} x_{sat} S \tag{2.70}$$

$$j_{k,i}^{-II} = k_{k,i}^{-} x_W \tag{2.71}$$

Applying eq 2.62 to case II and making use of eq 2.74 forms an apparent driving force for crystallization:

$$\Delta_n G_i^{II} = nkT \ln S - nkT \ln \frac{x_W}{x_{W,sat}} \tag{2.72}$$

The general kink rate expression for case II is:

$$u_i^{II} = nk^{+} \frac{(x_{sat}^{II} S)^n - (1 - x_{sat}^{II} S)^n \exp\left(-\sum_{k=1}^{n} \Delta W_{k,i}/kT\right)}{\sum_{r=1}^{n} (x_{sat}^{II} S)^{n-r} (1 - x_{sat}^{II} S)^{r-1} \sum_{k=1}^{n} \exp(-\sum_{j=0}^{r-2} \Delta W_{k+j,i}/kT)} \tag{2.73}$$

At equilibrium ($u_i = 0$, $S = 1$), we obtain eq 2.32:

$$\ln \frac{x_{sat}^{II}}{1 - x_{sat}^{II}} = -\frac{\overline{\Delta W_i}}{kT} \tag{2.74}$$

2.B.3 Case III

For case III, the non-centrosymmetric expressions are:

$$j^{+III} = k^{+} x_{sat} S x_W \tag{2.75}$$

$$j_{k,i}^{-III} = k_{k,i}^{-} x_W \tag{2.76}$$

Making use of eq 2.62 together with eq 2.79, the apparent crystallization driving force for case III is again identical to case I:

$$\Delta_n G_i^{III} = nkT \ln S \tag{2.77}$$

The kink rate for Case III is:

$$u_i^{III} = nk^{+}(1 - x_{sat}^{III} S) \frac{(x_{sat}^{III} S)^n - \exp\left(-\sum_{k=1}^{n} \Delta W_{k,i}/kT\right)}{\sum_{r=1}^{n} (x_{sat}^{III} S)^{n-r} \sum_{k=1}^{n} \exp(-\sum_{j=0}^{r-2} \Delta W_{k+j,i}/kT)} \tag{2.78}$$

which is the case I expression with the additional prefactor $(1 - x_{sat} S)$. However, relative growth rates do not depend on this prefactor, which drops out of the equations together with k^{+}; so in terms of shape predictions cases I and III are identical. Considering eq 2.78 at equilibrium provides the same solubility relation as case I:

$$n \ln x_{sat}^{III} = -\sum_{k=1}^{n} \Delta W_{k,i}/kT \tag{2.79}$$

Therefore, cases I and III are equivalent for the purpose of steady-state crystal growth habit predictions under a spiral mechanism.

2.B.4 Kink Rates for Two Different Kink Sites

Here, we present the kink rates under each case for a non-centrosymmetric growth unit with two different kink sites. We label the detachment works ΔW_1 and ΔW_2.

$$u^I = 2k^+(x^I_{sat})^2 \frac{S^2-1}{2x^I_{sat}S + e^{-\Delta W_1/kT} + e^{-\Delta W_2/kT}} \tag{2.80}$$

$$u^{II} = 2k^+(x^{II}_{sat})^2 \frac{S^2 - \left(\frac{1-x^{II}_{sat}S}{1-x^{II}_{sat}}\right)^2}{2x^{II}_{sat}S + (1-x^{II}_{sat}S)\left(e^{-\Delta W_1/kT} + e^{-\Delta W_2/kT}\right)} \tag{2.81}$$

$$u^{III} = u^I\left(1 - x^I_{sat}S\right) \tag{2.82}$$

Bibliography

[1] A. A. Chernov, L. N. Rashkovich, and J. J. De Yoreo. ABC of kink kinetics and density in a complex solution. *AIP Conf Proc*, 916(1):34–47, 2007.

[2] P. G. Vekilov. What determines the rate of growth of crystals from solution? *Cryst. Growth Des.*, 7(12):2796–2810, 2007.

[3] M. A. Lovette, A. R. Browning, D. W. Griffin, J. P. Sizemore, R. C. Snyder, and M. F. Doherty. Crystal Shape Engineering. *Ind. Eng. Chem. Res.*, 47(24):9812–9833, 2008.

[4] P. Dandekar, Z. B. Kuvadia, and M. F. Doherty. Engineering crystal morphology. *Annu. Rev. Mater. Res.*, 43:359–386, 2013.

[5] F. Otalora and J. M. Garcia-Ruiz. Nucleation and growth of the naica giant gypsum crystals. *Chem. Soc. Rev.*, 43:2013–2026, 2014.

[6] W. Kossel. Zur theorie des kristallwachstums. *Nachr Ges Wiss Goettingen, Math-Phys Kl*, 1927:135–143, 1927.

[7] I. Stranski. Zur theorie des kristallwachstums. *Z Phys Chem*, 136(259):259–278, 1928.

[8] J. Zhang and G. H. Nancollas. Kink density and rate of step movement during growth and dissolution of an ab crystal in a nonstoichiometric solution. *J. Colloid Interface Sci.*, 200(1):131 – 145, 1998.

[9] J. Frenkel. On the surface motion of particles in crystals and the natural roughness of crystalline faces. *J. Phys. (Moscow)*, 9:392–398, 1945.

[10] W. K. Burton, N. Cabrera, and F. C. Frank. The growth of crystals and the equilibrium structure of their surfaces. *Philos. Trans. R. Soc., A*, 243:299–358, 1951.

[11] M. A. Lovette and M. F. Doherty. Multisite models to determine the distribution of kink sites adjacent to low-energy edges. *Phys. Rev. E*, 2012.

[12] H. Cuppen, H. Meekes, E. van Veenendaal, W. van Enckevort, P. Bennema, M. Reedijk, J. Arsic, and E. Vlieg. Kink density and propagation velocity of the [0 1 0] step on the kossel (1 0 0) surface. *Surf. Sci.*, 506(3):183 – 195, 2002.

[13] J. A. Dirksen and T. A. Ring. Fundamentals of crystallization: Kinetic effects on particle size distributions and morphology. *Chem Eng Sci*, 46(10):2389–2427, 1991.

[14] K. Chen and P. G. Vekilov. Evidence for the surface-diffusion mechanism of solution crystallization from molecular-level observations with ferritin. *Phys. Rev. E*, 2002.

[15] H. M. Cuppen, H. Meekes, W. J. P. van Enckevort, and E. Vlieg. Birth-and-spread growth on the Kossel and a non-Kossel surface. *J Cryst Growth*, 286(1):188–196, 2006.

[16] M. A. Lovette and M. F. Doherty. Predictive Modeling of Supersaturation-Dependent Crystal Shapes. *Cryst. Growth Des.*, 12(2):656–669, 2012.

[17] R. C. Snyder and M. F. Doherty. Predicting crystal growth by spiral motion. *Proc. R. Soc. London, Ser. A*, 465(2104):1145–1171, 2009.

[18] A. A. Chernov. The spiral growth of crystals. *Sov. Phys.-Usp.*, 4(1):116, 1961.

[19] D. N. Petsev, K. Chen, O. Gliko, and P. G. Vekilov. Diffusion-limited kinetics of the solution-solid phase transition of molecular substances. *Proc Natl Acad Sci USA*, 100(3):792–796, 2003.

[20] I. V. Markov. *Crystal Growth for Beginners: Fundamentals of Nucleation, Growth and Epitaxy*. Singapore: World Scientific,, 2003.

[21] V. V. Voronkov. The movement of an elementary step by means of the formation of one-dimensional nuclei. *Sov Phys Crystallogr*, 15:8–13, 1970.

[22] S. H. Kim, P. Dandekar, M. A. Lovette, and M. F. Doherty. Kink rate model for the general case of organic molecular crystals. *Cryst. Growth Des.*, 14(5):2460–2467, 2014.

[23] Z. B. Kuvadia and M. F. Doherty. Spiral growth model for faceted crystals of non-centrosymmetric organic molecules grown from solution. *Cryst. Growth Des.*, 11(7):2780–2802, 2011.

[24] H. Eyring. The activated complex in chemical reactions. *J. Chem. Phys.*, 3(2):107–115, 1935.

[25] H. Kramers. Brownian motion in a field of force and the diffusion model of chemical reactions. *Physica*, 7(4):284 – 304, 1940.

[26] A. A. Chernov. *Modern Crystallography III: Crystal Growth*, volume 36. Berlin: Springer-Verlag,, 1984.

[27] J. Zhang and G. Nancollas. Kink densities along a crystal surface step at low temperatures and under nonequilibrium conditions. *J. Cryst. Growth*, 106(23):181 – 190, 1990.

[28] P. Dandekar and M. F. Doherty. A mechanistic growth model for inorganic crystals: Growth mechanism. *AIChE J*, 60(11):3720–3731, 2014.

[29] Z. B. Kuvadia and M. F. Doherty. Reformulating multidimensional population balances for predicting crystal size and shape. *AIChE J.*, 59(9):3468–3474, 2013.

[30] J. Christiansen. The elucidation of reaction mechanisms by the method of intermediates in quasi-stationary concentrations. *Adv. Catal.*, 5:311–353, 1953.

[31] M. Temkin. Kinetics of steady-state complex reactions. *Int. Chem. Eng.*, 11(4):709, 1971.

[32] M. Boudart and G. Djéga-Mariadassou. *Kinetics of Heterogeneous Catalytic Reactions*. Princeton University Press, 2014.

[33] J. P. Sizemore and M. F. Doherty. A stochastic model for the critical length of a spiral edge. *J Cryst Growth*, 312(6):785–792, 2010.

[34] A. G. Stack, P. Raiteri, and J. D. Gale. Accurate rates of the complex mechanisms for growth and dissolution of minerals using a combination of rare-event theories. *J. Am. Chem. Soc.*, 134(1):11–14, 2012. PMID: 21721566.

[35] Z. Xu, Y. Yang, W. Zhao, Z. Wang, W. J. Landis, Q. Cui, and N. Sahai. Molecular mechanisms for intrafibrillar collagen mineralization in skeletal tissues. *Biomaterials*, 39:59 – 66, 2015.

[36] A. Warshel. Dynamics of reactions in polar solvents. semiclassical trajectory studies of electron-transfer and proton-transfer reactions. *J. Phys. Chem.*, 86:2218–2224, 1982.

[37] R. G. Mullen, J.-E. Shea, and B. Peters. Transmission coefficients, committors, and solvent coordinates in ion-pair dissociation. *J. Chem. Theory Comput.*, 10(2):659–667, 2014. PMID: 26580043.

[38] G. H. Gilmer and P. Bennema. Simulation of crystal growth with surface diffusion. *J. Appl. Phys.*, 43(4):1347–1360, 1972.

[39] J. van der Eerden, P. Bennema, and T. Cherepanova. Survey of monte carlo simulations of crystal surfaces and crystal growth. *Prog. Cryst. Growth Charact.*, 1(3):219 – 254, 1978.

[40] J. J. De Yoreo and P. G. Vekilov. Principles of crystal nucleation and growth. *Rev. Mineral. Geochem.*, 54(1):57–93, 2003.

[41] B. R. Goldsmith, T. Hwang, S. Seritan, B. Peters, and S. L. Scott. Rate-enhancing roles of water molecules in methyltrioxorhenium-catalyzed olefin epoxidation by hydrogen peroxide. *J. Am. Chem. Soc.*, 137(30):9604–9616, 2015. PMID: 26138433.

[42] F. A. Lindemann, S. Arrhenius, I. Langmuir, N. R. Dhar, J. Perrin, and W. C. McC. Lewis. Discussion on "the radiation theory of chemical action". *Trans. Faraday Soc.*, 17:598–606, 1922.

[43] M. Ohara and R. C. Reid. *Modeling Crystal Growth Rates from Solution*. New Jersey: Prentice Hall,, 1973.

[44] I. Reviakine, D. K. Georgiou, and P. G. Vekilov. Capillarity effects on crystallization kinetics: Insulin. *J. Am. Chem. Soc.*, 125(38):11684–11693, 2003. PMID: 13129373.

[45] R. E. Sours, A. Z. Zellelow, and J. A. Swift. An in situ atomic force microscopy study of uric acid crystal growth. *J Phys Chem B*, 109(20):9989–9995, 2005.

[46] T. Hwang, B. R. Goldsmith, B. Peters, and S. L. Scott. Water-catalyzed activation of H_2O_2 by methyltrioxorhenium: A combined computational-experimental study. *Inorg. Chem.*, 52(24):13904–13917, 2013.

[47] E. Ruiz-Agudo, M. Kowacz, C. V. Putnis, and A. Putnis. The role of background electrolytes on the kinetics and mechanism of calcite dissolution. *Geochim. Cosmochim. Acta*, 74:1256–1267, 2010.

[48] E. Ruiz-Agudo, C. V. Putnis, L. Wang, and A. Putnis. Specific effects of background electrolytes on the kinetics of step propagation during calcite growth. *Geochim. Cosmochim. Acta*, 75:3803–3814, 2011.

[49] J. J. De Yoreo, L. A. Zepeda-Ruiz, R. W. Friddle, S. R. Qiu, L. E. Wasylenki, A. A. Chernov, G. H. Gilmer, and P. M. Dove. Rethinking classical crystal growth mmodel through molecular scale insights: Consequences of kink-limited kinetics. *Cryst. Growth Des.*, 9:5135–5144, 2009.

[50] J. D. Rimer, Z. An, Z. Zhu, M. H. Lee, D. S. Goldfarb, J. A. Wesson, and M. D. Ward. Crystal growth inhibitors for the prevenction of L-cystine kidney stones through molecular design. *Science*, 330:337–341, 2010.

[51] J. R. A. Godinho and A. G. Stack. Growth kinetics and morphology of barite crystals derived from face-specific growth rates. *Cryst. Growth Des.*, 15:2064–2071, 2015.

[52] Z. B. Kuvadia and M. F. Doherty. Effect of structurally similar additives on crystal habit of organic molecular crystals at low supersaturation. *Cryst. Growth Des.*, 13(4):1412–1428, 2013.

[53] N. Cabrera and R. Coleman. *The Art and Science of Growing Crystals*. John Wiley & Sons, Inc., New York, 1963.

[54] N. Cabrera and D. Vermilyea. *Growth and Perfection of Crystals*, chapter The Growth of Crystals from Solution, pages 393–410. John Wiley & Sons, Inc., New York, 1958.

[55] J. P. Sizemore and M. F. Doherty. A new model for the effect of molecular imposters on the shape of faceted molecular crystals. *Cryst. Growth Des.*, 9(6):2637–2645, 2009.

Chapter 3

Modeling Layered Crystal Growth at Increasing Supersaturation by Connecting Growth Regimes

Reproduced in part with permission from:

Carl J. Tilbury and Michael F. Doherty, "Modeling Layered Crystal Growth at Increasing Supersaturation by Connecting Growth Regimes," *AIChE Journal*, **2017**, *63*, 1338-1352.

DOI: 10.1002/aic.15617. AIChE Journal Editor's Choice April 2017.

3.1 Introduction

Crystal morphology is often supersaturation-dependent. As indicated in Chapter 1, the simpler non-mechanistic models predict a single habit regardless of growth conditions; they cannot account for supersaturation as an influential parameter. Simulations can offer

insight, but are largely impractical for an industrial screening step and often require the face growth mechanism as an input. In contrast, the mechanistic structure presented in Figures 1.3 and 1.7 can account for the effect of supersaturation, by considering the distinct operation of different growth regimes on each face. This chapter provides a framework to determine the dominant growth regimes and, therefore, correctly account for supersaturation.

Our group has previously developed a mechanistic description of spiral growth [1, 2]. Extensions to the model have been made for non-centrosymmetric molecules [3], birth-and-spread two-dimensional (2D) nucleation [4] and inorganic systems [5, 6]. This work extends the existing [4] model for 2D nucleation and introduces a framework for connecting the various regimes of crystal growth, for centrosymmetric molecules (certain expressions would require generalization to describe the more general class of non-centrosymmetric growth units). At low supersaturations, faces grow via a spiral growth mechanism [7], but upon increasing the supersaturation faces can crossover to a 2D-nucleation growth mechanism [1, 4]. The new framework enables the crossover supersaturation to be predicted for each face, to ensure the correct growth rate expression is used on each face at the particular supersaturation for which crystal growth is to be modeled. One application of this model could be predicting the active layer morphology of organic electronics fabricated from small conjugated molecules at large supersaturation [8–12].

Note that spiral and 2D-nucleation growth mechanisms can be readily identified upon imaging the surface structure of grown crystals [13, 14] and transitions between regimes have been observed experimentally for various systems, notably through the use of in-situ atomic force microscopy (AFM) [15, 16].

3.2 Mechanistic Modeling of Growth Regimes

To model the crystal growth mechanistically, a face's normal growth rate under a layered mechanism is defined by

$$G_{hkl} = \left(\frac{h}{\tau}\right)_{hkl} \tag{3.1}$$

where h is the step height (an elementary step is assumed, leading to a step height equal to the interplanar spacing, or a simple multiple of it depending on the growth unit and the crystallography) and τ is the time taken to advance the face one layer. The form of τ depends on the dominant growth regime operating on that face.

Expressions for τ under different layered growth mechanisms must consider how surface structures such as spirals and 2D nuclei act to complete successive layers. Accounting for the advance of crystal steps is important, which depends on incorporation at kink sites (see Chapter 1). Layered mechanisms are typically governed by kinetics (see Chapter 2), but mass transport effects can become important as the crystallization driving force increases [1]. Note that the heat of crystallization must also be liberated, but this process is usually fast in comparison [1, 17].

We define the relative supersaturation, σ, as

$$\sigma \equiv \frac{x - x_{sat}}{x_{sat}} = S - 1 \tag{3.2}$$

which can be related to the crystallization driving force (eq 2.14):

$$\frac{\Delta\mu}{kT} = \ln(1 + \sigma) \tag{3.3}$$

Note that the approximation $\ln(1+\sigma) \approx \sigma$ is sometimes used in the literature, which holds

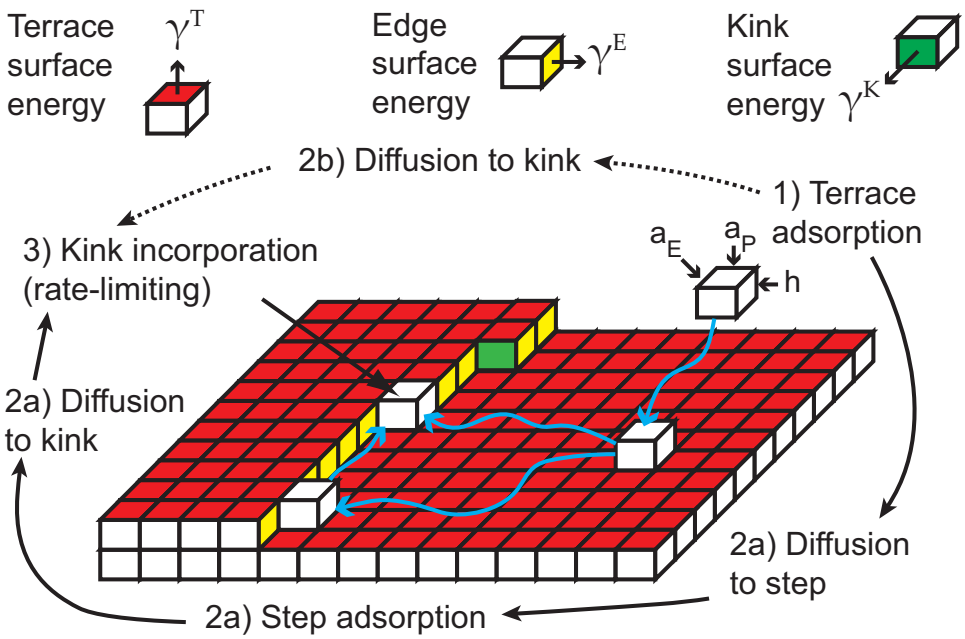

Figure 3.1: The surface structure of a crystal, showing sequential events of the incorporation mechanism. Terrace (γ^T), edge (γ^E) and kink (γ^K) surface energies are defined, along with surface dimensions. Reprinted with permission from Tilbury et al. [28]. Copyright 2016 American Chemical Society.

at low supersaturation but must be avoided for a model at higher σ. Additionally, for certain multicomponent or ionic systems, it may be necessary to express the driving force in terms of activities (see Chapter 2); however, eqs 3.2 and 3.3 are typically appropriate for the crystallization of small organic molecules.

Growth unit incorporation at kink sites is favorable for three reasons: first, it produces no change in total surface energy around the kink site (for centrosymmetric systems); second, it completes solid-state interactions in three directions (terrace, edge and kink); and third, it is regenerative (enabled by thermal step reorganization) [1,7,18–24]. Figure 3.1 portrays the surface structure of a face, including relevant surface energies in the kink/edge/terrace directions and the terrace-mediated incorporation processes expected for organic molecular crystals [7, 17, 23, 25–27], see Chapter 4).

With known growth rates for each family of faces, one can determine the steady-state

crystal growth shape using the Frank-Chernov condition [29, 30]:

$$\frac{G_{hkl}}{H_{hkl}} = \text{constant} \tag{3.4}$$

where H_{hkl} is the perpendicular distance of face (hkl) from the crystal center. The Frank-Chernov condition can be recast in terms of relative growth rates and distances by normalizing with a reference face ($R_{hkl} = G_{hkl}/G_{ref}, x_{hkl} = H_{hkl}/H_{ref}$) [31]:

$$\frac{R_{hkl}}{x_{hkl}} = 1 \tag{3.5}$$

As will be shown later, relative growth rate expressions formed between surface-integration-limited regimes can be calculated without the need for values of those parameters that require molecular simulations for reliable estimates (the resulting expressions are independent of such quantities). This technique enables rapid shape predictions, although it cannot predict absolute growth rates or crystal sizes.

Within the mechanistic expressions for each regime, both solid-state crystal and interfacial (i.e., solvent-modified) energetics are required to obtain various parameters. The crystallography is a primary input, so calculations are made for a selected polymorph. Solid-state interaction energies between molecules are then calculated by applying a force field; the CLP package developed by Gavezzotti [32] has been applied here. Under solution growth, the interfacial surface energies must be appropriately modified; full details for this procedure are contained within Chapter 4.

Periodic bond chains (PBCs) are defined as directions of strong repeated interactions within the solid state [33]. Their determination is essential to find the 'flat' faces on a crystal, which contain 2 or more in-plane PBCs and are those faces that can grow via a layered mechanism (rough growth occurs on 'stepped' (1 PBC) and 'kinked' (0

PBC) faces) [33]. The PBC directions are also approximated as the edges of a spiral or 2D nucleus [2, 4], which is an acceptable assumption providing the supersaturation or temperature has not initiated a roughening transition [34] (at high driving forces, or thermal energy, there is less preference to crystallize in these PBC directions). The calculated intermolecular interactions are organized by face and PBC before the spiral and 2D-nucleation growth models are implemented. An overview of the modeling process and its potential automation, from crystallography to shape prediction, is described in Chapter 6.

3.2.1 Spiral Growth

The presence of a screw dislocation on the surface of a face provides a continuous source of steps, since as the initial step present at the dislocation advances it exposes the next spiral edge, corresponding to the adjacent PBC [2, 7]. This process continues until the initial edge has reappeared one layer higher (the spiral has gone through a full rotation). The steps continue to flow outward to the face edges and complete the layers; it is the spiral rotation time that must be used in eq 3.1.

There exists a critical length that an edge must reach before it will grow, since step advancement lengthens the adjacent edges, introducing a surface energy penalty. The critical length can be calculated by considering both the surface energy penalty and the reward for crystallization (eq 3.3), to form the free energy change for monolayer step addition: [2, 35, 36]

$$\frac{\Delta G_i(n_i)}{kT} = 2\left(\frac{\phi_i^K}{kT}\right)(1-\delta_{n_i}) - n_i \ln(1+\sigma) \tag{3.6}$$

The number of molecules along edge i is n_i, which is related to the edge's length, l_i, and

intermolecular width along the edge, $a_{E,i}$ (see Figure 3.1):

$$n_i = \frac{l_i}{a_{E,i}} \tag{3.7}$$

The surface energy penalty in eq 3.6 is represented by the kink energy [36], ϕ_i^K, and the Kronecker delta δ_{n_i} is used to make this penalty term vanish at $n_i = 0$. The critical length is where eq 3.6 equals zero:

$$l_{C,i} = 2\frac{a_{E,i}}{\ln(1+\sigma)}\left(\frac{\phi_i^K}{kT}\right) \tag{3.8}$$

The kink energy relates to the energetic penalty of kink formation. It is possible to determine this penalty by considering geometrical step transformations [7,20]. For either solution or vapor growth, the kink energy is

$$\phi_i^K = \gamma_i^K a_{P,i} h \tag{3.9}$$

where γ_i^K is the interfacial surface energy in the kink direction for a kink on edge i, $a_{P,i}$ is the step propagation length (normal to the edge) for addition of a new row and h is the step height (see Figure 3.1). For vapor growth eq 3.9 reduces to half the total PBC interaction energy in the kink direction: $\phi_i^K = E_{PBC,i}^K/2$.

The spiral rotation time, τ_S, sums the time between each edge being exposed and growing to its critical length due to the continual advance of the preceding edge [2]:

$$\tau_S = \sum_{i=1}^{N} \frac{l_{C,i+1}\sin(\alpha_{i,i+1})}{v_i} \tag{3.10}$$

Here v_i is the step velocity of edge i and $\alpha_{i,i+1}$ is the angle between edge i and i+1.

The Voronkov step velocity profile [37] is adopted in this work, which takes the form of

a Heaviside function with zero velocity until the critical length is reached and a constant value (v_∞) afterwards. As a result, considering spiral edges emerging out of a screw dislocation, a constant inter-step distance in each edge direction would be expected under the Voronkov approximation. We expect this assumption to be reasonable, since constant inter-step distances are exhibited for many systems, as evidenced by electron and atomic-force microscopy [16,38–40]. Other forms for the step velocity profile consider a smoother increase of step velocity with edge length (up to this same v_∞ for a large edge) and have been summarized previously [4]. The error introduced by the Voronkov approximation is expected to be inconsequential for shape predictions, because it should be near-isotropic (which leaves the relative growth rates essentially unaffected) [4]. Hereafter the term 'step velocity' or v_i shall refer to v_∞.

The step velocity for edge i can be described by

$$v_i = a_{P,i}\rho_i u_i \tag{3.11}$$

where ρ_i is the number density of kink sites along the edge (i.e., the probability of a site being a kink) and u_i is the kink rate, which is the net frequency of attachment to each kink site [3,41]. The product $\rho_i u_i$ provides the rate of step edge monolayer addition (i.e., formation of a new row), which is converted into a velocity using the corresponding distance of advance, $a_{P,i}$. An equivalent construction considers the time needed for each kink to advance the average number of sites between kinks [4].

The distribution of kink sites at thermodynamic equilibrium can be determined by minimization of the Helmholtz free energy over an edge arrangement [20], or through the use of Boltzmann statistics [7]. These approaches make use of the kink energy (ϕ_i^K, eq

3.9) as the energetic penalty of a kink existing and result in

$$\rho_i = \frac{2\exp\left(-\frac{\phi_i^K}{kT}\right)}{1 + 2\exp\left(-\frac{\phi_i^K}{kT}\right)} \tag{3.12}$$

More accurate (and more complicated) expressions have been developed [22] for low kink energies, which we have used to calculate ρ_i on edges with $\phi_i^K \leq 3kT$, where results diverge from eq 3.12.

The kink rate is a balance between the attachment and detachment fluxes to a single kink site, where a positive value leads to an advance of the kink along the step (i.e., crystal growth) and a negative value leads to a retreat (i.e., crystal dissolution). These activated process of attachment and detachment can be treated as elementary surface reactions, where expressions are commonly developed from transition state theory [4, 7, 21]. Since the kink density is separately accounted for in eq 3.11, these events occur at a single kink site. As indicated previously, for organic crystals, the expected growth mechanism involves solute molecules first adsorbing to the terrace, and then possibly to the step, before attaching to a kink site [7, 23, 25, 26].

Assuming an edge-mediated incorporation process (see Appendix 2.A) the kink rate for a centrosymmetric crystal is [3, 42, 43]

$$u_i = j_i^{+K} - j_i^{-K} \tag{3.13}$$

where j_i^{+K} and j_i^{-K} are the attachment and detachment fluxes to and from a kink on edge i, respectively (these rates have units of inverse time). In Chapter 2, we determined the preferred set of attachment–detachment rate expressions. The kink attachment rate, j_i^{+K}, is expressed as first order in the fractional coverage of adsorbed growth units on

the step (θ_i^E):

$$j_i^{+K} = k_i^{+K}\theta_i^E = \nu_0 \exp\left(-\frac{\Delta G_i^{\ddagger K}}{kT}\right)\theta_i^E \tag{3.14}$$

The attachment rate constant k_i^{+K} has units of inverse time (from the frequency prefactor ν_0) and contains the transition state barrier $\Delta G_i^{\ddagger K}$ that represents partial desolvation in the kink direction [21, 41, 44, 45] (under solution growth).

The reverse rate (detachment, j_i^{-K}) is a zeroth order process, since a detachable growth unit is, by definition, present at a kink site:

$$j_i^{-K} = k_i^{-K} = \nu_0 \exp\left(-\frac{\Delta G_i^{\ddagger K} + \Delta W_i^K}{kT}\right) \tag{3.15}$$

The detachment rate constant k_i^{-K} (also units inverse time) maintains this transition state barrier and additionally incorporates the kink-direction detachment work, ΔW_i^K:

$$\Delta W_i^K = 2\phi_i^K = 2\gamma_i^K a_{P,i} h \tag{3.16}$$

Note that the release of solvent molecules from the solvation 'shell' is assumed to compensate the solute's degree of freedom reduction upon crystallization (which seems reasonable for small molecules [21]), so the detachment work represents an energetic barrier alone (see Chapter 2 for more details).

To obtain θ_i^E, a microkinetic model was developed (see Appendix 2.A) that considers the steady-state resulting from the reversible processes of adsorption/desorption and kink attachment/detachment in either a terrace-mediated or edge-mediated incorporation mechanism (see Figure 3.1). The following kink rate results for centrosymmetric systems:

$$u_i = k^{+T} \exp\left(-\frac{\Delta W_i^K + \Delta W_i^E + \Delta W^T}{kT}\right)\sigma \tag{3.17}$$

In eq 3.17, k^{+T} is the rate constant for terrace adsorption:

$$k^{+T} = \nu_0 \exp\left(-\frac{\Delta G^{\ddagger T}}{kT}\right) \tag{3.18}$$

where $\Delta G^{\ddagger T}$ is the transition state barrier involving desolvation in the terrace direction. ΔW_i^E and ΔW^T are the detachment barriers from edge-adsorbed to terrace-adsorbed, and from terrace-adsorbed to solution, respectively:

$$\Delta W_i^E = 2\gamma_i^E a_{E,i} h \tag{3.19}$$

$$\Delta W^T = 2\gamma^T \overline{a_E a_P} \tag{3.20}$$

where γ_i^E and γ^T are edge and terrace surface energies and $\overline{a_E a_P}$ represents the average area of a growth unit. Equation 3.17 produces the expected linearity with σ, which has been demonstrated experimentally for various systems [46–48].

For a crystal with centrosymmetric growth units, the sum $\Delta W_i^K + \Delta W_i^E + \Delta W^T$ is constant for each kink, edge and face triad (under sublimation growth this sum is also equivalent to the lattice energy, see Chapter 4). To a first approximation, k^{+T} can be taken as the same for each face, which, therefore, creates a single kink rate value for such crystals. These isotropic quantities can be assimilated into an aggregate, overall rate constant, k_O:

$$\begin{aligned} u_i &= k_O \sigma \\ k_O &\equiv k^{+T} \exp\left(-\frac{\Delta W_i^K + \Delta W_i^E + \Delta W^T}{kT}\right) \end{aligned} \tag{3.21}$$

Spiral edges can disappear during the spiral's rotation if tangential step velocities become negative [2]. This affects both whether to include them in eq 3.10 and their

appearance in the steady-state spiral shape. Additionally, the fastest rotation direction must be selected, since dislocations of both types should be present and faster growing spirals will overtake slower spirals to dominate the growth rate. The tangential step velocity, v_i^t, is given by

$$v_i^t = \frac{v_{i+1} - v_i \cos(\alpha_{i,i+1})}{\sin(\alpha_{i,i+1})} + \frac{v_{i-1} - v_i \cos(\alpha_{i-1,i})}{\sin(\alpha_{i-1,i})} \tag{3.22}$$

Note that, in general, the density of dislocations on a face will not affect its growth rate. Unless a spiral's rotation time is influenced on its first turn, eq 3.10 is unaffected (future annihilation of steps is irrelevant). If two dislocations are close enough, however, the steps emanating from each can influence one another during the first turn. If the dislocations are of opposite sense, their rotation rates can be slowed. Assuming an unaffected dislocation exists elsewhere on the face, this produces no effect on the normal face growth rate. If the dislocations are of the same sense, their rotation rates can be increased (up to a multiple of two [7]), which could impact the face growth rate; nonetheless, since this is a minor effect and the critical separation required reduces with supersaturation (since first-turn rotation times decrease), we do not consider the dislocation density in our model. For more detail see ref. [7].

3.2.2 Growth by Two-Dimensional (2D) Nucleation

Steps in the same crystallographic direction grow with identical velocity regardless of whether they are born from a spiral or 2D nucleus. Growth by 2D nucleation has various sub-regimes that depend on the rate of 2D nucleation, J, which is the number of nuclei formed per area per time. At low J, the mononuclear regime exists, where each nucleus completes a new crystal layer before another nucleation event [49–51]. The mononuclear regime would require $\tau_{2D,mono} = (JA_{face})^{-1}$ in eq 3.1, but normally it cannot

compete with spiral growth, so this regime does not warrant consideration [52]. As J rises, nucleation events begin to happen faster than a single nucleus can complete the layer, so the layer is formed from the combined action of multiple nuclei, where colliding steps annihilate as they meet. J increases with supersaturation, so it is at higher σ where growth by 2D nucleation becomes relevant against the spiral mechanism [4, 52]. Two limits can be used to model the action of 2D-nucleation crystal growth: when the initial nucleated area is negligible (the 'birth-and-spread' regime [51, 53]) and when the growth area is negligible (the 'polynuclear' regime [51]). It should be noted that the term 'polynuclear' has also been used to describe all regimes following mononuclear, but its use here is limited to the negligible nucleus growth regime.

Within the birth-and-spread regime, although multiple nuclei now collectively complete the layer, nucleation events are sparse enough that formation of the new crystal layer is dominated by growth of these nuclei (i.e., the advance of their step edges with velocity v_i, eq 3.11). Step–step annihilation only occurs after significant growth since it is unlikely for the sparse nucleation events to occur in close proximity, and so the nucleated area is negligible compared to the growth (or face) area. On the other hand, the polynuclear regime occurs at a very high nucleation rate, where the density of nuclei formed on the surface is so large that formation in close proximity is guaranteed. Steps emanating from adjacent nuclei quickly annihilate, which causes crystal layer formation to be dominated by nucleation events as opposed to nucleus growth; essentially, polynuclear growth corresponds to a 'patchwork' formation of critically-sized nuclei. Note that an interpretation of the polynuclear regime resulting from $v_i = 0$ is not realistic, although it produces the same growth rate expression; rapid step annihilation is instead the more physical explanation.

The time to complete a new layer is required in eq 3.1. Considering descriptions of the 2D birth-and-spread and 2D polynuclear growth mechanisms, expressions for the

coverage time for a face growing by 2D nucleation, τ_{2D}, can be developed. The fractional surface coverage under the 2D birth-and-spread regime as a function of time, $\theta_{2D,B+S}$, can be calculated from the growth of nuclei forming at rate J [53]:

$$\theta_{2D,B+S} = \int_0^t JA(t-\tau)\mathrm{d}\tau \tag{3.23}$$

Since the initial nucleated area is negligible compared to the growth area in this regime, the time-dependent area excludes that of the critical nucleus and is based on growth alone:

$$A(t) = \frac{1}{2}\left(\sum_{i=1}^{N} v_i v_i^t\right) t^2 \tag{3.24}$$

Note that v_i^t refers to the tangential step velocity, defined by eq 3.22. Assuming a constant nucleation rate, eq 3.23 solves to [4]

$$\theta_{2D,B+S} = Jft^3 \tag{3.25}$$

where f is defined by:

$$f \equiv \frac{1}{6}\sum_{i=1}^{N} v_i v_i^t \tag{3.26}$$

The fractional coverage for the 2D polynuclear case is given by

$$\theta_{2D,P} = JA_C t \tag{3.27}$$

where A_C is the area of a critical nucleus and can be determined using

$$A_C = \frac{1}{2}\sum_{i=1}^{N} H_{C,i}^{2D} l_{C,i}^{2D} \tag{3.28}$$

The term $H_{C,i}^{2D}$ is the perpendicular distance of edge i to the center of a critical nucleus;

$l_{C,i}^{2D}$ is the length of edge i on such a nucleus (see eqs 3.39 and 3.40 later, respectively).

The coverage time, τ_{2D}, is obtained by solving for a fractional coverage of unity. For 2D birth-and-spread this yields

$$\tau_{2D,B+S} = (Jf)^{-1/3} \tag{3.29}$$

which, when used in eq 3.1, provides the same growth rate scaling with nucleation rate ($G \propto J^{1/3}$) as previously established models [51, 54, 55]; note that it also collapses to the same step velocity scaling ($G \propto v^{2/3}$) under the assumption of isotropic step velocities and rectangular nuclei. For 2D polynuclear the coverage time is given by

$$\tau_{2D,P} = (JA_c)^{-1} \tag{3.30}$$

When eq 3.30 is substituted into eq 3.1 it corresponds to previous expressions for polynuclear growth [51, 56], but now provides a more general form than circular nuclei. To account for the step velocity being non-zero in the polynuclear regime, one could instead account for the packing problem on the surface by solving for a fractional coverage of less than unity (e.g., $\theta_{2D,P} = 0.7$); however, this decision simply introduces a numerical constant and does not affect the following framework.

Knowledge of J is required to use eqs 3.29 and 3.30. It can be defined by eq 3.31 [4], using a prefactor κ_{2D} and the free energy change upon forming a critical nucleus.

$$J = \kappa_{2D} \exp\left(-\frac{\Delta G_C}{kT}\right) \tag{3.31}$$

To calculate $\Delta G_C/kT$, we consider the balance between a 2D nucleus' (edge) surface energy penalty and its volume reward for crystallization [4], akin to the balance in eq

3.6:

$$\frac{\Delta G(n)}{kT} = \left(\frac{s_F\overline{\phi^E}}{kT}\right) n^{1/2} - n\ln(1+\sigma) \tag{3.32}$$

The shape factor s_F is the critical 2D nucleus perimeter (P) divided by the square root of its area (A):

$$s_F \equiv \frac{P}{A^{1/2}} = \frac{\sum_{i=1}^{N} l_{C,i}^{2D}}{\left(\frac{1}{2}\sum_{i=1}^{N} H_{C,i}^{2D} l_{C,i}^{2D}\right)^{1/2}} \tag{3.33}$$

s_F connects $n^{1/2} \approx (A/V_X^{2/3})^{1/2}$ to the number of edge molecules on the 2D nucleus ($\approx P/V_X^{1/3}$); V_X is the solute's molecular volume ($V_X = V_{m,X}/N_A$, where $V_{m,X}$ is the solute's molar volume and N_A is Avogadro's number). The average edge energy per molecule, $\overline{\phi^E}$, is given by eq 3.34, where $n_{C,i}$ is the number of molecules on critical nucleus edge i ($n_{C,i} = l_{C,i}^{2D}/a_{E,i}$).

$$\overline{\phi^E} \equiv \frac{\sum_{i=1}^{N} n_{C,i}\phi_i^E}{\sum_{i=1}^{N} n_{C,i}} = \frac{\sum_{i=1}^{N} n_{C,i}\gamma_i^E a_{E,i} h}{\sum_{i=1}^{N} n_{C,i}} \tag{3.34}$$

Differentiating eq 3.32 to find the maximum in the curve of free energy change against nucleus size results in eqs 3.35 and 3.36 for the number of molecules in the critical nucleus and its free energy change, respectively [4].

$$n_C = \frac{1}{4}\left(\frac{s_F\overline{\phi^E}}{kT}\right)^2 \left(\frac{1}{\ln(1+\sigma)}\right)^2 \tag{3.35}$$

$$\frac{\Delta G_C}{kT} = \frac{1}{4}\left(\frac{s_F\overline{\phi^E}}{kT}\right)^2 \left(\frac{1}{\ln(1+\sigma)}\right) = \frac{3\mathcal{F}}{\ln(1+\sigma)} \tag{3.36}$$

$$\mathcal{F} \equiv \frac{1}{12}\left(\frac{s_F\overline{\phi^E}}{kT}\right)^2 \tag{3.37}$$

The parameter $\mathcal{F}$ provides a dimensionless measure of the surface energy penalty for 2D nucleation on a given face.

The balance in eq 3.32 can be re-written in terms of edge dimensions for an arbitrary 2D polygon with perpendicular distances H_i^{2D} and lengths l_i^{2D}: [4]

$$\frac{\Delta G(l_1^{2D},...,l_N^{2D})}{kT} = h\left(\sum_{i=1}^{N} l_i^{2D}\frac{\gamma_i^E}{kT}\right) - \frac{\ln(1+\sigma)}{V_X}h\frac{1}{2}\sum_{i=1}^{N} H_i^{2D}l_i^{2D} \tag{3.38}$$

Since V_X is the solute's molecular volume in the lattice, V_X/h is the average growth unit area. The general critical nucleus shape can be obtained using calculus of variations [4] and corresponds to a 2D Wulff construction; the resulting perpendicular distance of each side from the crystal center is

$$H_{C,i}^{2D} = \frac{V_X}{\ln(1+\sigma)}\left(\frac{\gamma_i^E}{kT}\right) \tag{3.39}$$

A side's length on the critical nucleus, $l_{C,i}^{2D}$, can then be calculated from

$$l_{C,i}^{2D} = \frac{H_{C,i+1}^{2D} - H_{C,i}^{2D}\cos(\alpha_{i,i+1})}{\sin(\alpha_{i,i+1})} + \frac{H_{C,i-1}^{2D} - H_{C,i}^{2D}\cos(\alpha_{i-1,i})}{\sin(\alpha_{i-1,i})} \tag{3.40}$$

Equation 3.40 corresponds to the relation between normal and tangential velocities in eq 3.22. Note also that $l_{C,i}^{2D}$ is different from $l_{C,i}$ (eq 3.8), which still applies as a condition to be met before the forward step velocity via eq 3.11 is realized.

The second component to calculating J using eq 3.31 is the prefactor κ_{2D}. An expression for this prefactor can be developed by adapting established theory for the stationary 2D-nucleation rate of circular nuclei to system-specific polygons, which correspond to critically-sized nuclei whose edges are PBCs (the stationary rate is appropriate for modeling growth at constant supersaturation). J can be written as

$$J = zw_C^+ C_C^{2D} \tag{3.41}$$

where z is the Zeldovich factor [57], C_C^{2D} is the concentration of critically sized nuclei on the surface and w_C^+ is the total rate of growth unit attachment to a critical nucleus [58].

The Zeldovich factor is given by [57–59]

$$z = \frac{2\beta}{\pi^{1/2}(1 - \mathrm{erf}(\beta(1 - n_C)))} \approx \frac{\beta}{\pi^{1/2}} \tag{3.42}$$

where β is defined by

$$\beta^2 = \frac{-\left.\frac{\mathrm{d}^2\Delta G}{\mathrm{d}n^2}\right|_{n=n_C}}{2kT} \tag{3.43}$$

Note the approximation in eq 3.42 is excellent for $\beta(1-n_C) < -1$, which is expected [58].

The critical nucleus concentration can be expressed by [58]

$$C_C^{2D} = C_0^{2D} \exp\left(\frac{-\Delta G_C}{kT}\right) \tag{3.44}$$

where C_0^{2D} is the concentration of adsorption sites on the surface .

Substituting eqs 3.42-3.44 into eq 3.41 gives us a form that compares to eq 3.31, with κ_{2D} now expressed as

$$\kappa_{2D} = z w_C^+ C_0^{2D} = \left(\frac{-\left.\frac{\mathrm{d}^2\Delta G}{\mathrm{d}n^2}\right|_{n=n_c}}{2\pi kT}\right)^{1/2} w_C^+ C_0^{2D} \tag{3.45}$$

After differentiating eq 3.32 twice, the Zeldovich factor becomes

$$z = \left(\frac{s_F \overline{\phi^E}}{8\pi kT n_C^{3/2}}\right)^{1/2} \tag{3.46}$$

and upon use of eq 3.35

$$z = \frac{1}{\pi^{1/2}} \frac{kT}{s_F \overline{\phi^E}} (\ln(1+\sigma))^{3/2} \tag{3.47}$$

For w_C^+, we form the rate of attachment to a critical nucleus by considering attachment at each kink on each edge:

$$w_C^+ = \sum_{i=1}^{N} n_{C,i} \rho_i j_i^{+K} \tag{3.48}$$

where the rate of attachment at a given kink, j_i^{+K}, is provided in Appendix 2.A:

$$j_i^{+K} = k^{+T} \exp\left(-\frac{\Delta W_i^K + \Delta W_i^E + \Delta W^T}{kT}\right)(1+\sigma) = k_O(1+\sigma) \tag{3.49}$$

Note that eq 3.49 also contains the isotropic overall rate constant (k_O, eq 3.21), which can be taken out of the sum in eq 3.48. Using $n_{C,i} = l_{C,i}^{2D}/a_{E,i}$, the resulting expression for w_C^+ is

$$w_C^+ = k_O(1+\sigma) \sum_{i=1}^{N} \frac{l_{C,i}^{2D} \rho_i}{a_{E,i}} \tag{3.50}$$

The final quantity in eq 3.45 is the concentration of surface sites on the face, C_0^{2D}, which we estimate from the squared mean of the PBC intermolecular widths:

$$C_0^{2D} = \frac{1}{(\frac{1}{N}\sum_{i=1}^{N} a_{E,i})^2} \tag{3.51}$$

since each PBC width provides a characteristic dimension for growth units at the face surface.

Using eqs 3.47 and 3.50, κ_{2D} becomes

$$\kappa_{2D} = k_O \frac{C_0^{2D}}{\pi^{1/2}} \frac{kT}{s_F \overline{\phi^E}} \left(\sum_{i=1}^{N} \frac{l_{C,i}^{2D} \rho_i}{a_{E,i}}\right) (\ln(1+\sigma))^{3/2}(1+\sigma) \tag{3.52}$$

where each term can be calculated using the presented mechanistic expressions, with the exception of k_O, since the terrace adsorption rate constant k^{+T} is unknown. Nonetheless, with the assumption of an isotropic k^{+T}, relative growth rate expressions between surface-integration-limited regimes are independent of k_O, enabling their calculation. Appendix 3.A.4 provides analytical expressions for possible relative growth rate expressions.

3.2.3 Connecting Surface-Integration-Limited Regimes

On each face, the surface integration mechanism with the largest normal growth rate will dominate the surface structure. When no mass transport limitations are present, the growth rate then corresponds to the kinetically-limited rate of surface integration under the dominant mechanism. This section describes the procedure for connecting surface-integration-limited regimes, enabling determination of the dominant mechanism at a specified supersaturation. See Section 3.2.4 for comments relating to regimes that appear beyond spiral and/or 2D nucleation, such as rough and mass-transport-limited growth.

At a low supersaturation (i.e., low driving force for crystallization), the rate of 2D nucleation on a crystal face is small due to the opposing surface energy penalty. In contrast to growth by 2D nucleation, the spiral mechanism provides a renewable source of steps [7], so at lower σ this mechanism is dominant and commonly seen on the crystal surface. Since the surface energy penalty for 2D nucleation remains constant, at higher σ the increased driving force for crystallization increases the rate of 2D nucleation (this dependence is manifested in the mechanistic expressions above). As a result, at higher supersaturation 2D nuclei can overtake spirals as the primary source of steps and a 2D-nucleation growth regime can become the dominant surface-integration mechanism; this progression has been experimentally imaged using in-situ AFM on calcite [16]. Figure 3.2

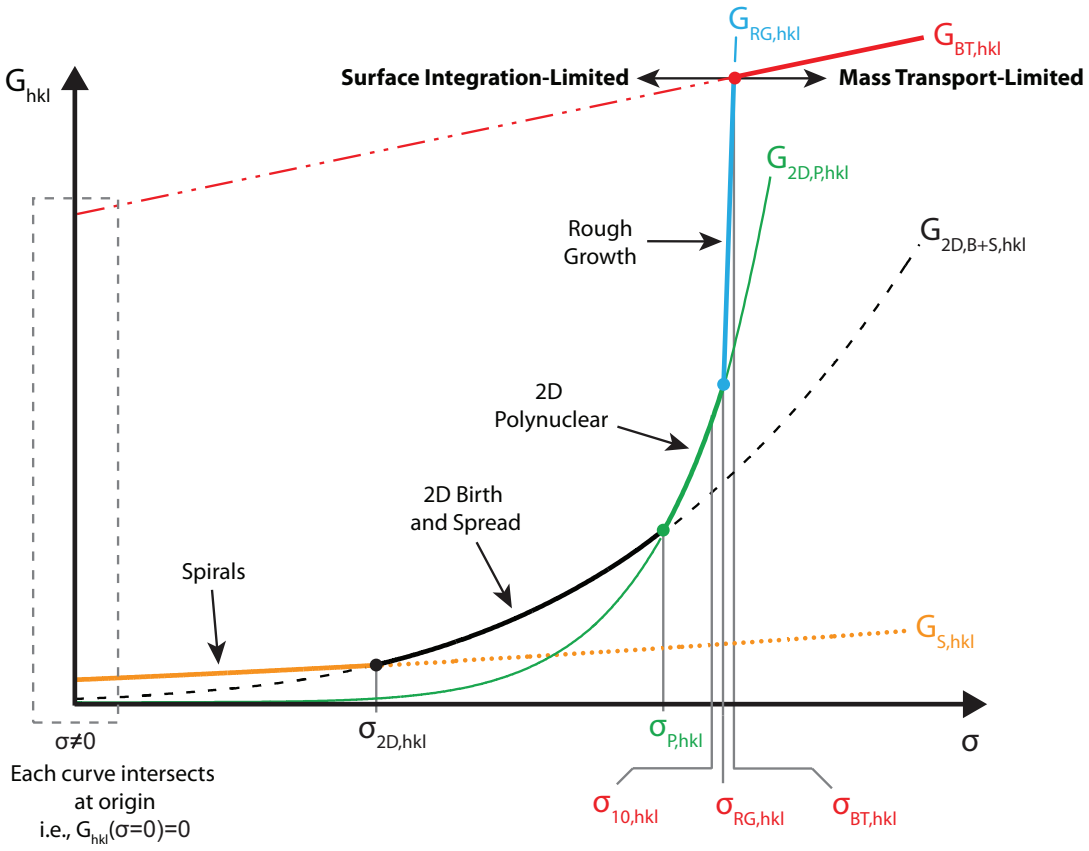

Figure 3.2: As supersaturation increases, a possible progression between regimes would be spirals, to 2D birth-and-spread, to 2D polynuclear, to rough growth, to mass-transport-limited, as indicated by the solid bold line. Subscripts are defined as follows: S = spiral, 2D = 2D nucleation, B+S = birth-and-spread, P = polynuclear, 10 = a nucleus size of 10 growth units, RG = rough growth and BT = bulk-transport-limited.

illustrates a possible progression between regimes (note to better portray the region of interest $\sigma = 0$ is not illustrated, but each growth rate curve intercepts the origin, by definition). Depending on the many face-specific parameters for each mechanistic expression, these curves can be dramatically shifted, potentially producing different progressions. For example, although spirals will always dominate at a low enough supersaturation, the 2D-nucleation growth regimes can be skipped, if mass-transport limitations arise before spirals are overtaken.

To find the crossover between different mechanisms on a face, we solve for the super-

saturation at which growth rate expressions for the two regimes are equal. It is, therefore, useful to make the σ-dependence explicit in the growth rate equations by extracting σ from the various parameters. Similarly, it is useful to extract the assumed-isotropic k_O parameter.

For spiral growth, the supersaturation dependence of τ_S arises from the critical length ($l_{C,i} \propto (\ln(1+\sigma))^{-1}$) and the step velocity ($v_i \propto \sigma$). Thus, we write the spiral growth rate as

$$G_S = \frac{h}{\tau_S} = \frac{h\sigma \ln(1+\sigma) k_O}{\tau_S^*} \tag{3.53}$$

where τ_S^* is independent of σ and k_O:

$$\tau_S^* \equiv \sum_{i=1}^{N} \frac{l_{C,i+1} \ln(1+\sigma) \sin(\alpha_{i,i+1})}{v_{rel,i}} \tag{3.54}$$

$$v_{rel,i} \equiv \frac{v_i}{\sigma k_O} = a_{P,i}\rho_i \tag{3.55}$$

Although τ_S^* is applicable to any supersaturation, it does depend on solvent and temperature.

Following the same process for the 2D birth-and-spread regime, we get

$$\begin{aligned} G_{2D,B+S} &= h(Jf)^{1/3} \\ &= h(\kappa_{2D}^* k_O)^{1/3} (\ln(1+\sigma))^{1/6} (1+\sigma)^{1/3} \exp\left(\frac{-\mathcal{F}}{\ln(1+\sigma)}\right) (\sigma^2 (k_O)^2 f^*)^{1/3} \end{aligned} \tag{3.56}$$

where κ_{2D}^*, $\mathcal{F}$ (eq 3.37) and f^* are the face-specific parameters that are independent of

both supersaturation and the rate constant k_O:

$$\kappa_{2D} = \kappa^*_{2D}(\ln(1+\sigma))^{1/2}(1+\sigma)k_O \tag{3.57}$$

$$\kappa^*_{2D} = \frac{C_0^{2D}}{\pi^{1/2}} \frac{kT}{s_F \overline{\phi^E}} \left(\sum_{i=1}^{N} \frac{l_{C,i}^{2D} \rho_i \ln(1+\sigma)}{a_{E,i}} \right) \tag{3.58}$$

$$f^* \equiv \frac{1}{6} \sum_{i=1}^{N} v_{rel,i} v_{rel,i}^t = \frac{f}{(\sigma k_O)^2} \tag{3.59}$$

Similarly, for the 2D polynuclear mechanism:

$$\begin{aligned} G_{2D,P} &= hJA_C \\ &= h\kappa^*_{2D} k_O (\ln(1+\sigma))^{1/2}(1+\sigma)\exp\left(\frac{-3\mathcal{F}}{\ln(1+\sigma)}\right)\frac{A^*_C}{(\ln(1+\sigma))^2} \end{aligned} \tag{3.60}$$

with A^*_C as another face-specific parameter:

$$A^*_C \equiv A_C(\ln(1+\sigma))^2 = \frac{1}{2}\sum_{i=1}^{N} H_{C,i}^{2D} l_{C,i}^{2D} (\ln(1+\sigma))^2 \tag{3.61}$$

The first crossover to calculate is σ_P, which connects the 2D birth-and-spread and 2D polynuclear regimes; we determine σ_P by setting equal eqs 3.56 and 3.60, for a single face, and numerically solving for σ. Next, we compute the crossover from spiral to 2D nucleation (σ_{2D}), noting that this crossover is to the faster 2D regime at the relevant supersaturation. Therefore, this solution must equate eq 3.53 with either eq 3.56 or 3.60 and once again solve numerically for σ. Further details are reported in Appendix 3.A. Another aspect that should be considered is the applicability of the mechanistic model for 2D nucleation. For very small nuclei, the assumption of defined edges with constant kink densities breaks down; as a result, the model should not be used for a critical nucleus size of less than ≈ 10 growth units. An expression for this supersaturation limit, $\sigma_{n_C=10}$,

can be analytically determined:

$$\sigma_{n_C=10} = \exp\left(\frac{1}{2\sqrt{10}}\left(\frac{s_F\overline{\phi^E}}{kT}\right)\right) - 1 \tag{3.62}$$

$\sigma_{n_C=10}$ provides an upper bound on supersaturation for which to search for σ_P and σ_{2D}, which means neither is guaranteed to exist on a given face. The principle mechanistic parameter in eq 3.62 is $\overline{\phi^E}$ (i.e. the average edge energy penalty to 2D nucleation). In the case of high edge energies, spirals can be predicted to remain the dominate growth mechanism until the advent of a regime beyond 2D nucleation, such as rough or mass-transport-limited growth.

To use eq 3.5 and determine the crystal shape, we require relative growth rates of the form $R_{hkl}(\sigma) = G_{hkl}(\sigma)/G_{ref}(\sigma)$. Depending on the value of σ at which the crystal shape prediction is desired, both G_{hkl} and G_{ref} may each be within either a spiral, 2D birth-and-spread or 2D polynuclear regime. With knowledge of the crossovers σ_{2D} and σ_P for each face, the correct growth rate expression, corresponding to the dominant regime, can be selected. Appendix 3.A.4 lists functional forms of the relative growth rate expression for potential combinations.

The typical change in crystal habit induced by an increase in supersaturation is either the disappearance of a face family, or a change in the crystal's aspect ratio. Both effects are due to the acceleration of the relative growth rate of face family $\{hkl\}$ with σ, once $\sigma > \sigma_{2D,hkl}$. When $\{hkl\}$ and the reference face are both in the spiral regime there is no supersaturation dependence of the relative growth rate (refer to eq 3.73). Once $\{hkl\}$ enters a 2D-nucleation growth regime, however, R_{hkl} increases rapidly with σ, which leads to disappearance of those faces from the crystal shape, or if that is geometrically impossible, to a shape which elongates in the normal direction of that $\{hkl\}$ family. The aspect ratio could correspondingly increase or decrease with supersaturation, when $\{hkl\}$

represents the previously fast-growing or slow-growing faces, respectively.

We have assumed here that the spiral and 2D-nucleation growth mechanisms can be treated exclusively (i.e., operating in isolation), as opposed to additively. With both spirals and nucleated islands on the surface, growth units will clearly attach at steps on either type of surface structure. If a spiral regime is dominant, the growth rate depends on the rotation time. This rate is independent of whether or not 2D nuclei are forming in front of advancing spiral steps, justifying considering the growth rate as the spiral expression alone. With 2D nucleation as the dominant mechanism, advancing spirals effectively lower the coverage by 2D nuclei needed to complete a face layer, by an amount that depends on the density of spirals and their speed of face coverage relative to the 2D-nucleation rate and nuclei growth. Deep in a 2D-nucleation regime this effect can be ignored, since the density of steps from spirals should be much lower than from 2D nuclei, again leading to the 2D-nucleation growth rate expressions alone to be an accurate representation of surface integration.

When in a 2D-nucleation regime but near the crossover point, where both mechanisms alone would give a similar normal face growth rate, selecting exclusively the 2D-nucleation rate expressions might underestimate the actual face growth rate, since the mechanisms are additive. To resolve this issue, we could find the time to reach a fractional coverage of less than 1, introducing a form of packing factor. However, in the birth-and-spread regime, annihilation of steps between two nuclei are neglected, together with edge effects; effectively, each nucleus is allowed to grow unhindered in contributing to reaching the required fractional coverage. Therefore, there is a contrasting argument to solve for a fractional coverage of greater than 1, since neglecting annihilation overestimates the rate of coverage. A decision to solve for a coverage other than unity would only introduce a numerical correction that propagates through the framework as a constant factor, but due to these competing possibilities of under or overestimation, we have elected

to solve for a coverage of unity. Note additionally that 2D birth-and-spread and 2D polynuclear regimes are similarly treated as exclusive, in lieu of the more physical additive interpretation. Effectively, the developed regimes are useful limiting cases for which analytical expressions can be developed.

3.2.4 Rough and Mass-Transport-Limited Growth

Thermal roughening of the step edge at equilibrium corresponds to a phase transition, beyond which the dividing point between upper and lower layers either side of a step edge cannot be pinpointed [60, 61]; it depends on temperature and interfacial energies. Away from equilibrium, the kink density similarly increases with temperature; the thermal reorganization events assumed to continually regenerate kink sites may produce a rough step. Under such conditions of crystal growth, roughening may result from increasing supersaturation, whereby a higher driving force for crystallization can overcome larger surface energy penalties. Thus, at higher supersaturations the crystal may appear less faceted, exposing high energy surfaces instead of sharp edges and vertices; spirals/2D nuclei may similarly lose their strictly faceted nature and expose non-PBC directions. However, since crystal growth is usually governed by kinetics, the onset of a rough regime is more likely to stem from favorable attachment at sites other than kinks on the crystal surface; transitions to such kinetic roughening do remain closely related to surface energy penalties [34]. Favorable step edge attachment can increase the density of incorporation sites along the step dramatically, leading to a much greater step velocity and roughened edge, though overall growth of the crystal face may remain layer-by-layer. The advent of favorable terrace attachment will cause a similarly dramatic increase in the density of incorporation sites on the face itself, which will would no longer grow in a layered fashion. This latter form of kinetic roughening is similar to the 2D polynuclear regime

as the nucleus size tends towards a single growth unit. While the rounding distance of a straight spiral side has been shown to decrease with supersaturation [45], we nonetheless expect crystals, spirals and 2D nuclei to become less faceted at high supersaturations. The resolution of this apparent discrepancy may be due to decreasing critical lengths and the aforementioned increasing density of favorable attachment sites around any vertices.

As the net rate of growth unit attachment at kink (or other) sites increases with supersaturation, crystal growth will eventually become limited by solute transport (e.g., bulk transport from solution, surface diffusion), instead of surface integration. On each face, this limit may commence from either spiral, 2D-nucleation or rough growth mechanisms, but becomes increasingly likely following the advent of kinetic roughening, where growth rapidly accelerates with the increasing density of favorable attachment sites. Note that before kinetic roughening, spiral/2D-nucleation surface features should still be visible, but if mass transport limitations are in effect then the presented mechanistic expressions must be modified to reflect the new rate-determining step, since the concentration of solute near incorporation sites will no longer be equal to that in bulk solution.

We expect single crystal growth in a laboratory setting to have little or no mixing, resulting in a low Peclet number; when the bulk transport limit becomes appropriate, it should correspond to diffusion across the face's boundary layer (see Supporting Information for ref. [1]):

$$G_{BT} = \frac{D}{\delta} V_{m,X} (C - C_S) \tag{3.63}$$

D is the diffusivity of solute in solution, C_S is the solute concentration at the crystal surface and δ is the boundary layer thickness (over which $\Delta C = C - C_S$ operates). Due to fast kink incorporation in this regime, $C_S \approx C_{sat}$; this produces

$$G_{BT} = \frac{D V_{m,X}}{\delta V_{m,S}} x_{sat} \sigma \tag{3.64}$$

where $V_{m,S}$ is the average molar volume of solution.

Connecting surface-integration limited regimes to the mass-transport limit requires an estimate for k_O, which does not enter eq 3.64 so will not cancel upon equating eqs 3.53, 3.56 or 3.60 to eq 3.64. Similarly, k_O is required to calculate relative growth rates where one face is mass-transport-limited. Since molecular simulations are required to accurately determine this overall rate constant, another method is required to estimate the supersaturation at which a face becomes mass-transport-limited (σ_{BT}).

The 2D-nucleation applicability limit could be used as an estimate for σ_{BT}, provided the crossover to transport-limited occurs from a 2D-nucleation regime (i.e., not directly from spiral growth). This supersaturation ($\sigma_{n_C=10}$) represents the point at which increasingly small nuclei are becoming stable; thereafter, it is expected that attachment becomes favorable at sites other than kinks, i.e., the advent of a rough growth regime is imminent. Figure 3.2 illustrates this point, where $\sigma_{RG,hkl}$ is expected to follow shortly after $\sigma_{10,hkl}$. The slope of $G_{RG,hkl}$ vs. σ should be high as all surface sites become favorable; thus, the crossover from rough growth to bulk-transport-limited ($\sigma_{BT,hkl}$) should not be sensitive to $G_{BT,hkl}$ (the unknown position of this line relative to the surface-integration-limited curves reflects the lack of a reliable value for k_O). Thus, $\sigma_{n_C=10}$ can be used as a proxy for σ_{BT}, though the method would ideally be used when σ_{2D} exists before $\sigma_{n_C=10}$. In the absence of a crossover to 2D nucleation, the mass transport limit is reached directly from the spiral growth regime, which this estimate of $\sigma_{n_C=10} \sim \sigma_{BT}$ is perhaps less applicable for; the $G_{S,hkl} \rightarrow G_{BT,hkl}$ crossover should instead utilize a value for k_O if at all possible.

When the growth rate of $\{hkl\}$ becomes mass-transport-limited, R_{hkl} starts to decrease with increasing σ (see relative growth rate expressions in Appendix 3.A.4), until the reference face is also bulk-transport-limited; eq 3.64 has no face specific parameters, so with both faces growing under the mass-transport limit, $R_{hkl} = 1$. Figure 3.3 shows a possible profile: under the spiral mechanism R_{hkl} has no σ-dependence, upon reaching

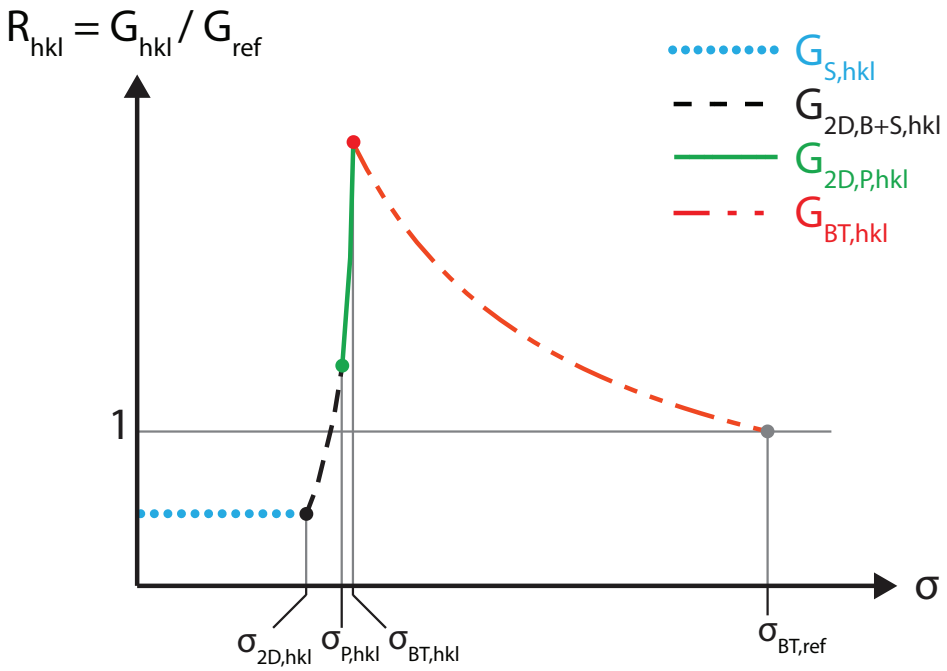

Figure 3.3: A typical progression of the relative growth rate, R_{hkl}, for a face family on which 2D-nucleation growth regimes become dominant (at which point R_{hkl} increases with σ). Once the mass transport limit is reached, R_{hkl} decreases with σ. Subscripts are defined as follows: S = spiral, 2D = 2D nucleation, B+S = birth-and-spread, P = polynuclear and BT = bulk-transport-limited.

a 2D-nucleation regime ($\sigma_{2D,hkl}$) R_{hkl} accelerates (potentially leading to faces growing out) up to a maximum at $\sigma_{BT,hkl}$, at which point it decreases to $R_{hkl} = 1$ at $\sigma_{BT,ref}$. At some point, as $R_{hkl} \to 1$, the $\{hkl\}$ face family may grow back into the steady-state crystal shape. Upon growing out of the shape an edge or vertex will be formed, which can grow at a maximum rate corresponding to the mass transport limit; if this limiting rate becomes insufficient for the face to remain absent from the morphology, due to acceleration of the surrounding faces, the previously grown-out faces may reappear [62]. Note that Figure 3.3 is an example profile only and it is possible for $G_{2D,P,hkl}$ to decrease with σ (because the nucleation rate is increasing, but A_C is decreasing); the exact profile is heavily dependent on the numerous face-specific parameters buried in the complex σ-dependence of these relative growth rates.

The above picture presents the limit of a faceted sphere in mass-transport-limited growth, which tends towards a fully spherical form following roughening transitions between faces. However, a sphere is an unstable growth form in the diffusive transport limit, where a concentration gradient exists in solution [63–66]. Fluctuations from a perfect sphere, through solute deposition, extend farther out to solution and experience locally higher supersaturations, an effect which is even more pronounced for edges and vertices on a faceted shape. The adsorption rate is, therefore, expected to be higher at these points; thus, if this effect cannot be dispersed by fast surface diffusion (in relation to incorporation rates) then such edges and vertices grow faster and lead to dendritic or spherulitic growth shapes (e.g., snowflake crystals [66, 67]). Thus, the dendritic regime becomes relevant once kinetic roughening and mass-transport limitations are in effect. While our model does not consider this growth regime mechanistically, at a high enough supersaturation it will be reached; we direct readers to ref. [66] for further details.

3.3 Case Study: Naphthalene Grown in Ethanol or Cyclohexane

The next sections present modeling results for various candidate crystal growth systems, which are compared to experimental shapes reported in the literature. It is important to note that the experimental growth of crystals under the same conditions usually results in a distribution of similar shapes (due to fluctuations in local growth conditions), though sometimes only a typical example is reported. Our predictions give us a single crystal growth shape, which we have compared to experimental habits (these predictions could be turned into a distribution of shapes via sensitivity analysis of operating conditions and physicochemical parameters). Minor discrepancies in predicted and re-

ported habits are, therefore, tolerable and expected. Aspects of naphthalene, biphenyl and pentaerythritol relating to the solvent effect are discussed in Chapter 4; mechanistic parameters relating to growth regimes, for each crystal system, are contained within Appendices 3.B and 4.A.

Naphthalene presents a useful case to model, with supersaturation-dependent growth shapes reported for both ethanol and cyclohexane. When grown in ethanol, the $\{11\bar{1}\}$ family of faces grows out of the crystal habit as supersaturation is increased [68]; this result had been predicted successfully using our earlier formulation [4] of the presented mechanistic approach.

For modeling purposes, naphthalene's crystallography was taken from Cambridge Structural Database (CSD) CIF file code NAPHTA10 [69]. Table 3.1 summarizes the predicted relative growth rates (with reference to face (001), i.e., $R_{hkl} = G_{hkl}/G_{001}$) for the predicted-dominant F faces of naphthalene grown in ethanol, at various supersaturations, using the current formulation of the model. Unless both faces are in the spiral regime, the relative growth rate is a function of supersaturation, so σ values for each set of relative growth rates are indicated. Crossovers from spiral to 2D nucleation (σ_{2D}) and 2D birth-and-spread to 2D polynuclear (σ_P) are listed; if no crossover is predicted before the applicability limit of our modeling, it is marked not applicable (n.a.). This applicability limit is $\sigma_{n_{C=10}}$, which is also shown and serves as an estimate to the onset of rough growth (this estimate is expected to be more accurate if σ_{2D} exists). Finally, the free energy change (in units of kT), $\frac{\Delta G_{2D}}{kT}(\sigma_{2D})$, to form a critical nucleus at σ_{2D} is provided.

Figure 3.4 shows the predicted shapes for these relative growth rates alongside those which have been reported experimentally [68]. In the new formulation of the model, at $\sigma = 0.13$ the $\{11\bar{1}\}$ family of faces is predicted to cross over to a 2D birth-and-spread mechanism, at which point its relative growth rate accelerates with σ and leads it to grow

Table 3.1: Relative growth rates and mechanistic crossovers for dominant naphthalene F faces when grown in ethanol (n.a. = not applicable)

	Face			
	(001)	$(20\bar{1})$	(110)	$(11\bar{1})$
$R(\sigma < 0.13)$	1	1.24	1.18	1.13
$R(\sigma = 0.16)$	1	1.24	1.18	2.10
$R(\sigma = 0.35)$	1	1.24	1.56	5.64
σ_{2D}	n.a.	0.36	0.30	0.13
$\frac{\Delta G_{2D}}{kT}(\sigma_{2D})$	n.a.	9.1	10	13
$\sigma_{n_{C=10}}$	3.1	0.70	0.67	0.49
σ_P	n.a.	n.a.	n.a.	0.35

out of the crystal shape. This value of $\sigma_{2D,11\bar{1}}$ is similar to before [4], but note that the estimate of $\frac{\Delta G_{2D}}{kT}(\sigma_{2D,11\bar{1}}) = 9.1$ is substantially less than the estimated range of 35 ± 10 for generic values in molecular organic systems stated in ref. [4].

The $\{110\}$ and $\{20\bar{1}\}$ families are also predicted to cross over to 2D nucleation (though not 2D polynuclear); these crossovers are predicted to exist at $\sigma = 0.30$ and $\sigma = 0.36$, respectively. Conversely, 2D nucleation on the $\{001\}$ family is not predicted to overtake spirals up to our modeling applicability limit; we predict a crossover to rough or mass-transport-limited growth directly from the spiral regime. Since $\sigma_{n_{C=10}}$ is significantly higher for the $\{001\}$ family, it suggests that the surrounding faces will each enter a rough regime at a much lower supersaturation than the $\{001\}$ faces. With these surrounding faces growing under rough mechanisms we would expect high relative growth rates and a platelet shape, which has been experimentally shown [4] (note the aspect ratio would be supersaturation-dependent).

Table 3.2 contains the analogous mechanistic predictions for naphthalene grown in cyclohexane. The reference face for relative growth rates is again (001). The $\{11\bar{1}\}$ family is predicted to cross over to 2D birth-and-spread at $\sigma = 0.0023$ and 2D polynuclear at $\sigma = 0.0033$; consequently, it grows out of the steady-state growth shape at very

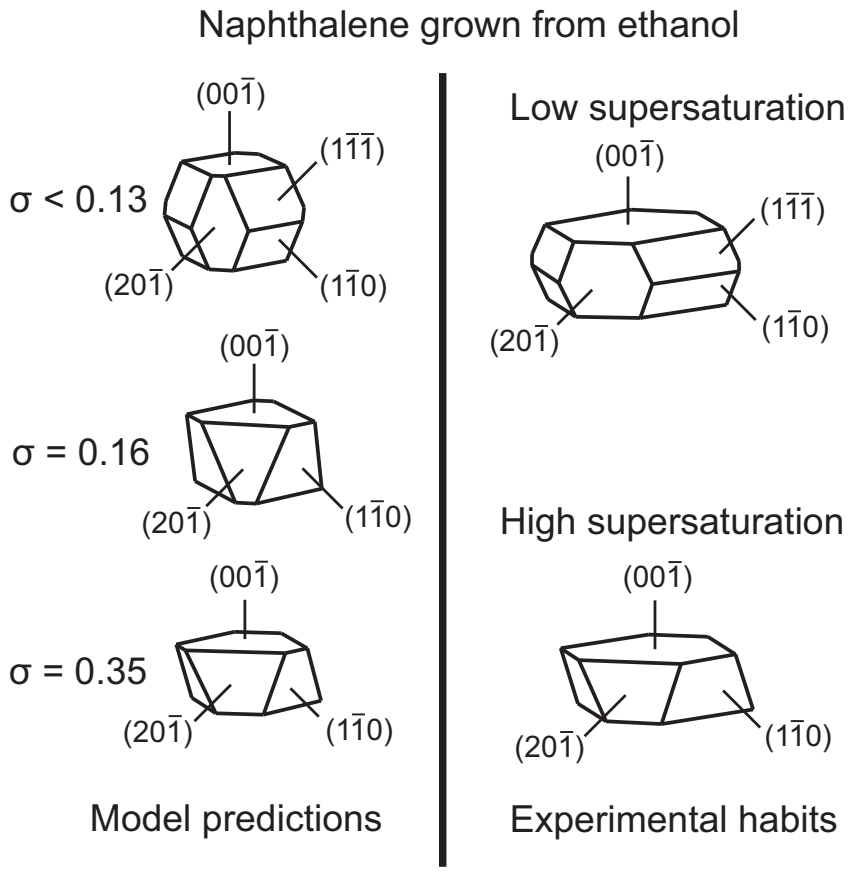

Figure 3.4: Predicted shape progression for naphthalene grown in ethanol as supersaturation is increased (left), showing the growth-out of the (11$\bar{1}$) family of faces and changing aspect ratio after that. Corresponding experimentally reported shapes (right, schematics traced from Grimbergen et al. [68]). Reprinted with permission from Tilbury et al. [28]. Copyright 2016 American Chemical Society.

Table 3.2: Relative growth rates and mechanistic crossovers for dominant naphthalene F faces when grown in cyclohexane (n.a. = not applicable)

	Face		
	(001)	$(20\bar{1})$	(110)
$R(\sigma = 0.0061)$	1	2.32	2.13
$R(\sigma = 0.0070)$	1	2.32	3.83
$R(\sigma = 0.0082)$	1	2.32	18.3
σ_{2D}	n.a.	0.011	0.0055
$\frac{\Delta G_{2D}}{kT}(\sigma_{2D})$	n.a.	13.9	18.3
$\sigma_{n_{C=10}}$	0.96	0.13	0.11
σ_P	n.a.	0.012	0.0070

low supersaturation, a fact which is supported by its absence from all the experimental morphologies [68, 70]. The $\{110\}$ and $\{20\bar{1}\}$ families are both predicted to cross over to 2D birth-and-spread ($\sigma = 0.0055$ and $\sigma = 0.011$, respectively) and 2D polynuclear ($\sigma = 0.0070$ and $\sigma = 0.012$, respectively), while the $\{001\}$ family is again predicted to remain under spiral growth up to the applicability limit of our 2D-nucleation model. These predictions give rise to a supersaturation-dependent aspect ratio, which Figure 3.5 demonstrates; such shape predictions show good agreement to the experimental determinations.

3.4 Case Study: Biphenyl Grown in Toluene

Biphenyl grown in toluene is another example previously studied by our group, using earlier formulations of mechanistic models for both spiral growth and 2D nucleation [71]. Using crystallography from CSD CIF file code BIPHEN04 [72], biphenyl's growth in toluene was modeled to appraise the current mechanistic approach relative to earlier predictions. Table 3.3 summarizes the predicted faces, mechanistic parameters and relative growth rates (again with reference to face (001), i.e., $R_{hkl} = G_{hkl}/G_{001}$), at various su-

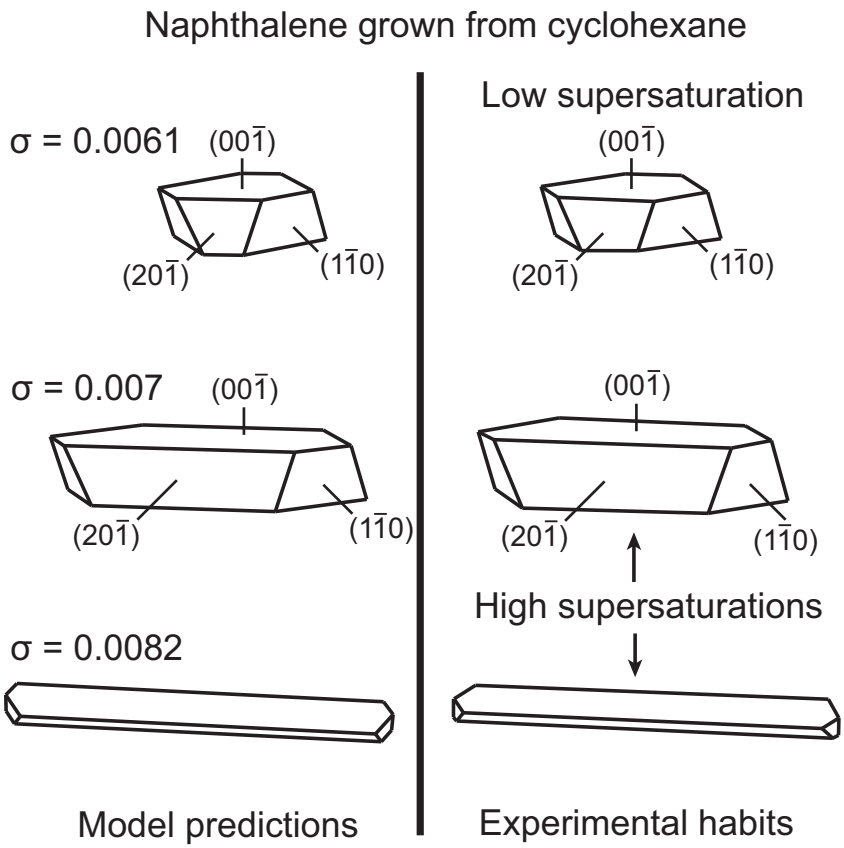

Figure 3.5: Predicted shape progression for naphthalene grown in cyclohexane as supersaturation is increased (left), demonstrating the changing aspect ratio. Corresponding experimentally reported shapes (right, schematics traced from Grimbergen et al. [68] and Wells [70]). Reprinted with permission from Tilbury et al. [28]. Copyright 2016 American Chemical Society.

Table 3.3: Relative growth rates and mechanistic crossovers for dominant biphenyl F faces when grown in toluene (n.a. = not applicable)

	Face		
	(001)	(110)	$(11\bar{1})$
$R(\sigma = 0.005)$	1	1.3	17
$R(\sigma = 0.006)$	1	3.2	84
$R(\sigma = 0.007)$	1	15	240
σ_{2D}	n.a.	0.005	0.003
$\frac{\Delta G_{2D}}{kT}(\sigma_{2D})$	n.a.	20	21
$\sigma_{n_{C=10}}$	0.93	0.10	0.09
σ_P	n.a.	0.006	0.004

persaturations. At $\sigma = 0.003$ and $\sigma = 0.004$, the $\{11\bar{1}\}$ face family is predicted to cross over to 2D birth-and-spread and then 2D polynuclear, respectively; thus, these faces grow out of the crystal shape at very low supersaturation. The $\{110\}$ face family has higher values at $\sigma_{2D,110} = 0.005$ and $\sigma_{P,110} = 0.006$. No crossover to 2D nucleation is predicted for the $\{001\}$ family, so above $\sigma = 0.005$ the predicted crystal habit is a rhombic platelet bounded by $\{110\}$ faces with an aspect ratio that increases with supersaturation, as shown in Figure 3.6. This rhombic platelet has been experimentally reported [73].

The previous modeling effort by Winn and Doherty [71] predicted a roughening transition for the $\{110\}$ faces at $\sigma = 0.0069$ and Jetten et al. [73] also noted that above $\sigma = 0.007$ this family begins to lose its faceted nature. Using the calculated value $\sigma_{n_{C=10},110} = 0.1$ as a bound for rough growth would, therefore, appear to overestimate this transition. However, since $\sigma_{P,110} = 0.006$, this reduction in faceted nature may instead result from growth becoming mass-transport-limited immediately following the transition to a 2D polynuclear regime (which could permit the reappearance of higher index faces).

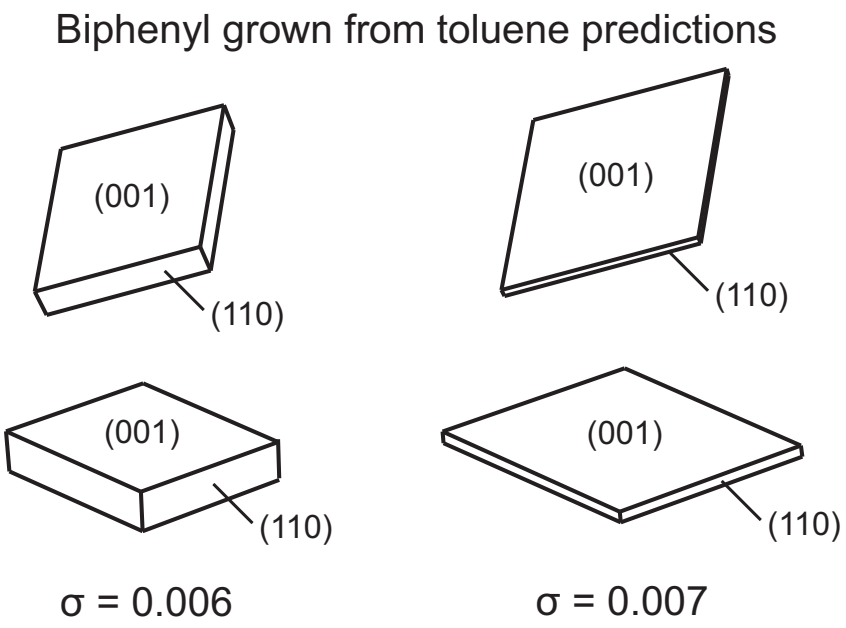

Figure 3.6: Two views of the predicted shapes of biphenyl grown in toluene at $\sigma = 0.006$ (left) and $\sigma = 0.007$ (right). Reprinted with permission from Tilbury et al. [28]. Copyright 2016 American Chemical Society.

3.5 Case Study: Pentaerythritol Grown in Water

Pentaerythritol grown in water was modeled using CSD CIF code PERYTO04 [74]. Table 3.4 summarizes the relevant face predictions, where relative growth rates are with reference to face (101), i.e., $R_{hkl} = G_{hkl}/G_{101}$. At $\sigma = 0.15$ the {110} face family is predicted to cross over to 2D birth-and-spread, growing out of the crystal shape by $\sigma = 0.18$.

Figure 3.7 shows the predicted shapes at low and high supersaturation. The low supersaturation shape with the {110} faces included has been reported experimentally [70] and following the predicted disappearance of the {110} family at higher supersaturation, the commonly observed [75, 76] bipyramidal crystal habit is produced.

Table 3.4: Relative growth rates and mechanistic crossovers for dominant pentaerythritol F faces when grown in water (n.a. = not applicable)

	Face		
	(101)	$(10\bar{1})$	(110)
$R(\sigma < 0.15)$	1	1	0.86
$R(\sigma = 0.18)$	1	1	1.87
σ_{2D}	n.a.	n.a.	0.15
$\frac{\Delta G_{2D}}{kT}(\sigma_{2D})$	n.a.	n.a.	17
$\sigma_{n_{C=10}}$	6.1	6.1	0.61
σ_P	n.a.	n.a.	n.a.

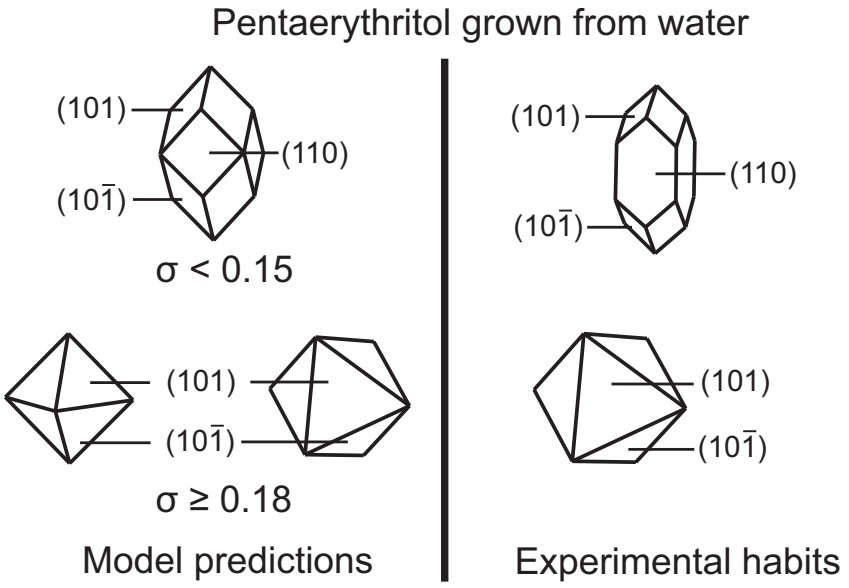

Figure 3.7: Predicted morphologies of pentaerythritol grown in water at $\sigma < 0.15$ and $\sigma \geq 0.18$ (left); experimentally reported habits (right: schematics traced from Wells [70] (top) and Bernardo and Giulietti [76] (bottom)). Reprinted with permission from Tilbury et al. [28]. Copyright 2016 American Chemical Society.

Table 3.5: Relative growth rates and mechanistic crossovers for dominant β-HMX F faces when grown in acetone (n.a. = not applicable)

	Face			
	(011)	(110)	(020)	(101)
R	1	3.64	1.07	2.97
σ_{2D}	n.a.	n.a.	n.a.	n.a.
$\frac{\Delta G_{2D}}{kT}(\sigma_{2D})$	n.a.	n.a.	n.a.	n.a.
$\sigma_{n_{C=10}}$	11	4.5	3.0	2.0
σ_P	n.a.	n.a.	n.a.	n.a.

3.6 Case Study: β-HMX Grown in Acetone

The growth of β-HMX (a crystalline explosive) in acetone has recently been studied by Shim and Koo [77], who utilized an earlier formulation [4] of this mechanistic model for 2D nucleation alongside kinetic Monte Carlo techniques to successfully predict an elongated morphology at high supersaturation (they verified this change in crystal habit experimentally).

We used CSD CIF code OCHTET14 [78] to model the growth of β-HMX in acetone; Table 3.5 summarizes the relevant results, where relative growth rates are $R_{hkl} = G_{hkl}/G_{011}$. Up to the 2D-nucleation applicability limit of our current mechanistic framework, no crossover to 2D nucleation is predicted on any of the dominant F faces. The calculated crystal morphology is shown in Figure 3.8 alongside the reported [77] experimental shapes at low and high supersaturation; the predicted habit corresponds favorably to the spectrum of experimentally produced crystals at low supersaturation. Figure 3.9 compares predicted spirals on the (020) and (011) faces to the informative experimental images from Shim and Koo [77]. These spiral shapes are fairly well predicted by the model, though the aspect ratio for the (020) spiral is over-estimated. Note the experimental (011) spiral is slightly asymmetric, which is unexpected since β-HMX is a nonpolar [79] lattice with a centrosymmetric growth unit.

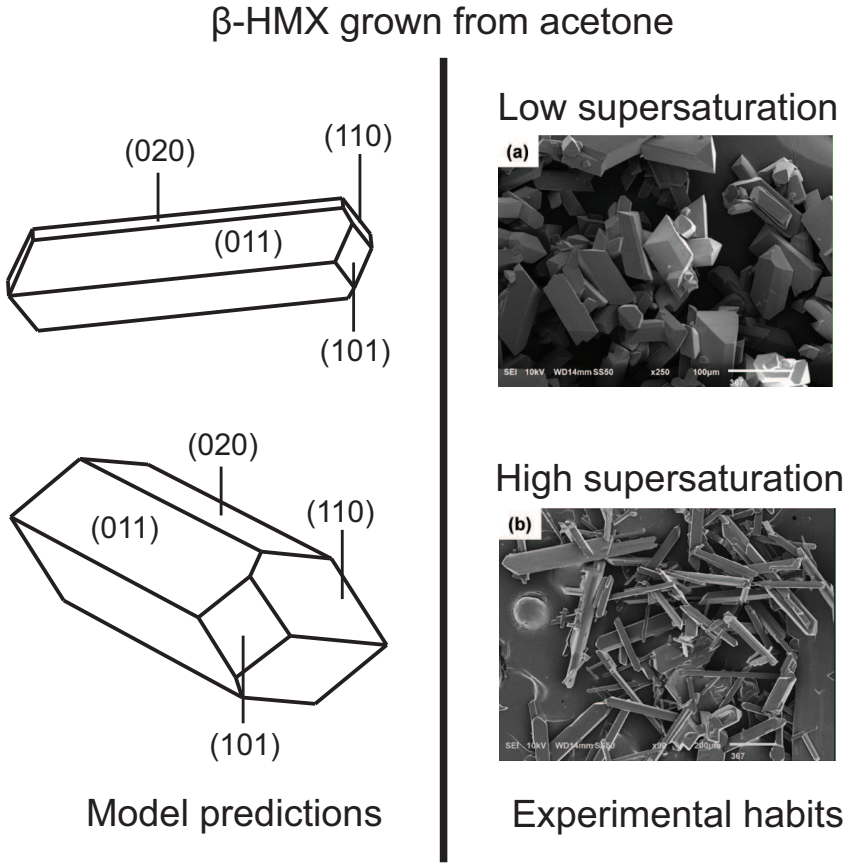

Figure 3.8: Two views of the predicted morphology of β-HMX grown in acetone (left); images of experimental habits at low and high supersaturation (right, reprinted with permission from Shim and Koo [77], copyright 2015 American Chemical Society).

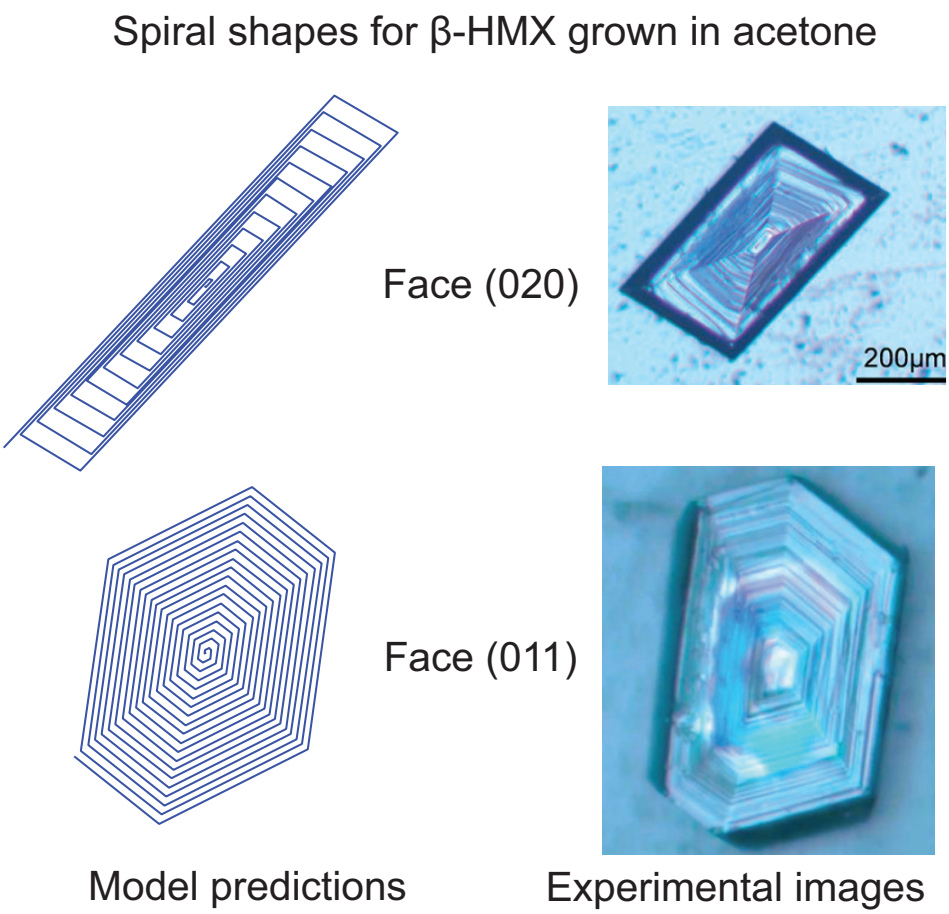

Figure 3.9: Predicted spiral shapes on the (020) and (011) faces of β-HMX grown in acetone, alongside corresponding experimental images reprinted with permission from Shim and Koo [77], copyright 2015 American Chemical Society).

Our current formulation of the model suggests that the faces have different transitions to a rough growth mechanism, the order of which can be estimated by comparing values for $\sigma_{n_{C=10}}$. Note that this rough mechanism may contain characteristics of 2D nucleation, but the shrinking nucleus size renders the picture of a nucleus with well-defined PBC edges and average kink densities ill-advised. The {101} and {020} face families have the lowest $\sigma_{n_{C=10}}$ values, so are expected to transition to a rough regime first, leading to their disappearance from the crystal shape (i.e., they grow out). When the {110} face family enters a rough growth regime, it cannot geometrically grow out of the crystal shape, so instead the aspect ratio elongates with supersaturation. Therefore, the difference in $\sigma_{n_{C=10}}$ values is able to qualitatively explain the observed supersaturation-dependent growth shape. This explanation additionally aligns with the reported [77] image of the rough {110} surface on the elongated crystal morphologies.

3.7 Conclusions

The mechanistic approach presented provides a framework with which it is possible to connect the important regimes of layered crystal growth and predict supersaturation-dependent morphologies. The primary effects, as supersaturation is increased, are face families growing out of the crystal shape or producing a changing aspect ratio; these effects result from crossing over to 2D nucleation or rough growth. Comparing predicted crossover supersaturations between face families can determine the order of such events and provide further insight into the possible morphological changes with supersaturation.

This new formulation of determining crossovers develops face-specific parameters and values, as opposed to typical estimates for organic molecular growth units, which are unlikely to provide a universal description for each face on every crystal system. We tested the model for a variety of centrosymmetric cases, and it is able to predict morphological

changes in a fashion that should prove useful for enabling rational design within crystal shape engineering.

Experimentally imaging the surface structure during a transition between different growth mechanisms on a specific face may be challenging via single crystal growth in solution, since the face can disappear from the crystal morphology following such transitions. Instead, epitaxial growth and in-situ imaging of a single face may provide the ability to more quantitatively test the accuracy of predicted crossovers.

Appendices

3.A Crossovers and Relative Growth Rates

In determining crossovers, we equate rate expressions and solve for the supersaturation. Upper and lower bounds can be set in searching for the solution, for example, picking a very low (e.g., $\sigma = 0.0001$) supersaturation as a lower bound and the limit of 2D applicability ($\sigma_{n_C=10}$) as the upper bound. The typical case of a single crossover can be solved using a simple half interval method.

3.A.1 2D Birth-and-Spread to 2D Polynuclear Crossover (σ_P)

We consider this crossover first, since it is independent of the other regimes. Setting equal eqs 3.56 and 3.60, we obtain

$$\frac{(f^*)^{1/3}}{A_C^*(\kappa_{2D}^*)^{2/3}} = \frac{(1+\sigma_P)^{2/3}}{\sigma_P^{2/3}(\ln(1+\sigma_P))^{5/3}} \exp\left(\frac{-2\mathcal{F}}{\ln(1+\sigma_P)}\right) \tag{3.65}$$

Using eqs 3.37, 3.58, 3.59 and 3.61, the only unknown in eq 3.65 is σ_P, which can subsequently be solved for numerically. Note that the value of k_O is not required. Below

σ_P, the birth-and-spread mechanism should be used for the 2D nucleation growth regime, while above σ_P, the 2D polynuclear mechanism should be used. The growth rate may be underestimated near σ_P, since either initial nucleation area or nucleus growth has been ignored.

3.A.2 Spiral to 2D Nucleation Crossover (σ_{2D})

For the crossover from a spiral to a 2D nucleation growth mechanism, we first assume a crossover to the 2D birth-and-spread regime. After this σ_{2D} is found, if $\sigma_P < \sigma_{2D}$ we must re-solve instead considering a crossover from spiral growth to the 2D polynuclear regime. Setting equal eqs 3.53 and 3.56, eq 3.66 results, which again can be numerically solved to find σ_{2D} (using eqs 3.37, 3.54, 3.58 and 3.59).

$$\frac{1}{\tau_S^*(f^*\kappa_{2D}^*)^{1/3}} = \frac{(1+\sigma_{2D})^{1/3}}{\sigma_{2D}^{1/3}(\ln(1+\sigma_{2D}))^{5/6}}\exp\left(\frac{-\mathcal{F}}{\ln(1+\sigma_{2D})}\right) \tag{3.66}$$

After determining σ_{2D} from eq 3.66, if $\sigma_P < \sigma_{2D}$, σ_{2D} should be re-calculated from

$$\frac{1}{\tau_S^* A_C^* \kappa_{2D}^*} = \frac{(1+\sigma_{2D})}{\sigma_{2D}(\ln(1+\sigma_{2D}))^{5/2}}\exp\left(\frac{-3\mathcal{F}}{\ln(1+\sigma_{2D})}\right) \tag{3.67}$$

3.A.3 Crossover to Mass-Transport-Limited Growth (σ_{BT})

The crossover to mass-transport-limited growth can occur from any surface-integration-limited regime, depending on which is the dominant mechanism when a face's growth rate becomes equal to (and then limited to) G_{BT} (eq 3.64). Thus, which mechanism precedes mass-transport-limited growth depends on face-specific mechanistic parameters. This crossover supersaturation corresponds to a Damköhler (Da) number of unity (where $\mathrm{Da} = G_{SI}^D/G_{BT}$ and G_{SI}^D refers to the dominant surface-integration-limited mechanism). One could determine σ_{BT} by solving $G_{SI}(\sigma_{BT}) = G_{BT}(\sigma_{BT})$ for each surface-integration-

limited mechanism; the lowest σ_{BT} will be the correct crossover, since at this supersaturation, the selected growth mechanism must be fastest and, therefore, dominant.

The crossover from spiral to mass-transport-limited growth ($G_{BT} = G_S$) can be solved explicitly to

$$\sigma_{BT} = \exp\left(\frac{D\tau_S^* V_{m,X} x_{sat}}{\delta h V_{m,S} k_O}\right) - 1 \tag{3.68}$$

On the other hand, the crossovers from 2D birth-and-spread ($G_{BT} = G_{2D,B+S}$) and 2D polynuclear ($G_{BT} = G_{2D,P}$) result in eqs 3.69 and 3.70 respectively, which require numerical solution:

$$\frac{DV_{m,X}x_{sat}}{\delta V_{m,S} h (f^* \kappa_{2D}^*)^{1/3} k_O} = \frac{(\ln(1+\sigma_{BT}))^{1/6}(1+\sigma_{BT})^{1/3}}{\sigma_{BT}^{1/3}} \exp\left(\frac{-\mathcal{F}}{\ln(1+\sigma_{BT})}\right) \tag{3.69}$$

$$\frac{DV_{m,X}x_{sat}}{\delta V_{m,S} h A_C^* \kappa_{2D}^* k_O} = \frac{(1+\sigma_{BT})}{\sigma_{BT}(\ln(1+\sigma_{BT}))^{3/2}} \exp\left(\frac{-3\mathcal{F}}{\ln(1+\sigma_{BT})}\right) \tag{3.70}$$

Note that k_O appears in eqs 3.68 – 3.70 and an estimate must be provided to determine σ_{BT} mechanistically.

With a reliable value for k_O, these equations can be solved. The average molar volume in solution, $V_{m,S}$, can be approximated as that of the pure solvent, while the diffusion coefficient, D, can be estimated using the Stokes-Einstein equation:

$$D = \frac{kT}{6\pi\eta r_e} \tag{3.71}$$

In eq 3.71, η is the dynamic viscosity of the solvent and r_e is the equivalent spherical radius of a solute molecule, which can be calculated using

$$r_e = \left(\frac{3\chi V_{m,X}}{4\pi N_A}\right)^{\frac{1}{3}} \tag{3.72}$$

where χ is a packing factor equaling 0.76 for hard spheres). Note that the diffusion

coefficient is another avenue for the solvent effect. The boundary layer thickness, δ, can be estimated from correlations, but has a degree of uncertainty based on the unknown and/or varied fluid flow conditions during crystal growth.

3.A.4 Relative Growth Rates

Expressions for different forms of the relative growth rate $R_{hkl}(\sigma) = G_{hkl}(\sigma)/G_{ref}(\sigma)$ are listed below.

$$\frac{G_{S,hkl}}{G_{S,ref}} = \frac{\frac{h_{hkl}\sigma\ln(1+\sigma)k_O}{\tau^*_{S,hkl}}}{\frac{h_{ref}\sigma\ln(1+\sigma)k_O}{\tau^*_{S,ref}}} = \frac{h_{hkl}\tau^*_{S,ref}}{h_{ref}\tau^*_{S,hkl}} \tag{3.73}$$

$$\begin{aligned}\frac{G_{2D,B+S,hkl}}{G_{S,ref}} &= \frac{h_{hkl}(\kappa^*_{2D,hkl})^{1/3}(\ln(1+\sigma))^{1/6}(1+\sigma)^{1/3}\exp\left(\frac{-\mathcal{F}_{hkl}}{\ln(1+\sigma)}\right)(\sigma^2 f^*_{hkl})^{1/3}k_O}{\frac{h_{ref}\sigma\ln(1+\sigma)k_O}{\tau^*_{S,ref}}} \\ &= \frac{h_{hkl}\tau^*_{S,ref}(\kappa^*_{2D,hkl}f^*_{hkl})^{1/3}(1+\sigma)^{1/3}\exp\left(\frac{-\mathcal{F}_{hkl}}{\ln(1+\sigma)}\right)}{h_{ref}\sigma^{1/3}(\ln(1+\sigma))^{5/6}}\end{aligned} \tag{3.74}$$

$$\begin{aligned}\frac{G_{2D,P,hkl}}{G_{S,ref}} &= \frac{h_{hkl}\kappa^*_{2D,hkl}k_O(\ln(1+\sigma))^{1/2}(1+\sigma)\exp\left(\frac{-3\mathcal{F}_{hkl}}{\ln(1+\sigma)}\right)\frac{A^*_{C,hkl}}{(\ln(1+\sigma))^2}}{\frac{h_{ref}\sigma\ln(1+\sigma)k_O}{\tau^*_{S,ref}}} \\ &= \frac{h_{hkl}\tau^*_{S,ref}\kappa^*_{2D,hkl}A^*_{C,hkl}(1+\sigma)\exp\left(\frac{-3\mathcal{F}_{hkl}}{\ln(1+\sigma)}\right)}{h_{ref}\sigma(\ln(1+\sigma))^{5/2}}\end{aligned} \tag{3.75}$$

$$\begin{aligned}\frac{G_{2D,B+S,hkl}}{G_{2D,B+S,ref}} &= \frac{h_{hkl}(\kappa^*_{2D,hkl})^{1/3}(\ln(1+\sigma))^{1/6}(1+\sigma)^{1/3}\exp\left(\frac{-\mathcal{F}_{hkl}}{\ln(1+\sigma)}\right)(\sigma^2 f^*_{hkl})^{1/3}k_O}{h_{ref}(\kappa^*_{2D,ref})^{1/3}(\ln(1+\sigma))^{1/6}(1+\sigma)^{1/3}\exp\left(\frac{-\mathcal{F}_{ref}}{\ln(1+\sigma)}\right)(\sigma^2 f^*_{ref})^{1/3}k_O} \\ &= \frac{h_{hkl}(\kappa^*_{2D,hkl}f^*_{hkl})^{1/3}\exp\left(\frac{-\mathcal{F}_{hkl}}{\ln(1+\sigma)}\right)}{h_{ref}(\kappa^*_{2D,ref}f^*_{ref})^{1/3}\exp\left(\frac{-\mathcal{F}_{ref}}{\ln(1+\sigma)}\right)}\end{aligned} \tag{3.76}$$

$$\begin{aligned}\frac{G_{2D,P,hkl}}{G_{2D,B+S,ref}} &= \frac{h_{hkl}\kappa^*_{2DD,hkl}k_O(\ln(1+\sigma))^{1/2}(1+\sigma)\exp\left(\frac{-3\mathcal{F}_{hkl}}{\ln(1+\sigma)}\right)\frac{A^*_{C,hkl}}{(\ln(1+\sigma))^2}}{h_{ref}(\kappa^*_{2D,ref})^{1/3}(\ln(1+\sigma))^{1/6}(1+\sigma)^{1/3}\exp\left(\frac{-\mathcal{F}_{ref}}{\ln(1+\sigma)}\right)(\sigma^2 f^*_{ref})^{1/3}k_O} \\ &= \frac{h_{hkl}\kappa^*_{2D,hkl}A^*_{C,hkl}(1+\sigma)^{2/3}\exp\left(\frac{-3\mathcal{F}_{hkl}}{\ln(1+\sigma)}\right)}{h_{ref}(\kappa^*_{2D,ref}f^*_{ref})^{1/3}\sigma^{2/3}(\ln(1+\sigma))^{5/3}\exp\left(\frac{-\mathcal{F}_{ref}}{\ln(1+\sigma)}\right)}\end{aligned} \tag{3.77}$$

$$\begin{aligned}\frac{G_{2D,P,hkl}}{G_{2D,P,ref}} &= \frac{h_{hkl}\kappa^*_{2D,hkl}k_O(\ln(1+\sigma))^{1/2}(1+\sigma)\exp\left(\frac{-3\mathcal{F}_{hkl}}{\ln(1+\sigma)}\right)\frac{A^*_{C,hkl}}{(\ln(1+\sigma))^2}}{h_{ref}\kappa^*_{2D,ref}k_O(\ln(1+\sigma))^{1/2}(1+\sigma)\exp\left(\frac{-3\mathcal{F}_{ref}}{\ln(1+\sigma)}\right)\frac{A^*_{C,ref}}{(\ln(1+\sigma))^2}} \\ &= \frac{h_{hkl}\kappa^*_{2D,hkl}A^*_{C,hkl}\exp\left(\frac{-3\mathcal{F}_{hkl}}{\ln(1+\sigma)}\right)}{h_{ref}\kappa^*_{2D,ref}A^*_{C,ref}\exp\left(\frac{-3\mathcal{F}_{ref}}{\ln(1+\sigma)}\right)}\end{aligned} \tag{3.78}$$

Note that when $ref = hkl$ these equations reproduce the crossover equations presented earlier. Equations 3.73 – 3.78 do not require estimates for k_O to compute. Equations 3.79 – 3.81 (relative growth rates if a face is growing under a bulk transport limit) do, however:

$$\frac{G_{BT,hkl}}{G_{S,ref}} = \frac{\frac{DV_{m,X}}{\delta V_{m,S}}\sigma x_{sat}}{\frac{h_{ref}\sigma\ln(1+\sigma)k_O}{\tau^*_{S,ref}}} = \frac{DV_{m,X}x_{sat}\tau^*_{S,ref}}{\delta V_{m,S}h_{ref}\ln(1+\sigma)k_O} \tag{3.79}$$

$$\begin{aligned}\frac{G_{BT,hkl}}{G_{2D,B+S,ref}} &= \frac{\frac{DV_{m,X}}{\delta V_{m,S}}\sigma x_{sat}}{h_{ref}(\kappa^*_{2D,ref})^{1/3}(\ln(1+\sigma))^{1/6}(1+\sigma)^{1/3}\exp\left(\frac{-\mathcal{F}_{ref}}{\ln(1+\sigma)}\right)(\sigma^2 f^*_{ref})^{1/3}k_O} \\ &= \frac{DV_{m,X}x_{sat}\sigma^{1/3}}{\delta V_{m,S}h_{ref}(\kappa^*_{2D,ref}f^*_{ref})^{1/3}(\ln(1+\sigma))^{1/6}(1+\sigma)^{1/3}\exp\left(\frac{-\mathcal{F}_{ref}}{\ln(1+\sigma)}\right)k_O}\end{aligned} \tag{3.80}$$

$$\begin{aligned}\frac{G_{BT,hkl}}{G_{2D,P,ref}} &= \frac{\frac{DV_{m,X}}{\delta V_{m,S}}\sigma x_{sat}}{h_{ref}\kappa^*_{2D,ref}k_O(\ln(1+\sigma))^{1/2}(1+\sigma)\exp\left(\frac{-3\mathcal{F}_{ref}}{\ln(1+\sigma)}\right)\frac{A^*_{C,ref}}{(\ln(1+\sigma))^2}} \\ &= \frac{DV_{m,X}x_{sat}\sigma(\ln(1+\sigma))^{3/2}}{\delta V_{m,S}h_{ref}\kappa^*_{2D,ref}A^*_{C,ref}(1+\sigma)\exp\left(\frac{-3\mathcal{F}_{ref}}{\ln(1+\sigma)}\right)k_O}\end{aligned} \tag{3.81}$$

$$\frac{G_{BT,hkl}}{G_{BT,ref}} = \frac{\frac{DV_{m,X}}{\delta V_{m,S}}\sigma x_{sat}}{\frac{DV_{m,X}}{\delta V_{m,S}}\sigma x_{sat}} = 1 \tag{3.82}$$

3.B Case Study Parameters

For each case study presented in the text, a summary of relevant quantities in the mechanistic model (for each family of F faces) is presented below. Those quantities listed are sufficient to calculate the relative growth rates (as a function of supersaturation) that are required for shape predictions.

In each case, the calculated lattice energy is within order RT of the experimental sublimation enthalpy, which lends support to the force field used to determine solid-state energetics. See Appendix 4.A for more details.

For each face (where (hkl) represent its Miller indices), h is the elementary step height (equal to a single interplanar spacing, d_{hkl}) and relevant 2D nucleation mechanistic parameters (see text for definitions) are indicated. For each periodic bond chain (PBC) with crystallographic direction [uvw], H_C^{2D*} is the supersaturation-independent distance of that edge from the center of a critical nucleus (i.e., $H_C^{2D*} = H_C^{2D}\ln(1+\sigma)$, see eq 3.39); ϕ^K is the kink energy. See Appendix 4.A for a_P (propagation length), a_E (growth unit width) and $\alpha_{i,i+1}$ (angle to next edge) values for naphthalene, biphenyl and pentaerythritol.

3.B.1 Naphthalene Grown in Ethanol or Cyclohexane

CSD code NAPHTA10 [69] was used for modeling at a temperature of $T = 291$ K (ethanol) and $T = 290$ K (cyclohexane), to match the experimental determinations [68]. The calculated lattice energy of 77.4 kJ/mol compares well with the sublimation enthalpy of 76.1 kJ/mol ($T = 328-398$ K) [80]. Table 3.6 contains mechanistic parameters for the dominant F faces of naphthalene grown in ethanol: (001), $(11\bar{1})$, (110) and $(20\bar{1})$. Table 3.7 contains mechanistic parameters for the dominant F faces of naphthalene grown in cyclohexane: (001), (110) and $(20\bar{1})$.

3.B.2 Biphenyl Grown in Toluene

CSD code BIPHEN04 [72] was used for modeling at a temperature of $T = 302$ K, to match the experimental determination [73]. The calculated lattice energy of 89.1 kJ/mol compares well with the sublimation enthalpy of 83.3 kJ/mol ($T = 283 - 338$ K) [81]. Table 3.8 contains mechanistic parameters for the dominant F faces of biphenyl grown in toluene: (001) and (110).

Table 3.6: Naphthalene faces, grown in ethanol

Face (001)			
Parameter		Units	Value
	h	nm	0.724
	τ_S^*	-	36.9
	κ_{2D}^*	cm^{-2}	9.28e+13
	f^*	cm^2	2.15e−16
	A_C^*	cm^2	4.18e−14
	C_0^{2D}	cm^{-2}	3.46e+14
	s_F	-	3.74
	$\mathcal{F}$	-	6.59
[010] PBC	H_C^{2D*}	nm	1.04
	ϕ^K	kT	0.75
[$\bar{1}$10] PBC	H_C^{2D*}	nm	1.12
	ϕ^K	kT	1.00
[110] PBC	H_C^{2D*}	nm	1.12
	ϕ^K	kT	1.00

Face (20$\bar{1}$)			
Parameter		Units	Value
	h	nm	0.409
	τ_S^*	-	16.8
	κ_{2D}^*	cm^{-2}	6.22e+13
	f^*	cm^2	4.52e−16
	A_C^*	cm^2	1.17e−14
	C_0^{2D}	cm^{-2}	1.91e+14
	s_F	-	3.83
	$\mathcal{F}$	-	0.95
[010] PBC	H_C^{2D*}	nm	0.468
	ϕ^K	kT	0.75
[$\bar{1}\bar{1}\bar{2}$] PBC	H_C^{2D*}	nm	0.667
	ϕ^K	kT	0.31
[$\bar{1}$1$\bar{2}$] PBC	H_C^{2D*}	nm	0.667
	ϕ^K	kT	0.31

Face (110)			
Parameter		Units	Value
	h	nm	0.450
	τ_S^*	-	19.4
	κ_{2D}^*	cm^{-2}	6.82e+13
	f^*	cm^2	3.92e−16
	A_C^*	cm^2	1.10e−14
	C_0^{2D}	cm^{-2}	1.93e+14
	s_F	-	3.92
	$\mathcal{F}$	-	0.88
[001] PBC	H_C^{2D*}	nm	0.656
	ϕ^K	kT	0.26
[$\bar{1}$1$\bar{2}$] PBC	H_C^{2D*}	nm	0.692
	ϕ^K	kT	0.31
[$\bar{1}$10] PBC	H_C^{2D*}	nm	0.427
	ϕ^K	kT	1.00

Face (11$\bar{1}$)			
Parameter		Units	Value
	h	nm	0.465
	τ_S^*	-	21.0
	κ_{2D}^*	cm^{-2}	8.32e+13
	f^*	cm^2	3.78e−16
	A_C^*	cm^2	6.78e−15
	C_0^{2D}	cm^{-2}	2.05e+14
	s_F	-	4.24
	$\mathcal{F}$	-	0.52
[101] PBC	H_C^{2D*}	nm	0.703
	ϕ^K	kT	0.37
[$\bar{1}$10] PBC	H_C^{2D*}	nm	0.294
	ϕ^K	kT	1.00
[$\bar{1}\bar{1}\bar{2}$] PBC	H_C^{2D*}	nm	0.551
	ϕ^K	kT	0.31

Table 3.7: Naphthalene faces, grown in cyclohexane

Face (001)			
Parameter		Units	Value
	h	nm	0.724
	τ_S^*	-	6.27
	κ_{2D}^*	cm^{-2}	1.04e+14
	f^*	cm^2	2.70e−16
	A_C^*	cm^2	9.57e−15
	C_0^{2D}	cm^{-2}	3.46e+14
	s_F	-	3.75
	$\mathcal{F}$	-	1.52
[010] PBC	H_C^{2D*}	nm	0.485
	ϕ^K	kT	0.11
[$\bar{1}$10] PBC	H_C^{2D*}	nm	0.541
	ϕ^K	kT	0.20
[110] PBC	H_C^{2D*}	nm	0.541
	ϕ^K	kT	0.20

Face (20$\bar{1}$)			
Parameter		Units	Value
	h	nm	0.409
	τ_S^*	-	1.53
	κ_{2D}^*	cm^{-2}	8.05e+13
	f^*	cm^2	4.82e−16
	A_C^*	cm^2	6.75e−16
	C_0^{2D}	cm^{-2}	1.91e+14
	s_F	-	4.30
	$\mathcal{F}$	-	0.05
[010] PBC	H_C^{2D*}	nm	0.081
	ϕ^K	kT	0.11
[$\bar{1}\bar{1}\bar{2}$] PBC	H_C^{2D*}	nm	0.208
	ϕ^K	kT	0.01
[$\bar{1}1\bar{2}$] PBC	H_C^{2D*}	nm	0.208
	ϕ^K	kT	0.01

Face (110)			
Parameter		Units	Value
	h	nm	0.450
	τ_S^*	-	2.87
	κ_{2D}^*	cm^{-2}	1.10e+14
	f^*	cm^2	4.37e−16
	A_C^*	cm^2	5.05e−16
	C_0^{2D}	cm^{-2}	1.93e+14
	s_F	-	4.79
	$\mathcal{F}$	-	0.03
[001] PBC	H_C^{2D*}	nm	0.201
	ϕ^K	kT	0.03
[$\bar{1}1\bar{2}$] PBC	H_C^{2D*}	nm	0.225
	ϕ^K	kT	0.01
[$\bar{1}$10] PBC	H_C^{2D*}	nm	0.058
	ϕ^K	kT	0.20

Table 3.8: Biphenyl faces, growth in toluene

Face (001)				Face (110)			
Parameter		Units	Value	Parameter		Units	Value
	h	nm	0.947		h	nm	0.462
	τ_S^*	-	5.68		τ_S^*	-	3.82
	κ_{2D}^*	cm^{-2}	1.15e+14		κ_{2D}^*	cm^{-2}	8.39e+13
	f^*	cm^2	2.52e−16		f^*	cm^2	5.19e−16
	A_C^*	cm^2	8.70e−15		A_C^*	cm^2	5.82e−16
	C_0^{2D}	cm^{-2}	3.74e+14		C_0^{2D}	cm^{-2}	1.46e+14
	s_F	-	3.74		s_F	-	4.36
	$\mathcal{F}$	-	1.45		$\mathcal{F}$	-	0.029
[010] PBC	H_C^{2D*}	nm	0.524	[001] PBC	H_C^{2D*}	nm	0.191
	ϕ^K	kT	0.065		ϕ^K	kT	0.021
$[1\bar{1}0]$ PBC	H_C^{2D*}	nm	0.490	$[\bar{1}1\bar{2}]$ PBC	H_C^{2D*}	nm	0.200
	ϕ^K	kT	0.204		ϕ^K	kT	0.093
[110] PBC	H_C^{2D*}	nm	0.490	$[1\bar{1}0]$ PBC	H_C^{2D*}	nm	0.076
	ϕ^K	kT	0.204		ϕ^K	kT	0.204

3.B.3 Pentaerythritol Grown in Water

CSD code PERYTO04 [74] was used for modeling at a temperature of $T = 313$ K, to match experimental determinations [76,82]. The calculated lattice energy of 184.5 kJ/mol compares well with the sublimation enthalpy of 161.1 kJ/mol ($T = 418 - 455$ K) [83]. Table 3.9 contains mechanistic parameters for the dominant F faces of pentaerythritol grown in water: (101), $(10\bar{1})$ and (110).

3.B.4 β-HMX Grown in Acetone

CSD code OCHTET14 [78] was used for modeling at a temperature of $T = 293$ K, to match the experimental determination [77]. The calculated lattice energy of 161.5 kJ/mol compares well with the sublimation enthalpy of 175.3 kJ/mol ($T = 387$ K; therefore a difference of ~ 4 RT) [84]. Tables 3.10 and 3.11 contain mechanistic parameters for the

Table 3.9: Pentaerythritol faces, growth in water

Face (101)			
Parameter		Units	Value
	h	nm	0.500
	τ_S^*	-	1398
	κ_{2D}^*	cm^{-2}	1.87e+12
	f^*	cm^2	2.69e−18
	A_C^*	cm^2	6.76e−15
	C_0^{2D}	cm^{-2}	2.67e+14
	s_F	-	4.62
	$\mathcal{F}$	-	12.9
$[1\bar{1}\bar{1}]$ PBC	H_C^{2D*}	nm	0.356
	ϕ^K	kT	4.36
$[\bar{1}\bar{1}1]$ PBC	H_C^{2D*}	nm	0.356
	ϕ^K	kT	4.36

Face ($10\bar{1}$)			
Parameter		Units	Value
	h	nm	0.500
	τ_S^*	-	1398
	κ_{2D}^*	cm^{-2}	1.87e+12
	f^*	cm^2	2.69e−18
	A_C^*	cm^2	6.76e−15
	C_0^{2D}	cm^{-2}	2.67e+14
	s_F	-	4.62
	$\mathcal{F}$	-	12.9
[111] PBC	H_C^{2D*}	nm	0.356
	ϕ^K	kT	4.36
$[1\bar{1}1]$ PBC	H_C^{2D*}	nm	0.356
	ϕ^K	kT	4.36

Face (110)			
Parameter		Units	Value
	h	nm	0.430
	τ_S^*	-	1398
	κ_{2D}^*	cm^{-2}	1.59e+12
	f^*	cm^2	3.13e−18
	A_C^*	cm^2	5.05e−16
	C_0^{2D}	cm^{-2}	2.06e+14
	s_F	-	3.89
	$\mathcal{F}$	-	0.748
$[1\bar{1}\bar{1}]$ PBC	H_C^{2D*}	nm	0.113
	ϕ^K	kT	4.36
$[1\bar{1}1]$ PBC	H_C^{2D*}	nm	0.113
	ϕ^K	kT	4.36

dominant F faces of β-HMX grown in acetone: (011), (110), (020) and (101).

Table 3.10: β-HMX faces, grown in acetone

Face (011)				Face (020)			
Parameter		Units	Value	Parameter		Units	Value
	h	nm	0.600		h	nm	0.549
	τ_S^*	-	218		τ_S^*	-	187
	κ_{2D}^*	cm^{-2}	2.51e+13		κ_{2D}^*	cm^{-2}	2.81e+13
	f^*	cm^2	5.34e−17		f^*	cm^2	7.10e−17
	A_C^*	cm^2	2.42e−13		A_C^*	cm^2	9.42e−14
	C_0^{2D}	cm^{-2}	1.99e+14		C_0^{2D}	cm^{-2}	2.08e+14
	s_F	-	4.12		s_F	-	4.52
	$\mathcal{F}$	-	21.0		$\mathcal{F}$	-	6.51
	a_P	nm	0.656		a_P	nm	0.717
	a_E	nm	0.653		a_E	nm	0.653
$[\bar{1}00]$ PBC	$\alpha_{i,i+1}$	°	58.2	$[\bar{1}00]$ PBC	$\alpha_{i,i+1}$	°	77.4
	H_C^{2D*}	nm	1.82		H_C^{2D*}	nm	0.938
	ϕ^K	kT	3.88		ϕ^K	kT	3.88
	a_P	nm	0.555		a_P	nm	0.637
	a_E	nm	0.772		a_E	nm	0.735
$[11\bar{1}]$ PBC	$\alpha_{i,i+1}$	°	121.8	[001] PBC	$\alpha_{i,i+1}$	°	102.6
	H_C^{2D*}	nm	2.92		H_C^{2D*}	nm	2.45
	ϕ^K	kT	1.51		ϕ^K	kT	1.32

Table 3.11: β-HMX faces, grown in acetone (continued)

Face (110)			
Parameter		Units	Value
	h	nm	0.551
	τ_S^*	-	55.0
	κ_{2D}^*	cm^{-2}	4.36e+13
	f^*	cm^2	3.22e−16
	A_C^*	cm^2	1.14e−13
	C_0^{2D}	cm^{-2}	1.85e+14
	s_F	-	3.87
	$\mathcal{F}$	-	9.69
	a_P	nm	0.635
	a_E	nm	0.735
[001] PBC	$\alpha_{i,i+1}$	°	65.0
	H_C^{2D*}	nm	1.74
	ϕ^K	kT	1.32
	a_P	nm	0.666
	a_E	nm	0.701
[1$\bar{1}$1] PBC	$\alpha_{i,i+1}$	°	59.6
	H_C^{2D*}	nm	2.37
	ϕ^K	kT	0.84
	a_P	nm	0.604
	a_E	nm	0.772
[$\bar{1}$11] PBC	$\alpha_{i,i+1}$	°	55.4
	H_C^{2D*}	nm	1.50
	ϕ^K	kT	1.51

Face (101)			
Parameter		Units	Value
	h	nm	0.432
	τ_S^*	-	52.7
	κ_{2D}^*	cm^{-2}	3.44e+13
	f^*	cm^2	3.99e−16
	A_C^*	cm^2	7.12e−14
	C_0^{2D}	cm^{-2}	1.29e+14
	s_F	-	4.00
	$\mathcal{F}$	-	3.99
	a_P	nm	0.542
	a_E	nm	1.10
[0$\bar{1}$0] PBC	$\alpha_{i,i+1}$	°	44.6
	H_C^{2D*}	nm	1.88
	ϕ^K	kT	0.51
	a_P	nm	0.772
	a_E	nm	0.772
[$\bar{1}$11] PBC	$\alpha_{i,i+1}$	°	90.8
	H_C^{2D*}	nm	1.33
	ϕ^K	kT	1.51
	a_P	nm	0.772
	a_E	nm	0.772
[11$\bar{1}$] PBC	$\alpha_{i,i+1}$	°	44.6
	H_C^{2D*}	nm	1.33
	ϕ^K	kT	1.51

Bibliography

[1] M. A. Lovette, A. R. Browning, D. W. Griffin, J. P. Sizemore, R. C. Snyder, and M. F. Doherty. Crystal Shape Engineering. *Ind. Eng. Chem. Res.*, 47(24):9812–9833, 2008.

[2] R. C. Snyder and M. F. Doherty. Predicting crystal growth by spiral motion. *Proc. R. Soc. London, Ser. A*, 465(2104):1145–1171, 2009.

[3] Z. B. Kuvadia and M. F. Doherty. Spiral growth model for faceted crystals of non-centrosymmetric organic molecules grown from solution. *Cryst. Growth Des.*, 11(7):2780–2802, 2011.

[4] M. A. Lovette and M. F. Doherty. Predictive Modeling of Supersaturation-Dependent Crystal Shapes. *Cryst. Growth Des.*, 12(2):656–669, 2012.

[5] P. Dandekar and M. F. Doherty. A mechanistic growth model for inorganic crystals: Solid-state interactions. *AIChE J*, 60(11):3707–3719, 2014.

[6] P. Dandekar and M. F. Doherty. A mechanistic growth model for inorganic crystals: Growth mechanism. *AIChE J*, 60(11):3720–3731, 2014.

[7] W. K. Burton, N. Cabrera, and F. C. Frank. The growth of crystals and the equilibrium structure of their surfaces. *Philos. Trans. R. Soc., A*, 243:299–358, 1951.

[8] R. Ruiz, D. Choudhary, B. Nickel, T. Toccoli, K.-C. Chang, A. C. Mayer, P. Clancy, J. M. Blakely, R. L. Headrick, S. Iannotta, and G. G. Malliaras. Pentacene thin film growth. *Chem Mater*, 16(23):4497–4508, 2004.

[9] S. C. B. Mannsfeld, J. Locklin, C. Reese, M. E. Roberts, A. J. Lovinger, and Z. Bao. Probing the anisotropic field-effect mobility of solution-deposited dicyclohexyl-α-quaterthiophene single crystals. *Adv Funct Mater*, 17(10):1617–1622, 2007.

[10] G. Giri, S. Park, M. Vosgueritchian, M. M. Shulaker, and Z. Bao. High-mobility, aligned crystalline domains of TIPS-pentacene with metastable polymorphs through lateral confinement of crystal growth. *Adv Mater (Weinheim, Ger)*, 26(3):487–493, 2014.

[11] T. S. van der Poll, J. A. Love, T.-Q. Nguyen, and G. C. Bazan. Non-basic high-performance molecules for solution-processed organic solar cells. *Adv Mater (Weinheim, Ger)*, 24(27):3646–3649, 2012.

[12] H. Hoppe and N. S. Sariciftci. Organic solar cells: An overview. *J Mater Res*, 2004.

[13] P. Dandekar and M. F. Doherty. Imaging crystallization. *Science*, 344(6185):705–706, 2014.

[14] Y. Hayashi, M. Maruyama, M. Yoshimura, S. Okada, H. Y. Yoshikawa, S. Sugiyama, H. Adachi, H. Matsumura, T. Inoue, K. Takano, S. Murakami, and Y. Mori. Spiral growth can enhance both the normal growth rate and quality of tetragonal lysozyme crystals grown under a forced solution flow. *Crystal Growth & Design*, 15(5):2137–2143, 2015.

[15] T. A. Land and J. J. De Yoreo. The evolution of growth modes and activity of growth sources on canavalin investigated by in situ atomic force microscopy. *Journal of Crystal Growth*, 208(14):623 – 637, 2000.

[16] H. H. Teng, P. M. Dove, and J. J. De Yoreo. Kinetics of calcite growth: surface processes and relationships to macroscopic rate laws. *Geochim Cosmochim Acta*, 64(13):2255–2266, 2000.

[17] T. Kuroda. Growth of a crystal surface with non-uniformity in supersaturation due to laminar flow of solution along the surface. *J Cryst Growth*, 71(1):84–94, 1985.

[18] W. Kossel. Zur theorie des kristallwachstums. *Nachr Ges Wiss Goettingen, Math-Phys Kl*, 1927:135–143, 1927.

[19] I. Stranski. Zur theorie des kristallwachstums. *Z Phys Chem*, 136(259):259–278, 1928.

[20] J. Frenkel. On the surface motion of particles in crystals and the natural roughness of crystalline faces. *J. Phys. (Moscow)*, 9:392–398, 1945.

[21] P. G. Vekilov. What determines the rate of growth of crystals from solution? *Cryst. Growth Des.*, 7(12):2796–2810, 2007.

[22] M. A. Lovette and M. F. Doherty. Multisite models to determine the distribution of kink sites adjacent to low-energy edges. *Phys. Rev. E*, 2012.

[23] P. Dandekar, Z. B. Kuvadia, and M. F. Doherty. Engineering crystal morphology. *Annu. Rev. Mater. Res.*, 43:359–386, 2013.

[24] F. Otalora and J. M. Garcia-Ruiz. Nucleation and growth of the naica giant gypsum crystals. *Chem. Soc. Rev.*, 43:2013–2026, 2014.

[25] D. Elwell and H. J. Scheel. *Crystal Growth from High-Temperature Solutions*. London: Academic Press,, 1975.

[26] J. A. Dirksen and T. A. Ring. Fundamentals of crystallization: Kinetic effects on particle size distributions and morphology. *Chem Eng Sci*, 46(10):2389–2427, 1991.

[27] K. Chen and P. G. Vekilov. Evidence for the surface-diffusion mechanism of solution crystallization from molecular-level observations with ferritin. *Phys. Rev. E*, 2002.

[28] C. J. Tilbury, D. A. Green, W. J. Marshall, and M. F. Doherty. Predicting the Effect of Solvent on the Crystal Habit of Small Organic Molecules. *Cryst Growth Des*, 16(5):2590–2604, 2016.

[29] F. C. Frank. On the kinematic theory of crystal growth and dissolution processes. In R. H. Doremus, B. W. Roberts, and D. Turnbull, editors, *Growth and Perfection of Crystals*, pages 411–419. New York: Wiley,, 1958.

[30] A. A. Chernov. Crystal growth forms and their kinetic stability. *Kristallografiya*, 8:87–93, 1963.

[31] Y. Zhang, J. P. Sizemore, and M. F. Doherty. Shape evolution of 3-dimensional faceted crystals. *AIChE J.*, 52(5):1906–1915, 2006.

[32] A. Gavezzotti. Efficient computer modeling of organic materials. The atom–atom, Coulomb–London–Pauli (AA-CLP) model for intermolecular electrostatic-polarization, dispersion and repulsion energies. *New J Chem*, 35(7):1360–1368, 2011.

[33] P. Hartman and W. G. Perdok. On the relations between structure and morphology of crystals. I. *Acta Crystallogr.*, 1955.

[34] H. Cuppen, H. Meekes, W. van Enckevort, E. Vlieg, and H. Knops. Nonequilibrium free energy and kinetic roughening of steps on the kossel (001) surface. *Phys. Rev. B: Condens. Matter Mater. Phys.*, 69(24):245404, 2004.

[35] H. H. Teng, P. M. Dove, C. A. Orme, and J. J. De Yoreo. Thermodynamics of calcite growth: Baseline for understanding biomineral formation. *Science*, 282(5389):724–727, 1998.

[36] M. A. Lovette and M. F. Doherty. Reinterpreting edge energies calculated from crystal growth experiments. *J. Cryst. Growth*, 327(1):117 – 126, 2011.

[37] V. V. Voronkov. Dislocation mechanism of growth with a low kink density. *Sov Phys Crystallogr*, 18:19–23, 1973.

[38] I. M. Dawson and V. Vand. The observation of spiral growth-steps in n-paraffin single crystals in the electron microscope. *Proc R Soc A*, 206(1087):555–562, 1951.

[39] I. M. Dawson. The study of crystal growth with the electron microscope. II. The observation of growth steps in the paraffin n-hectane. *Proc R Soc A*, 214(1116):72–79, 1952.

[40] J. D. Rimer, Z. An, Z. Zhu, M. H. Lee, D. S. Goldfarb, J. A. Wesson, and M. D. Ward. Crystal growth inhibitors for the prevenction of L-cystine kidney stones through molecular design. *Science*, 330:337–341, 2010.

[41] S. H. Kim, P. Dandekar, M. A. Lovette, and M. F. Doherty. Kink rate model for the general case of organic molecular crystals. *Cryst. Growth Des.*, 14(5):2460–2467, 2014.

[42] V. V. Voronkov. The movement of an elementary step by means of the formation of one-dimensional nuclei. *Sov Phys Crystallogr*, 15:8–13, 1970.

[43] A. A. Chernov, L. N. Rashkovich, and J. J. De Yoreo. ABC of kink kinetics and density in a complex solution. *AIP Conf Proc*, 916(1):34–47, 2007.

[44] A. A. Chernov. The spiral growth of crystals. *Sov. Phys.-Usp.*, 4(1):116, 1961.

[45] J. P. Sizemore and M. F. Doherty. A stochastic model for the critical length of a spiral edge. *J Cryst Growth*, 312(6):785–792, 2010.

[46] I. Reviakine, D. K. Georgiou, and P. G. Vekilov. Capillarity effects on crystallization kinetics: Insulin. *J. Am. Chem. Soc.*, 125(38):11684–11693, 2003. PMID: 13129373.

[47] D. N. Petsev, K. Chen, O. Gliko, and P. G. Vekilov. Diffusion-limited kinetics of the solution-solid phase transition of molecular substances. *Proc Natl Acad Sci USA*, 100(3):792–796, 2003.

[48] R. E. Sours, A. Z. Zellelow, and J. A. Swift. An in situ atomic force microscopy study of uric acid crystal growth. *J Phys Chem B*, 109(20):9989–9995, 2005.

[49] T. Erdey-Gruz and M. Volmer. Zur frage der elektrolytischen metalliiberspannung. *Z Phys Chem, Abt A*, 157:165–181, 1931.

[50] R. Kaischew and I. N. Stranski. On the kinetic deflection rate of germ formation. *Z Phys Chem, Abt B*, 26:317–326, 1934.

[51] M. Ohara and R. C. Reid. *Modeling Crystal Growth Rates from Solution*. New Jersey: Prentice Hall,, 1973.

[52] W. K. Burton, N. Cabrera, and F. C. Frank. Role of Dislocations in Crystal Growth. *Nature*, 163(4141):398–399, 1949.

[53] H. M. Cuppen, H. Meekes, W. J. P. van Enckevort, and E. Vlieg. Birth-and-spread growth on the Kossel and a non-Kossel surface. *J Cryst Growth*, 286(1):188–196, 2006.

[54] W. Obreten, D. Kashchiev, and V. Bostanov. Unified description of the rate of nucleation-mediated crystal growth. *J Cryst Growth*, 96(4):843–848, 1989.

[55] I. V. Markov. *Crystal Growth for Beginners: Fundamentals of Nucleation, Growth and Epitaxy*. Singapore: World Scientific,, 2003.

[56] M. S. Viola, K. A. V. Wormer, and G. D. Botsaris. A new technique for simulating two-dimensional nucleation models of crystal growth. *J Cryst Growth*, 47(1):127–129, 1979.

[57] Y. B. Zeldovich. On the theory of new phase formation; cavitation. *Acta Physicochim URSS*, 18(1):1–22, 1943.

[58] D. Kashchiev. *Nucleation: Basic Theory with Applications*. Boston: Butterworth Heinemann,, 2000.

[59] A. C. Zettlemoyer. *Nucleation*. New York: M. Dekker,, 1969.

[60] L. Onsager. Crystal statistics. I. A two-dimensional model with an order-disorder transition. *Physical Review*, 65(3-4):117–149, 1944.

[61] P. Bennema and H. Meekes. Two centuries of morphology of crystals: integration of principles of mathematical crystallography, statistical mechanics of surface models and chemistry. In X. Y. Lui and J. J. De Yoreo, editors, *Nanoscale Structure and Assembly at Solid-Fluid Interfaces*, volume Volume I: Interfacial Structures versus Dynamics, pages 177–208. Kluwer Academic, Boston, 2004.

[62] H. E. Buckley. *Crystal Growth*. New York: John Wiley & Sons, Inc.,, 1951.

[63] A. A. Chernov. *Modern Crystallography III: Crystal Growth*, volume 36. Berlin: Springer-Verlag,, 1984.

[64] K. Kassner. Morphological instability: Dendrites, seaweed, and fractals. In J. P. van der Eerden and O. S. L. Bruinsma, editors, *Science and Technology of Crystal Growth*, pages 193–208. Netherlands: Springer,, 1995.

[65] T. Kuroda, T. Irisawa, and A. Ookawa. Transition from polyhedral to dendritic morphology. In I. Sunagawa, editor, *Morphology of Crystals*, chapter 8, pages 589–612. Tokyo: TERRAPUB,, 1987.

[66] K. G. Libbrecht. The physics of snow crystals. *Rep Prog Phys*, 68(4):855–895, 2005.

[67] M. E. Glicksman and A. O. Lupulescu. Dendritic crystal growth in pure materials. *J Cryst Growth*, 264(4):541–549, 2004.

[68] R. F. P. Grimbergen, M. F. Reedijk, H. Meekes, and P. Bennema. Growth behavior of crystal faces containing symmetry-related connected nets: A case study of naphthalene and anthracene. *J. Phys. Chem. B*, 102(15):2646–2653, 1998.

[69] C. P. Brock and J. D. Dunitz. Temperature dependence of thermal motion in crystalline naphthalene. *Acta Crystallogr., Sect. B: Struct. Crystallogr. Cryst. Chem.*, 1982.

[70] A. F. Wells. XXI. Crystal habit and internal structure. *Philos Mag (1798–1977)*, 37(266):184–199, 1946.

[71] D. Winn and M. F. Doherty. A new technique for predicting the shape of solution-grown organic crystals. *AIChE J*, 44(11):2501–2514, 1998.

[72] G. P. Charbonneau and Y. Delugeard. Biphenyl: three-dimensional data and new refinement at 293 k. *Acta Crystallogr., Sect. B: Struct. Crystallogr. Cryst. Chem.*, 1977.

[73] L. Jetten, H. Human, P. Bennema, and J. Van der Eerden. On the observation of the roughening transition of organic crystals, growing from solution. *J. Cryst. Growth*, 68(2):503–516, 1984.

[74] D. Eilerman and R. Rudman. Refinement of pentaerythritol. *Acta Crystallogr., Sect. B: Struct. Crystallogr. Cryst. Chem.*, 1979.

[75] J. F. Rogers and D. E. Creasy. Crystallisation of pentaerythritol. *J. Appl. Chem. Biotechnol.*, 24(3):171–180, 1974.

[76] A. Bernardo and M. Giulietti. Modeling of crystal growth and nucleation rates for pentaerythritol batch crystallization. *Chem. Eng. Res. Des.*, 88(10):1356–1364, 2010.

[77] H.-M. Shim and K.-K. Koo. Prediction of growth habit of β-cyclotetramethylene-tetranitramine crystals by the first-principles models. *Cryst. Growth Des.*, 15(8):3983–3991, 2015.

[78] J. R. Deschamps, M. Frisch, and D. Parrish. Thermal expansion of HMX. *J Chem Crystallogr*, 41(7):966–970, 2011.

[79] M. M. Kuklja, R. V. Tsyshevsky, and O. Sharia. Effect of polar surfaces on decomposition of molecular materials. *J Am Chem Soc*, 136(38):13289–13302, 2014.

[80] J. P. Murray, K. J. Cavell, and J. O. Hill. A DSC study of benzoic acid: a suggested calibrant compound. *Thermochim. Acta*, 36(1):97–101, 1980.

[81] K. Sasse, J. N'guimbi, J. Jose, and J. C. Merlin. Tension de vapeur d'hydrocarbures polyaromatiques dans le domaine 10^{-3}-10 Torr. *Thermochim. Acta*, 146:53–61, 1989.

[82] S. Genbo, L. Zhengdong, P. Rfen, W. Dexiang, and Y. Tongqin. Growth of large crystals of pentaerythritol and trishydroxymethylaminomethone. *J. Cryst. Growth*, 119(34):368–370, 1992.

[83] G. Barone, G. D. Gatta, D. Ferro, and V. Piacente. Enthalpies and entropies of sublimation, vaporization and fusion of nine polyhydric alcohols. *J. Chem. Soc., Faraday Trans.*, 86:75–79, 1990.

[84] J. M. Rosen and C. Dickinson. Vapor pressures and heats of sublimation of some high-melting organic explosives. *J. Chem. Eng. Data*, 14(1):120–124, 1969.

Chapter 4

Predicting the Effect of Solvent on the Crystal Habit of Small Organic Molecules

Reproduced in part with permission from:

Carl J. Tilbury, Daniel A. Green, William J. Marshall and Michael F. Doherty, "Predicting the Effect of Solvent on the Crystal Habit of Small Organic Molecules," *Crystal Growth & Design*, **2016**, *16*, 2590–2604.

DOI: 10.1021/acs.cgd.5b01660.

4.1 Introduction

The choice of solvent is perhaps the most critical design decision in crystallization from solution, with implications for solubility and impurity rejection as well as crystal morphology. Understanding and being able to predict its effect on crystal habit would be valuable from an engineering perspective, so the optimum morphology can be achieved.

Accounting for the interaction energetics is critical to the mechanistic model, and the presence of a solvent alters the relevant surface interactions due to solvation of the crystal surface. To correctly predict this effect one must determine how these interactions are modified by the presence of a solvent, which is the focus of this chapter. The most accurate method for obtaining the relevant free energies, kink densities and kink rates used in the model (see Section 4.4) would be molecular simulations. This might be practical for simple crystal systems where there are few types of kink sites, but even so it would be computationally expensive. For more complicated crystal systems there can be many distinct kink sites (the $(10\bar{1}4)$ surface of calcite has 32 kink sites [1], while aragonite has 112 distinct kinks [2]), which further multiplies the necessary number of molecular simulations to obtain the input parameters required by the model, rendering this approach impractical for engineering purposes. Using a mechanistic model that relies on such simulations provides little advantage over an experimental screening of the design space, due to the required computational time and effort.

The challenge was to find a practical method to estimate solvent-modified interactions that offered an improvement upon previous methodologies adopted within the mechanistic model [3–6]. The resulting short-cut methods are necessarily a compromise that cannot compete with molecular simulations in terms of fidelity, but nonetheless result in useful and rapid engineering predictions.

4.2 Intermolecular Interactions

Before considering models for interfacial energies in the presence of a solvent, types of intermolecular interactions and how they are modeled will be briefly reviewed.

In principle, all intermolecular interactions are a result of coulombic effects from the constituent sub-atomic particles [7, 8]. While the nuclear positions are often known, the

electron cloud must be computed in order for this purely coulombic representation of an interaction to be calculated. Such quantum mechanical calculations are not close to being feasible for large numbers of molecules in the solid state, but for isolated molecules they can be carried out at reasonable computational cost [8]. Intermolecular interactions in condensed matter can instead be partitioned into various contributions (that together account for the real interaction), estimates for which can be obtained by using information on isolated molecule electron densities.

Van der Waals forces are a common subset and can refer to Keesom, Debye and London interactions [9]. Keesom (orientation) forces exist between permanent dipoles, Debye (induction) forces exist between a permanent dipole and one induced by it and London (dispersion) forces exist between an instantaneous dipole and one induced by it. While all three van der Waals forces are important in the vapor phase, it is the London dispersion forces that dominate in condensed phases [10, 11]. These dispersion interactions are non-directional and exist between any pair of molecules.

Acid-base interactions represent the opposite picture, where there is a donating and accepting character needed to form a bond, so the specific molecules involved dictate whether an interaction will exist. Hydrogen bonds are the most ubiquitous of these and are particularly strong owing to the small size of the hydrogen atom and its electron cloud. These have some characteristics of weak covalent bonds, such as directionality, alongside a significant electrostatic characteristic, where the partial charges on the functional groups involved lead to a coulombic interaction. The strength of typical hydrogen bonds is of the order of $10-40$ kJ mol^{-1}, hence far below full intramolecular covalent bonds or ionic bonds (~ 500 kJ mol^{-1}) but above van der Waals interactions (~ 1 kJ mol^{-1}) [9].

4.2.1 Solubility Parameters

Solubility parameters aim to correlate the intermolecular interactions between solvent molecules. They represent a cohesive energy density (i.e., δ^2 = energy per unit volume), as indicated by eq 4.1, where δ is the overall (Hildebrand) solubility parameter, V_m is the molar volume and $\Delta H_{vap} - RT$ is the enthalpy change between the condensed phase and isolated molecules [12–16].

$$\delta^2 = \frac{\Delta H_{vap} - RT}{V_m} \tag{4.1}$$

These are often split into components to separate the interactions according to their type. Hansen has tabulated 3-component solubility parameters corresponding to dispersive, polarization and hydrogen bonding interactions [17, 18]. These parameters were developed by splitting the interaction into a 'non-polar' portion (the dispersive parameter) and a 'polar' portion, which was further subdivided into contributions from permanent dipole Keesom forces (the polarization parameter) and hydrogen bonds (the hydrogen bonding parameter) [19–21]. This subdivision of the polar portion is not on sound theoretical footing [19] and more generally the use of the term 'polar' to describe non-dispersive interactions has been criticized since these are more accurately termed as acid-base interactions [10, 11]. They depend on donating and accepting characteristics of the solvent molecules, which the 'polar' designation oversimplifies (see Section 4.3.1).

In order to use the equations in Section 4.3, solvent surface energies are required. Correlations exist to convert solubility parameters into interfacial energies. The simplest approach is to relate the overall solubility parameter to the measured solvent surface energy; the value of the empirical constant ϵ is found that satisfies eq 4.2. This approach is used by Kaelble [22] and can be generalized to any solvent for which an overall solubility parameter (δ, units $(\text{cal/cm}^3)^{0.5}$ or $\text{MPa}^{0.5}$), the molar volume (V_m) and an experimental

value for the surface energy (γ_s^{exp}) exists.

$$\gamma_s^{exp} = \epsilon \left(\frac{V_m}{N_A} \right)^{1/3} \delta^2 \tag{4.2}$$

More specifically however, interfacial energy models require knowledge of a subset of the solvent's interactions. One could use the proportionality constant ϵ determined using eq 4.2 alongside component solubility parameters (Hansen's 3-component, for example), to obtain component values for the interfacial energy (e.g. γ_s^d using δ_d, where s denotes the solvent and d denotes the dispersive portion).

However, this assumes the various portions of the solvent interaction as described by solubility parameters contribute equally to the interfacial energy. Beerbower developed correlations for three classes of solvents using 3-component Hansen parameters with different constants in front of each term [20]. For alcohols, the correlation is:

$$\gamma_s = 0.0715 V_m^{1/3} (\delta_d^2 + \delta_p^2 + 0.06\delta_h^2) \tag{4.3}$$

For acids, phenols, amines and water the correlation is:

$$\gamma_s = 0.0715 V_m^{1/3} (\delta_d^2 + 2.0\delta_p^2 + 0.481\delta_h^2) \tag{4.4}$$

For all other solvents the correlation is:

$$\gamma_s = 0.0715 V_m^{1/3} (\delta_d^2 + 0.632\delta_p^2 + 0.632\delta_h^2) \tag{4.5}$$

These correlations use solubility parameters in units of $\text{cal}^{1/2}\text{cm}^{-3/2}$, molar volume in units of $\text{cm}^3\text{mol}^{-1}$ and produce surface energies in units of erg cm^{-2}.

This, in principle, allows for a more physical description, since for alcohols there is

a tendency to align the OH groups inwards away from an interface that cannot form hydrogen bonds, so as to satisfy them internally. Therefore, the measured surface energy has a reduced contribution from the solvent's hydrogen bonds (hence the 0.06 prefactor in eq 4.3).

In using Hansen parameters and Beerbower's correlations, one should apply an extra correction factor (ϵ) to scale the resulting surface energy to match a measured value from experiments, in the same way as eq 4.2. This should help account for temperature effects, since the correlations are developed for 25°C, but nonetheless the correction should be close to unity or it is doubtful the solvent's energetics are being described appropriately. For example for alcohols one could write:

$$\epsilon = \frac{\gamma_s^{exp}}{0.0715 V_m^{1/3}(\delta_d^2 + \delta_p^2 + 0.06\delta_h^2)} \tag{4.6}$$

Thus, the predicted solvent hydrogen bonding-component surface energy for an alcohol would then be:

$$\gamma_s^h = 0.0715 \epsilon V_m^{1/3} 0.06 \delta_h^2 \tag{4.7}$$

4.2.2 Force Fields

Atom-atom force fields are entrenched within the physical sciences [8,23] as a means of describing forces between atoms and by extension between molecules, upon consideration of the relevant interatomic force pairs (i.e. summation of potential E_{ij} between atom i in molecule 1 and atom j in molecule 2 as indicated in eq 4.8 as a per molecule energy).

$$E_{12} = \frac{1}{2} \sum_i \sum_j E_{ij} \tag{4.8}$$

All such force fields choose a functional form for the potential and fit various param-

eters to reproduce existing physical data. The function is often chosen to represent the individual components of intermolecular interactions; commonly there is a term to the inverse sixth power of the distance corresponding to attractive van der Waals forces. The total interaction strength is directly linked to physical data used in the parameterization, so one can have confidence in its value. On the other hand, it is difficult to trust that the functional decomposition provides accurate values of these contributions, since it is entirely possible that a cancellation of errors provides the correct total interaction [23].

Atom-atom force fields commonly assign point charges to atoms in a molecule, based on a quantum mechanical electron density calculation performed for an isolated molecule. This description is an inherently inaccurate picture of the real interactions (which are effectively purely coulombic), even if the electron cloud were not distorted in the solid state. The PIXEL method [24, 25] uses a discretized electron cloud in order to better account for this coulombic interaction and move away from a simple point-charge description, but is necessarily more complicated to compute. Regardless of whether a point-charge or density description of the coulombic portion around the isolated molecule is used, extra terms in the functional form of the force field aim to account for how the cloud is distorted in the solid state and how this contributes to the intermolecular force [23].

The force field that is used in this study's mechanistic modeling is the CLP force field developed by Gavezzotti [23]. This is particularly relevant since it has been principally parameterized to crystal lattice energies, so is more appropriate for solid state modeling than other force fields that are often developed focusing on gas or liquid phase properties.

This force field contains 4 terms: a (C)oulombic term ($\propto r^{-1}$), a polarization term ($\propto r^{-4}$), a (L)ondon dispersion term ($\propto r^{-6}$) and a (P)auli repulsion term ($\propto r^{-12}$). The coulombic term represents interactions between the point charges, i.e. electrostatic forces from nuclei and the electron density (corresponding to the undistorted cloud from an isolated molecule) and also relates to the Keesom forces between permanent dipoles.

The polarization term represents distortion of the electron cloud by the surroundings and hence Debye permanent dipole-induced dipole interactions. The London dispersion term represents the instantaneous dipole-induced dipole effects from electron motion correlation, and the Pauli term accounts for short-range repulsion due to electronic spin exclusion. This partitioning is useful for describing effects between different types of intermolecular interactions, where high dipoles and hence significant partial charges are reflected in the coulombic term; molecules that are easily polarized have higher polarization and London components, while repulsion comes into play at short distances, for example in hydrogen bonds. Atom-specific parameters are used to develop these terms, such as polarizabilities, ionization potentials, partial charges and valence electrons; this should help parameterization retain a reflection of the underlying physics within these separate terms [26]. One should not forget that this is still an atom-atom approach, which is inherently unrealistic as none of these contributions depend solely on the nuclear positions [7].

The hydrogen atoms' positions can be critical to the intermolecular interaction, since for nearest neighbors in an organic crystal lattice these are often the peripheral atoms so have shorter interatomic distances [23]. Their positions as determined from x-ray diffraction are inaccurate, hence their positions are renormalized within the CLP software package according to known configurations [27]. Atomic partial charges are also assigned within the software package (using a Mulliken population analysis on an Extended Huckel Theory wavefunction, which gives similar point charges to an MP2/6-31G** calculation [23]) and the force field has been parameterized using this internal method, so to be consistent our modeling will adopt this also in lieu of using a commercial package such as Gaussian [28].

All three van der Waals components (Keesom, Debye, London) can be represented by a term ($\propto r^{-6}$) and in the vapor phase all are important. However, for condensed matter

the dominant contribution comes from London dispersion forces and the other two can effectively be neglected [10,11]. Therefore, although the coulombic and polarization terms might appear to represent Keesom/Debye forces, they in fact mainly confer information about the possible acid-base interactions that can exist, which up to now have been absent from the force field picture, but are clearly present and important in reality.

Hydrogen bonding is the principal acid-base interaction and should such a bond exist and be described by the force field it will manifest primarily through increased coulombic and polarization terms [23], though the repulsive term is also modified.

Although based on some fundamental physics, attaching much physical meaning to the partitioned force field energetics is still ill-advised [8,29]. Nonetheless, the dispersion energies are similar to those calculated using the more physical PIXEL and dispersion-corrected DFT approach [30]. There is also some disparity between force field partitions and the theory of intermolecular interactions dividing them into van der Waals and acid-base forces. Furthermore, the solubility parameter description is again different from either, with the polarization solubility parameter corresponding to Keesom forces and therefore under the CLP force field this corresponds, if any, to the coulombic and not the polarization term. Deciphering this mixture of descriptions for both solvent (through solubility parameters) and crystal (through the atom-atom CLP force field), in order to use interfacial energy models, is treated in the Section 4.4.

4.3 Interfacial Energy Models

The focus of this chapter is determining how to appropriately modify the crystal surface energies at edge and kink sites in the presence of the solvent. The bulk interface approximation (eq 4.9) describes an interfacial energy in terms of the two phases' own

cohesive energies (γ_1 and γ_2) and their work of adhesion ($W_{ad,12}$).

$$\gamma_{12} = \gamma_1 + \gamma_2 - W_{ad,12} \tag{4.9}$$

All terms in eq 4.9 have units of energy per unit area. In order to form a new crystal surface in solution the internal crystalline and internal solvent bonds must be broken (hence the cohesive energy penalty), but crystal-solvent bonds can then form (hence the adhesive energy reward). How favorable this work of adhesion is depends on the degree to which the different phases match and what interactions can be reformed; for a hypothetical internal interface in a pure substance the work of adhesion must correspond to the work of cohesion so γ_{ii} should be zero using any formulation of $W_{ad,ii}$. Expressions for the work of adhesion will now be presented. The simplest is a simple geometric mean of the cohesive energies (eq 4.10), which historically stems from the empirical Berthelot relation for attractive constants in the van der Waals equation of state [12, 31–33].

$$W_{ad,12} = 2\sqrt{\gamma_1\gamma_2} \tag{4.10}$$

This expression for the work of adhesion fails to consider the type of interactions, so it is unable to account for how solutes prefer different solvents based on their ability to form acid-base interactions. Girifalco and Good proposed [32] the first modification and incorporated a parameter ξ to correct the geometric mean expression (eq 4.11).

$$W_{ad,12} = 2\xi\sqrt{\gamma_1\gamma_2} \tag{4.11}$$

Another modification was proposed by Owens and Wendt [34]; they split the internal cohesive energy into 'non-polar' (dispersive, superscript d) and 'polar' (superscript p) interactions ($\gamma_i = \gamma_i^d + \gamma_i^p$), then use separate geometric mean terms for these respec-

tive types (eq 4.12). While this attempts to match like-interactions, the 'polar' portion accounts for internal acid-base interactions within each phase, so may not correspond to those formed against a new phase, with a potentially different donating or accepting characteristic than the original phase.

$$W_{ad,12} = 2\sqrt{\gamma_1^d \gamma_2^d} + 2\sqrt{\gamma_1^p \gamma_2^p} \tag{4.12}$$

The geometric mean for the dispersive component of $W_{ad,12}$ actually has a theoretical basis based on London's theory; if the molecules are assumed to have the same ionization potential, the geometric mean results and is an acceptable approximation [33, 35–38]. Wu instead proposed a harmonic mean (eq 4.13) for the dispersive component [38, 39], based on assuming equal polarizability, but this results in only a small change compared to the geometric mean [33, 35]. Note that these justifications do not extend to the 'polar' term but such forms have been adopted anyway. One would expect the Girifalco and Good parameter ξ to therefore be close to unity if both phases are composed of predominantly dispersive forces, whereas the low value of ξ for water in hydrocarbons indicates a mismatch of interactions [32].

$$W_{ad,12} = \frac{4\sqrt{\gamma_1^d \gamma_2^d}}{\gamma_1^d + \gamma_2^d} + \frac{4\sqrt{\gamma_1^p \gamma_2^p}}{\gamma_1^p + \gamma_2^p} \tag{4.13}$$

These simple models suffer from an inability to accurately describe the acid-base contribution to the work of adhesion, which prompted the development of new interfacial models with higher fidelity. We now introduce these more recent interfacial models and evaluate their practicality for our purposes.

4.3.1 Fowkes' Method

Fowkes has strongly criticized using a geometric mean for 'polar' (more accurately acid-base) contributions to the work of adhesion [10, 37, 40]. The term 'polar' also over-simplifies the variety of possible acid-base interactions, instead a more specific description should be used [10, 11, 40]. A polar compound can be monopolar (with either electron-accepting acidic character, e.g., chloroform, or electron-donating basic character, e.g., pyridine) or bipolar (which could also be described as amphoteric or self-associating, e.g., water). Such a description accounts for the ability to act as a donor and/or an acceptor within acid-base interactions. A monopolar liquid has no self-association or internal hydrogen bonds, but is still able to form acid-base interactions with molecules in the other phase that have either a bipolar character or a monopolar one of the opposite sense.

To enable the acid-base (superscript AB) component of adhesion, $W_{ad,12}^{AB}$, to capture the possible interactions between any types of molecules, Fowkes and Mostafa proposed [41] eq 4.14 (note the dispersive contribution to the work of adhesion retains the geometric mean). This relates the acid-base adhesion component to the enthalpy of formation for an acid-base adduct, ΔH_{12}^{AB} (normally negative), and the density of sites for adduct formation across an interface, n_{12}^{AB}. The prefactor f_{12} acts as an entropy correction that has been approximated as unity [37,40,41], but may be far lower and system specific [42].

$$W_{ad,12} = 2\sqrt{\gamma_1^d \gamma_2^d} + W_{ad,12}^{AB} \tag{4.14}$$
$$W_{ad,12}^{AB} = -f_{12} n_{12}^{AB} \Delta H_{12}^{AB}$$

The principal requirement for this method is an estimate of the acid-base enthalpy between phases 1 and 2. Fowkes proposes two approaches; firstly, one could use Gutmann's

donor/acceptor numbers (DN_1 and AN_2 in eq 4.15, where phase 1 is the donor and phase 2 is the acceptor), providing tabulated values are available for various compounds to determine ΔH_{12}^{AB} (in kcal/mol) [43].

$$\Delta H_{12}^{AB} = \frac{DN_1.AN_2}{100} \tag{4.15}$$

Secondly, one could use Drago's EC model (eq 4.16, which assumes phases 1 and 2 to have acidic and basic character, respectively), where parameters have been tabulated for various compounds [44–46]. The E and C parameters exist to describe the electrostatic (E) and covalent (C) characteristics of an acid-base interaction.

$$\Delta H_{12}^{AB} = E_{A,1}E_{B,2} + C_{A,1}C_{B,2} \tag{4.16}$$

This, in principle, allows for a much more physical description of any acid-base effects, since it directly considers specific compounds and the functional groups that are responsible. However, the available data is limited and dominated by highly acidic and basic compounds, omitting many solvents that could be applicable to crystallization. One could follow the method and tabulate E and C values for new donors or acceptors, which may be feasible for the solvent but could be difficult to perform for crystals, since effects are face-dependent. Critically, it would also be essentially impossible to obtain specific E and C parameters for individual edge and kink sites, whose energies are important values in the mechanistic model but steric effects differentiate their solvation from adduct formation between free molecules (on which the Drago EC model is based). Essentially, for us to apply this method we would have to infer E and C parameters based on available data for molecules with similar functional groups to those exposed at edge and kink sites, which might prove unreliable.

Additionally, it is unclear how to deal with amphoteric molecules via this method (e.g. adipic acid crystallization in water), a property that Drago largely chose to ignore [10]. One could generalize eq 4.16 to have an extra 2 terms on the right hand side that switched subscripts 1 and 2, providing that one has E_A, C_A, E_B and C_B values for each compound. For such a self-associating compound, the internal interfacial energy (γ_{11}) is zero, so the required $W_{ad,11}^{AB}$ could be calculated from known cohesive energies. If $E_{A,1}$ and $C_{A,1}$ are known and the basic counterparts are assumed to have the same E/C ratio, they can be calculated. This is not necessarily an advisable approach, since for water the acidic and basic E/C ratios do not correspond [47].

As a result of these limitations and the f parameter uncertainty, the application of Fowkes' model to our mechanistic crystal growth modeling is not possible with much confidence. It does highlight ideal characteristics of how the solvent effect should be treated, however, particularly the requirement to be functional group-dependent.

4.3.2 The van Oss, Chaudhury and Good (vOCG) Method

The method developed by van Oss, Chaudhury and Good [11, 48, 49] represents the cohesive energy as a dispersive component plus an acid-base component, which is formed as a geometric mean of electron accepting (Lewis acid, γ_i^+) and electron donating (Lewis base, γ_i^-) components (see eq 4.17).

$$\begin{aligned} \gamma_i &= \gamma_i^d + \gamma_i^{AB} \\ \gamma_i^{AB} &= 2\sqrt{\gamma_i^+ \gamma_i^-} \end{aligned} \tag{4.17}$$

The dispersive work of adhesion is then the usual geometric mean; the form for $W_{ad,12}^{AB}$ arbitrarily retains geometric mean terms, but crucially it matches the donating

characteristic of phase 1 with the accepting of phase 2, and vice-versa.

$$\begin{aligned} W_{ad,12} &= 2\sqrt{\gamma_1^d \gamma_2^d} + W_{ad,12}^{AB} \\ W_{ad,12}^{AB} &= 2\sqrt{\gamma_1^+ \gamma_2^-} + 2\sqrt{\gamma_1^- \gamma_2^+} \end{aligned} \tag{4.18}$$

Incorporating the vOCG model into eq 4.9, one can divide the interfacial energy into dispersive and acid-base components ($\gamma_{12} = \gamma_{12}^d + \gamma_{12}^{AB}$):

$$\begin{aligned} \gamma_{12}^d &= \gamma_1^d + \gamma_2^d - 2\sqrt{\gamma_1^d \gamma_2^d} \\ \gamma_{12}^{AB} &= 2\sqrt{\gamma_1^+ \gamma_1^-} + 2\sqrt{\gamma_2^+ \gamma_2^-} - 2\sqrt{\gamma_1^+ \gamma_2^-} - 2\sqrt{\gamma_1^- \gamma_2^+} \end{aligned} \tag{4.19}$$

While $\gamma_{12}^d = (\sqrt{\gamma_1^d} - \sqrt{\gamma_2^d})^2$ must be greater than or equal to zero, γ_{12}^{AB} can be negative. For example if phase 1 is monopolar basic ($\gamma_1^+ = 0$) and phase 2 is monopolar acidic ($\gamma_2^- = 0$), the cohesive terms vanish but the $-2\sqrt{\gamma_1^- \gamma_2^+}$ adhesion term remains. Therefore, this formulation is able to deal with interactions across the interface that are different to internal ones.

The special case of $\gamma_1^+ = \gamma_1^-$ and $\gamma_2^+ = \gamma_2^-$ actually recovers the geometric mean expression (eq 4.12, with γ^p's replaced with γ^{AB}'s). Thus we can expect the geometric mean to hold for the acid-base portion providing both compounds across the interface are themselves equally donating and accepting (e.g., the solid-state hydrogen bonding of adipic acid).

Values for γ^+ and γ^- cannot be obtained without a choice of reference compound. In the original vOCG scale, water was selected to be equally donating and accepting (fixing $\gamma_w^+ = \gamma_w^- = \gamma_w^{AB}/2 = 25.5$ mJ/m^2) and tabulated values for other compounds [35, 50, 51] are tethered to this assumption. A criticism of the vOCG scale is that many compounds appear largely basic [52–54]. However, the resulting value of W_{ad}^{AB} is independent of scale,

providing it is implemented consistently [52–55]; as a result Della Volpe and Siboni developed [52, 56] an alternative scale (DVS), with parameters for water at $\gamma_w^+ = 48.5$ mJ/m^2 and $\gamma_w^- = 11.2$ mJ/m^2. The DVS scale will be adopted here, since on the whole its resulting parameters align more closely with chemical intuition. As indicated in the next section, utilizing the vOCG model requires us to determine the electron accepting/donating γ^+/γ^- ratio for both the solvent and solute. Some solvents have been parameterized under the DVS scale, but for solute molecules and other solvents, this ratio may require estimation. Neutral compounds (e.g., alkanes) have no acid-base character so a ratio $\gamma^+/\gamma^- = 1$ is appropriate; amphoteric compounds should have a γ^+/γ^- ratio near unity (e.g., formamide); acidic compounds (e.g., chloroform) should have a high γ^+/γ^- ratio and basic compounds (e.g., methyl iodide, acetone) should have a low γ^+/γ^- ratio.

The mechanistic crystal growth model requires kink and edge energies in order to calculate relative growth rates. Experimentally determining γ^+ and γ^- for a specific edge or kink site appears infeasible via current measurement techniques; instead, we use an atom-atom force field to obtain location specific energies (see eqs 4.21 and 4.22). However, terrace surface energies can be measured; Heng et al. determined γ^+'s and γ^-'s for 3 facets of a macroscopic aspirin crystal [57] (demonstrating prior application of the vOCG model to crystalline systems). The range of terrace γ^+/γ^- ratios measured for a crystalline system might be combined with the determination of specific edge and kink site energetics from the applied force field to form an improved description of the surface chemistry. An alternative technique to contact angle measurements is inverse gas chromatography, which can determine surface energies of powders and non-flat surfaces [58]. This produces an energy distribution and deconvolution into individual surface energies has been demonstrated [59, 60]. While such techniques have downstream industrial importance, the ability to pinpoint the surface energy at each specific edge or kink site would be required to incorporate such results directly into mechanistic crystal growth

models.

Chen and Chang proposed another interfacial energy model that is similar to that of van Oss et al. but with a slightly different functional form for the acid-base work of adhesion that actually allows for a repulsive $W_{ad,12}^{AB}$ [33, 35, 61, 62]. The evidence for repulsive acid-base adhesion is that the dispersive geometric mean over-predicts the measured adhesive energy for some perfluoro polymers in methyl iodide; a negative (repulsive) $W_{ad,12}^{AB}$ would align the interfacial model with experiments in this case and entropic effects are suggested as a possible explanation [62]. In the crystallization of small organic solute molecules, however, entropic forces will be reduced and we expect the solvent molecules to be capable of reorienting at the interface to mitigate any repulsive acid-base interactions. Thus, we do not expect these forces to manifest in our systems and including a functional form capable of describing them is unnecessary.

The vOCG model allows for an appropriate description of acid-base interactions and is considered to be one of the more successful models [33, 35, 53, 54, 63, 64], but criticism still exists, such as the lack of an entropic effect [63, 65]. Nonetheless, due to the absence of a practical method that corrects its various shortcomings, the vOCG interfacial model will be incorporated into our mechanistic crystal growth model.

4.4 Incorporation into Mechanistic Models

The mechanistic parameters introduced in Chapter 3 require us to estimate surface energies in the kink, edge, and terrace directions (γ^K, γ^E, and γ^T, respectively) along each periodic bond chain. These directional surface energies are indicated in Figure 4.1, alongside the incorporation mechanism (a terrace-mediated process is typically expected [66–68]).

This incorporation mechanism is realistic since it offers a pathway of incremental

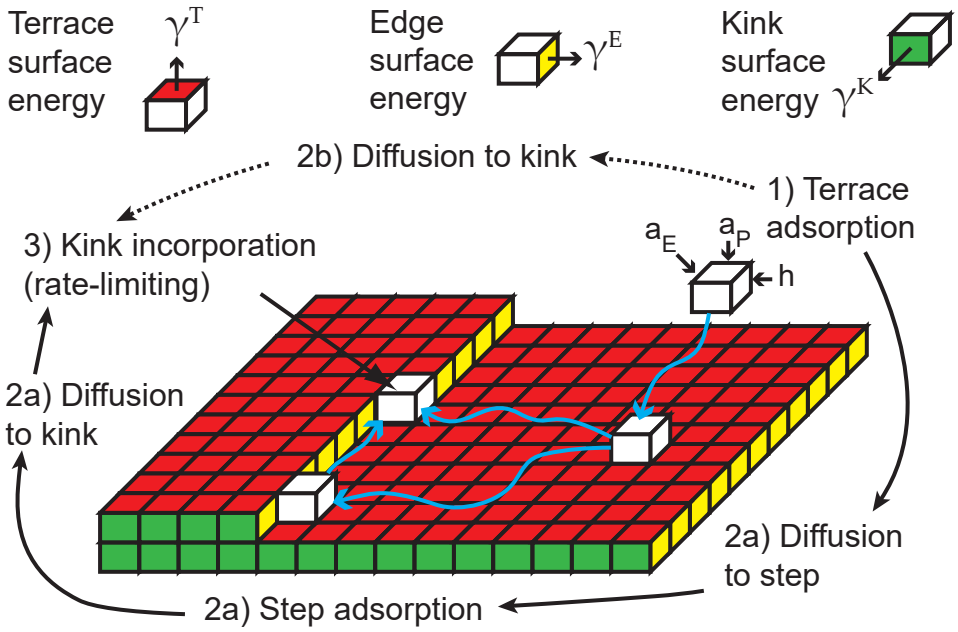

Figure 4.1: The surface structure of a crystal, showing sequential events of the incorporation mechanism (either solution-terrace-edge-kink or solution-terrace-kink). Terrace (γ^T), edge (γ^E), and kink (γ^K) surface energies are defined, alongside surface dimensions.

desolvation and accounts for the low density of kink sites on the face. Upon arrival from solution, a solvated growth unit is likely to impinge on a terrace site (not a kink site), where it can attach following desolvation of both the growth unit and surface. It can then diffuse on the surface until contacting an edge. For low kink densities it is unlikely to arrive at a kink directly following terrace diffusion, and so will adsorb to the edge after additional desolvation. It can diffuse along the step edge until finding a kink site, where the remaining desolvation precedes actual incorporation. Alternatively, for high kink densities the growth unit may diffuse directly to a kink from the terrace, and incorporate without prior edge adsorption. Both mechanisms are indicated on Figure 4.1 (for kinetic models, see Appendix 2.A). These terrace-mediated processes reflect relative site densities and represent pathways with lower energy barriers than incorporation direct from solution.

Of course, we have assumed fast surface diffusion for the above analysis. This assumption is often accurate for organic molecules, where favorable interactions exist between each molecule on the surface and diffusion simply requires hopping between local free energy minima, a process which should have low energetic barriers. For ionic systems, however, diffusion across the surface or along an edge would be much slower, owing to repulsive interactions between like ions; as a result, kink incorporation directly from solution seems more applicable.

Kink incorporation is the rate-limiting step, even within a terrace-mediated process; again, this is due to relative site densities and desolvation barriers. The solvent has 360° to 'escape' for terrace adsorption, 180° for edge adsorption and 90° for kink incorporation. This effect, coupled with the density of kink sites on a face being far lower than that of edge or terrace sites, renders the final stage, kink incorporation, rate-limiting.

For the detailed mechanistic growth rate expressions, see Chapter 3. Here, we summarize which mechanistic parameters are influenced by the interfacial energies: γ_i^K, γ_i^E, and γ^T. For centrosymmetric growth units, kink and edge energies are specific to step edge i on face (hkl), while terrace energies are specific to face (hkl). For non-centrosymmetric growth units, multiple types of each site can exist on each step edge (see Chapter 5). Note that the energetic modification to account for the solvent must be implemented individually for each type of site on each crystal face. The base mechanistic parameters affected are the kink, edge and terrace energies (centrosymmetric formulations presented below); key mechanistic parameters that these energies then influence are indicated:

- Kink energy $\phi_i^K = \gamma_i^K a_{P,i} h$
  - Critical length: eq 3.8
  - Kink density: eq 3.12
  - Kink detachment work: eq 3.16

- Edge energy $\phi_i^E = \gamma_i^E a_{E,i} h$
  - Critical 2D nucleus size, free energy, and shape: eqs 3.35, 3.36, and 3.39
  - 2D nucleation rate prefactor: 3.52
  - Edge detachment work: eq 3.19
- Terrace energy $\phi^T = \gamma^T \overline{a_E a_P}$
  - Terrace detachment work: eq 3.20

Note $a_{P,i}$ is the propagation length of the step, $a_{E,i}$ is the intermolecular width along the step, and h is the step height (see Figure 4.1). Note also that the detachment work in each direction is related to the corresponding energy by a multiple of two, to account for two surfaces being formed (i.e., $\Delta W_i^K = 2\phi_i^K$, $\Delta W_i^E = 2\phi_i^E$, $\Delta W^T = 2\phi^T$).

The kink energy impacts both step velocity (eq 3.11, through the kink density) and the spiral rotation time (eq 3.10, through the critical length and step velocity). Step velocities are also important in the 2D birth-and-spread regime (eq 3.56) and the kink density enters into the 2D nucleation rate prefactor (eq 3.52). Thus, the kink energy is an important parameter for each surface-integration-limited regime (spirals, 2D birth-and-spread, 2D polynuclear). For the 2D regimes, the edge energy is additionally important, affecting both the 2D nucleation rate (eq 3.31, through both the prefactor and free energy) and critical nucleus area (eq 3.28).

For centrosymmetric crystals under sublimation growth, the sum $\Delta W = \Delta W_i^K + \Delta W_i^E + \Delta W^T$ (see eq 3.17) corresponds to the lattice energy (it is the same for each kink on the crystal due to symmetry, and corresponds to the total work required to remove a growth unit from the crystal). Although under solution growth each surface is modified due to the solvent, the isotropic nature of ΔW should be maintained, since the entire set of solid-state interactions are involved. Thus, for centrosymmetric crystals, the kink rate

is isotropic under both sublimation and solution growth (i.e., it has the same value for a given crystal-solvent system, regardless of kink site type). This isotropic kink rate drops out of relative growth rate expressions, so the effect of solvent on kink rate is not relevant. For non-centrosymmetric growth units, however, the effect of solvent on anisotropic kink rates becomes relevant (the unique detachment work from each site must be applied: $\Delta W_{k,i}$, for site k on edge i, see Chapters 2 and 5).

For sublimation growth, there are no solvent effects, so the required surface energies are determined by summing all the solid-state intermolecular interactions (obtained using the CLP force field alone) that must be broken to form the surface. Considering terrace surface energies (γ^T), the PBCs broken upon detachment from terrace-adsorbed to solution are summed (the full solid-state interaction energy, E_{PBC}, in each case) and divided by $2\overline{a_E a_P}$, since 2 surfaces are formed ($a_{P,i}$'s and $a_{E,i}$'s are averaged to represent the surface area of a typical terrace growth unit). Edge and kink surface energies follow the same procedure but for γ_i^E, it is detachment from edge-adsorbed to terrace-adsorbed and the area is $2a_{E,i}h$; for γ_i^K, it is detachment from kink-incorporated to edge-adsorbed and the area is $2a_{P,i}h$. As a result, for sublimation growth, the kink energy is equal to half the in-chain (K direction) PBC interaction energy: $\phi_i^K = E_{PBC,i}^K/2$.

Within this analysis, periodic bond chains (PBCs) [69–71] are assumed to represent the energetics entirely (they are the strong, directional, repeating interactions within the crystal). An energy cutoff of $0.5kT$ is used that allows the PBCs to encompass at least 90 % of the lattice energy; furthermore, this should be appropriate since $1kT$ serves as a boundary estimate for step roughening [72–74].

Eq 4.20 describes the overall bulk interface approximation used to modify the surface energies when accounting for the solvent effect. Subscript x refers to the crystal (γ could

be γ^T, γ_i^E or γ_i^K but this has been omitted for clarity) and s refers to the solvent.

$$\gamma_{XS} = (\gamma_X^d + \gamma_X^{AB}) + (\gamma_S^d + \gamma_S^{AB}) - (W_{ad,XS}^d + W_{ad,XS}^{AB}) \tag{4.20}$$

For the solvent, the dispersive energy γ_S^d is calculated using the dispersive solubility parameter in the form of eq 4.7. The acid-base energy γ_S^{AB} is calculated by subtracting γ_S^d from the total experimentally determined solvent surface energy. This circumvents the need to deal with polarization and hydrogen bonding solubility parameters that are less rigorously partitioned.

For the crystal, the following equations are used:

$$\gamma_X^d = \frac{\sum \frac{L}{C+L} E_{PBC}}{SA} \tag{4.21}$$

$$\gamma_X^{AB} = \frac{\sum \frac{C}{C+L} E_{PBC}}{SA} \tag{4.22}$$

This technique is the same as for sublimation surface energies: it uses full PBC interaction strengths (E_{PBC}) broken during the relevant detachment events indicated earlier and the surface area (SA) is $2\overline{a_E a_P}$ for γ^T, $2a_{E,i}h$ for γ_i^E and $2a_{P,i}h$ for γ_i^K. To find dispersive and acid-base portions, the total PBC strengths are scaled using terms from the CLP force field: 'L' refers to the r^{-6} London dispersion term and 'C' refers to the sum of the r^{-1} and r^{-4} terms, which are important for hydrogen bonds [23]. This methodology is necessary as partitioned force field terms are not required to retain their physical interpretations following parameterization; it is only the total interaction strength which can be trusted as accurate. The dispersive component may be most justifiable but even this cannot be taken as an absolute value; for example, considering the hydrogen-bonded PBC in adipic acid, the r^{-6} London term has a greater magnitude than the total interaction, which, if true, would require a repulsive acid-base effect that is not a physical

description of the hydrogen bond. There are 3 attractive terms: dispersive, polarization and coulombic (for acid-base interactions this is attractive due to a manifestation as opposite dipoles by a force field). Therefore, using the ratios of these terms to divide the total interaction into dispersive and acid-base effects (as indicated in eqs 4.21 and 4.22) provides the most practical method to determine these required quantities from the force field.

Additionally, when implementing the vOCG method, we determine the locations of potential sites for acid-base interactions between the solvent and the crystal. To a first approximation these can be taken as those PBCs corresponding to solid-state hydrogen bonds (or more general acid-base interactions, examples of which are self-association in acetonitrile, dimethylformamide and nitrobenzene [40]). For such sites, their partitioned energies are determined using eqs 4.21 and 4.22. For non-hydrogen-bonded PBCs, however, the solid-state acid-base energy is taken as zero and the entire PBC interaction is taken as the dispersive contribution, which leads to a bulk interface approximation in the form of eq 4.23. One would expect a dominant London term anyway in these cases, but this manual correction helps remove acid-base artifacts from a solvent with large γ_S^{AB}, when in actuality no such interaction exists (i.e., because the solvent molecules can rotate and orient acid/base groups away from the surface to satisfy interactions internally).

$$\gamma_{XS} = (\gamma_X^d + \gamma_X^{AB}) + (\gamma_S^d + \gamma_S^{AB}) - 2\sqrt{\gamma_X \gamma_S^d} \tag{4.23}$$

Therefore, $W_{ad,XS}^{AB}$ only exists for the hydrogen-bonded PBCs. With γ_S^d, γ_S^{AB}, γ_X^d and γ_X^{AB} determined, we must split the acid-base portions further into electron donating (-) and accepting (+) characteristics. Alongside eq 4.17, this requires values for the ratios γ_X^+/γ_X^- and γ_S^+/γ_S^-. If parameters exist for the chosen solvent or can be inferred from

compounds with similar functional groups, these ratios could be determined, but as will be demonstrated later (see adipic acid case study), predicted crystal shapes are often insensitive to their actual values. The bulk interface approximation for the hydrogen-bonded PBCs is given by eq 4.24.

$$\gamma_{XS} = (\gamma_X^d + \gamma_X^{AB}) + (\gamma_S^d + \gamma_S^{AB}) - (2\sqrt{\gamma_X^d \gamma_S^d} + 2\sqrt{\gamma_X^+ \gamma_S^-} + 2\sqrt{\gamma_X^- \gamma_S^+}) \tag{4.24}$$

This insensitivity to accepting/donating ratios is due to the significant contribution of $W_{ad,XS}^{AB}$ (usually resulting in a low surface energy) for those PBCs capable of forming acid-base interactions with the solvent (termed hydrogen-bonded PBCs for simplicity). Thus, under an appropriate solvent, a step with hydrogen-bonded PBCs in the kink direction can have low kink energy, high kink density and fast step velocity. Under the spiral mechanism, the rotation time on a face can be independent of the fastest growing edges [5], so faces with few in-slice hydrogen-bonded PBCs may have growth rates that are not sensitive to exact kink energies on those hydrogen-bonded-PBC edges (providing they remain low relative to the other edges that do not represent hydrogen-bonded PBCs). On faces with multiple in-slice hydrogen-bonded PBCs, one would expect a low spiral rotation time and fast face growth rate; such faces typically grow out of the crystal morphology and the shape is again insensitive to the uncertainty in $W_{ad,XS}^{AB}$. When the low energy hydrogen-bonded PBCs are in the edge direction, the penalty for 2D nucleation is reduced, which is another effect leading faces with multiple in-slice hydrogen-bonded PBCs to have fast growth rates. In summary, hydrogen-bonded PBCs often grow out of spirals, and faces with many hydrogen-bonded PBCs often grow out of the crystal shape, so the shape predictions can be insensitive to estimated accepting/donating ratios. Adjusting this ratio provides a sensitivity test of whether the prediction is robust and the uncertainty can be tolerated.

However, this formulation still struggles to account for solvent-crystal acid-base adhesion interactions when both phases separately have no acid-base contributions (e.g., solvent molecules act purely as donors and crystal molecules act purely as acceptors). Relying on a force field (to describe internal crystal interactions) and solubility parameters (to describe internal solvent interactions) provides limited information to estimate donating and accepting characteristics that only manifest upon contact with a molecule of opposite character. Therefore, a monopolar acidic solvent and monopolar basic crystal will have an acid-base interfacial interaction that is not easily determined. A potential solution would be taking a typical hydrogen bond strength and adding it manually to the adhesion interaction where appropriate.

Finally, there are cases where it makes sense to manually activate or deactivate $W_{ad,XS}^{AB}$ to better describe real systems. Steric hindrance might prohibit solvation of a surface in certain cases. As explained for pentaerythritol later, it is possible for solvent-crystal adhesive forces in the terrace direction (γ^T) to only become satisfied upon formation of step edges, where growth units at the edge can complete such interactions as the adjacent crystal growth units previously obstructing solvation have been removed. In this case $W_{ad,XS}^{AB}$ should be activated for the edge surface energy, following the same procedure for hydrogen-bonded PBCs (even if no solid-state hydrogen-bonded PBCs extend out in the edge direction). This can correct for acid-base crystal-solvent interactions that are completed after the formation of the surface they technically extend from.

Asymmetric spirals might also result if the solvent-accessible surface area [75, 76] is different on symmetrically opposite spiral edges or, alternatively, for non-centrosymmetric crystal systems where different functional groups are accessible on opposite edges. These effects could lead to different solvent-modified edge and kink energies on symmetrically opposite spiral edges, which in turn would provide different step velocities and asymmetric spirals. Manually activating or deactivating the acid-base portion of the solvent effect

formulation presented here may offer a way to account for these effects upon inspection of the relevant edges using crystal visualization software such as Mercury [77].

These modifications may provide success for more complicated systems. However, if subtler solvent effects cannot be accounted for, molecular simulations could be required to determine surface energies or other relevant quantities needed in the mechanistic model. This would, unfortunately, render the developed framework less applicable as a practical engineering tool.

4.5 Comparing Sublimation and Solution Shapes

Evaluating predictions obtained from the mechanistic model against experimentally determined crystal shapes provides a useful test of our modeling performance. Moreover, a comparison between such tests for both sublimation and solution growth of crystals provides a way to isolate the effect of the solvent and determine whether it has been captured accurately. The sublimation growth of crystals provides a general test of the modeling framework without any energetic modifications due to the solvent (i.e., a test solely of the solid-state chemistry and surface physics of the crystal growth model). Therefore, if modeling predictions align with experimental shapes for both vapor and solution growth, it supports the accuracy of both our mechanistic framework as well as our ability to modify energetics appropriately and account for the solvent effect. Four example cases are reported; predicted and experimental shapes are summarized, while details of relevant parameters within the mechanistic model for each face are contained in Appendix 4.A. For the final example, naphthalene, we selected 2 solvents for solution growth predictions. This demonstrates the applicability of our approach not only across different crystal-solvent systems, but also for the same crystal growing from multiple solvents.

Figure 4.2: Thermal gradient sublimation apparatus with glass sublimation tubes containing biphenyl and pentaerythritol in the foreground.

To determine sublimation growth morphologies of biphenyl, adipic acid and pentaerythritol, crystals were grown with a thermal gradient sublimation apparatus using glass tubes of length 60 cm and 1 cm inside diameter. Solid material was lowered in a small glass open-ended vial to ensure no crystals were on the inner surface of the tube before crystallization. The tube was placed under vacuum prior to and during heating. The apparatus and final sublimation tubes are shown in Figure 4.2.

Single crystal X-ray diffraction data for face indexing were collected using a 3-circle Bruker Platform goniometer equipped with Mo radiation. The data were indexed to give unit cell parameters and the orientation relative to the diffractomer enabling the faces to be determined. The Bruker APEX-II suite of programs were used for indexing and face determination.

When modeling each crystal system, the CLP force field [23] (including renormalization of the hydrogen atomic positions) was used to determine the intermolecular interactions from the crystallography. For the solvent, Hansen 3-component parameters [18] were used with appropriate correlations [20].

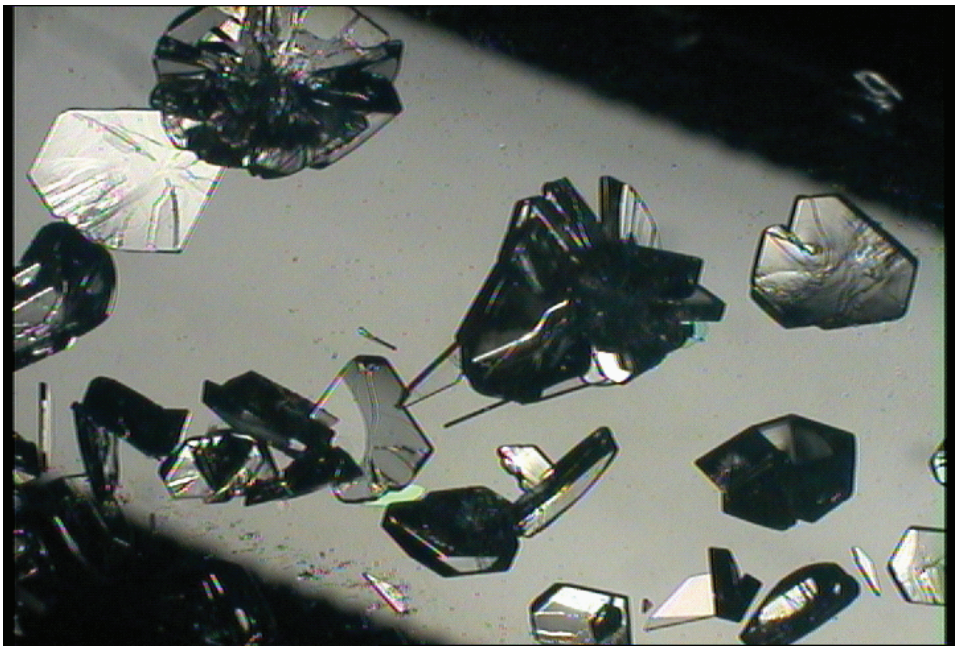

Figure 4.3: An image of biphenyl crystals inside the sublimation tube indicating the overall non-uniformity of grown crystal shapes and the dominant expression of the {001} family.

4.5.1 Case Study: Biphenyl Grown from Toluene

Biphenyl crystallizes in the monoclinic space group $P2_1/a$ with lattice parameters: $a = 8.12$ Å, $b = 5.63$ Å, $c = 9.51$ Å and $\beta = 95.1°$ [78] (CSD CIF file code BIPHEN04 was used for modeling). Biphenyl crystals were grown by thermal gradient sublimation under vacuum with a source temperature of $\sim 40°$C. The data crystal (right hand side, Figure 4.4) was indexed via our X-ray diffraction measurements with monoclinic unit cell parameters $a = 8.13$ Å, $b = 5.66$ Å, $c = 9.54$ Å and $\beta = 95.2°$ in space group $P2_1/c$. The overall shapes of the crystals were not uniform (see Figure 4.3), but did uniformly have the {001} family as the largest faces.

Figure 4.4 shows the predicted crystal habit for sublimation growth of biphenyl using the mechanistic model, alongside one instance from the population of experimentally grown sublimation shapes. The model correctly predicts the {001} family to be the

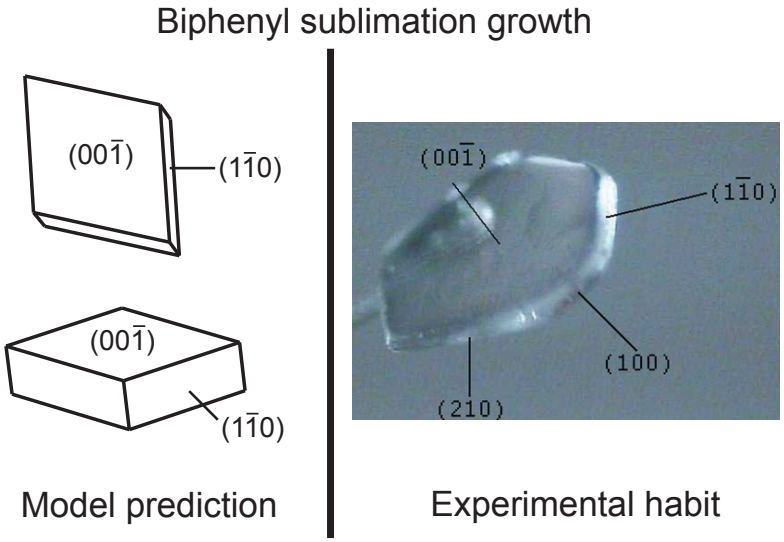

Figure 4.4: Two views of the crystal habit prediction for sublimation growth of biphenyl (left) and corresponding experimentally grown shape (right). The model correctly predicts the {001} family to be largest faces.

largest faces on the crystal habit. This is the one common feature of the experimentally grown crystals, which are overall non-uniform. Of the surrounding indexed faces, the {110} family is indeed predicted to exist on the steady-state morphology, while the (100) face is predicted to be an F face but narrowly grow out of the steady-state crystal growth shape. The (210) face is predicted to be an S face (i.e., containing a single PBC), so one would not expect its presence on the steady-state morphology. The imaged crystal is asymmetric, which should not be the case for unhindered growth of a non-polar crystal. This implies part of the shape is an artifact of the sublimation experiment, which did not correspond to free, unhindered growth of each face (the situation for which we model crystal growth). Furthermore, it is unclear whether the (100) and (210) faces that are not predicted to appear on the steady-state morphology exist prevalently on the other grown crystals. Since each face is predicted to grow under a spiral mechanism and the crystal is centrosymmetric, the shape has no supersaturation-dependence (while it remains in the layered growth regime).

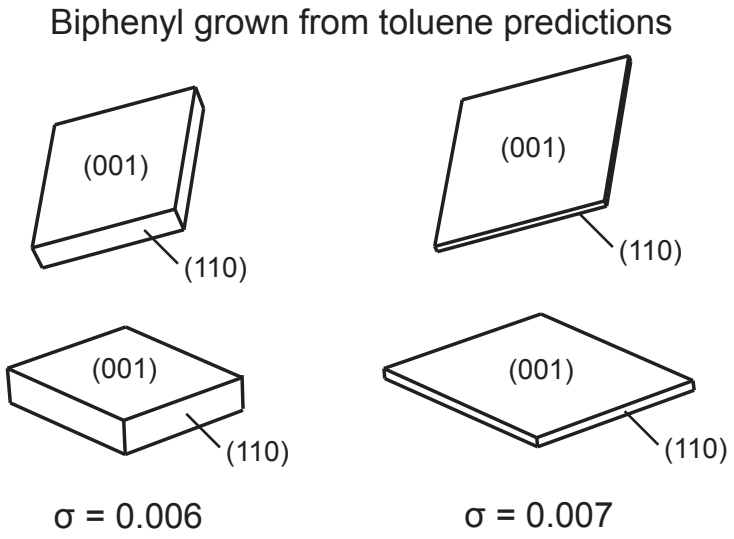

Figure 4.5: Two views of the crystal habit prediction of biphenyl grown from toluene at $\sigma = 0.006$ (left) and $\sigma = 0.007$ (right).

The growth of biphenyl from toluene presents the simplest possible solvent effect, with both biphenyl and toluene containing entirely dispersive interactions. Thus, there are no acid-base terms to consider and one would expect the geometric mean to perform adequately in the interfacial energy model.

Figure 4.5 shows the predicted crystal habit of biphenyl grown from toluene. Above $\sigma \approx 0.005$, each face family except {001} is predicted to grow via a 2D-nucleation mechanism. Most faces, therefore, grow out of the crystal habit at low supersaturation; the {110} family is not geometrically able to do so, which leads to a rhombic {001} platelet bounded by the {110} family (this shape has been experimentally reported [79]). The aspect ratio increases with supersaturation, as shown in Figure 4.5 (see Chapter 3 for more detail).

4.5.2 Case Study: Adipic Acid Grown from Water

Adipic acid crystallizes in the monoclinic space group $P2_1/c$ with lattice parameters: $a = 10.01$ Å, $b = 5.15$ Å, $c = 10.06$ Å and $\beta = 136.8°$ [80] (CSD CIF file code ADIPAC was used for modeling; almost identical results are obtained using other CIF files: ADIPAC04 [81], ADIPAC09 and ADIPAC14 [82]). Adipic acid crystals were grown by thermal gradient sublimation under vacuum with a source temperature of ~ 160°C. The data crystal (right hand side, Figure 4.6) was indexed with monoclinic unit cell parameters $a = 7.24$ Å, $b = 5.17$ Å, $c = 10.12$ Å and $\beta = 110.7°$ in space group $P2_1/n$. This corresponds to a different choice of unit cell but otherwise equivalent crystallography to the CIF file used for modeling purposes. The observed crystals showed a rod/needle-like morphology.

Figure 4.6 shows the predicted crystal habit for sublimation growth of adipic acid using the mechanistic model, alongside an experimentally grown sublimation shape; the rod/needle-like morphology is correctly predicted. There is a mismatch between the faces predicted to be on the steady-state morphology and those indexed experimentally, even when correcting for the different unit cell choice. This could be a result of the small face areas available for indexing. Similarly to biphenyl, each face is predicted to grow via the spiral mechanism so there is no dependence of shape on supersaturation.

For adipic acid crystals grown from water, both crystal and solvent have internal hydrogen bonds, so there exists a potential for acid-base adhesion at the interface. Using the DVS scale for water, $\gamma_S^+/\gamma_S^- = 4.35$; for adipic acid we have estimated $\gamma_X^+/\gamma_X^- = 1$ since it possess both donating and accepting character.

Figure 4.7 shows the predicted crystal habit of adipic acid grown from water. The calculated {100} hexagonal platelet shape aligns closely with experimental reports [83,84]. Each face is predicted to grow under a spiral growth mechanism so no supersaturation-

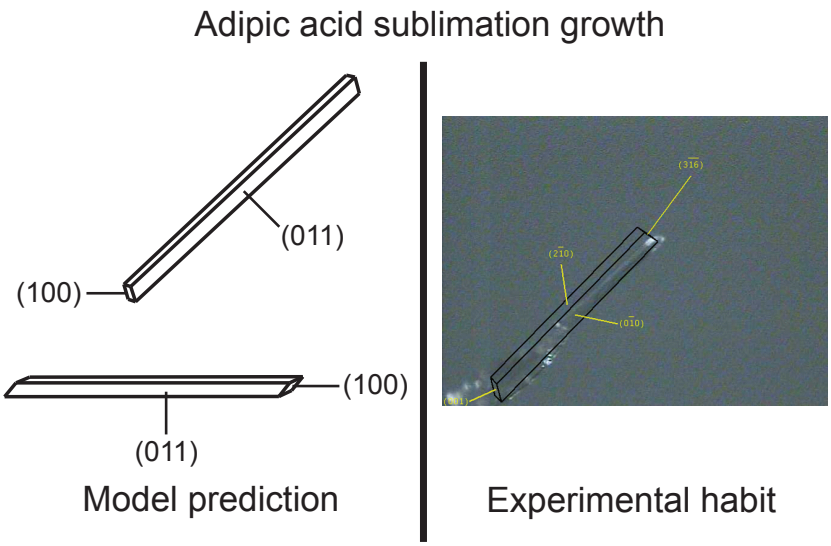

Figure 4.6: Two views of the crystal habit prediction for sublimation growth of adipic acid (left) and the corresponding experimentally grown shape (right). The rod/needle-like morphology is correctly predicted.

dependent shape is expected. This dramatic change of shape from the rod/needle-like sublimation shape can be explained through an increase in the growth rate of the {011} family of faces compared to the {100} family. In sublimation growth the hydrogen-bonded PBC within the {011} family has a high kink energy, which leads to a low kink density and step velocity, causing large spiral rotation times and thus low growth rates. During solution growth, water can hydrogen bond with this exposed PBC, dramatically lowering the kink energy via the contribution from W_{ad}^{AB}. This lowered kink energy decreases the spiral rotation time for the {011} family relative to the {100} family and leads to the predicted and observed shape change.

The predicted shape is not sensitive to the assumed ratio of $\gamma_X^+/\gamma_X^- = 1$ for adipic acid. This is because no faces on the steady-state growth shape have spiral sides with hydrogen bonds in the kink direction. Faces including the hydrogen-bonded PBCs in the kink direction are fast growing, since the favorable acid-base adhesion with the solvent produces a low kink energy (fast step velocity and face growth rate). The γ_X^+/γ_X^- ratio

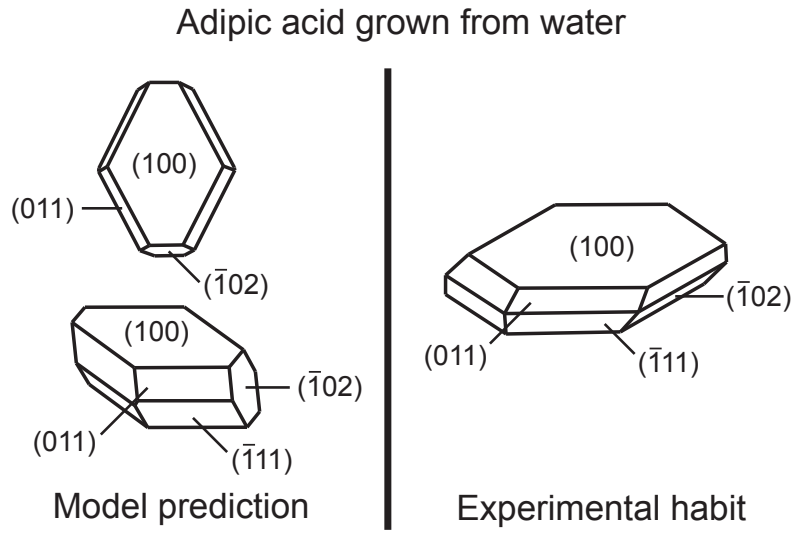

Figure 4.7: Two views of the crystal habit prediction of adipic acid grown from water (left) and the experimentally reported shape (right: schematic traced from Davey et al. [83]). The model correctly predicts a hexagonal shape with the {100} family dominant and surrounding faces to include the {011}, {$\bar{1}$11} and {$\bar{1}$02} families.

only affects these hydrogen-bonded PBCs, so the shape prediction is insensitive to our assumption and is robust.

4.5.3 Case Study: Pentaerythritol Grown from Water

Pentaerythritol crystallizes in the tetragonal space group $I\bar{4}$ with lattice parameters: $a = b = 6.09$ Å and $c = 8.76$ Å [85] (CSD CIF file code PERYTO04 was used for modeling). The growth unit is near-centrosymmetric, which alongside the singular orientation within the lattice leads to a centrosymmetric network of interactions. Crystals of pentaerythritol were grown by thermal gradient sublimation under vacuum with a source temperature of ~ 140°C. The data crystal (right hand side, Figure 4.8) was indexed with tetragonal unit cell parameters $a = b = 6.09$ Å and $c = 8.76$ Å in space group $I\bar{4}$. The overall shapes of the crystals were not uniform but did uniformly have the {001} family as the largest faces.

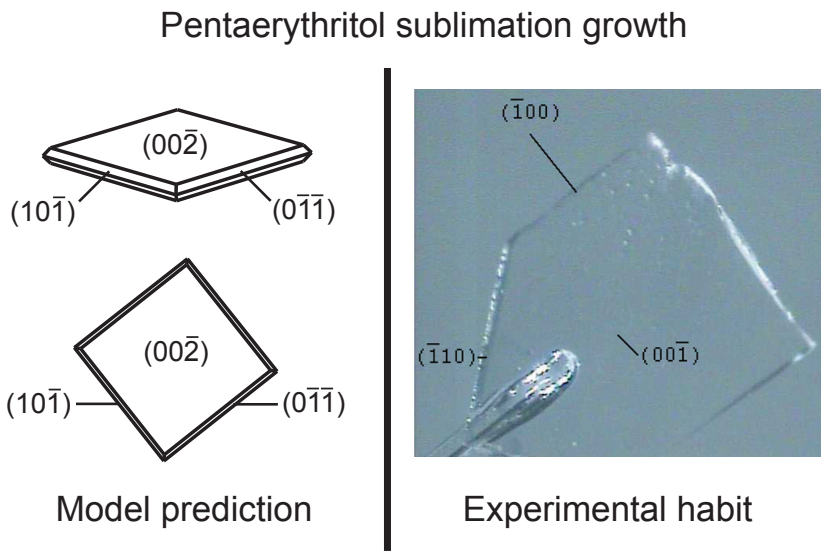

Figure 4.8: Two views of the crystal habit prediction for sublimation growth of pentaerythritol (left) and corresponding experimentally grown shape (right). The model correctly predicts the {002} family to be the largest faces.

Figure 4.8 shows the predicted crystal habit for sublimation growth of pentaerythritol using the mechanistic model (the spiral mechanism is predicted on each face so the shape is independent of supersaturation), alongside an experimentally grown sublimation shape. The model correctly predicts the {002} family to be the largest on the crystal habit. Similarly to biphenyl, the asymmetric shape is not predicted and this discrepancy is expected to result from hindered growth of certain faces during the course of the sublimation experiment, leading to the observed non-uniformity of crystal shapes. The mismatch between the predicted and indexed surrounding faces is also expected to stem from this non-uniformity, in addition to the small face areas available for indexing.

Growth of pentaerythritol from water provides a similar test to adipic acid, since hydrogen bonds are present within both phases, so at the crystal-solvent interface an acid-base interaction exists with both phases possessing some accepting and donating character. For water we again use $\gamma_S^+/\gamma_S^- = 4.35$; for pentaerythritol we have estimated $\gamma_X^+/\gamma_X^- = 3.79$ (DVS value for glycerol).

On the {110} family in pentaerythritol, water molecules are not expected to be able to interface with the recessed layer of −OH groups on the terrace, which is a steric effect that prohibits completion of the potential solvent-crystal acid-base interaction in the terrace direction. Upon the formation of steps on the surface this steric hindrance is eliminated, however, meaning the edge surface energy possesses some acid-base character due to completion of solvation in the terrace direction. To account for this, the work of adhesion is applied using eq 4.24 (to introduce a contribution from $W_{ad,XS}^{AB}$) even though there are no hydrogen-bonded PBCs in the edge direction. Note that the terrace surface energy does not enter the mechanistic model (since centrosymmetric expressions apply), so its change is irrelevant. The necessity of including such a manual modification for a general system can be determined by using Mercury [77] to visualize the crystal faces, but the decision to activate or deactivate the acid-base effect may not always be simple.

Figure 4.9 shows the predicted crystal habits of pentaerythritol grown from water, alongside experimentally reported shapes [86,87]. For $\sigma < 0.15$, each face is predicted to grow via a spiral mechanism, which leads to the top-left shape in Figure 4.9 and corresponds to the shape reported by Wells [86]. At $\sigma = 0.15$, the {110} family is predicted to cross over to a 2D-nucleation growth mechanism, so upon increasing supersaturation these faces grow out of the steady-state growth shape. This leads to a bipyramidal form predicted for $\sigma \geq 0.18$, which is the commonly reported morphology [87–89].

The predicted crossover supersaturation for the {110} face family to hit 2D nucleation is sensitive on the selected γ_X^+/γ_X^- ratio, but shape predictions within each regime are not. This is a result of the steric effect included above, where sterically hindered hydrogen bonds in the terrace direction can be solvated upon edge formation, leaving the edge surface energy to have a dependence on the acid-base adhesion. As a result, the predicted crossover supersaturation should be treated as an estimate with significant uncertainty.

Interestingly, using the solvent-modified terrace surface energies within the attach-

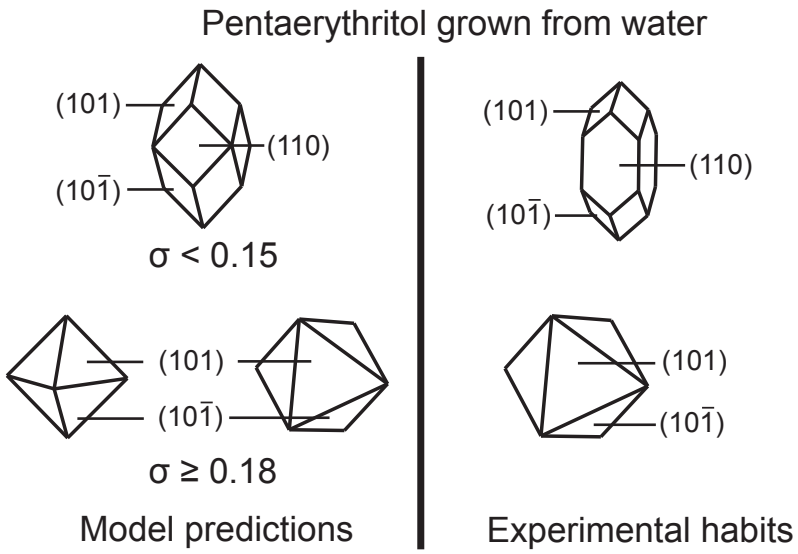

Figure 4.9: Crystal habit predictions of pentaerythritol grown from water at $\sigma < 0.15$ and $\sigma \geq 0.18$ (left) and experimentally reported shapes (right: schematics traced from Wells [86] (top) and Bernado and Giulietti [87] (bottom)).

ment energy model provides the bipyramidal shape prediction also, which is a vast improvement on the base attachment energy prediction [90]. This demonstrates the broad utility of successfully modifying crystal energies to describe the solvent effect, but the ability to reproduce the low supersaturation growth shape of pentaerythritol using the attachment energy model is clearly lost, alongside any potential mechanistic insights.

4.5.4 Case Study: Naphthalene Grown from Ethanol or Cyclohexane

The final example presented is naphthalene, which crystallizes in the monoclinic space group $P2_1/a$ with lattice parameters: $a = 8.21$ Å, $b = 5.97$ Å, $c = 8.67$ Å and $\beta = 123.4°$ [91] (CSD CIF file code NAPHTA10 was used for modeling).

Figure 4.10 shows the predicted crystal habit for sublimation growth of naphthalene using the mechanistic model, alongside an experimentally reported [92] shape. The model

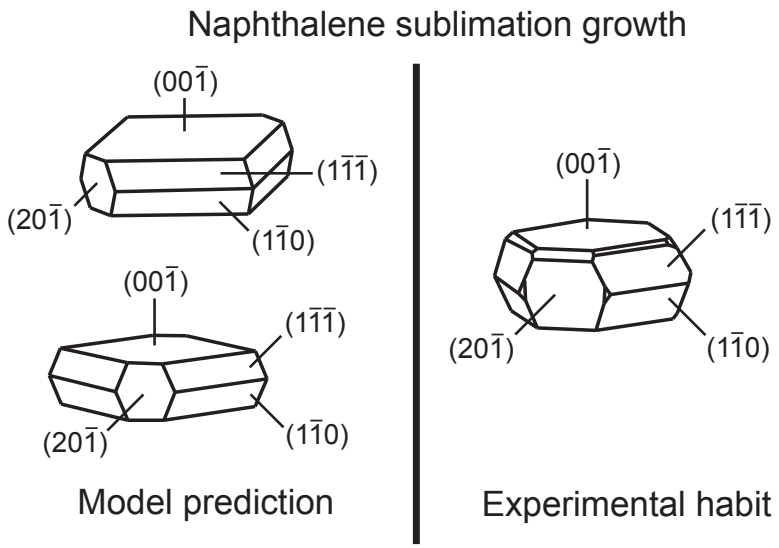

Figure 4.10: Two views of the crystal habit prediction for sublimation growth of naphthalene (left) and corresponding experimentally reported shape (schematic traced from Grimbergen et al. [92]; right).

correctly predicts the dominant face families and the calculated habit is close to the experimental shape. Each face is predicted to grow under a spiral mechanism.

For studying the solution growth of naphthalene, the first solvent we selected was ethanol. Naphthalene itself has negligible internal acid-base character, unlike ethanol, which is self-associating with internal hydrogen bonds. As a result, there exists little potential for interfacial acid-base adhesion between the crystal and solvent. Additionally, since ethanol molecules have the ability to orient back into solution and present their non-polar ends towards the growing crystal, the cohesive energy of the solvent must be modified to remove the hydrogen-bonding portion of the internal interaction (these interactions can still be satisfied internally). This is calculated using eq 4.7 with the hydrogen-bonding solubility parameter and is subtracted from the total solvent surface energy to form a modified cohesive energy that reflects what portion is actually broken upon the formation of the crystal-solvent interface.

Figure 4.11 shows predicted crystal habits of naphthalene grown from ethanol at vari-

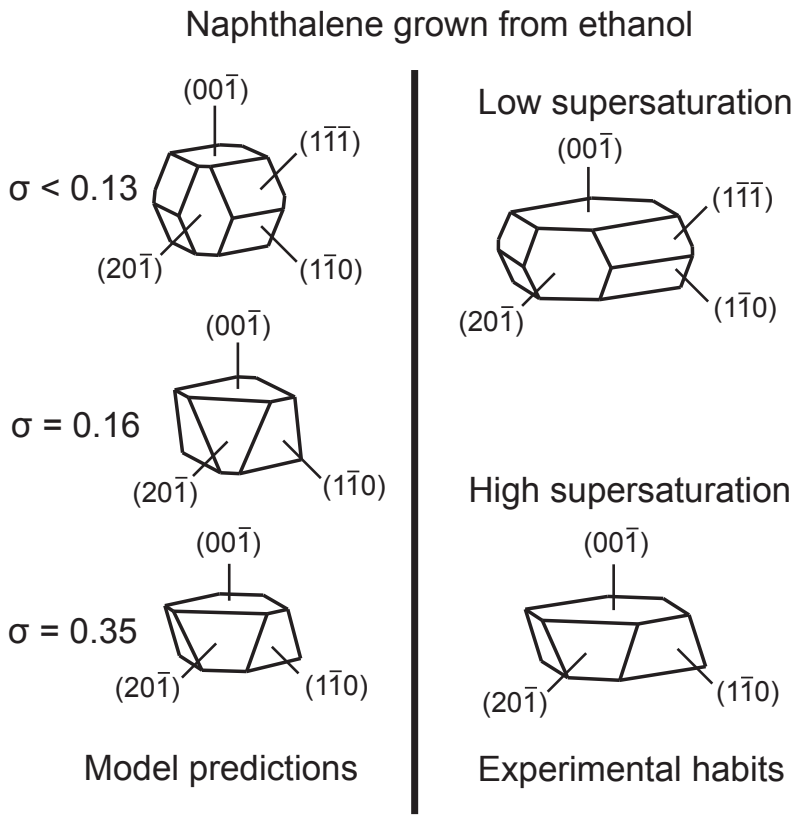

Figure 4.11: Crystal habit predictions of naphthalene grown from ethanol at $\sigma < 0.13$, $\sigma = 0.16$ and $\sigma = 0.35$ (left) and experimentally reported shapes (schematics traced from Grimbergen et al. [92]) at low and high supersaturation (right). The model correctly predicts the dominant face families and is able to capture the observed supersaturation-dependence shape, where the $\{1\bar{1}\bar{1}\}$ family grows out after crossing over to a 2D-nucleation growth regime.

ous supersaturations, alongside experimentally reported [92] shapes. The model correctly predicts the dominant face families in the morphology. The $\{1\bar{1}\bar{1}\}$ family is predicted to cross over to 2D nucleation at $\sigma = 0.13$ and grow out of the crystal growth shape at higher supersaturation, matching the experimental observation. The $\{1\bar{1}0\}$ and $\{20\bar{1}\}$ families are predicted to cross over to 2D-nucleation regimes at $\sigma = 0.30$ and $\sigma = 0.36$, respectively. These faces do not grow out of the crystal morphology, but instead cause a supersaturation-dependent aspect ratio, which aligns well with the experimentally reported [92] shape pictured bottom right in Figure 4.11 and also explains the $\{001\}$ platelet morphology that has been observed [93] during growth at very high supersaturation.

The second solvent we considered for the crystallization of naphthalene was cyclohexane. The interfacial action in this case is purely dispersive, since cyclohexane is a neutral solvent offering no acid-base character. Figure 4.12 displays the predicted crystal habits of naphthalene grown from cyclohexane at various supersaturations, alongside experimentally reported shapes [86, 92]. The model correctly predicts the morphology to include the $\{001\}$, $\{1\bar{1}0\}$ and $\{20\bar{1}\}$ face families and matches the experimentally determined shapes. The $\{1\bar{1}0\}$ and $\{20\bar{1}\}$ families are predicted to grow via 2D nucleation, which is responsible for the aspect ratio that increases with supersaturation.

4.6 Conclusions

The solvent can significantly affect crystal habit and, thus, accurately accounting for it is important for a useful predictive modeling tool. Rapid predictions are desired, to ensure practical utility, which leaves bulk interface approximations as the principal option to include solvent-induced energetic modifications within the mechanistic model. Of these, the interfacial model by van Oss, Chaudhury and Good represents the most practical option for small organic molecules and provides the ability to properly account

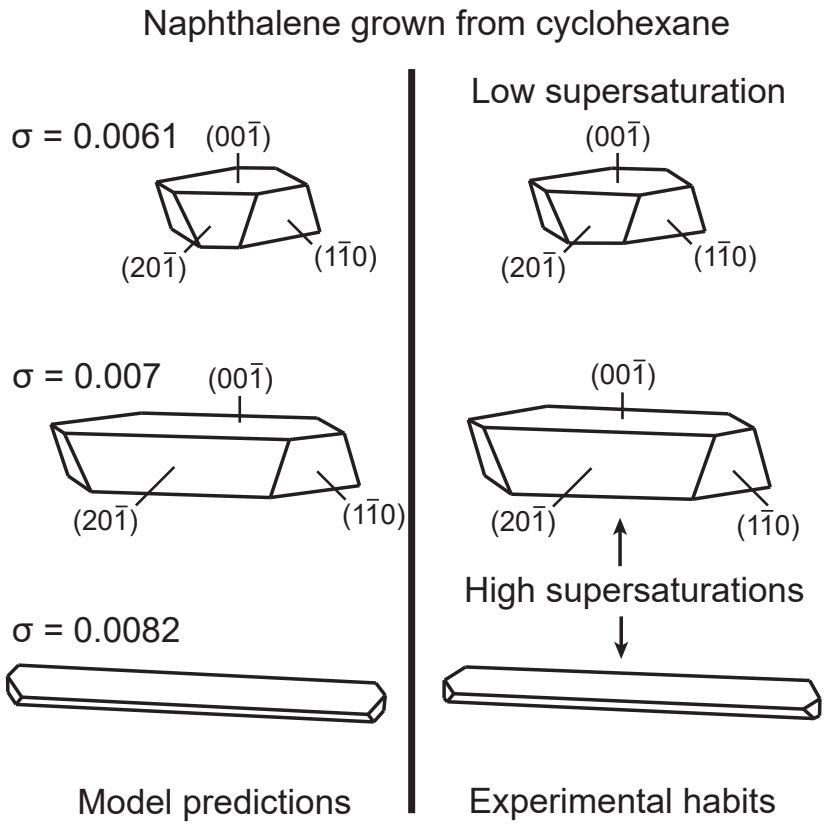

Figure 4.12: Crystal habit predictions of naphthalene grown from cyclohexane at $\sigma = 0.0061$, $\sigma = 0.007$ and $\sigma = 0.0082$ (left) and experimentally reported shapes (schematics traced from Grimbergen et al. [92] and Wells [86]) at low and high supersaturations (right). The model correctly predicts the dominant face families and the supersaturation-dependent shape and aspect ratio.

for acid-base interactions across the interface.

Nonetheless, challenges exist to forming an accurate description of the crystal surface chemistry with the vOCG interfacial model; these are summarized below, with comments:

1. The potential sites for interfacial acid-base interactions between the crystal and solvent must be located; it is here that the acid-base work of adhesion is relevant and must be calculated. One should consider existing solid-state hydrogen bonds and relevant functional groups.

2. Selecting the γ^+/γ^- ratio in the absence of tabulated data requires either experiments (time-consuming) or estimation via chemical intuition (prone to error). Nonetheless, as described earlier in the text, shape predictions are often insensitive to this uncertainty.

3. Steric effects on solvation are not naturally accounted for. Manual activation or deactivation of the acid-base portion of adhesion may be able to account for recessed, inaccessible hydrogen-bonding solute groups, though this technique is somewhat crude.

4. For oppositely monopolar solute/solvent pairs, force fields and solubility parameters contain no information about potential acid base interactions. In this case experiments would be required, or typical interaction strengths could be introduced.

Overall, the simplest interfacial system to model is where either the solute or solvent is exclusively dispersive. Where acid-base effects exist, applying the vOCG model has the potential to describe the surface chemistry; ideally one would use experiments to guide selection of γ^+/γ^- ratios as far as possible, but we have shown the ability to obtain useful predictions from sensible estimates. More complicated effects might be accounted for as described in points 3 and 4 above, but molecular simulations may prove unavoidable to

ensure an accurate treatment in the most complex of these cases. In our approach, such simulations are a last resort not a first resort.

The interfacial model was tested within a mechanistic crystal growth model for centrosymmetric small organic molecules growing via either a spiral or 2D-nucleation mechanism. The procedure for calculating the interfacial energy is equally applicable to more general models such as the non-centrosymmetric spiral growth model [94].

Evidently, the effect of solvent on crystal habit can either be significant (e.g., adipic acid, pentaerythritol) or relatively minor (e.g., naphthalene, biphenyl). The mechanistic model has been able to account accurately for both scenarios, which supports the utility of the proposed methodology. There are a variety of assumptions and input data uncertainties in both the interfacial model and mechanistic framework, yet satisfactory and useful results have been obtained. Furthermore, one should remember that experimentally reported crystals are themselves a sample of the distribution; whereas our model predicts a single shape. Thus, the discrepancies between predicted and observed crystal habits are relatively minor and although bulk interface models do have limitations, they offer an attractive option for rapidly predicting the effect of solvent on the crystal habit of small organic molecules.

Finally, our investigation suggests an optimum path for process development. By first performing a sublimation experiment, one obtains information about the crystal habit without first requiring a 'suitable' solvent (reasonable solubility, habit etc.). Comparing the sublimation shape to that which is desired determines how relative growth rates must be modified, if at all. Considering the functional groups exposed at the relevant faces may then enable the selection of candidate solvents to achieve a desirable modification. In essence, starting with a sublimation experiment and combining mechanistic/chemical intuition could facilitate crystal habit engineering.

Appendices

4.A Mechanistic Parameters

Relevant quantities within the mechanistic model (those which enable the crystal habit calculation) are summarized in the sections below for each system studied. For each face family present on a steady-state growth shape prediction, a single face's parameters are provided.

The calculated lattice energy for each crystal can be compared to an experimentally reported sublimation enthalpy. The two quantities differ through a degree of freedom correction, so if the difference between the calculated lattice energy and experimental sublimation enthalpy is of the order RT (which is the case for each system) it lends support to the accuracy of the force field used and, therefore, the energetic calculations within the mechanistic model.

For each face (miller indices (hkl)), h is the step height (a single interplanar spacing, d_{hkl}) and R is the relative growth rate, where the reference face is indicated on the denominator. If the face is predicted to cross over to 2D nucleation and growth, the crossover supersaturation (σ_{2D}) is listed, alongside the supersaturation corresponding to a critical nucleus size of 10 growth units ($\sigma_{n_C=10}$), which serves as a limit of our modeling applicability within the 2D regime. Unlike when both faces are in the spiral regime, if a face is growing via 2D nucleation and growth its relative growth rate is dependent on the supersaturation, so σ values for the supplied relative growth rates are indicated where relevant. Refer to Chapter 3 for detailed explanations of and expressions for the mechanistic parameters.

Periodic bond chains (PBCs) on each face are also listed, where their vector [uvw] corresponds to the crystallographic axes. For each PBC, a_P is the propagation length,

a_E is the width of a growth unit along the step, $\alpha_{i,i+1}$ is the angle between that edge and the next and ϕ^K is the kink energy (note in calculating the kink density, the multi-site expressions developed by Lovette and Doherty [95] have been used where $\phi^K \leq 3kT$.

4.A.1 Biphenyl

The lattice energy of biphenyl (CSD code BIPHEN04 [78]) is calculated to be 21.3 kcal/mol. The sublimation enthalpy has been reported [96] as 19.9 kcal/mol for $T = 283 - 338$ K, which corresponds to a difference of ~ 2 RT from the lattice energy.

Sublimation Growth

Table 4.1 contains the relevant mechanistic parameters for the (001) and (110) faces of biphenyl under sublimation growth. Crystal growth was modeled at $T = 313$ K, corresponding to the crystals grown by sublimation at $T \sim 40°$C.

Table 4.1: Biphenyl faces, sublimation growth

Face (001)			
Parameter		Units	Value
	h	Å	9.47
	$R = \frac{G_{001}}{G_{001}}$	-	1
[1$\bar{1}$0] PBC	a_P	Å	4.63
	a_E	Å	4.94
	$\alpha_{i,i+1}$	°	69.5
	ϕ^K	kT	4.39
[110] PBC	a_P	Å	4.63
	a_E	Å	4.94
	$\alpha_{i,i+1}$	°	110.5
	ϕ^K	kT	4.39

Face (110)			
Parameter		Units	Value
	h	Å	4.62
	$R = \frac{G_{110}}{G_{001}}$	-	2.43
[1$\bar{1}$0] PBC	a_P	Å	9.48
	a_E	Å	4.94
	$\alpha_{i,i+1}$	°	85.8
	ϕ^K	kT	4.39
[001] PBC	a_P	Å	4.93
	a_E	Å	9.51
	$\alpha_{i,i+1}$	°	94.2
	ϕ^K	kT	1.35

Growth from Toluene

Table 4.2 contains the relevant mechanistic parameters for the (001) and (110) faces of biphenyl grown from toluene. Crystal growth was modeled at $T = 302$ K, corresponding to the experimentally reported [79] crystals grown from toluene at $T = 28.85°$C.

Table 4.2: Biphenyl faces, growth from toluene

Face (001)			
Parameter		Units	Value
	h	Å	9.47
	$R = \frac{G_{001}}{G_{001}}$	-	1
[010] PBC	a_P	Å	4.06
	a_E	Å	5.63
	$\alpha_{i,i+1}$	◦	55.3
	ϕ^K	kT	0.065
[1$\bar{1}$0] PBC	a_P	Å	4.63
	a_E	Å	4.94
	$\alpha_{i,i+1}$	◦	69.5
	ϕ^K	kT	0.204
[110] PBC	a_P	Å	4.63
	a_E	Å	4.94
	$\alpha_{i,i+1}$	◦	55.3
	ϕ^K	kT	0.204

Face (110)			
Parameter		Units	Value
	h	Å	4.62
($\sigma = 0.006$)	$R = \frac{G_{110}}{G_{001}}$	-	3.2
($\sigma = 0.007$)	$R = \frac{G_{110}}{G_{001}}$	-	15
	σ_{2D}	-	0.005
	$\sigma_{n_C=10}$	-	0.1
[001] PBC	a_P	Å	4.93
	a_E	Å	9.51
	$\alpha_{i,i+1}$	◦	28.3
	ϕ^K	kT	0.021
[$\bar{1}$1$\bar{2}$] PBC	a_P	Å	4.51
	a_E	Å	10.4
	$\alpha_{i,i+1}$	◦	65.9
	ϕ^K	kT	0.093
[1$\bar{1}$0] PBC	a_P	Å	9.48
	a_E	Å	4.94
	$\alpha_{i,i+1}$	◦	85.8
	ϕ^K	kT	0.204

4.A.2 Adipic Acid

The lattice energy of adipic acid (CSD code ADIPAC [80]) is calculated to be 31.9 kcal/mol. The sublimation enthalpy has been reported [97] as 30.8 kcal/mol for $T = 298 - 353$ K, which corresponds to a difference of ~ 2 RT from the lattice energy.

Sublimation Growth

Table 4.3 contains the relevant mechanistic parameters for the (011) and (100) faces of adipic acid under sublimation growth. Crystal growth was modeled at $T = 433$ K, corresponding to the crystals grown by sublimation at $T \sim 160$°C.

Table 4.3: Adipic acid faces, sublimation growth

Face (011)			
Parameter		Units	Value
	h	Å	4.13
	$R = \frac{G_{011}}{G_{011}}$	-	1
[100] PBC	a_P	Å	4.30
	a_E	Å	10.0
	$\alpha_{i,i+1}$	°	49.6
	ϕ^K	kT	5.53
[0$\bar{1}$1] PBC	a_P	Å	7.62
	a_E	Å	5.65
	$\alpha_{i,i+1}$	°	130.4
	ϕ^K	kT	2.60

Face (100)			
Parameter		Units	Value
	h	Å	6.86
	$R = \frac{G_{100}}{G_{011}}$	-	14.0
[0$\bar{1}\bar{1}$] PBC	a_P	Å	4.58
	a_E	Å	5.65
	$\alpha_{i,i+1}$	°	54.2
	ϕ^K	kT	2.60
[0$\bar{1}$1] PBC	a_P	Å	4.58
	a_E	Å	5.65
	$\alpha_{i,i+1}$	°	125.8
	ϕ^K	kT	2.60

Growth from Water

Table 4.4 contains the relevant mechanistic parameters for the (100), (011), (11$\bar{1}$) and (10$\bar{2}$) faces of adipic acid when grown from water. Crystal growth was modeled at $T = 307$ K, corresponding to experimentally reported [83] crystals grown from water at $T = 34$°C.

Table 4.4: Adipic acid faces, grown from water

Face (100)			
Parameter		Units	Value
	h	Å	6.86
	$R = \frac{G_{100}}{G_{100}}$	-	1
[010] PBC	a_P	Å	5.03
	a_E	Å	5.15
	$\alpha_{i,i+1}$	°	62.9
	ϕ^K	kT	5.19
$[0\bar{1}\bar{1}]$ PBC	a_P	Å	4.58
	a_E	Å	5.65
	$\alpha_{i,i+1}$	°	54.2
	ϕ^K	kT	5.63
$[0\bar{1}1]$ PBC	a_P	Å	4.58
	a_E	Å	5.65
	$\alpha_{i,i+1}$	°	62.9
	ϕ^K	kT	5.63

Face $(10\bar{2})$			
Parameter		Units	Value
	h	Å	4.78
	$R = \frac{G_{10\bar{2}}}{G_{100}}$	-	2.46
[010] PBC	a_P	Å	7.22
	a_E	Å	5.15
	$\alpha_{i,i+1}$	°	70.4
	ϕ^K	kT	5.19
$[\bar{2}\bar{1}\bar{1}]$ PBC	a_P	Å	4.85
	a_E	Å	7.67
	$\alpha_{i,i+1}$	°	39.2
	ϕ^K	kT	3.86
$[2\bar{1}1]$ PBC	a_P	Å	4.85
	a_E	Å	7.67
	$\alpha_{i,i+1}$	°	70.4
	ϕ^K	kT	3.86

Face $(11\bar{1})$			
Parameter		Units	Value
	h	Å	4.51
	$R = \frac{G_{11\bar{1}}}{G_{100}}$	-	1.89
$[0\bar{1}\bar{1}]$ PBC	a_P	Å	6.97
	a_E	Å	5.65
	$\alpha_{i,i+1}$	°	114.6
	ϕ^K	kT	5.63
$[2\bar{1}1]$ PBC	a_P	Å	5.14
	a_E	Å	7.67
	$\alpha_{i,i+1}$	°	65.4
	ϕ^K	kT	3.86

Face (011)			
Parameter		Units	Value
	h	Å	4.13
	$R = \frac{G_{011}}{G_{100}}$	-	1.79
$[0\bar{1}1]$ PBC	a_P	Å	7.62
	a_E	Å	5.65
	$\alpha_{i,i+1}$	°	96.3
	ϕ^K	kT	5.63
$[2\bar{1}1]$ PBC	a_P	Å	5.62
	a_E	Å	7.67
	$\alpha_{i,i+1}$	°	83.7
	ϕ^K	kT	3.86

4.A.3 Pentaerythritol

The lattice energy of pentaerythritol (CSD code PERYTO04 [85]) is calculated to be 44.1 kcal/mol. The sublimation enthalpy has been reported [98] as 38.5 kcal/mol for $T = 418 - 455$ K, which corresponds to a difference of ~ 6 RT from the lattice energy.

Sublimation Growth

Table 4.5 contains the relevant mechanistic parameters for the (002), (101) and $(10\bar{1})$ faces of pentaerythritol under sublimation growth. Crystal growth was modeled at $T =$ 413 K, corresponding to the crystals grown by sublimation at $T \sim 140°$C.

Growth from Water

Table 4.6 contains the relevant mechanistic parameters for the (101), $(10\bar{1})$ and (110) faces of pentaerythritol when grown from water. Crystal growth was modeled at $T =$ 313 K (within the range of typical experimentally reported [87, 89] temperatures for pentaerythritol grown from water).

Table 4.5: Pentaerythritol faces, sublimation growth

Face (002)			
Parameter		Units	Value
	h	Å	4.38
	$R = \frac{G_{002}}{G_{002}}$	-	1
[100] PBC	a_P	Å	6.09
	a_E	Å	6.09
	$\alpha_{i,i+1}$	°	90
	ϕ^K	kT	7.85
[010] PBC	a_P	Å	6.09
	a_E	Å	6.09
	$\alpha_{i,i+1}$	°	90
	ϕ^K	kT	7.85

Face (101)			
Parameter		Units	Value
	h	Å	5.00
	$R = \frac{G_{101}}{G_{002}}$	-	9.34
[0$\bar{1}$0] PBC	a_P	Å	5.33
	a_E	Å	6.09
	$\alpha_{i,i+1}$	°	60.3
	ϕ^K	kT	7.85
[1$\bar{1}\bar{1}$] PBC	a_P	Å	5.29
	a_E	Å	6.14
	$\alpha_{i,i+1}$	°	59.4
	ϕ^K	kT	1.88
[$\bar{1}\bar{1}$1] PBC	a_P	Å	5.29
	a_E	Å	6.14
	$\alpha_{i,i+1}$	°	60.3
	ϕ^K	kT	1.88

Face (10$\bar{1}$)			
Parameter		Units	Value
	h	Å	5.00
	$R = \frac{G_{10\bar{1}}}{G_{002}}$	-	9.34
[0$\bar{1}$0] PBC	a_P	Å	5.33
	a_E	Å	6.09
	$\alpha_{i,i+1}$	°	60.3
	ϕ^K	kT	7.85
[111] PBC	a_P	Å	5.29
	a_E	Å	6.14
	$\alpha_{i,i+1}$	°	59.4
	ϕ^K	kT	1.88
[1$\bar{1}$1] PBC	a_P	Å	5.29
	a_E	Å	6.14
	$\alpha_{i,i+1}$	°	60.3
	ϕ^K	kT	1.88

Table 4.6: Pentaerythritol faces, growth from water

Face (101)			
Parameter		Units	Value
	h	Å	5.00
	$R = \frac{G_{101}}{G_{101}}$	-	1
$[1\bar{1}\bar{1}]$ PBC	a_P	Å	5.29
	a_E	Å	6.14
	$\alpha_{i,i+1}$	°	59.4
	ϕ^K	kT	4.36
$[\bar{1}\bar{1}1]$ PBC	a_P	Å	5.29
	a_E	Å	6.14
	$\alpha_{i,i+1}$	°	120.6
	ϕ^K	kT	4.36

Face $(10\bar{1})$			
Parameter		Units	Value
	h	Å	5.00
	$R = \frac{G_{10\bar{1}}}{G_{101}}$	-	1
[111] PBC	a_P	Å	5.29
	a_E	Å	6.14
	$\alpha_{i,i+1}$	°	59.4
	ϕ^K	kT	4.36
$[1\bar{1}1]$ PBC	a_P	Å	5.29
	a_E	Å	6.14
	$\alpha_{i,i+1}$	°	120.6
	ϕ^K	kT	4.36

Face (110)			
Parameter		Units	Value
	h	Å	4.30
$(\sigma < 0.15)$	$R = \frac{G_{110}}{G_{101}}$	-	0.86
$(\sigma = 0.18)$	$R = \frac{G_{110}}{G_{101}}$	-	1.87
	σ_{2D}	-	0.15
	$\sigma_{n_C=10}$	-	0.61
$[1\bar{1}\bar{1}]$ PBC	a_P	Å	6.14
	a_E	Å	6.14
	$\alpha_{i,i+1}$	°	89.0
	ϕ^K	kT	4.36
$[1\bar{1}1]$ PBC	a_P	Å	6.14
	a_E	Å	6.14
	$\alpha_{i,i+1}$	°	91.0
	ϕ^K	kT	4.36

4.A.4 Naphthalene

The lattice energy of naphthalene (CSD code NAPHTA10 [91]) is calculated to be 18.5 kcal/mol. The sublimation enthalpy has been reported [99] as 18.2 kcal/mol for $T = 328 - 398$ K, which corresponds to a difference of ~ 0.5 RT from the lattice energy.

Sublimation Growth

Table 4.7 contains the relevant mechanistic parameters for the (001), $(11\bar{1})$, (110) and $(20\bar{1})$ faces of naphthalene under sublimation growth. Crystal growth was modeled at $T = 283$ K, corresponding to the growth temperature of experimentally reported [92] sublimation-grown crystals.

Growth from Ethanol

Tables 4.8 and 4.9 contains the relevant mechanistic parameters for the (001), $(11\bar{1})$, (110) and $(20\bar{1})$ faces of naphthalene when grown from ethanol. Crystal growth was modeled at $T = 291$ K, corresponding to the experimentally reported [92] crystals grown from ethanol.

Growth from Cyclohexane

Tables 4.10 and 4.11 contains the relevant mechanistic parameters for the (001), (110) and $(20\bar{1})$ faces of naphthalene when grown from cyclohexane. Crystal growth was modeled at $T = 290$ K, corresponding to the experimentally reported [92] crystals grown from cyclohexane.

Table 4.7: Naphthalene faces, sublimation growth

Face (001)			
Parameter		Units	Value
	h	Å	7.24
	$R = \frac{G_{001}}{G_{001}}$	-	1
$[\bar{1}10]$ PBC	a_P	Å	4.83
	a_E	Å	5.08
	$\alpha_{i,i+1}$	°	72.1
	ϕ^K	kT	3.85
[110] PBC	a_P	Å	4.83
	a_E	Å	5.08
	$\alpha_{i,i+1}$	°	107.9
	ϕ^K	kT	3.85

Face (110)			
Parameter		Units	Value
	h	Å	4.50
	$R = \frac{G_{110}}{G_{001}}$	-	2.89
$[\bar{1}1\bar{2}]$ PBC	a_P	Å	5.02
	a_E	Å	7.86
	$\alpha_{i,i+1}$	°	81.1
	ϕ^K	kT	1.27
$[\bar{1}10]$ PBC	a_P	Å	7.77
	a_E	Å	5.08
	$\alpha_{i,i+1}$	°	98.9
	ϕ^K	kT	3.85

Face $(11\bar{1})$			
Parameter		Units	Value
	h	Å	4.65
	$R = \frac{G_{11\bar{1}}}{G_{001}}$	-	2.98
$[\bar{1}10]$ PBC	a_P	Å	7.52
	a_E	Å	5.08
	$\alpha_{i,i+1}$	°	73.0
	ϕ^K	kT	3.85
$[\bar{1}\bar{1}\bar{2}]$ PBC	a_P	Å	4.86
	a_E	Å	7.86
	$\alpha_{i,i+1}$	°	107.0
	ϕ^K	kT	1.27

Face $(20\bar{1})$			
Parameter		Units	Value
	h	Å	4.09
	$R = \frac{G_{20\bar{1}}}{G_{001}}$	-	3.84
[010] PBC	a_P	Å	7.27
	a_E	Å	5.97
	$\alpha_{i,i+1}$	°	67.7
	ϕ^K	kT	2.99
$[\bar{1}\bar{1}\bar{2}]$ PBC	a_P	Å	5.53
	a_E	Å	7.86
	$\alpha_{i,i+1}$	°	44.6
	ϕ^K	kT	1.27
$[\bar{1}1\bar{2}]$ PBC	a_P	Å	5.53
	a_E	Å	7.86
	$\alpha_{i,i+1}$	°	67.7
	ϕ^K	kT	1.27

Table 4.8: Naphthalene faces, grown from ethanol

Face (001)			
Parameter		Units	Value
	h	Å	7.24
	$R = \frac{G_{001}}{G_{001}}$	-	1
[010] PBC	a_P	Å	4.11
	a_E	Å	5.97
	$\alpha_{i,i+1}$	°	54.0
	ϕ^K	kT	0.75
[$\bar{1}$10] PBC	a_P	Å	4.83
	a_E	Å	5.08
	$\alpha_{i,i+1}$	°	72.1
	ϕ^K	kT	1.00
[110] PBC	a_P	Å	4.83
	a_E	Å	5.08
	$\alpha_{i,i+1}$	°	54.0
	ϕ^K	kT	1.00

Face (20$\bar{1}$)			
Parameter		Units	Value
($\sigma < 0.36$)	h	Å	4.09
	$R = \frac{G_{20\bar{1}}}{G_{001}}$	-	1.24
	σ_{2D}	-	0.36
	$\sigma_{n_C=10}$	-	0.70
[010] PBC	a_P	Å	7.27
	a_E	Å	5.97
	$\alpha_{i,i+1}$	°	67.7
	ϕ^K	kT	0.75
[$\bar{1}\bar{1}\bar{2}$] PBC	a_P	Å	5.53
	a_E	Å	7.86
	$\alpha_{i,i+1}$	°	44.6
	ϕ^K	kT	0.31
[$\bar{1}$1$\bar{2}$] PBC	a_P	Å	5.53
	a_E	Å	7.86
	$\alpha_{i,i+1}$	°	67.7
	ϕ^K	kT	0.31

Table 4.9: Naphthalene faces, grown from ethanol (continued)

Face (110)			
Parameter		Units	Value
	h	Å	4.50
$(\sigma < 0.30)$	$R = \frac{G_{110}}{G_{001}}$	-	1.18
$(\sigma = 0.35)$	$R = \frac{G_{110}}{G_{001}}$	-	1.56
	σ_{2D}	-	0.30
	$\sigma_{n_C=10}$	-	0.67
[001] PBC	a_P	Å	4.55
	a_E	Å	8.67
	$\alpha_{i,i+1}$	◦	35.3
	ϕ^K	kT	0.26
$[\bar{1}1\bar{2}]$ PBC	a_P	Å	5.02
	a_E	Å	7.86
	$\alpha_{i,i+1}$	◦	81.1
	ϕ^K	kT	0.31
$[\bar{1}10]$ PBC	a_P	Å	7.77
	a_E	Å	5.08
	$\alpha_{i,i+1}$	◦	63.6
	ϕ^K	kT	1.00

Face $(11\bar{1})$			
Parameter		Units	Value
	h	Å	4.65
$(\sigma < 0.13)$	$R = \frac{G_{11\bar{1}}}{G_{001}}$	-	1.13
$(\sigma = 0.16)$	$R = \frac{G_{11\bar{1}}}{G_{001}}$	-	2.10
$(\sigma = 0.35)$	$R = \frac{G_{11\bar{1}}}{G_{001}}$	-	5.64
	σ_{2D}	-	0.13
	$\sigma_{n_C=10}$	-	0.49
[101] PBC	a_P	Å	4.76
	a_E	Å	8.02
	$\alpha_{i,i+1}$	◦	69.7
	ϕ^K	kT	0.37
$[\bar{1}10]$ PBC	a_P	Å	7.52
	a_E	Å	5.08
	$\alpha_{i,i+1}$	◦	73.0
	ϕ^K	kT	1.00
$[\bar{1}\bar{1}\bar{2}]$ PBC	a_P	Å	4.86
	a_E	Å	7.86
	$\alpha_{i,i+1}$	◦	37.3
	ϕ^K	kT	0.31

Table 4.10: Naphthalene faces, grown from cyclohexane

Face (001)			
Parameter		Units	Value
	h	Å	7.24
	$R = \frac{G_{001}}{G_{001}}$	-	1
	σ_{2D}	-	n/a
	$\sigma_{n_C=10}$	-	0.96
[010] PBC	a_P	Å	4.11
	a_E	Å	5.97
	$\alpha_{i,i+1}$	°	54.0
	ϕ^K	kT	0.11
[$\bar{1}$10] PBC	a_P	Å	4.83
	a_E	Å	5.08
	$\alpha_{i,i+1}$	°	72.1
	ϕ^K	kT	0.20
[110] PBC	a_P	Å	4.83
	a_E	Å	5.08
	$\alpha_{i,i+1}$	°	54.0
	ϕ^K	kT	0.20

Face (20$\bar{1}$)			
Parameter		Units	Value
	h	Å	4.09
($\sigma < 0.011$)	$R = \frac{G_{20\bar{1}}}{G_{001}}$	-	2.32
	σ_{2D}	-	0.011
	$\sigma_{n_C=10}$	-	0.13
[010] PBC	a_P	Å	7.27
	a_E	Å	5.97
	$\alpha_{i,i+1}$	°	67.7
	ϕ^K	kT	0.11
[$\bar{1}\bar{1}\bar{2}$] PBC	a_P	Å	5.53
	a_E	Å	7.86
	$\alpha_{i,i+1}$	°	44.6
	ϕ^K	kT	0.01
[$\bar{1}$1$\bar{2}$] PBC	a_P	Å	5.53
	a_E	Å	7.86
	$\alpha_{i,i+1}$	°	67.7
	ϕ^K	kT	0.01

Table 4.11: Naphthalene faces, grown from cyclohexane (continued)

Face (110)			
Parameter		Units	Value
	h	Å	4.50
$(\sigma = 0.0061)$	$R = \frac{G_{110}}{G_{001}}$	-	2.13
$(\sigma = 0.0070)$	$R = \frac{G_{110}}{G_{001}}$	-	3.83
$(\sigma = 0.0082)$	$R = \frac{G_{110}}{G_{001}}$	-	18.3
	σ_{2D}	-	0.0055
	$\sigma_{n_C=10}$	-	0.11
[001] PBC	a_P	Å	4.55
	a_E	Å	8.67
	$\alpha_{i,i+1}$	◦	35.3
	ϕ^K	kT	0.03
$[\bar{1}1\bar{2}]$ PBC	a_P	Å	5.02
	a_E	Å	7.86
	$\alpha_{i,i+1}$	◦	81.1
	ϕ^K	kT	0.01
$[\bar{1}10]$ PBC	a_P	Å	7.77
	a_E	Å	5.08
	$\alpha_{i,i+1}$	◦	63.6
	ϕ^K	kT	0.20

Bibliography

[1] P. Dandekar and M. F. Doherty. A mechanistic growth model for inorganic crystals: Solid-state interactions. *AIChE J*, 60(11):3707–3719, 2014.

[2] P. Dandekar. *Modeling Solution Growth of Inorganic Crystals*. PhD thesis, University of California, Santa Barbara, 2014.

[3] D. Winn and M. F. Doherty. A new technique for predicting the shape of solution-grown organic crystals. *AIChE J*, 44(11):2501–2514, 1998.

[4] D. Winn and M. F. Doherty. Predicting the shape of organic crystals grown from polar solvents. *Chem. Eng. Sci.*, 57(10):1805 – 1813, 2002.

[5] R. C. Snyder and M. F. Doherty. Predicting crystal growth by spiral motion. *Proc. R. Soc. London, Ser. A*, 465(2104):1145–1171, 2009.

[6] M. A. Lovette and M. F. Doherty. Needle-shaped crystals: Causality and solvent selection guidance based on periodic bond chains. *Cryst. Growth Des.*, 13(8):3341–3352, 2013.

[7] J. D. Dunitz and A. Gavezzotti. Molecular recognition in organic crystals: directed intermolecular bonds or nonlocalized bonding? *Angew. Chem., Int. Ed.*, 44(12):1766–1787, 2005.

[8] J. D. Dunitz and A. Gavezzotti. How molecules stick together in organic crystals: weak intermolecular interactions. *Chem. Soc. Rev.*, 38(9):2622–2633, 2009.

[9] J. N. Israelachvili. *Intermolecular and surface forces: revised third edition*. Academic press, 2011.

[10] F. M. Fowkes. Quantitative characterization of the acid-base properties of solvents, polymers, and inorganic surfaces. *J. Adhes. Sci. Technol.*, 4(1):669–691, 1990.

[11] C. van Oss, R. Good, and M. Chaudhury. Additive and nonadditive surface tension components and the interpretation of contact angles. *Langmuir*, 4(4):884–891, 1988.

[12] J. Hildebrand and R. Scott. *The solubility of nonelectrolytes*. Reinhold Publishing Corporation, 3 edition, 1950.

[13] J. H. Hildebrand and R. L. Scott. *Regular solutions*. Prentice-Hall, 1962.

[14] J. L. Gardon. Critical review of concepts common to cohesive energy density, surface tension, tensile strength, heat of mixing, interfacial tension, and butt joint strength. *J. Colloid Interface Sci.*, 59(3):582–596, 1977.

[15] A. F. M. Barton. Solubility parameters. *Chem. Rev.*, 75(6):731–753, 1975.

[16] A. F. Barton. *CRC handbook of solubility parameters and other cohesion parameters*. CRC press, 1991.

[17] C. M. Hansen. The universality of the solubility parameter. *Ind. Eng. Chem. Prod. Res. Dev.*, 8(1):2–11, 1969.

[18] C. M. Hansen. *Hansen solubility parameters: a user's handbook*. CRC press, 2007.

[19] H. Burrell. The challenge of the solubility parameter concept. *J. Paint Technol.*, 40(520):197–208, 1968.

[20] A. Beerbower. Surface free energy: a new relationship to bulk energies. *J. Colloid Interface Sci.*, 35(1):126–132, 1971.

[21] J. Panzer. Components of solid surface free energy from wetting measurements. *J. Colloid Interface Sci.*, 44(1):142–161, 1973.

[22] D. H. Kaelble. *Physical Chemistry of Adhesion*. New Jersey: Wiley-Interscience,, 1971.

[23] A. Gavezzotti. Efficient computer modeling of organic materials. The atom–atom, Coulomb–London–Pauli (AA-CLP) model for intermolecular electrostatic-polarization, dispersion and repulsion energies. *New J Chem*, 35(7):1360–1368, 2011.

[24] A. Gavezzotti. Calculation of intermolecular interaction energies by direct numerical integration over electron densities. 2. an improved polarization model and the evaluation of dispersion and repulsion energies. *J. Phys. Chem. B*, 107(10):2344–2353, 2003.

[25] A. Gavezzotti. Non-conventional bonding between organic molecules. the 'halogen bond' in crystalline systems. *Mol. Phys.*, 106(12-13):1473–1485, 2008.

[26] A. Stone. The theory of intermolecular forces, international series of monographs on chemistry vol. 32. Clarendon Press, Oxford, 1996.

[27] A. Gavezzotti. Structure and energy in organic crystals with two molecules in the asymmetric unit: causality or chance? *CrystEngComm*, 10(4):389–398, 2008.

[28] M. Frisch, G. Trucks, H. Schlegel, G. Scuseria, M. Robb, J. Cheeseman, G. Scalmani, V. Barone, B. Mennucci, G. Petersson, H. Nakatsuji, M. Caricato, X. Li, H. Hratchian, A. Izmaylov, J. Bloino, G. Zheng, J. Sonnenberg, M. Hada, M. Ehara, K. Toyota, R. Fukuda, J. Hasegawa, M. Ishida, T. Nakajima, Y. Honda, O. Kitao, H. Nakai, T. Vreven, J. M. Jr., J. Peralta, F. Ogliaro, M. Bearpark, J. Heyd, E. Brothers, K. Kudin, V. Staroverov, R. Kobayashi, J. Normand, K. Raghavachari, A. Rendell, J. Burant, S. Iyengar, J. Tomasi, M. Cossi, N. Rega, J. Millam, M. Klene, J. Knox, J. Cross, V. Bakken, C. Adamo, J. Jaramillo, R. Gomperts, R. Stratmann,

O. Yazyev, A. Austin, R. Cammi, C. Pomelli, J. Ochterski, R. Martin, K. Morokuma, V. Zakrzewski, G. Voth, P. Salvador, J. Dannenberg, S. Dapprich, A. Daniels, O. Farkas, J. Foresman, J. Ortiz, J. Cioslowski, and D. Fox. Gaussian 09, revision a. 02; gaussian, inc. *Wallingford, CT*, 19:227–238, 2009.

[29] A. J. Pertsin and A. I. Kitaigorodsky. *The atom-atom potential method*. Springer, 1987.

[30] L. Maschio, B. Civalleri, P. Ugliengo, and A. Gavezzotti. Intermolecular interaction energies in molecular crystals: comparison and agreement of localized møller–plesset 2, dispersion-corrected density functional, and classical empirical two-body calculations. *J. Phys. Chem. A*, 115(41):11179–11186, 2011.

[31] D. Berthelot. Sur le mélange des gaz. *Compt. Rendus*, 126:1703–1706, 1898.

[32] L. Girifalco and R. Good. A theory for the estimation of surface and interfacial energies. i. derivation and application to interfacial tension. *J. Phys. Chem.*, 61(7):904–909, 1957.

[33] F. M. Etzler. Surface free energy of solids: a comparison of models. In K. Mittal, editor, *Contact angle, wettability and adhesion*, volume 4, pages 215–236. VSP: Ultrecht, The Netherlands, 2006.

[34] D. K. Owens and R. Wendt. Estimation of the surface free energy of polymers. *J. Appl. Polym. Sci.*, 13(8):1741–1747, 1969.

[35] F. Etzler. Characterization of surface free energies and surface chemistry of solids. In K. Mittal, editor, *Contact angle, wettability and adhesion*, volume 3, pages 219–264. VSP: Ultrecht, The Netherlands, 2003.

[36] F. M. Fowkes. Attractive forces at interfaces. *Ind. Eng. Chem.*, 56(12):40–52, 1964.

[37] F. M. Fowkes, F. L. Riddle, W. E. Pastore, and A. A. Weber. Interfacial interactions between self-associated polar liquids and squalane used to test equations for solid-liquid interfacial interactions. *Colloids Surf.*, 43(2):367–387, 1990.

[38] S. Wu. Polar and nonpolar interactions in adhesion. *J. Adhes.*, 5(1):39–55, 1973.

[39] S. Wu. Calculation of interfacial tension in polymer systems. *J. Polym. Sci., Part C: Polym. Symp.*, 34(1):19–30, 1971.

[40] F. M. Fowkes. Role of acid-base interfacial bonding in adhesion. *J. Adhes. Sci. Technol.*, 1(1):7–27, 1987.

[41] F. M. Fowkes and M. A. Mostafa. Acid-base interactions in polymer adsorption. *Ind. Eng. Chem. Prod. Res. Dev.*, 17(1):3–7, 1978.

[42] M. D. Vrbanac and J. C. Berg. The use of wetting measurements in the assessment of acid-base interactions at solid-liquid interfaces. *J. Adhes. Sci. Technol.*, 4(1):255–266, 1990.

[43] V. Gutmann. Empirical parameters for donor and acceptor properties of solvents. *Electrochim. Acta*, 21(9):661–670, 1976.

[44] R. S. Drago, N. Wong, and D. C. Ferris. The e, c, t interpretation of bond dissociation energies and anion-neutral molecule interactions. *J. Am. Chem. Soc.*, 113(6):1970–1977, 1991.

[45] G. C. Vogel and R. S. Drago. The ecw model. *J. Chem. Educ.*, 73(8):701, 1996.

[46] R. S. Drago, A. P. Dadmun, and G. C. Vogel. Addition of new donors to the e and c model. *Inorg. Chem.*, 32(11):2473–2479, 1993.

[47] R. S. Drago. *Applications of Electrostatic-Covalent Models in Chemistry*. Surfside Scientific Publishers, 1994.

[48] C. J. van Oss, M. K. Chaudhury, and R. J. Good. Monopolar surfaces. *Adv Colloid Interface Sci*, 28:35–64, 1987.

[49] C. J. van Oss, M. K. Chaudhury, and R. J. Good. Interfacial lifshitz-van der waals and polar interactions in macroscopic systems. *Chem. Rev.*, 88(6):927–941, 1988.

[50] A. Holländer. On the selection of test liquids for the evaluation of acid-base properties of solid surfaces by contact angle goniometry. *J. Colloid Interface Sci.*, 169(2):493–496, 1995.

[51] C. J. van Oss. *Interfacial forces in aqueous media*. CRC press, 2006.

[52] C. Della Volpe and S. Siboni. Troubleshooting of surface free energy acid-base theory applied to solid surfaces: The case of good, van oss and chaudhury theory. In K. Mittal, editor, *Acid-Base Interactions: Relevance to Adhesion Science and Technology*, volume 2, pages 55–91. VSP: Ultrecht, The Netherlands, 2000.

[53] C. Della Volpe, D. Maniglio, M. Brugnara, S. Siboni, and M. Morra. The solid surface free energy calculation: I. in defense of the multicomponent approach. *J. Colloid Interface Sci.*, 271(2):434 – 453, 2004.

[54] S. Siboni and C. D. Volpe. Acid-base theory of adhesion: A critical review. *Rev. Adhes. Adhes.*, 3(3):253–310, 2015.

[55] C. van Oss. Irrelevance of the ratio of the electron-accepticity to the electron donicity of water with respect to the determination of polar surface tension components, interfacial tensions and free energies of interaction of liquids and/or solids. In K. Mittal, editor, *Acid-Base Interactions: Relevance to Adhesion Science and Technology*, volume 2, pages 181–186. VSP: Ultrecht, The Netherlands, 2000.

[56] C. Della Volpe and S. Siboni. Acid-base surface free energies of solids and the definition of scales in the good-van oss-chaudhury theory. *J. Adhes. Sci. Technol.*, 14(2):235–272, 2000.

[57] J. Y. Heng, A. Bismarck, A. F. Lee, K. Wilson, and D. R. Williams. Anisotropic surface chemistry of aspirin crystals. *J. Pharm. Sci.*, 96(8):2134–2144, 2007.

[58] R. Ho and J. Y. Heng. A review of inverse gas chromatography and its development as a tool to characterize anisotropic surface properties of pharmaceutical solids. *KONA Powder Part. J.*, 30(0):164–180, 2013.

[59] A. E. Jefferson, D. R. Williams, and J. Y. Heng. Computing the surface energy distributions of heterogeneous crystalline powders. *J. Adhes. Sci. Technol.*, 25(4-5):339–355, 2011.

[60] R. R. Smith, D. R. Williams, D. J. Burnett, and J. Y. Y. Heng. A new method to determine dispersive surface energy site distributions by inverse gas chromatography. *Langmuir*, 30(27):8029–8035, 2014. PMID: 24946213.

[61] F. Chen and W. Chang. Applicability study of a new acid base interaction model in polypeptides and polyamides. *Langmuir*, 7(10):2401–2404, 1991.

[62] W. Chang and X. Qin. "repulsive acid-base interactions": Fantasy or reality. In K. Mittal, editor, *Acid-Base Interactions: Relevance to Adhesion Science and Technology*, volume 2, pages 3–53. VSP: Ultrecht, The Netherlands, 2000.

[63] I. Peterson. Towards a theory of adhesion with predictive power. *Surf. Coat. Int., Part B*, 88(1):1–8, 2005.

[64] M. Żenkiewicz. Methods for the calculation of surface free energy of solids. *J. Achieve. Mater. Manuf. Eng.*, 24(1):137–145, 2007.

[65] J. Lyklema. The surface tension of pure liquids: Thermodynamic components and corresponding states. *Colloids Surf., A*, 156(1):413–421, 1999.

[66] W. K. Burton, N. Cabrera, and F. C. Frank. The growth of crystals and the equilibrium structure of their surfaces. *Philos. Trans. R. Soc., A*, 243:299–358, 1951.

[67] D. Elwell and H. J. Scheel. *Crystal Growth from High-Temperature Solutions*. London: Academic Press,, 1975.

[68] J. A. Dirksen and T. A. Ring. Fundamentals of crystallization: Kinetic effects on particle size distributions and morphology. *Chem Eng Sci*, 46(10):2389–2427, 1991.

[69] P. Hartman and W. G. Perdok. On the relations between structure and morphology of crystals. I. *Acta Crystallogr.*, 1955.

[70] P. Hartman and W. G. Perdok. On the relations between structure and morphology of crystals. II. *Acta Crystallogr*, 1955.

[71] P. Hartman and W. Perdok. On the relations between structure and morphology of crystals. III. *Acta Crystallogr.*, 8(9):525–529, 1955.

[72] H. Cuppen, H. Meekes, W. van Enckevort, E. Vlieg, and H. Knops. Nonequilibrium free energy and kinetic roughening of steps on the kossel (001) surface. *Phys. Rev. B: Condens. Matter Mater. Phys.*, 69(24):245404, 2004.

[73] P. Bennema and H. Meekes. Two centuries of morphology of crystals: integration of principles of mathematical crystallography, statistical mechanics of surface models and chemistry. In X. Y. Lui and J. J. De Yoreo, editors, *Nanoscale Structure and Assembly at Solid-Fluid Interfaces*, volume Volume I: Interfacial Structures versus Dynamics, pages 177–208. Kluwer Academic, Boston, 2004.

[74] L. Onsager. Crystal statistics. I. A two-dimensional model with an order-disorder transition. *Physical Review*, 65(3-4):117–149, 1944.

[75] B. Lee and F. Richards. The interpretation of protein structures: Estimation of static accessibility. *J. Mol. Biol.*, 55(3):379 – IN4, 1971.

[76] A. Shrake and J. Rupley. Environment and exposure to solvent of protein atoms. lysozyme and insulin. *J. Mol. Biol.*, 79(2):351 – 371, 1973.

[77] C. F. Macrae, P. R. Edgington, P. McCabe, E. Pidcock, G. P. Shields, R. Taylor, M. Towler, and J. van de Streek. Mercury: visualization and analysis of crystal structures. *Journal of Applied Crystallography*, 39(3):453–457, 2006.

[78] G. P. Charbonneau and Y. Delugeard. Biphenyl: three-dimensional data and new refinement at 293 k. *Acta Crystallogr., Sect. B: Struct. Crystallogr. Cryst. Chem.*, 1977.

[79] L. Jetten, H. Human, P. Bennema, and J. Van der Eerden. On the observation of the roughening transition of organic crystals, growing from solution. *J. Cryst. Growth*, 68(2):503–516, 1984.

[80] J. Housty and M. Hospital. Localisation des atomes d'hydrogène dans l'acide adipique $COOH[CH_2]_4COOH$. *Acta Crystallogr.*, 1965.

[81] R. S. Gopalan, P. Kumaradhas, and G. Kulkarni. Structural phase transition in adipic acid. *J. Solid State Chem.*, 148(1):129 – 134, 1999.

[82] S. Bhattacharya, V. G. Saraswatula, and B. K. Saha. Thermal expansion in alkane diacids - another property showing alternation in an odd-even series. *Cryst. Growth Des.*, 13(8):3651–3656, 2013.

[83] R. J. Davey, S. N. Black, D. Logan, S. J. Maginn, J. E. Fairbrother, and D. J. W. Grant. Structural and kinetic features of crystal growth inhibition: adipic acid growing in the presence of n-alkanoic acids. *J. Chem. Soc., Faraday Trans.*, 88:3461–3466, 1992.

[84] Y. Zhang, J. P. Sizemore, and M. F. Doherty. Shape evolution of 3-dimensional faceted crystals. *AIChE J.*, 52(5):1906–1915, 2006.

[85] D. Eilerman and R. Rudman. Refinement of pentaerythritol. *Acta Crystallogr., Sect. B: Struct. Crystallogr. Cryst. Chem.*, 1979.

[86] A. F. Wells. XXI. Crystal habit and internal structure. *Philos Mag (1798–1977)*, 37(266):184–199, 1946.

[87] A. Bernardo and M. Giulietti. Modeling of crystal growth and nucleation rates for pentaerythritol batch crystallization. *Chem. Eng. Res. Des.*, 88(10):1356–1364, 2010.

[88] J. F. Rogers and D. E. Creasy. Crystallisation of pentaerythritol. *J. Appl. Chem. Biotechnol.*, 24(3):171–180, 1974.

[89] S. Genbo, L. Zhengdong, P. Rfen, W. Dexiang, and Y. Tongqin. Growth of large crystals of pentaerythritol and trishydroxymethylaminomethone. *J. Cryst. Growth*, 119(34):368–370, 1992.

[90] M. Brunsteiner and S. L. Price. Morphologies of organic crystals: sensitivity of attachment energy predictions to the model intermolecular potential. *Cryst. Growth Des.*, 1(6):447–453, 2001.

[91] C. P. Brock and J. D. Dunitz. Temperature dependence of thermal motion in crystalline naphthalene. *Acta Crystallogr., Sect. B: Struct. Crystallogr. Cryst. Chem.*, 1982.

[92] R. F. P. Grimbergen, M. F. Reedijk, H. Meekes, and P. Bennema. Growth behavior of crystal faces containing symmetry-related connected nets: A case study of naphthalene and anthracene. *J. Phys. Chem. B*, 102(15):2646–2653, 1998.

[93] M. A. Lovette and M. F. Doherty. Predictive Modeling of Supersaturation-Dependent Crystal Shapes. *Cryst. Growth Des.*, 12(2):656–669, 2012.

[94] Z. B. Kuvadia and M. F. Doherty. Spiral growth model for faceted crystals of non-centrosymmetric organic molecules grown from solution. *Cryst. Growth Des.*, 11(7):2780–2802, 2011.

[95] M. A. Lovette and M. F. Doherty. Multisite models to determine the distribution of kink sites adjacent to low-energy edges. *Phys. Rev. E*, 2012.

[96] K. Sasse, J. N'guimbi, J. Jose, and J. C. Merlin. Tension de vapeur d'hydrocarbures polyaromatiques dans le domaine 10^{-3}-10 Torr. *Thermochim. Acta*, 146:53–61, 1989.

[97] K. C. Albyn. Extension of the enthalpy of sublimation for adipic acid to temperatures below 80 c. *J. Chem. Eng. Data*, 46(6):1415–1416, 2001.

[98] G. Barone, G. D. Gatta, D. Ferro, and V. Piacente. Enthalpies and entropies of sublimation, vaporization and fusion of nine polyhydric alcohols. *J. Chem. Soc., Faraday Trans.*, 86:75–79, 1990.

[99] J. P. Murray, K. J. Cavell, and J. O. Hill. A DSC study of benzoic acid: a suggested calibrant compound. *Thermochim. Acta*, 36(1):97–101, 1980.

Chapter 5

Modeling Step Velocities and Edge Surface Structures during Growth of Non-Centrosymmetric Crystals

Reproduced in part with permission from:

Carl J. Tilbury, Mark N. Joswiak, Baron Peters and Michael F. Doherty, "Modeling Step Velocities and Edge Surface Structures during Growth of Non-Centrosymmetric Crystals," *Crystal Growth & Design*, **2017**, *17*, 2066-2080.

DOI: 10.1021/acs.cgd.7b00058.

5.1 Introduction

As indicated in Chapter 3, under conditions of controlled crystallization the dominant faces on crystal morphologies typically grow via layered mechanisms: spiral growth or two-dimensional nucleation regimes [1, 2]. The presented mechanistic formulations for face growth rates under either of these regimes depend on the velocity of step edges on

the crystal surface. Obtaining an accurate expression for the step velocity is, therefore, vital for a successful mechanistic description of layered crystal growth.

The step velocity essentially depends on two factors: the concentration of kinks on the step (the kink density) and the net rate of growth unit incorporation into those kink sites (the kink rate) [3–9]. Kink sites on the step edge are the favorable positions for growth unit attachment and assimilation into the lattice, since no additional surfaces are created and solid-state interactions can be formed in kink, terrace, and edge directions [2, 5, 10].

Centrosymmetric growth units possess an inversion center of symmetry within the molecule. As a result, the interaction sphere around a crystal growth unit in the lattice is symmetric, which produces energetically identical sites along the step edge and provides significant simplifications to calculating kink densities, kink rates, and step velocities [3]. However, most molecules of industrial relevance are not centrosymmetric. Mechanistic models must, therefore, be extended to capture phenomena that appear for the more general non-centrosymmetric case. With no inversion center forcing equivalent opposite interactions, these growth units typically have asymmetric interaction spheres and multiple types of spheres within the lattice. We consider these distinct molecular orientations/environments as different types of growth units [3]; they are distinguishable much like the case of ionic or cocrystal growth units, although the differentiation only occurs following lattice incorporation, not in solution. The presence of different types of growth units (whether the difference is present in solution or solely in the lattice) produces various distinct kink sites on each step edge and each crystal face. These different sites commonly show anisotropic kinetics that greatly affect growth shapes; Poloni et al. [11] recently examined such growth kinetics and energies on 32 distinct kink sites on dissymmetric surfaces of a nonopioid drug candidate for chronic pain treatment. Appropriately accounting for multiple sites in kink densities, kink rates and their combination into an overall step velocity is the central complication for modeling non-centrosymmetric

crystal growth. While we consider the case of identical molecules in solution, the following models could be adapted to growth units of different chemical entities in solution by considering procedures previously developed for ionic systems [12].

Kuvadia and Doherty provided an approach [3] to modeling non-centrosymmetric molecules, which proved successful for paracetamol and lovastatin. This technique has been successfully applied by Shim and co-workers to various other crystal systems (RDX [13], L-Methionine [14] and ϵ-HNIW [15]), further supporting its utility. In this approach, Kuvadia and Doherty introduced the concept of unstable step rows (their terminology was layers), which may show dissolution behavior under conditions of overall crystal growth. Their case-by-case tactic was to consider only the dominant kink site surface structure and progression on each step edge. We expect this approach to be valid only for sufficient interaction anisotropy between rows; at less extreme differentials, the contributions of other surface structures and progressions must not be neglected. Mechanistic habit predictions require step velocities of each step edge on each face and rely on capturing their differences accurately. Thus, we require a model that is generally applicable across different degrees of anisotropy.

The focus of this chapter is to investigate step edge row instability and develop a more general step velocity model that captures the emergence of instability and its increasing effect on edge surface structures and step motion, considering both thermodynamic and kinetic contributions. We first summarize the step velocity determination for centrosymmetric growth units and then establish new phenomena that exist for non-centrosymmetric systems and present our framework to account for them. We consider in depth the specific example of an A–B step edge (alternating rows of A and B growth units), to illustrate these concepts and compare our modeling results to kinetic Monte Carlo simulations.

5.2 Centrosymmetric Step Velocities

Figure 5.1 shows an example of a centrosymmetric growth unit: adipic acid. The monoclinic form [16] does technically contain two distinct growth units (from the perspective of spatial orientation within the lattice), but due to symmetry these molecules have identical and spatially symmetric interaction environments. Figure 5.1 also shows a tetragonal form of pentaerythritol [17], which does not have an inversion center, but contains a single molecular orientation within the lattice that again shows symmetric interactions. In either case, the centrosymmetric expressions are applicable, since each molecule is in the same energetic environment.

Before introducing mechanistic expressions, it is important to clarify our definitions of surface energies (consistent with Kuvadia and Doherty [3]), since these quantities will be used throughout this chapter. Figure 5.2 indicates these definitions, which are divided into kink, edge, and terrace directions (and the reverse of each); note that in the presence of solvent all these surface energies are modified from the base solid-state interactions (Chapter 4).

For the purpose of calculating kink densities and kink rates, we require absolute values of energies, rather than surface energies. The following equations for kink (K), edge (E), and terrace (T) energies demonstrate the conversion:

$$\phi_{k,i}^{K} = \gamma_{k,i}^{K} a_{P,i} h \tag{5.1}$$

$$\phi_{k,i}^{E} = \gamma_{k,i}^{E} a_{E,i} h \tag{5.2}$$

$$\phi_{k,i}^{T} = \gamma_{k,i}^{T} a_{P,i} a_{E,i} \tag{5.3}$$

where the subscripts refer to a growth unit in single-row kink (single-kink) k on step edge i; k cycles across both rows, growth units, and kink directions (either "east" or

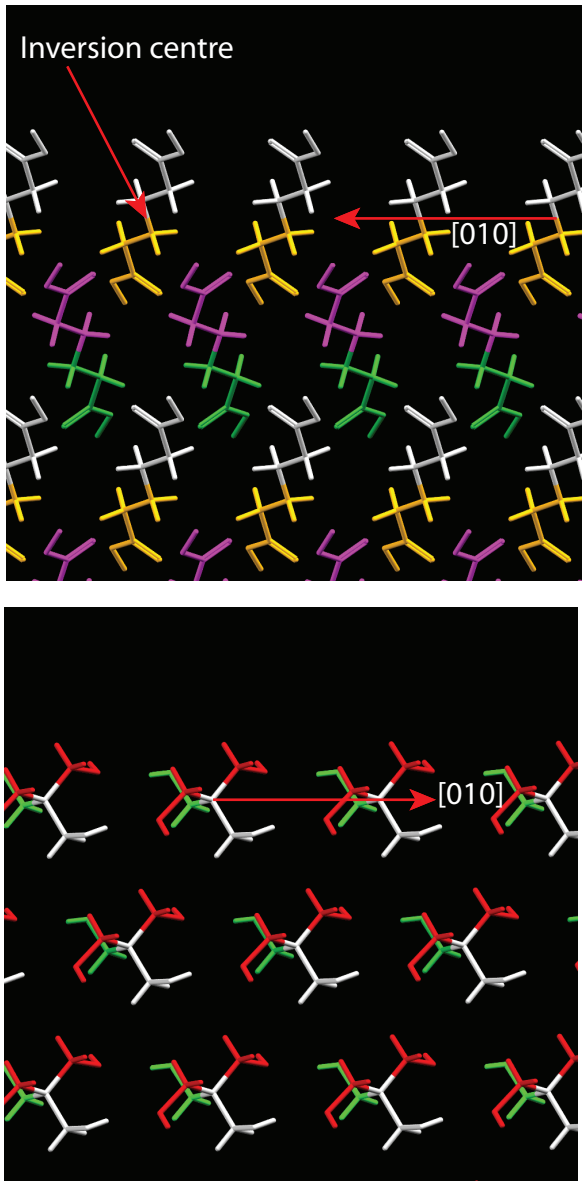

Figure 5.1: Top: A view of the [010] step on the (100) face of adipic acid (CSD code ADIPAC [16]); two growth units exist in the lattice, but both have identical and symmetric interaction environments. Bottom: A view of the [010] step on the (101) face of pentaerythritol (CSD code PERYTO04 [17]); a single growth unit exists, again with a symmetric interaction environment. Images created using Mercury [18].

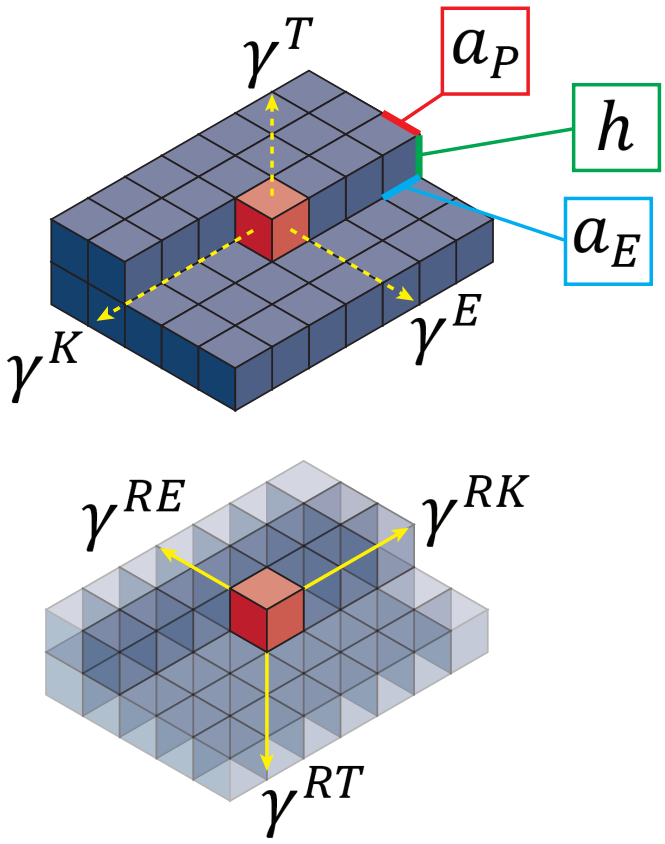

Figure 5.2: Our definitions of directional surface energies around a specific growth unit (edge and growth unit subscripts are omitted for clarity). Interactions are classified as intrarow (kink), inter-row (edge), or interslice (terrace). Note that all interactions in each class should be included, though nearest and next-nearest neighbor contributions should dominate. The orthogonal directions pictured above are merely intended as aggregate descriptors. The terrace (γ^T), edge (γ^E), and kink (γ^K) surface energies correspond to incomplete lattice interactions, while reverse terrace (γ^{RT}), reverse edge (γ^{RE}), and reverse kink (γ^{RK}) hypothetical-surface energies represent completed interactions binding the growth unit to the bulk crystal lattice. Step dimensions are also pictured: step height (h), propagation length (a_P), and growth unit width (a_E).

"west", depending on the side exposed to form a kink [19]). The sublimation surface energies are determined from half of each solid-state interaction that must be broken to form the surface (see Chapter 4). Reverse energies follow identical constructions; Figure 5.2 indicates their directions, alongside illustrations of the step height (h), propagation length ($a_{P,i}$) and growth unit width ($a_{E,i}$). For the centrosymmetric case, reverse energies are equivalent: $\phi_i^K = \phi_i^{RK}$, $\phi_i^E = \phi_i^{RE}$, and $\phi_i^T = \phi_i^{RT}$; this produces just one type of single-kink site on step edge i, so we have dropped the k subscript.

For centrosymmetric systems, it is simple to combine the effect of kink density (ρ_i) and kink rate (u) in forming the velocity (v_i) of step edge i: [5, 7]

$$v_i = a_{P,i}\rho_i u \tag{5.4}$$

The propagation length $a_{P,i}$ corresponds to the normal advance of a step with deposition of a new row (see Figure 5.2). For centrosymmetric systems the kink rate is edge-independent [3].

5.2.1 Centrosymmetric Kink Density

The centrosymmetric kink density, ρ_i, can be determined from Boltzmann statistics [20] or minimization of Helmholtz free energy [21, 22]. The former tactic uses geometrical step transformations to extract the energetic penalty of kink formation; the latter considers kinks as disturbances and determines the number by considering both this energetic penalty and entropic effect of different edge configurations. Both strategies are simplified by the existence of only one type of single-kink site for each edge. The resulting expression is

$$\rho_i = \frac{2\exp\left(-\frac{\phi_i^K}{kT}\right)}{1 + 2\exp\left(-\frac{\phi_i^K}{kT}\right)} \tag{5.5}$$

ϕ_i^K is the penalty of kink formation on step edge i (see Figure 5.2 and eq 5.1); ϕ_i^E and ϕ_i^T are site-independent across step edge i, so do not need to be included. Since ϕ_i^K can be edge-dependent, even for a centrosymmetric system with a symmetric interaction sphere, ρ_i varies between edges. Strictly, eq 5.5 represents the kink density under equilibrium conditions, which we adopt as an approximate description of the crystal surface during growth; nonequilibrium formulations have also been developed [23], which are asymptotic to eq 5.5 as $S \to 1$.

5.2.2 Centrosymmetric Kink Rate

The kink rate, u, is the net incorporation rate into a kink site. For centrosymmetric systems, u can be calculated from the difference between rates of kink attachment (j^+) and detachment (j^-) [4–9, 24]:

$$u = j^+ - j^- \tag{5.6}$$

From Chapter 2, the most appropriate attachment and detachment rate expressions are:

$$j^+ = k^+ x = k^+ x_{sat} S \tag{5.7}$$

$$j^- = k^- \tag{5.8}$$

The attachment rate is first order in solute solution concentration, x (which can be related to supersaturation ratio: $S = x/x_{sat}$), while the detachment rate is zeroth order. The

rate constants are given by

$$k^+ = \nu_0 \exp\left(-\frac{\Delta G^\ddagger}{kT}\right) \tag{5.9}$$

$$k^- = k^+ \exp\left(-\frac{\Delta W}{kT}\right) \tag{5.10}$$

In eq 5.9, ν_0 is a frequency factor and $\Delta G^\ddagger$ represents a desolvation barrier (for solution growth) [5,6,8]. To predict crystal growth shapes mechanistically, k^+ is often assumed to be site-independent [3,4,12,22,24,25]. In eq 5.10, ΔW represents a reference free energy that we calculate as the work required to detach a growth unit from kink to solution (or vapor), which depends on that growth unit's reverse energies:

$$\Delta W = 2\phi_i^{RK} + 2\phi_i^{RE} + 2\phi_i^{RT} \tag{5.11}$$

The factors of 2 in eq 5.11 account for the creation of two surfaces in each direction upon detachment (reverse energies are modified by the solvent akin to their outward-facing counterparts, to properly account for this process). For centrosymmetric systems, ΔW is edge-independent, since the combined interactions collectively form half of the symmetric interaction sphere.

The attachment and detachment rate expressions in eqs 5.7 and 5.8 can be considered as aggregate descriptions that represent the terrace/edge-adsorption-mediated incorporation process that is expected for organic molecules [20,26,27]. Considering either these aggregate kinetics, or a more complete microkinetic description (Appendix 2.A), the same kink rate results:

$$u = (S-1)k^+ \exp\left(-\frac{\Delta W}{kT}\right) \tag{5.12}$$

which is edge-independent. Thus, the principal factor driving anisotropic step velocities

for centrosymmetric systems is the kink density (in eq 5.4, ρ_i can vary much more than $a_{P,i}$).

5.3 Non-Centrosymmetric Step Velocities

For non-centrosymmetric growth units, the step velocity still derives from the combined action of kink densities and kink rates, but now there are extra phenomena to consider when calculating these quantities and developing a subsequent step velocity expression. Reverse kink/edge/terrace energies are no longer necessarily equivalent to their kink/edge/terrace counterparts, which means all interactions must be considered in developing Boltzmann penalties for kink formation. Additionally, there may now be multiple growth units with distinct, asymmetric interaction spheres within the lattice; these produce site-dependent $\Delta W_{k,i}$'s, which can vary between each step edge (subscript i) and each kink (subscript k, which depends on the specific kink along the step edge, i.e., row, growth unit, orientation). With multiple $\Delta W_{k,i}$'s possible on each edge, different surface structures and incorporation progressions may exist; their motion may be interdependent and their collective contribution to step velocity must be correctly accounted for.

5.3.1 Non-Centrosymmetric Kink Density

The typical strategies employed to derive centrosymmetric kink densities become impractical for non-centrosymmetric growth units. To generalize the equilibrium Boltzmann distribution of eq 5.5, we form site-specific energy penalties by directly considering the kink, edge, and terrace energies from eqs 5.1–5.3. Introducing edge and terrace energies into the Boltzmann weightings allows us to capture a thermodynamic effect of row stability (note that incorporating edge energies has also been applied by Cuppen and

co-workers [28]).

Figure 5.3 illustrates our method. We define a "site" to be the junction between growth units, then formulate its energy penalty to include the following contributions:

1. Half the average terrace energy for the row that is west of the junction
2. Half the average edge energy for the row that is west of the junction
3. Half the average terrace energy for the row that is east of the junction
4. Half the average edge energy for the row that is east of the junction
5. The full kink energies of any growth units exposed in the kink direction

This definition ensures a fair comparison between edge and kink sites. Using half of the row-averaged terrace and edge energies ensures the summation of penalties across all sites along an edge would reproduce the overall surface energy present at the step front. The row-averaging of terrace/edge contributions is necessary for rows containing multiple growth units; this captures thermodynamic stability/instability of the full row, which is our goal.

With this site definition and consideration of surrounding surface energies, we can form a Boltzmann weight for any site and, by considering each possible edge/kink site on the step, calculate the corresponding distribution for kinks of any depth (i.e., spanning any number of rows in the edge direction). Note that east and west orientations must be included for kink sites (always) and edge sites (when different growth units exist either side of the junction; see Chapter 6 for examples). With anisotropic interactions, multirow kinks can become thermodynamically favorable, given that they can avoid expressing high $\phi^E_{k,i}$'s or $\phi^T_{k,i}$'s, at the cost of additional $\phi^K_{k,i}$ contributions. Considering Figure 5.3, if $\phi^T_B/2+\phi^E_B/2 > \phi^T_A/2+\phi^E_A/2+\phi^K_A$, the Boltzmann weight for (b) is greater than (c) (note,

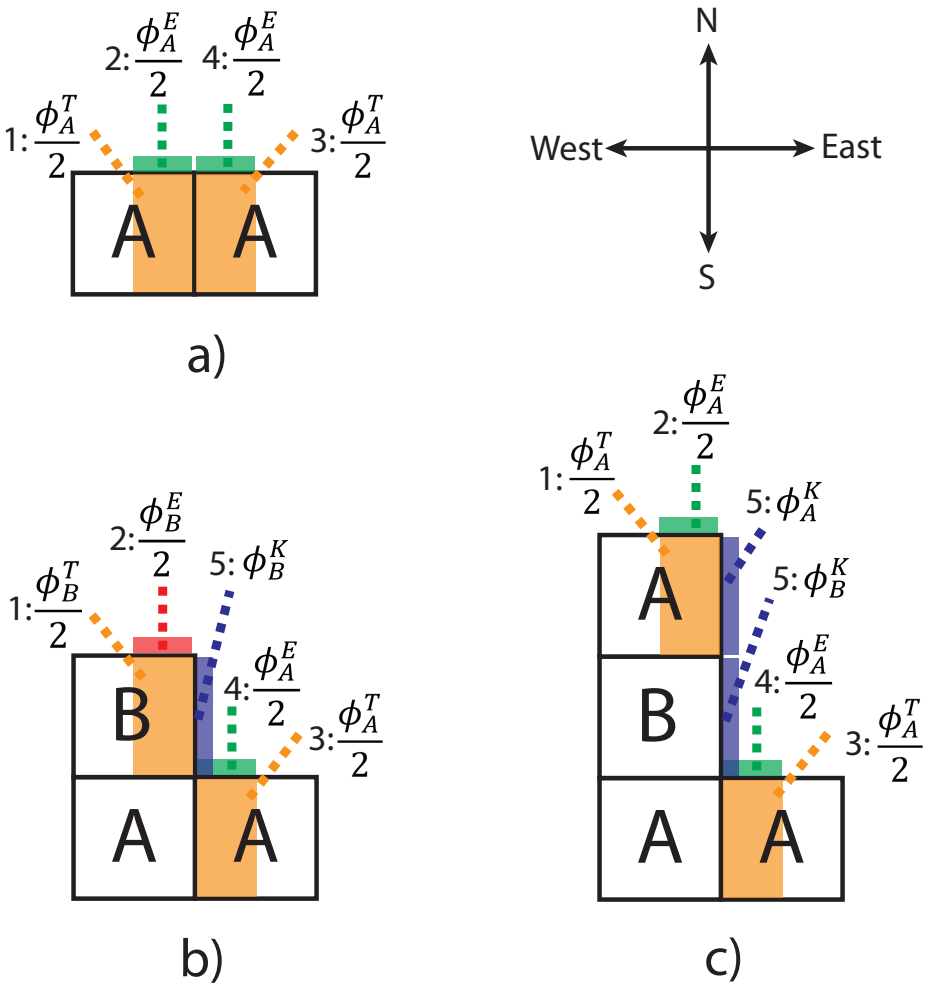

Figure 5.3: Example site definitions and corresponding Boltzmann weights for (a) A edge site, (b) B single-kink site (east), (c) AB double-kink site (east). East/west kinks directions are defined using north as the direction of step motion (equivalently, north = edge direction, south = reverse edge direction). Each site represents a junction between adjacent growth units in the east–west direction. Contributions to the Boltzmann penalty are labeled numerically by type (see text) and color-coded as follows: orange = A/B terrace energy, green = A edge energy, red = B edge energy, blue = A/B kink energy.

we removed $\phi_B^K + \phi_A^E/2 + \phi_A^T/2$ from both sides of the inequality); this would indicate double-row kink (double-kink) favorability and the potential thermodynamic influence of unstable rows.

This approach can be feasibly implemented for non-centrosymmetric edges of any complexity and can capture thermodynamic row stability. Another key quality is that it collapses to the centrosymmetric expression when each growth unit has the same terrace, edge and kink interactions; equation 5.13 demonstrates this for the case of one growth unit, though it remains true for multiple growth units under the same limit (see Chapter 6):

$$\rho_i = \frac{2\exp\left(-\frac{\phi_i^T+\phi_i^E+\phi_i^K}{kT}\right)}{\exp\left(-\frac{\phi_i^T+\phi_i^E}{kT}\right) + 2\exp\left(-\frac{\phi_i^T+\phi_i^E+\phi_i^K}{kT}\right)} = \frac{2\exp\left(-\frac{\phi_i^K}{kT}\right)}{1+2\exp\left(-\frac{\phi_i^K}{kT}\right)} \tag{5.13}$$

This ensures that for infinitesimal anisotropy results tend to the centrosymmetric case, which is necessary for a physically realistic model.

5.3.2 Non-Centrosymmetric Kink Rate

The lack of interaction symmetry for non-centrosymmetric growth units leads to an anisotropic detachment rate:

$$j_{k,i}^- = k_{k,i}^- = k^+ \exp\left(-\frac{\Delta W_{k,i}}{kT}\right) \tag{5.14}$$

since the detachment-to-solution work, $\Delta W_{k,i}$, now depends on the specific kink/edge/face combination:

$$\Delta W_{k,i} = 2\phi_{k,i}^{RK} + 2\phi_{k,i}^{RE} + 2\phi_{k,i}^{RT} \tag{5.15}$$

This is edge- and site-dependent due to the asymmetric interaction sphere.

Kinks progress along an edge according to periodic cycles of growth unit incorpora-

tion. Kuvadia and Doherty developed [3] an expression for the net incorporation rate around a cycle containing n growth units (eqs 5.16–5.17, see Chapter 2 for more detail), following previous treatments for the cases of two [9] and three [8] growth units.

$$u_{k,i} = n \frac{(j^+)^n - \prod_{k=1}^{n} j^-_{k,i}}{\sum_{r=1}^{n} (j^+)^{n-r} (j^-_i)^{r-1}}, \tag{5.16}$$

$$(j^-_i)^{r-1} = \sum_{k=1}^{n} (j^-_k \, j^-_{k+1} \cdots j^-_{k+r-2})_i \tag{5.17}$$

equations 5.16–5.17 enable calculation of the kink rate, provided the cycle progression is specified, with rate constants calculated from eqs 5.7 and 5.14.

Kinks within the same cycle have equivalent $u_{k,i}$ (this can be proved from the cycle's master equation, see Chapter 2), but for non-centrosymmetric growth units, different cyclic kink progressions may exist on the same step edge. We consider a cycle for each possible single-junction starting kink structure k on the step edge (i.e., for each kink site accounted for in our kink density formulation above). If multiple types of rows exist, kink structures spanning more than one row will have different cycles from those on a single row ("single-kinks"); furthermore, each row's single-kink cycle will be distinct, according to the sets of growth units contained. Figure 5.4 portrays example cycles with $n = 4$ for starting kinks of various depths (the four types of growth units – A, B, C, D – form the unit cell and are repeated throughout the lattice due to translational symmetry). When we consider multirow kink cycles, we assume a fill order that acts to maintain the full depth of the starting kink: each "column" is filled before advancing the kink farther along the edge. Intermediate structures in multirow cycles (e.g., Figure 5.4b,c) can span multiple sites/junctions; separate cycles should be considered with each kink (i.e., single-junction site) on these intermediate structures as the starting kink. Our

fill order assumption is justified by considering sequential attachment events. In Figure 5.4c, for example, the addition of growth unit A produces two adjacent kink sites, which will compete for incoming growth units. Only successive attachment to the B row (on top of the A row) corresponds to our definition of a stable multirow kink structure; if the next attachment is also into the A row it implies that row should be treated independently (we consider unstable multirow kinks to immediately split into their most stable intermediates). Kinetic aspects of row stability are discussed later; the important point here is that the incorporation rate into kinks of any depth can be described via the cyclic consideration of eqs 5.16–5.17.

The concept of stable and unstable edge rows was introduced by Kuvadia and Doherty [3]; this phenomenon can appear when multiple types of rows exist on the step, with anisotropic interactions. Their condition for stability was $\phi^{RE} + \phi^{RT} \geq \phi^{E} + \phi^{T}$: the step row is stable when interactions binding it to the lattice are greater than or equal to incomplete interactions extending out to solution; otherwise, the row is unstable. Their subsequent tactic was to determine the favorable multirow kink exposing only the rows with low edge energy and declare a fill order that best captured stability; this was then taken to be the exclusive structure by which the step advances. As shown later in this chapter, such a case is essentially the limit of sufficiently high anisotropy, where that multirow kink cycle is indeed the only relevant step edge structure.

Our new framework aims to capture the degree of instability present, i.e., relative stability between rows, rather than adopt a binary classification of being either stable or unstable. Additionally, we divide our description of stability into thermodynamic and kinetic components. The step rows with highest $\overline{\phi^{E}_{k,i} + \phi^{T}_{k,i}}$ (i.e., averaged across the growth units within that row) are the most thermodynamically unstable; we capture this by incorporating those row-averaged terrace and edge energies into the Boltzmann weights to appropriately penalize the expression of sites involving such rows along the

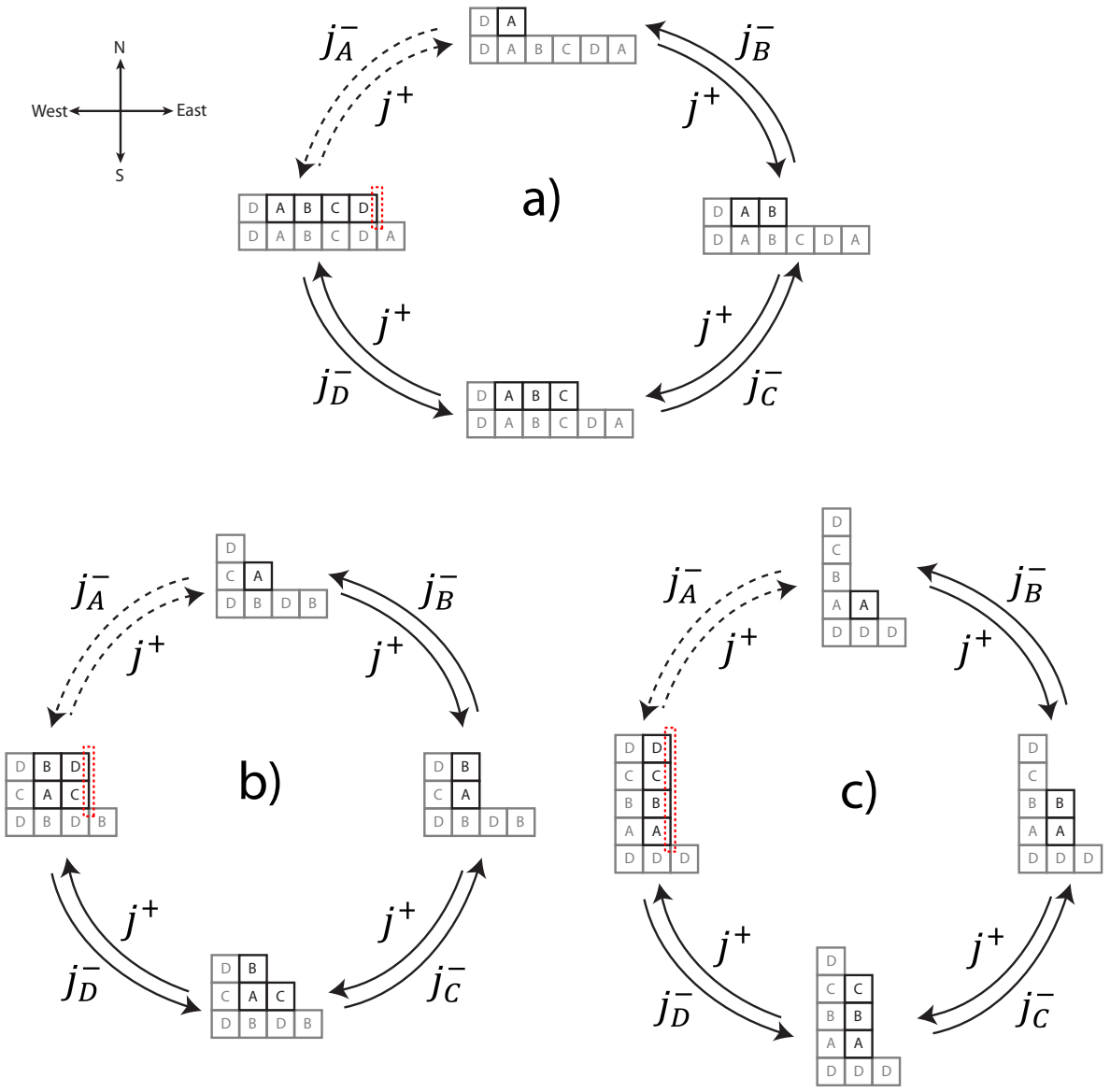

Figure 5.4: Top views of steps with example east-direction cyclic kink progressions of edge-direction depth (a) = 1 row, (b) = 2 rows, and (c) 4 rows (all cycles contain four growth units, with starting kinks indicated by red dotted lines). Paracetamol (CSD HXACAN01 [29]) has steps corresponding to each case (a): step $[1\bar{1}0]$ face (110); (b): step [010] face (001); (c): step [001] face (110); see also Figure 12 in [11] for other examples of type-b) steps. Detachment rates are anisotropic, according to the work required to remove that growth unit. The dashed lines indicate the point in each cycle where an ABCD repeat unit has either been deposited or removed. The vertical fill order corresponds to a stable multirow kink; additional cycles must be considered for kinks on the intermediate structures (see text).

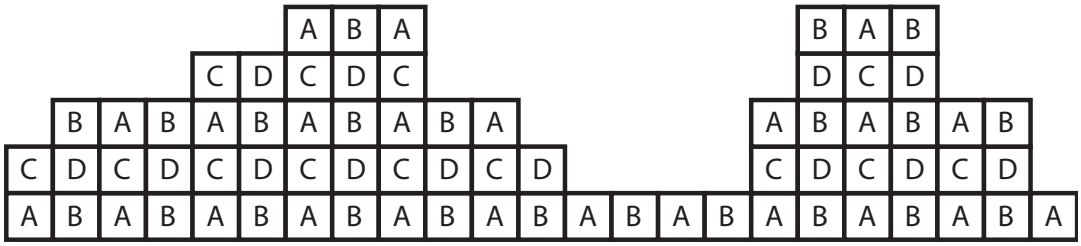

Figure 5.5: Example non-centrosymmetric step structure (top view) with four distinct growth units. If the AB row has lower edge energy it is more likely to be exposed on the advancing step. With increasing anisotropy, double-kinks may become the principal step edge surface structures, but the effect of single-kinks should not be neglected.

edge. Similarly, the step rows with lowest (or most negative) single-kink incorporation rates are the most kinetically unstable (because detachment rates are large relative to attachment rates). This effect is examined further in the following section.

The picture of an edge with only the most thermodynamically stable kink structure present is unlikely to be accurate except in the limit of significant anisotropy. Until Boltzmann fractions of less stable kink structures do become negligible, their contributions to step motion must be considered. Figure 5.5 portrays an example AB–CD step configuration. If the CD row is thermodynamically unstable, double-kinks exposing the AB row's edge may indeed be favorable surface structures, but for a complete description of how the step advances, the AB and CD single-kink cycles should also be considered. Double-kinks may also exist for centrosymmetric systems, though their kink rate is identical to that of a single-kink. See Appendix 5.A for the centrosymmetric kink density expression that accounts for double-kinks.

The new picture of multiple types of kink cycles acting on each step edge is more physically correct; however, it introduces new phenomena, since each distinct kink cycle has a unique kink rate (eq 5.16); i.e., the AB and CD single-kink incorporation rates will

typically be different. By moving at different speeds along the edge, distinct kink structures can collide and transform, so their motion is no longer independent. Additionally, we will show that distinct kink structures may actually move in different directions (i.e., one can grow while the other dissolves, even under supersaturated conditions of overall growth), since the solute mole fraction in solution that divides growth and dissolution regimes becomes different for each kink cycle. We next discuss the determination of x_{sat} for non-centrosymmetric systems and the phenomenon of kinetic row stability.

5.3.3 Determination of x_{sat} for Non-Centrosymmetric Growth Units

With our established choice of attachment/detachment rate expressions (Chapter 2), the solution to $u_{k,i}(x^*_{k,i}) = 0$ is

$$(k^+ x^*_{k,i})^n = \prod_{k=1}^{n} k^+ \exp\left(-\frac{\Delta W_{k,i}}{kT}\right) \tag{5.18}$$

$$x^*_{k,i} = \exp\left(-\frac{\sum_{k=1}^{n} \Delta W_{k,i}}{nkT}\right) = \exp\left(-\frac{\overline{\Delta W}_{k,i}}{kT}\right) \tag{5.19}$$

where n is the number of growth units (and, therefore, events) in the kink cycle; n is uniquely defined by the starting kink k and our fill order assumption presented earlier. The average detachment work, $\overline{\Delta W}_{k,i}$, is equivalently an average binding energy for growth units within the cycle; $\overline{\Delta W}_{k,i}$ can vary between cycles and cause different kink structures to stop growing at distinct solute concentrations, $x^*_{k,i}$. This introduces a key question: is there an edge-dependent $x_{sat,i}$, or a single constant (isotropic) value x_{sat} (at a given T) for each crystal-solvent system? An edge-dependent $x_{sat,i}$ implies different edges and crystal faces stop growing at different solute concentrations in solution. Even with a spiral mechanism operating on each face, this would lead to dramatic changes in steady-

state growth habit as solute concentration is decreased; as some faces stop growing, other faces that still have a sufficient number of supersaturated spiral sides may grow out of the shape or change the aspect ratio. Where such morphological changes do occur, they result from transitions to two-dimensional nucleation or other mechanisms rather than manifesting from spiral growth alone [24] (see Chapter 3). Thus, we hypothesize that a single constant value of x_{sat} exists (according to the crystal system and growth conditions), and each edge on each face should stop growing at this solute concentration.

Nonetheless, distinct kink cycles retain unique mathematical solutions to eq 5.19. To resolve this, we select our definition of x_{sat} to be when cycles containing every type of growth unit within the crystal lattice (maximal cycles) do not grow or dissolve:

$$x_{sat} = \exp\left(-\frac{\sum_{k=1}^{N} \Delta W_{k,i}}{NkT}\right) = \exp\left(-\frac{\overline{\Delta W}_{sat}}{kT}\right) \tag{5.20}$$

where N is the number of growth units in the unit cell (this is the maximum number of growth units in a cycle, i.e., $n \leq N$). Such maximal cycles ensure a constant average growth unit binding energy, $\overline{\Delta W}_{sat}$, by involving the full set of crystalline interactions. This thermodynamic criterion results in the same value of x_{sat} for each step edge i; it must be satisfied for a consistent implementation of our model (refer to Section 6.3.2 for some practical comments relating to its application).

This tactic ensures that maximal cycles (i.e., those containing every type of growth unit) halt at $x = x_{sat}$; such cycles correspond to a repeat unit structure on the step. For kink cycles that do not contain every type of growth unit (submaximal cycles), the detachment work contains only a subset of lattice interactions. Thus, the behavior of these submaximal cycles along the edge then depends on whether their average detachment work, $\overline{\Delta W}_{k,i}$, is larger or smaller than that of the repeat unit kink cycle, $\overline{\Delta W}_{sat}$. The

numerator of eq 5.16 has the following scaling:

$$u_{k,i}^{num} \propto S^n - \left(\frac{x_{k,i}^*}{x_{sat}}\right)^n \tag{5.21}$$

If $\overline{\Delta W}_{k,i} > \overline{\Delta W}_{sat}$, $x_{k,i}^* < x_{sat}$ and kink cycle k,i will have a faster net incorporation rate than a maximal cycle (it essentially experiences a site-specific supersaturation, $S_{k,i}^* = x/x_{k,i}^*$, that is higher than the overall supersaturation ratio, $S = x/x_{sat}$). Conversely, if $\overline{\Delta W}_{k,i} < \overline{\Delta W}_{sat}$, $x_{k,i}^* > x_{sat}$ and then kink cycle k,i will have a slower incorporation rate than a maximal cycle, which may be negative (dissolution) for sufficient anisotropy. The condition for dissolution is $x_{k,i}^* > Sx_{sat}$ (i.e., site-specific undersaturation $S_{k,i}^* = x/x_{k,i}^* < 1$). Note that if a non-centrosymmetric step has multiple rows, but each row contains only one type of growth unit, the single-kink incorporation rates retain the form $j^+ - j^-$, but this form no longer collapses to eq 5.12, since x_{sat} is defined for the edge as a whole (see Case 2 later).

Thus, kinetic instability is determined by detachment work anisotropy: rows may dissolve if growth unit removal is easy relative to other rows. At x_{sat}, submaximal kink cycles may still grow or dissolve, but will soon collapse with other rows to transform into the starting kink structure of a maximal cycle, which is then stationary. Thus, this model ensures each edge stops moving at the calculated value of x_{sat}.

5.3.4 Developing a New Step Velocity Expression

The Boltzmann construction presented earlier allows us to calculate the site distribution along a non-centrosymmetric step edge and extract specific densities for each type of kink (including multiple-row kinks). Each kink then belongs to a cycle, which is the sequence of growth units that must be added in order to regenerate the original kink. With their cycles defined, we can calculate the net incorporation rates into each type of

kink using eqs 5.16–5.17.

Next, we must consider the potential interactions between kink structures having different cycles, some of which may exist as kinetically unstable rows. The overall step velocity results from incorporation events into all of these sites, but with kink cycles moving at different speeds, their motion is no longer independent. This phenomenon of interacting kink structures is not relevant for the centrosymmetric case, where all cycles move at the same net incorporation rate.

Kink collisions are either transformations, where rows combine to form a new kink structure that can continue to grow, or annihilations, where kinks are lost as rows complete (or disappear under dissolution annihilations). Both possibilities must be considered to accurately portray step motion. The general assumption in modeling the steady-state step velocity is that the edge remains in its Boltzmann distribution, due to the propensity for thermal reorganization above absolute zero Kelvin [2, 20–22]. If this rearrangement were instantaneous, the step velocity would be a simple summation of site densities multiplied by incorporation rates (i.e., eq 5.4, for each kink). However, instantaneous reorganization is unphysical, and instead we would expect it to occur over some finite time frame. Thus, we expect kinks to move at their respective incorporation rates until collision with another kink; if this corresponds to a transformation, then the combined rows move at a new incorporation rate (according to the new kink structure) until reorganization to the step's Boltzmann distribution. Kinks where the collision time scale is larger than the reorganization time scale continually move at their native rates (they do not transform before annihilation).

We can determine the possible kink transformations and annihilations on a given edge, according to which rows / kink structures may collide (this is fixed by the pattern of growth units on the step). For each type of collision, we can calculate a time scale using relative kink structure speeds along the edge (from kink rates) and a characteristic

distance between sites (from the kink density). Using such time scales, we can develop an approximate mathematical description of non-centrosymmetric step motion. This approach has elements of a population balance, but considers dominant effects rather than attempting a comprehensive description; as will be demonstrated, the model nonetheless shows a powerful ability to capture important new phenomena. We denote the transformation time scale for a given kink structure k as τ_k^T; up to this point the kink moves at its native incorporation rate, u_k, and beyond τ_k^T it moves at a new kink rate, u_k^T, according to the structure formed. Though the new kink will span additional rows, u_k^T should describe just the contribution to completing those of the original kink structure. To obtain the step's reorganization time scale, τ^R, we must determine the relative importance of potential annihilation events and choose the dominant method by which kinks disappear. The relevant time scale for kink annihilation corresponds to reorganization since we are interested in modeling the steady-state step velocity; any loss in kinks must be balanced by their regeneration during the reorganization for a step to continue advancing. The following expression demonstrates this step velocity framework:

$$\begin{aligned} v_i &= a_{P,i} \sum_k \rho_{k,i} \left[\frac{\tau_k^T}{\tau^R} u_k + \left(1 - \frac{\tau_k^T}{\tau^R}\right) u_k^T \right]_i && \text{, if } \frac{\tau_k^T}{\tau^R} < 1 \\ &= a_{P,i} \sum_k \rho_{k,i} u_{k,i} && \text{, if } \frac{\tau_k^T}{\tau^R} \geq 1 \end{aligned} \tag{5.22}$$

The subscript k loops over the relevant kink sites (and their respective cycles) on step edge i; $\rho_{k,i}$ is the density of each kink structure along the step (where the starting structure for each cycle is considered, to ensure a single "junction" for the kink density description). Equation 5.22 assumes one transformation for each kink structure, but could be generalized beyond this. The fractional time scale τ_k^T/τ^R is a dimensionless group describing the average fraction of k-type sites moving at their native incorporation

rate. Thus, eq 5.22 represents an aggregate steady-state description of the step velocity for an edge containing multiple sites of each type. Note if $\tau_k^T/\tau^R \geq 1$, then all kink structures of type k move at their native velocity.

With the assumption of an isotropic attachment rate constant, each kink rate shows proportional dependence: $u_{k,i} \propto k^+$. This enables us to calculate fractional time scales τ_k^T/τ^R (see later for example expressions), without the need to estimate k^+. The form of eq 5.22 also maintains this proportional dependence ($v_i \propto k^+$), which allows us to calculate relative step velocities and face growth rates, again without an estimate for k^+. As demonstrated in Chapter 3, this assumption is a key tactic employed in mechanistic modeling to predict crystal shapes quickly, which is an ability preserved by this more general step velocity framework.

The next section will illustrate application of this strategy to calculate the step velocity of a simple non-centrosymmetric step.

5.4 Example: A–B Step

The above concepts and strategies are best illustrated by example; we have elected to study an alternating-row A–B step, where within each row there is one type of growth unit. For this case, $\phi_A^K = \phi_A^{RK}$, $\phi_B^K = \phi_B^{RK}$, $\phi_A^{RE} = \phi_B^E$ and $\phi_B^{RE} = \phi_A^E$. As indicated previously, we are studying the case of identical molecules in solution that form different types of growth units upon incorporation into the crystal lattice. We consider three cases: centrosymmetric, anisotropic edge energies, and anisotropic kink energies.

5.4.1 Case 1: Centrosymmetric

The centrosymmetric case ($\phi_A^K = \phi_B^K \equiv \phi^K$, $\phi_A^E = \phi_B^E \equiv \phi^E$, $\phi_A^T = \phi_A^{RT} = \phi_B^T = \phi_B^{RT} \equiv \phi^T$) permits us to benchmark the performance of simple expressions (eqs 5.4,

5.5, and 5.12), against kinetic Monte Carlo (KMC) simulations (performed using the KMCLib program [30]). We shall also use further KMC results to judge our new framework's predictions for non-centrosymmetric cases; see Appendix 5.A for explanation of parameters and rate expressions. Since a_P and k^+ are constants, we can extract them and plot a normalized step velocity ($v_{A-B}/a_P k^+ x_{sat}$), where we have also extracted x_{sat}. As $\overline{\Delta W}_{sat}$ increases, x_{sat} and the resulting step velocity decrease; it is useful to remove this effect and retain contributions to changing step velocities from kink densities and kinetic instability alone. Figure 5.6 shows the comparison between calculated step velocities and those determined from the simulations (after a steady-state is reached); it is clear that the centrosymmetric expressions accurately describe step motion (in this case, the change in normalized step velocity is primarily due to the kink density). We have included double-kinks in the Boltzmann expression for kink density here, which provides marginally improved results at low ϕ^K from the base expression in eq 5.5, which accounts only for single-kinks (the contribution from double-kinks becomes negligible for $\phi^K > 3kT$). The minor discrepancies that exist may result from using the equilibrium Boltzmann kink density under nonequilibrium conditions, or from neglecting the contribution to step growth from molecular attachment during one-dimensional nucleation events.

5.4.2 Case 2: Anisotropic Edge Energies

In this scenario, the kink/terrace energies on both rows are equal ($\phi_A^K = \phi_B^K \equiv \phi^K$, $\phi_A^T = \phi_B^T \equiv \phi^T$ and, by extension, $\phi_A^{RT} = \phi_B^{RT} \equiv \phi^T$), but the B row has greater edge energy. The [001] step on the (200) face of paracetamol is an example of such a step (see Figure 5.7).

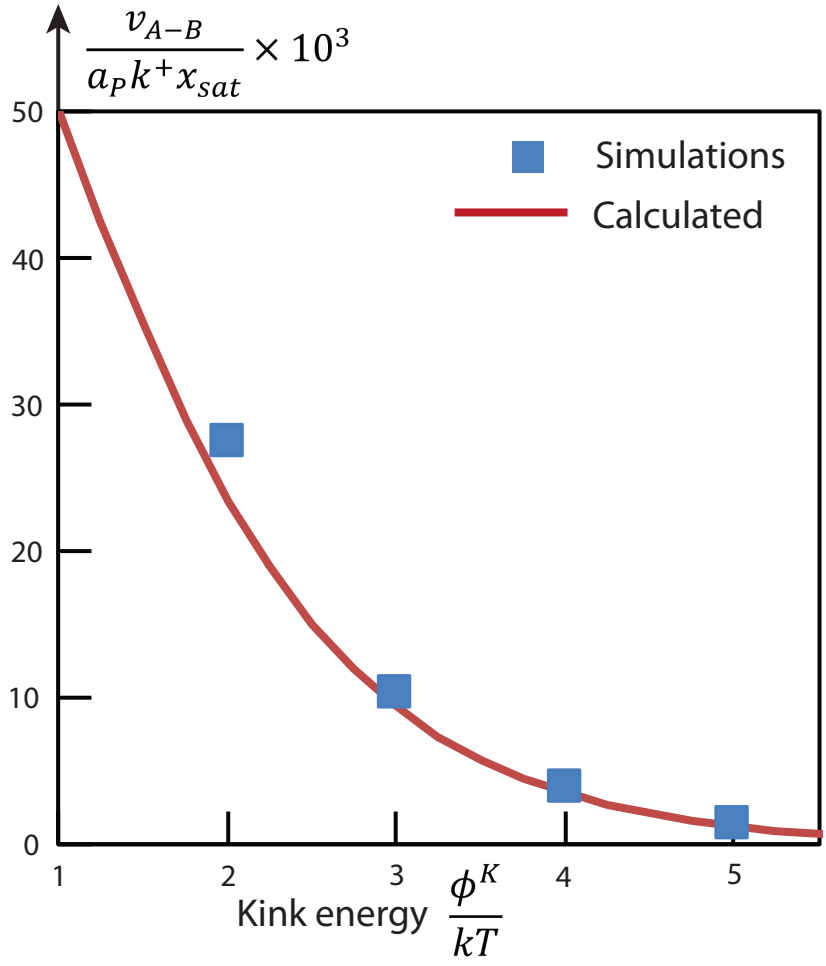

Figure 5.6: Plot of normalized step velocity against kink energy for a centrosymmetric step at S=1.1 (isotropic ϕ^E and ϕ^T). Blue squares are values determined from the KMC simulations, and the red solid line shows calculated values from eq 5.4.

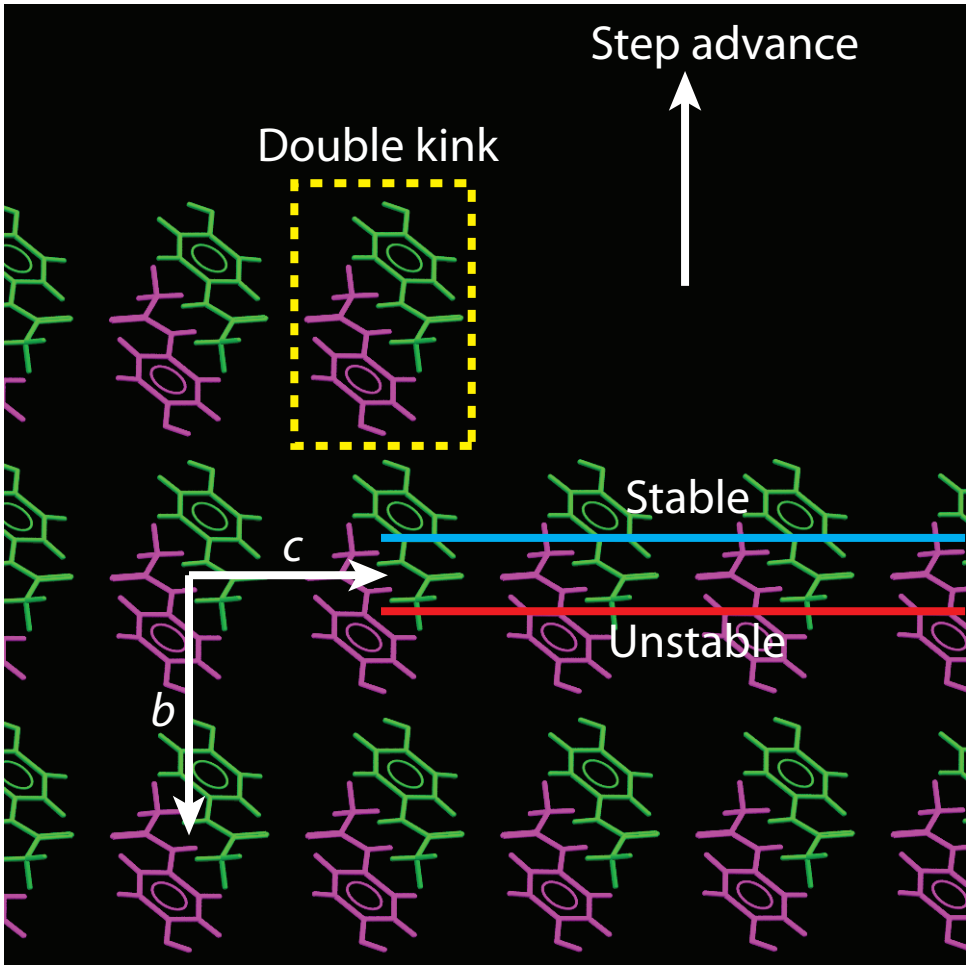

Figure 5.7: [001] step on a slice of the (200) face of paracetamol has alternating rows of growth units (CSD code HXACAN01 [29]; the (200) slice is in the plane of the page, the a axis is angled out of the page). The interactions in the kink direction on each row are symmetric and equivalent, but the edge energies are anisotropic. To avoid exposing the high-edge-energy unstable row, double-kinks may form on the step edge.

Kink Densities

A reasonable bound for the maximum size of multirow kink is the number of distinct step rows. Multirow kinks have increasing kink energy penalties, so are generally only relevant when this effect is counteracted by lower edge and/or terrace energy penalties, which can exist by exposing only the most stable rows. A kink of depth equal to the number of step rows can expose the row with lowest edge and terrace energy on either side; any kinks of greater depth necessarily have higher energy penalties, so should have negligible contribution to the Boltzmann distribution. Thus, for our case of a two-row step, only single and double-kinks need to be considered.

Figure 5.8 indicates the edge/kink sites for this A–B step, along with their Boltzmann penalties and our labeling convention. The east and west orientations are equivalent (because each row has one type of growth unit), so essentially four kink structures exist: A, B, AB, and BA. The corresponding kink densities are

$$\rho_A = \frac{2\exp\left(-\frac{0.5(\phi_A^E+\phi_B^E)+\phi_A^K}{kT}\right)}{Q} \tag{5.23}$$

$$\rho_B = \frac{2\exp\left(-\frac{0.5(\phi_A^E+\phi_B^E)+\phi_B^K}{kT}\right)}{Q} \tag{5.24}$$

$$\rho_{AB} = \frac{2\exp\left(-\frac{\phi_A^E+\phi_A^K+\phi_B^K}{kT}\right)}{Q} \tag{5.25}$$

$$\rho_{BA} = \frac{2\exp\left(-\frac{\phi_B^E+\phi_A^K+\phi_B^K}{kT}\right)}{Q} \tag{5.26}$$

$$\begin{aligned} Q = {} & \exp\left(-\frac{\phi_A^E}{kT}\right) + \exp\left(-\frac{\phi_B^E}{kT}\right) \\ & + 2\exp\left(-\frac{0.5(\phi_A^E+\phi_B^E)+\phi_A^K}{kT}\right) + 2\exp\left(-\frac{0.5(\phi_A^E+\phi_B^E)+\phi_B^K}{kT}\right) \\ & + 2\exp\left(-\frac{\phi_A^E+\phi_A^K+\phi_B^K}{kT}\right) + 2\exp\left(-\frac{\phi_B^E+\phi_A^K+\phi_B^K}{kT}\right) \end{aligned} \tag{5.27}$$

where the factors of 2 account for both kink orientations (east, west). For simplicity of presentation, we have elected to study the case of row-independent terrace energies, where ϕ^T contributions cancel out of the Boltzmann density expressions, so have not been included above. Figure 5.9 shows the relative population of kinks for increasing edge energy anisotropy and $\phi_A^K = \phi_B^K = 2kT$.

Kink Rates

The solution of eq 5.19 for the double-kink defines the saturation solute mole fraction:

$$x_{sat,AB} = \exp\left(-\frac{\Delta W_A + \Delta W_B}{2kT}\right) = \exp\left(-\frac{\overline{\Delta W}_{AB}}{kT}\right) \tag{5.28}$$

where ΔW_A and ΔW_B follow eq 5.15 ($\Delta W_A = 2\phi^K + 2\phi_B^E + 2\phi^T$ and $\Delta W_B = 2\phi^K + 2\phi_A^E + 2\phi^T$, since $\phi_A^{RE} = \phi_B^E$ and $\phi_B^{RE} = \phi_A^E$). Growth of A and B single-kinks follows the centrosymmetric construction ($j^+ - j^-$), with x_{sat} defined by eq 5.28. Their kink rates are given by

$$u_A = k^+ x_{sat,AB}\left[S - \exp\left(-\frac{\Delta W_A - \overline{\Delta W}_{AB}}{kT}\right)\right] \tag{5.29}$$

$$u_B = k^+ x_{sat,AB}\left[S - \exp\left(-\frac{\Delta W_B - \overline{\Delta W}_{AB}}{kT}\right)\right] \tag{5.30}$$

The edge anisotropy dictates $\Delta W_A - \overline{\Delta W}_{AB} = \phi_B^E - \phi_A^E > 0$ and $\Delta W_B - \overline{\Delta W}_{AB} = \phi_A^E - \phi_B^E < 0$; $u_A > u_B$, and with sufficient anisotropy, u_B can become negative. These kink rates represent the net number of incorporations per unit time; since the kinks are single-row, they equivalently correspond to the speed of kink motion on the step edge in terms of sites per time.

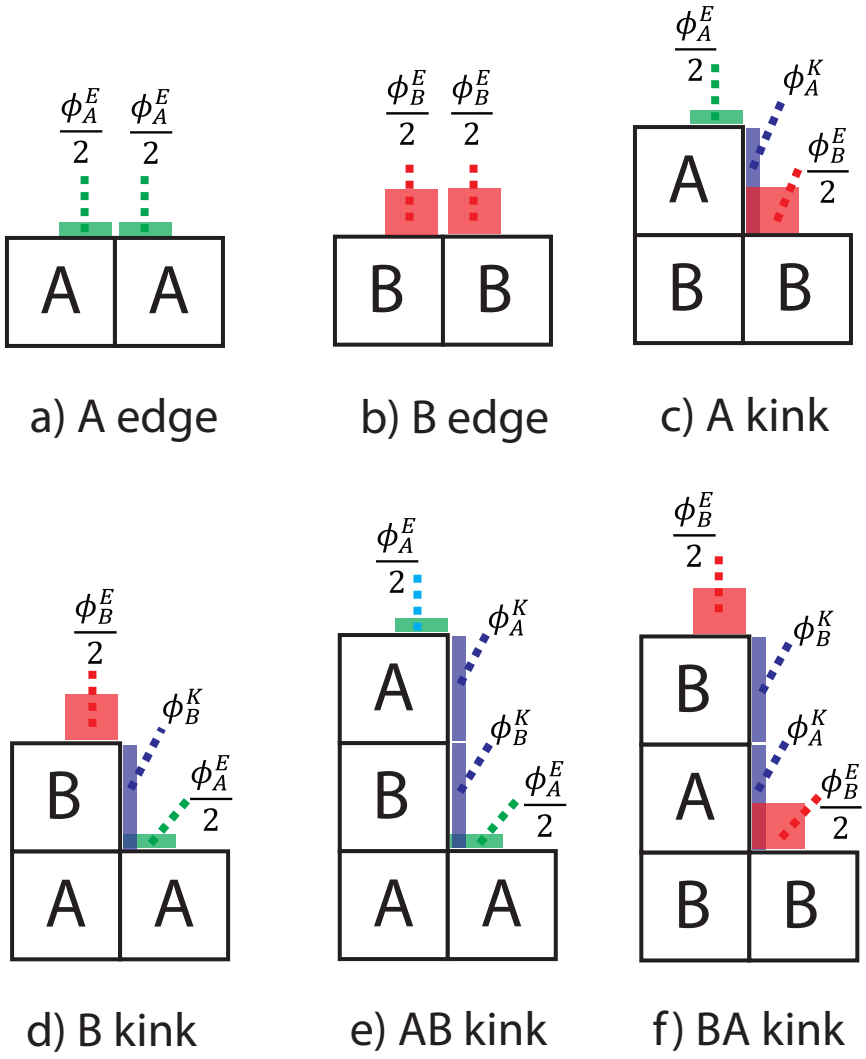

Figure 5.8: Relevant surface sites for an AB step: (a) A edge, (b) B edge, (c) A single-kink, (d) B single-kink, (e) AB double-kink, (f) BA double-kink. Boltzmann weights are indicated in terms of solid state interactions: green = A edge energy, red = B edge energy, blue = A/B kink energy. Note terrace energies have been omitted, since these contributions cancel out for row-independent terrace interactions. Only the east kink orientations are shown (the west orientations are energetically equivalent in this case).

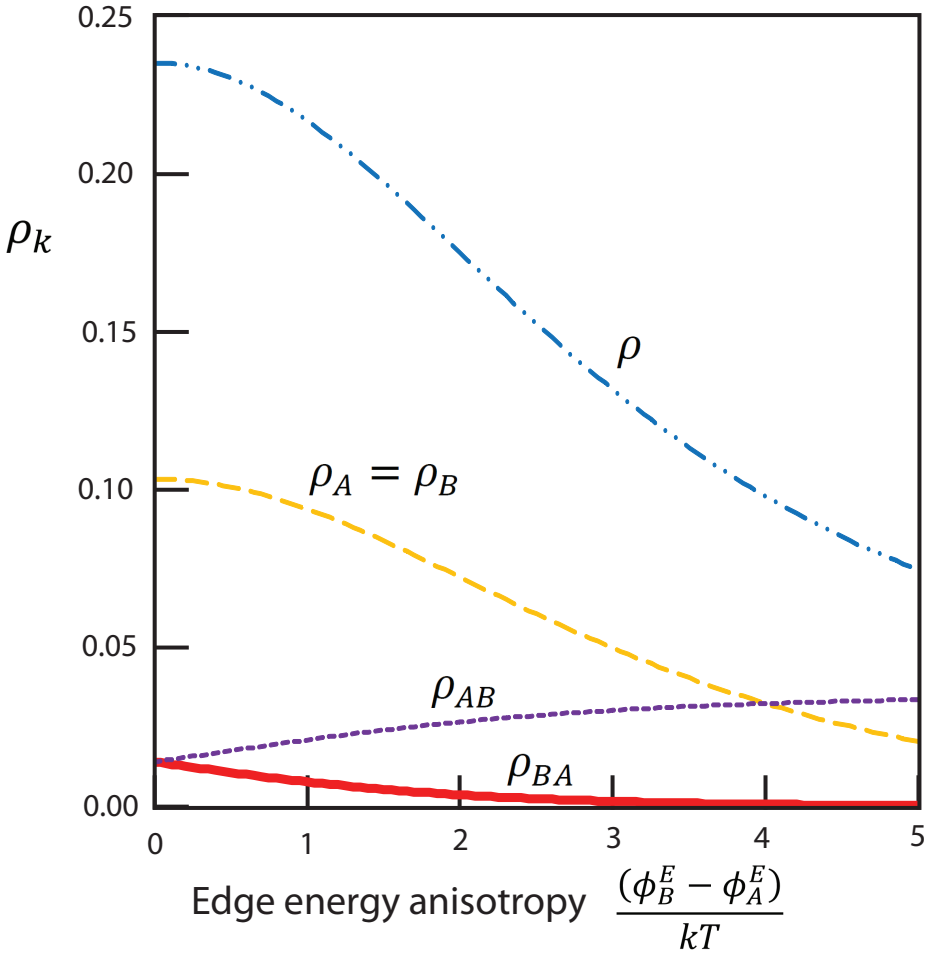

Figure 5.9: Plots of overall ($\rho = \sum \rho_k$) and site-specific (ρ_k) kink densities using eqs 5.23–5.26 for $\phi_A^K = \phi_B^K = 2kT$, as a function of increasing edge energy anistropy. For $\phi_B^E - \phi_A^E > 4kT$, the AB double-kink has the lowest energy penalty.

The AB double-kink incorporation rate is given by

$$u_{AB} = 2k^{+}x_{sat,AB}^{2}\frac{S^2-1}{2Sx_{sat,AB}+\exp\left(-\frac{\Delta W_A}{kT}\right)+\exp\left(-\frac{\Delta W_B}{kT}\right)} \tag{5.31}$$

At $S = 1$, $u_{AB} = 0$. Since the double kink spans two rows, u_{AB} no longer corresponds to the speed at which the double-kink advances along the step, which is instead given by $u_{AB}/2$ (two incorporations are needed to advance the double-kink one site along the edge).

A cycle starting with the BA double-kink is unphysical, since the upper B row moves more slowly (or in the opposite direction) to the A row below. Thus, BA double-kinks instantly split into two single-kinks, according to our steady-state framework. The Boltzmann contribution of BA double-kinks should, therefore, increase the effective distribution of single-kinks (i.e., $\rho_A^e = \rho_A + \rho_{BA}$ and $\rho_B^e = \rho_B + \rho_{BA}$). Note that the AB double-kink is a physical cycle because $u_A > u_B$, which requires the rows to advance together.

Kink Transformations and Annihilations

The A–B step row presents a simple example from the perspective of possible transformations, since we only need to consider A kinks colliding with B kinks on the row below. This collision does not occur in a steady-state framework for the centrosymmetric case, where their kink rates are identical. As anisotropy increases and $u_A > u_B$, this collapse is feasible; for negative u_B, it becomes increasingly rapid. Figure 5.10 illustrates the transformation. To determine the time scale, we divide a characteristic number of sites between kinks ($1/\rho$) by the relative kink rate ($u_A - u_B$):

$$\tau_{A:B} = \frac{1}{(u_A - u_B)\rho} \tag{5.32}$$

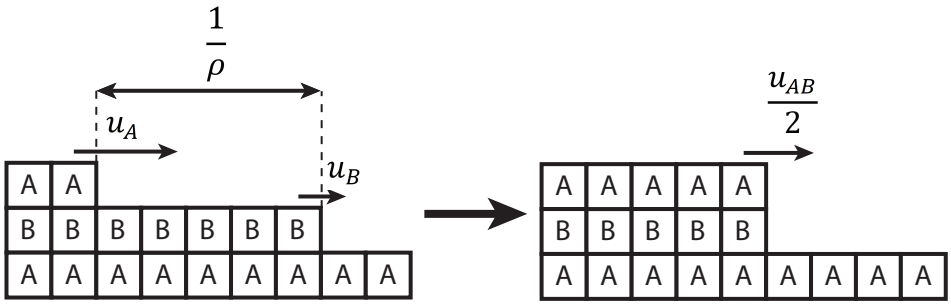

Figure 5.10: Diagram of A:B kink transformation, indicating characteristic separation distance and kink speeds along the edge. Note that u_{AB} is the rate of growth unit addition to an AB kink; its speed along the edge is half that due to completing two rows.

Note that this kink density is the sum $\rho = \rho_A + \rho_B + \rho_{AB} + \rho_{BA}$ from eqs 5.23–5.26. Although the BA kink is unstable and we established ρ_{BA} should be added to both ρ_A and ρ_B for computing effective densities, it is the original Boltzmann probabilities that should be used for eq 5.32. The A and B kinks emerging from an unstable BA site appear at the same point and diverge; this split does not act to reduce the characteristic distance between sites that can collapse under this transformation.

Possible kink annihilations are A:A, B:B, and AB:AB, which are shown in Figure 5.11. To determine the reorganization time scale, we must consider which annihilation events dominate the loss of kink sites. Expressions for each time scale are given by

$$\tau_{A:A} = \frac{1}{2u_A\rho} \tag{5.33}$$

$$\tau_{B:B} = \frac{1}{2|u_B|\rho} \tag{5.34}$$

$$\tau_{AB:AB} = \frac{1}{u_{AB}\rho^e_{AB}} \tag{5.35}$$

In eqs 5.33 and 5.34, the overall Boltzmann kink density (ρ) should be used, as in eq 5.32. The absolute value of u_B is needed in eq 5.34 to ensure a positive time scale during dissolution events where the B single-kink incorporation rate is negative. In eq

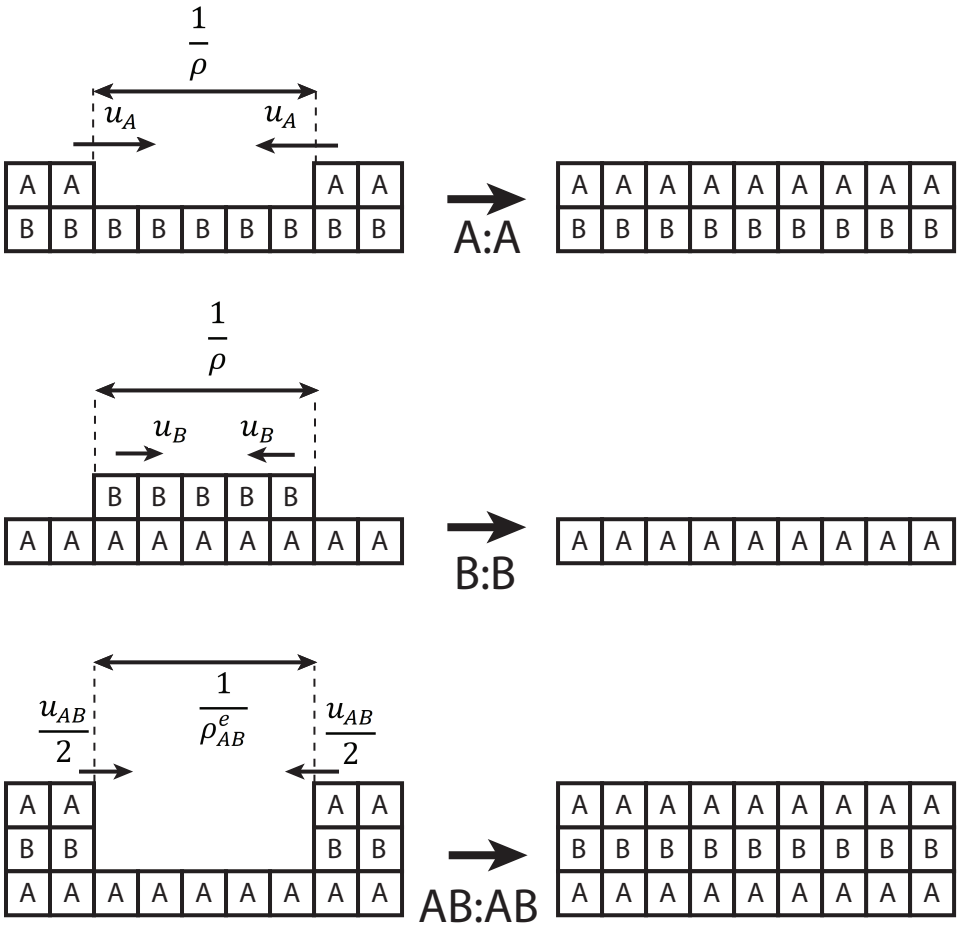

Figure 5.11: Diagrams of A:A, B:B, and AB:AB annihilations, indicating characteristic separation distances and kink speeds along the edge. The B:B annihilation is shown for the case of negative u_B, i.e., B edge dissolution.

5.35, there is no factor of 2 since the double-kink drift velocity along the edge is half the incorporation rate u_{AB}. The effective density of double-kinks (ρ^e_{AB}) is required in eq 5.35, to avoid underestimating the characteristic number of sites between double-kinks; to a first approximation we can assume all single-kinks become double-kinks: $\rho^e_{AB} = \rho_{AB} + \rho^e_A$ (note that $\rho^e_A = \rho^e_B$ for the case of equal kink energies).

To determine whether single-kink or double-kink annihilations are most important, we compare $\tau_{A:A}$ to $\tau_{A:B}$, since this comparison determines whether single-kinks have the tendency to transform before annihilation. If the transformation to double-kink is fa-

vored, then $\tau_{AB:AB}$ is the appropriate reorganization time scale; if single-kink annihilation occurs before transformation, then $\tau_{A:A}$ better characterizes step reorganization.

Note we do not consider $\tau_{B:B}$ for investigating the importance of single-kink annihilation, since u_B goes from growing to dissolving and $\tau_{B:B}$ will diverge to infinity at this crossover. Furthermore, B:B annihilation under conditions of negative u_B can be neglected since the B layer will not nucleate without a stabilizing A row on top. Since the step must eventually become stoichiometric upon advance, using $\tau_{A:A}$ and $\tau_{A:B}$ we can determine the relative importance of single- and double-kink annihilations.

The reciprocals $(\tau_{A:A})^{-1}$ and $(\tau_{A:B})^{-1}$ relate to the rates of A:A annihilation and A:B transformation. However, the A:A annihilation requires a completed B row below, in between the annihilating kinks. With increasing B edge instability, it becomes more difficult for a B edge to advance without the stabilizing influence of an A row on top (i.e., an AB double-kink); this makes completed B rows unlikely. To account for this and penalize the A:A annihilation, we incorporate a scaling factor describing kinetic instability of the B row: $\exp(-(\overline{\Delta W}_{AB} - \Delta W_B)/kT)$. This factor decreases with increasing B instability, capturing the reduced probability of finding a completed B row; it simplifies to describe edge anisotropy: $\exp(-(\phi_B^E - \phi_A^E)/kT)$. The relative annihilation rate between single and double-kinks, RAR_{1-2}, can then be calculated as

$$RAR_{1-2} = \frac{P(A:A)}{P(AB:AB)} = \frac{(\tau_{A:A})^{-1} \exp\left(-\frac{\overline{\Delta W}_{AB} - \Delta W_B}{kT}\right)}{(\tau_{A:B})^{-1}} = \frac{(\tau_{A:A})^{-1} \exp\left(-\frac{\phi_B^E - \phi_A^E}{kT}\right)}{(\tau_{A:B})^{-1}} \tag{5.36}$$

RAR_{1-2} can also be interpreted as the relative probability of A:A and AB:AB collapse. If $RAR_{1-2} > 1$, we expect single-kink annihilations to be the dominant factor driving loss of kink sites; in this region we use $\tau^R = \tau_{A:A}$. Conversely, if $RAR_{1-2} < 1$, we expect double-kink annihilations to be dominant and use $\tau^R = \tau_{AB:AB}$.

The step velocity for the A–B step, v_{A-B}, can then be determined using eq 5.22,

which results in

$$\begin{aligned}
\text{If } RAR_{1-2} > 1, \quad v_{A-B} =& a_P \rho_A^e u_A + a_P \rho_B^e u_B + a_P \rho_{AB} u_{AB} \\
\text{If } RAR_{1-2} < 1, \quad v_{A-B} =& a_P \rho_A^e \left(\frac{\tau_{A:B}}{\tau_{AB:AB}} u_A + \left(1 - \frac{\tau_{A:B}}{\tau_{AB:AB}}\right) \frac{u_{AB}}{2} \right) \\
&+ a_P \rho_B^e \left(\frac{\tau_{A:B}}{\tau_{AB:AB}} u_B + \left(1 - \frac{\tau_{A:B}}{\tau_{AB:AB}}\right) \frac{u_{AB}}{2} \right) \\
&+ a_P \rho_{AB} u_{AB}
\end{aligned} \tag{5.37}$$

The three contributions are from A single-kinks, B single-kinks, and AB double-kinks. Effective kink densities are used for A and B kinks, to account for BA kinks that separate; the effective kink density for AB kinks is not used, since it includes contributions from the single-kinks. Both A and B kinks have the same transformation (collapse to an AB double-kink), with time scale $\tau_{A:B}$; τ^R is determined by considering eq 5.36, as indicated above. When single-kink annihilation is dominant, all kinks move entirely at their native rates. Upon double-kink annihilation becoming appropriate, the single-kinks move at their native rates for a fraction of τ^R; following the transformation they move at $u_{AB}/2$ for the remaining fraction, where the 1/2 factor appears since half the double-kink incorporation rate is attributed to each single-kink. Original double-kinks from the Boltzmann distribution show no transformations.

Comparison to Kinetic Monte Carlo Simulations

Kinetic Monte Carlo simulations provide a useful test of our model's ability to capture instability phenomena. By extracting x_{sat}, our normalized step velocity depends only on edge/terrace energy anisotropy, rather than absolute values. We modeled step motion using $\phi_A^K = \phi_B^K = 2kT$ at $S = 1.1$. The simulations permit attachment and detachment events from solution at kink sites according to eqs 5.9 and 5.10; similar rates follow for edge attachment/detachment. This captures one-dimensional nucleation along the step

edge. Note a multirow step edge typically forms and overhangs are not permitted (see Appendix 5.A for further details).

We applied our mechanistic framework to calculate kink densities, kink rates, time scales and step velocities for the same kink/edge energies and supersaturation that we simulated. These quantities are tabulated and available online (see Supporting Information for ref. [31]), and various trends can be observed (refer back to Figure 5.9 for plots of kink densities). In the centrosymmetric limit ($\phi_B^E - \phi_A^E = 0kT$), the Boltzmann distribution is dominated by single-kinks, i.e., $\rho_A = \rho_B \gg \rho_{AB}$; at the extreme range of our tested anisotropy ($\phi_B^E - \phi_A^E = 5kT$), $\rho_{AB} > \rho_A = \rho_B$: now AB double-kinks are the most favorable structure, but single-kinks still show an appreciable probability. The thermodynamic effect of row stability is, therefore, somewhat minor, since AB double-kinks only dominate the Boltzmann distribution at extremely high anisotropy. Next, for $\phi_B^E - \phi_A^E \geq 0.1kT$ (when $\overline{\Delta W}_{AB} - \Delta W_B > kT \ln S$, see eq 5.30), we calculate a negative B single-kink incorporation rate, u_B; only minor anisotropy is required for exposed B rows to dissolve. This effect leads to a small $\tau_{A:B}$ transformation time scale; with increasing anisotropy, the collapse of single-kinks to double-kinks becomes rapid. The kinetic effect of instability appears more potent than the thermodynamic one: step motion becomes dominated by AB double-kinks primarily due to rapid collapse of single-kinks, rather than by AB kink thermodynamic dominance from the Boltzmann distribution. A value of $RAR_{1-2} = 1$ is reached at $\phi_B^E - \phi_A^E = 0.25kT$. This reinforces how the A:B transformation occurs at low anisotropy: $\tau^R = \tau_{A:A}$ is the relevant annihilation time scale only for $\phi_B^E - \phi_A^E < 0.25kT$; for $\phi_B^E - \phi_A^E > 0.25kT$, $\tau^R = \tau_{AB:AB}$.

In addition to applying our new non-centrosymmetric formulation, we can predict the step velocity under the assumption of AB kink thermodynamic dominance (refer to Appendix 5.A). This is essentially the earlier approach proposed by Kuvadia and Doherty [3]. We expect their method to underestimate the step velocity, particularly for

minor anisotropy, since it does not include contributions from single-kinks. For infinite anisotropy, the kink densities under either approach become mathematically identical (AB double-kinks are indeed the only thermodynamically possible surface structure), leading to equivalent predictions.

Figure 5.12 shows the calculated (using both eq 5.37 and the previous method [3]) and determined (from KMC simulations) values for normalized step velocity, plotted against $\phi_B^E - \phi_A^E$. As indicated earlier, extracting the variable x_{sat} removes its kinetic effect on step velocity, which allows us to plot against degree of anisotropy rather than absolute energetic values. For clarity, we include an expanded insert of the low anisotropy region ($0kT < \phi_B^E - \phi_A^E < 1kT$).

Our predicted step velocities using eq 5.37 and the presented framework compare very favorably to those from our KMC simulations. At $\phi_B^E - \phi_A^E = 0kT$, we recover the centrosymmetric case; note that eq 5.22 (and, therefore, eq 5.37) are equivalent to eq 5.4 for such symmetric interactions. Critically, eq 5.37 is able to successfully describe step motion from this centrosymmetric regime to where significant anisotropy exists; our formulation describes the emergence and increase of instability on the edge. At $\phi_B^E - \phi_A^E = 5kT$, ρ_{AB} is not yet the exclusive structure in the Boltzmann distribution (see Figure 5.9), but beyond this point the assumption of its thermodynamic dominance does provide accurate results. For this case, therefore, the two approaches converge before their kink densities are strictly equivalent, which may be due to single-kinks behaving primarily as double-kinks with increasingly quick kinetic collapse. The greatest discrepancy between our new model and the KMC simulations appears around $RAR_{1-2} = 1$, where the reorganization time scale switches from single-kink to double-kink annihilation. At this point, there is a discontinuity in step velocity due to the difference in $\tau_{A:A}$ and $\tau_{AB:AB}$. It is difficult to account for the combined action of both single and double-kink annihilations while retaining a simple model; our approximation of only considering the

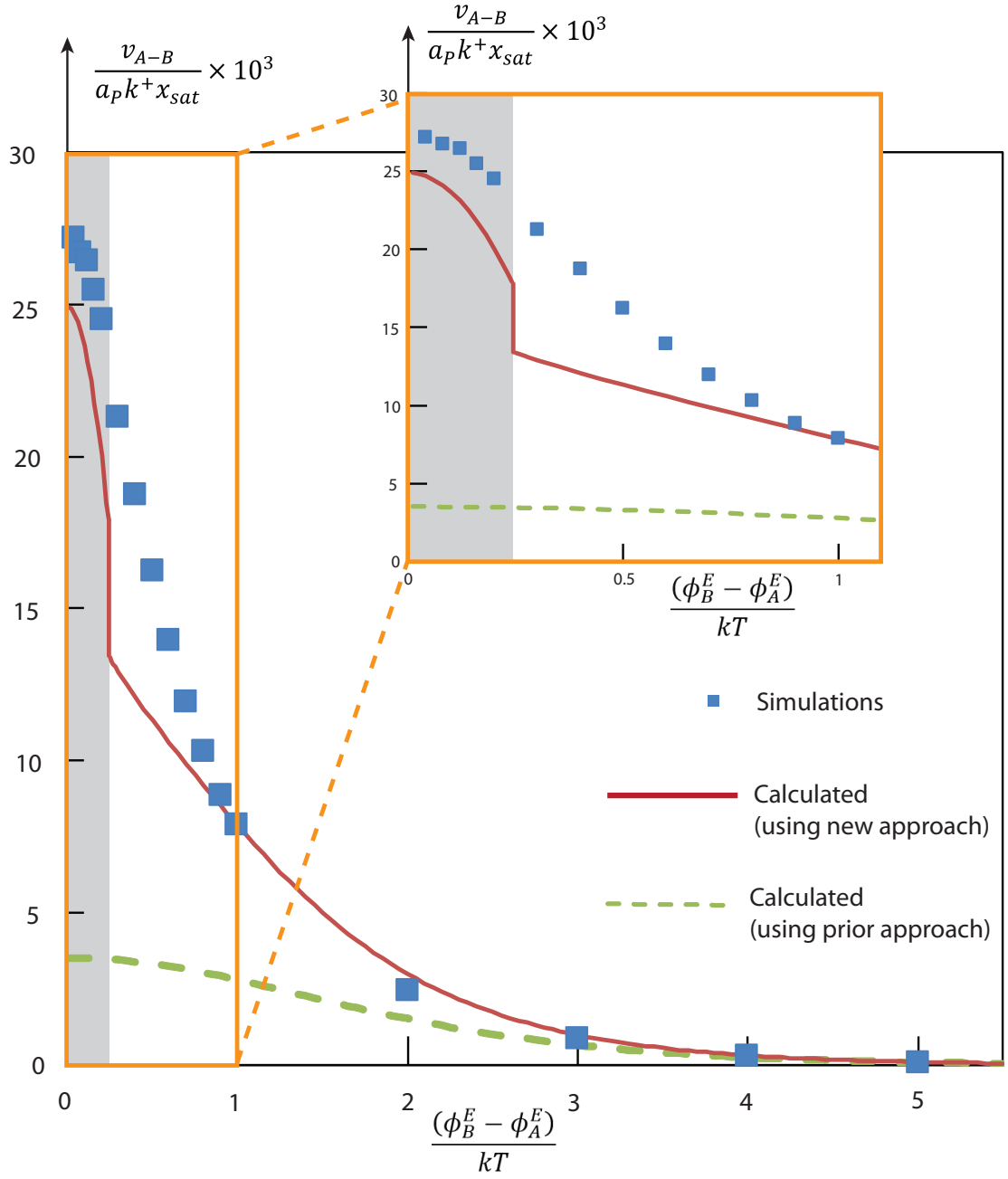

Figure 5.12: Plots of normalized step velocity against edge energy anisotropy (S=1.1, $\phi_A^K = \phi_B^K = 2kT$, $\phi_A^T = \phi_B^T$). Blue squares are values determined from the KMC simulations, the red solid line shows calculated values from eq 5.37, and the green dashed line shows calculated values assuming only AB double-kinks (the previous approach by Kuvadia and Doherty [3]). The shaded regions indicate where single-kink annihilation is dominant and characterizes step reorganization.

dominant mechanism provides a practical solution that nonetheless produces favorable results.

5.4.3 Case 3: Anisotropic Kink Energies

We now consider the case of an A–B step with anisotropic kink energies, $\phi_A^T = \phi_B^T \equiv \phi^T$ and $\phi_A^E = \phi_B^E \equiv \phi^E$. Much of the mechanistic description is identical to the previous case, though there are some important distinctions. The parameter values we have modeled are $S = 1.1$, $\phi_A^K = 4kT$ and varying $\phi_B^K = 2kT - 4.3kT$.

The expressions for kink densities are unchanged from eqs 5.23–5.26, but now $\rho_A \neq \rho_B$, except for the centrosymmetric case; calculated values are plotted in Figure 5.13. With no terrace or edge energy anisotropy, double-kinks are not *thermodynamically* relevant. Thus, to accurately describe step motion for this case, multiple kink cycles must be considered; there is no region where the previous mechanistic treatment is appropriate, since instability derives purely from kinetic effects rather than thermodynamic dominance of the Boltzmann distribution.

Kink rates still obey eqs 5.29–5.31, but now $\Delta W_A = 2\phi_A^K + 2\phi^E + 2\phi^T$ and $\Delta W_B = 2\phi_B^K + 2\phi^E + 2\phi^T$. For $\phi_B^K < 4kT$, the B row (and BA double-kink) is kinetically unstable, so $u_A > u_B$ and the A:B transformation is relevant. For $\phi_B^K > 4kT$, the A row (and AB double-kink) is kinetically unstable, so $u_B > u_A$ and the B:A transformation is relevant (forming a BA double-kink). If we consider the relative Boltzmann populations, we see that in each case the kinetically unstable row has a greater kink density on the step edge, due to a lower kink energy. This impacts possible transformations, since $\rho_A^e \neq \rho_B^e$. In either case, the minimum of ρ_A^e and ρ_B^e determines the potential number of A:B or B:A transformations.

For $\phi_B^K < 4kT$, our strategy is similar to case 2. Here, $\rho_A^e < \rho_B^e$, $\rho_A^e = \rho_A + \rho_{BA}$,

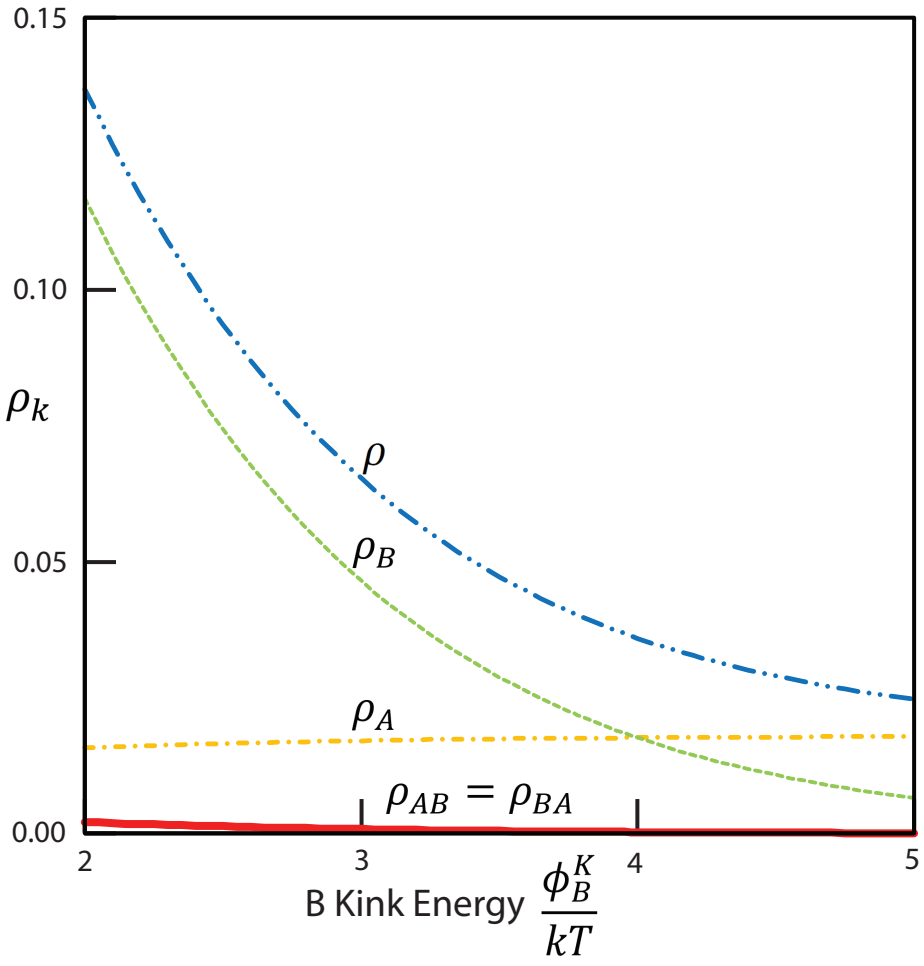

Figure 5.13: Plots of overall ($\rho = \sum \rho_k$) and site-specific (ρ_k) kink densities using eqs 5.23–5.26 for isotropic edge and terrace energies and $\phi_A^K = 4kT$, as a function of increasing B kink energy; $\phi_B^K = 4kT$ corresponds to the centrosymmetric case.

$\rho^e_B = \rho_B + \rho_{BA}$, and $\rho^e_{AB} = \rho_{AB} + \rho^e_A$. We can still determine transformation/annihilation time scales using eqs 5.32 – 5.35, but the kinetic instability scaling factor in eq 5.36 now reflects kink energy anisotropy:

$$RAR_{1-2} = \frac{P(A:A)}{P(AB:AB)} = \frac{(\tau_{A:A})^{-1}\exp\left(-\frac{\overline{\Delta W}_{AB}-\Delta W_B}{kT}\right)}{(\tau_{A:B})^{-1}} = \frac{(\tau_{A:A})^{-1}\exp\left(-\frac{\phi^K_A-\phi^K_B}{kT}\right)}{(\tau_{A:B})^{-1}} \tag{5.38}$$

Determination of τ^R is unchanged, but our expression for v_{A-B} must consider that since $\rho^e_B > \rho^e_A$, not all B single-kinks may transform to double-kinks. As for case 2 above, when single-kink annihilation is dominant, each kink moves at its native rate. When double-kink annihilation becomes dominant, however, we assume that ρ^e_A single-kinks undergo the A:B transformation; the remainder of B single-kinks ($\rho^e_B - \rho^e_A$) would annihilate after $\tau_{B:B}$:

$$\begin{aligned}
\text{If } RAR_{1-2} > 1, \quad v_{A-B} =& a_P\rho^e_A u_A + a_P\rho^e_B u_B + a_P\rho_{AB}u_{AB} \\
\text{If } RAR_{1-2} < 1, \quad v_{A-B} =& a_P\rho^e_A\left(\frac{\tau_{A:B}}{\tau_{AB:AB}}u_A + \left(1-\frac{\tau_{A:B}}{\tau_{AB:AB}}\right)\frac{u_{AB}}{2}\right) \\
&+ a_P\rho^e_A\left(\frac{\tau_{A:B}}{\tau_{AB:AB}}u_B + \left(1-\frac{\tau_{A:B}}{\tau_{AB:AB}}\right)\frac{u_{AB}}{2}\right) \\
&+ a_P(\rho^e_B - \rho^e_A)\left(\frac{\tau_{B:B}}{\tau_{AB:AB}}u_B\right) \\
&+ a_P\rho_{AB}u_{AB}
\end{aligned} \tag{5.39}$$

For $\phi^K_B > 4kT$, we must switch our expressions to account for the BA double-kink becoming kinetically relevant (the AB double-kink is instead unstable). Now, $\rho^e_B < \rho^e_A$, $\rho^e_A = \rho_A + \rho_{AB}$, $\rho^e_B = \rho_B + \rho_{AB}$, and $\rho^e_{BA} = \rho_{BA} + \rho^e_B$. Our transformation time scale is now

$$\tau_{B:A} = \frac{1}{(u_B - u_A)\rho} \tag{5.40}$$

and annihilation time scales are

$$\tau_{A:A} = \frac{1}{2|u_A|\rho} \tag{5.41}$$

$$\tau_{B:B} = \frac{1}{2u_B\rho} \tag{5.42}$$

$$\tau_{BA:BA} = \frac{1}{u_{BA}\rho^e_{BA}} \tag{5.43}$$

Determining the dominant annihilation now considers the stable B row:

$$RAR_{1-2} = \frac{P(B:B)}{P(BA:BA)} = \frac{(\tau_{B:B})^{-1}\exp\left(-\frac{\overline{\Delta W}_{AB}-\Delta W_A}{kT}\right)}{(\tau_{B:A})^{-1}} = \frac{(\tau_{B:B})^{-1}\exp\left(-\frac{\phi^K_B-\phi^K_A}{kT}\right)}{(\tau_{B:A})^{-1}} \tag{5.44}$$

Note the scaling factor here reflects that $\Delta W_B > \Delta W_A$ ($\phi^K_B > \phi^K_A$). If $RAR_{1-2} > 1$, $\tau^R = \tau_{B:B}$; if $RAR_{1-2} < 1$, $\tau^R = \tau_{BA:BA}$. Finally, our expressions for v_{A-B} are

$$\begin{aligned}
\text{If } RAR_{1-2} > 1, \quad v_{A-B} =& a_P\rho^e_A u_A + a_P\rho^e_B u_B + a_P\rho_{AB}u_{AB} \\
\text{If } RAR_{1-2} < 1, \quad v_{A-B} =& a_P\rho^e_B\left(\frac{\tau_{B:A}}{\tau_{BA:BA}}u_A + \left(1-\frac{\tau_{B:A}}{\tau_{BA:BA}}\right)\frac{u_{BA}}{2}\right) \\
&+ a_P(\rho^e_A-\rho^e_B)\left(\frac{\tau_{A:A}}{\tau_{BA:BA}}u_A\right) \\
&+ a_P\rho^e_B\left(\frac{\tau_{B:A}}{\tau_{BA:BA}}u_B + \left(1-\frac{\tau_{B:A}}{\tau_{BA:BA}}\right)\frac{u_{BA}}{2}\right) \\
&+ a_P\rho_{BA}u_{BA}
\end{aligned} \tag{5.45}$$

Figure 5.14 shows predicted step velocities for this A–B step as a function of ϕ^K_B, alongside values from KMC simulations. As indicated above and illustrated in Figure 5.13, the prior mechanistic treatment assuming double-kink thermodynamic dominance is invalid for this step edge; instead, row instability is a purely kinetic phenomenon, and different kink structures contribute to step motion. Our new formulation is capable of capturing these effects and again shows good agreement with KMC simulations. Non-

monotonic behavior of v_{A-B} with increasing ϕ_B^K is demonstrated by the simulations and correctly predicted using our model.

The centrosymmetric limit occurs at $\phi_B^K = 4kT$ for this step edge, and in this region single-kink annihilations are dominant. As ϕ_B^K moves away from this point, anisotropy increases and kink transformations lead double-kink annihilations to become dominant. For decreasing ϕ_B^K (below $4kT$) the B row becomes increasingly unstable, and for increasing ϕ_B^K (above $4kT$) the A row becomes increasingly unstable. This step presents a challenging case for our modeling framework, since those kinks most dominantly expressed in the Boltzmann distribution correspond to unstable rows; nonetheless, the presented framework is able to quite accurately portray step motion.

Note that the case of anisotropic terrace energies may correspond to either case 2 or 3. If $\phi_B^T > \phi_A^T$, the B row is thermodynamically unstable (assuming isotropic ϕ^K and ϕ^E). Depending on the stacking of layers in the terrace direction, ϕ_B^{RT} may be greater or less than ϕ_A^{RT}. If $\phi_B^{RT} < \phi_A^{RT}$, then $\Delta W_B < \overline{\Delta W}_{AB}$ and the B layer is kinetically unstable (in addition to being thermodynamically unstable); in this case, the terrace anisotropy will produce results corresponding to case 2. If $\phi_B^{RT} > \phi_A^{RT}$, however, then $\Delta W_A < \overline{\Delta W}_{AB}$ and the A layer is instead kinetically unstable; this is similar to case 3 where thermodynamic and kinetic instabilities are decoupled.

5.5 Conclusions

Non-centrosymmetric growth units can generate interaction anisotropy and multiple types of kink sites on a step edge. Our method for site identification and kink density calculation is applicable to any step edge and provides a simpler alternative to a transformation-based approach. Furthermore, it collapses to the established centrosymmetric expressions if growth unit interactions are equivalent (see Chapter 6), and also to

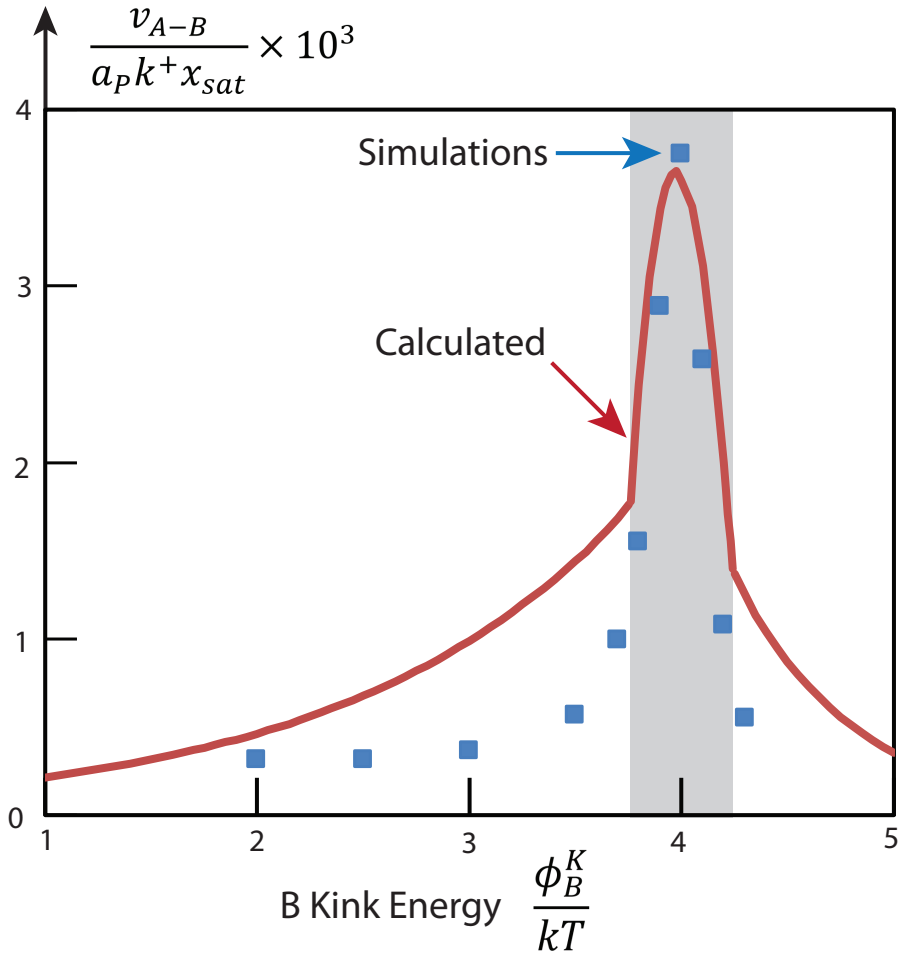

Figure 5.14: Plot of normalized step velocity against B kink energy (S=1.1, $\phi_A^K = 4kT$, $\phi_A^E = \phi_B^E$, and $\phi_A^T = \phi_B^T$). Blue squares are values determined from the KMC simulations, and the red solid line shows calculated values using eqs 5.39 and 5.45. The shaded region indicates where single-kink annihilation is dominant and characterizes step reorganization.

the method of Kuvadia and Doherty [3] at high edge row anisotropy.

Interaction anisotropy can also cause different rows on the step to be thermodynamically and/or kinetically unstable, relative to one another. Thermodynamic instability of a row implies its kink/edge sites have a low relative presence on the step edge at equilibrium; this is determined by the terrace/edge/kink energies that enter each Boltzmann weight. Kinetic instability implies a slower (or negative) net incorporation rate for the single-kink on a row; this is determined by anisotropy in growth unit detachment work (i.e., $\overline{\Delta W}_{k,i} - \overline{\Delta W}_{sat}$, which depends on each site's reverse kink/edge/terrace energies). Kinetic instability can lead to transformations between kink structures on the step edge that move at different speeds according to their distinct kink cycles. With sufficient anisotropy, unstable edge rows can have negative kink rates, corresponding to dissolution, under overall conditions of crystal growth.

To construct a multirow step velocity model that accounts for the effect of all possible sites on step motion, including instability phenomena, we consider both kink transformations and annihilation events. By calculating and comparing time scales, we can determine how kink structures move at their native and then post-transformation rates, before being regenerated via thermal reorganization (to counter the effect of annihilations).

We have applied this framework to the example of an A–B step with alternating rows containing different types of growth units, under conditions of both edge and kink interaction anisotropy. Our mechanistic predictions compare favorably to kinetic Monte Carlo simulations of such steps and confirm our ability to successfully predict changes in step velocity according to the degree of interaction anisotropy. This model connects the centrosymmetric regime to that of extreme anisotropy by capturing the emergence and increasing effect of row instability.

The kinetic effect of stability appears more important than thermodynamics, since single-kink to double-kink transformations cause an edge to grow primarily as double-

kinks before double-kink dominance of the Boltzmann distribution. Step rows with high edge/terrace energies (relative to other rows) are likely to have low detachment work, so thermodynamic and kinetic stability may be coupled, though this is not mandatory. Anisotropic kink energies can also decouple the two types of instabilities, where low kink energies may produce unstable rows that are actually the most prevalent kink structure in the Boltzmann distribution.

The method of assuming the stable-kink's thermodynamic dominance [3] provides a useful model check, since this should underestimate actual step velocities and become accurate under certain limits. It can, therefore, be used as a lower bound on v_i and guide whether or not the relevant transformations/annihilations are being captured effectively.

The challenges in applying this framework to a general step edge consisting of many rows and many kink types are 2-fold: determining possible kink transformations and determining the appropriate edge reorganization time scale. The number of collisions to consider depends on how many distinct rows exist on the step. Although we have presented the case for an A–B step here, our framework should be functionally identical for a two-row AB–CD step, except now the single and double-kink rates must encompass two and four growth units within the cyclic progression, respectively. The case of three rows seems unlikely from a symmetry perspective, and we expect the generalization to four rows and above to be feasible. Essentially, one must evaluate each row's stability, consider possible transformations and annihilations, and then use time scales to estimate dominant contributions and capture the most important effects of interaction anisotropy. Overall, this framework acts as a more systematic treatment of instability that provides an improved description of crystal growth physics for non-centrosymmetric systems.

Appendices

5.A Mechanistic Calculations and KMC Simulation Data

The spreadsheet online (Supporting Information, ref. [31]) contains mechanistic parameters for each studied case: 1) centrosymmetric, 2) A–B with anisotropic edge energies and 3) A–B with anisotropic kink energies. Our normalized step velocities are independent of isotropic terrace/edge energies, in both the simulations and mechanistic calculations. Thus, we can construct the simulations with such isotropic quantities set to zero for convenience of increased speed. For Case 2 (anisotropic edge energy), the isotropic kink energies are set above zero to maintain reasonable kink densities. We employ equivalent attachment rates for A and B, $j^+ = k^+ x_{sat} S$. The detachment work of growth unit i from site type m (kink, step, etc.) is the sum of bonds which must be broken, $\Delta W_{m,i}$, and the detachment rates are then $j^-_{m,i} = k^+ e^{-\Delta W_{m,i}/kT}$. We have arbitrarily set $k^+ = 10^5$ s^{-1} and $a_P = 1$ nm, to obtain realistic values for rates, timescales and step velocities in the given units. Normalized step velocities extracted from kMC simulations are included alongside our mechanistic calculations, for comparison.

For Case 1 (centrosymmetric), we include double-kinks in the kink density formulation:

$$\rho_{single} = \frac{2\exp\left(-\frac{\phi^K}{kT}\right)}{1 + 2\exp\left(-\frac{\phi^K}{kT}\right) + 2\exp\left(-\frac{2\phi^K}{kT}\right)} \tag{5.46}$$

$$\rho_{double} = \frac{2\exp\left(-\frac{2\phi^K}{kT}\right)}{1 + 2\exp\left(-\frac{\phi^K}{kT}\right) + 2\exp\left(-\frac{2\phi^K}{kT}\right)} \tag{5.47}$$

When assuming AB kink thermodynamic dominance for Case 2, we use the following expressions for kink density and step velocity:

$$\rho^*_{AB} = \frac{2\exp\left(-\frac{\phi^K_A+\phi^K_B}{kT}\right)}{1+2\exp\left(-\frac{\phi^K_A+\phi^K_B}{kT}\right)} \tag{5.48}$$

$$v^*_{A-B} = a_P u_{AB} \rho^*_{AB} \tag{5.49}$$

Bibliography

[1] W. K. Burton, N. Cabrera, and F. C. Frank. Role of Dislocations in Crystal Growth. *Nature*, 163(4141):398–399, 1949.

[2] M. A. Lovette, A. R. Browning, D. W. Griffin, J. P. Sizemore, R. C. Snyder, and M. F. Doherty. Crystal Shape Engineering. *Ind. Eng. Chem. Res.*, 47(24):9812–9833, 2008.

[3] Z. B. Kuvadia and M. F. Doherty. Spiral growth model for faceted crystals of non-centrosymmetric organic molecules grown from solution. *Cryst. Growth Des.*, 11(7):2780–2802, 2011.

[4] S. H. Kim, P. Dandekar, M. A. Lovette, and M. F. Doherty. Kink rate model for the general case of organic molecular crystals. *Cryst. Growth Des.*, 14(5):2460–2467, 2014.

[5] P. G. Vekilov. What determines the rate of growth of crystals from solution? *Cryst. Growth Des.*, 7(12):2796–2810, 2007.

[6] D. N. Petsev, K. Chen, O. Gliko, and P. G. Vekilov. Diffusion-limited kinetics of the solution-solid phase transition of molecular substances. *Proc Natl Acad Sci USA*, 100(3):792–796, 2003.

[7] I. V. Markov. *Crystal Growth for Beginners: Fundamentals of Nucleation, Growth and Epitaxy*. Singapore: World Scientific,, 2003.

[8] A. A. Chernov, L. N. Rashkovich, and J. J. De Yoreo. ABC of kink kinetics and density in a complex solution. *AIP Conf Proc*, 916(1):34–47, 2007.

[9] J. Zhang and G. H. Nancollas. Kink density and rate of step movement during growth and dissolution of an ab crystal in a nonstoichiometric solution. *J. Colloid Interface Sci.*, 200(1):131 – 145, 1998.

[10] P. Dandekar, Z. B. Kuvadia, and M. F. Doherty. Engineering crystal morphology. *Annu. Rev. Mater. Res.*, 43:359–386, 2013.

[11] L. N. Poloni, A. P. Ford, and M. D. Ward. Site discrimination and anisotropic growth inhibition by molecular imposters on highly dissymmetric crystal surfaces. *Crystal Growth & Design*, 16(9):5525–5541, 2016.

[12] P. Dandekar and M. F. Doherty. A mechanistic growth model for inorganic crystals: Growth mechanism. *AIChE J*, 60(11):3720–3731, 2014.

[13] H.-M. Shim and K.-K. Koo. Crystal Morphology Prediction of Hexahydro-1,3,5-trinitro-1,3,5-triazine by the Spiral Growth Model. *Cryst. Growth Des.*, 14(4):1802–1810, 2014.

[14] H.-M. Shim, A. S. Myerson, and K.-K. Koo. Molecular Modeling on the Role of Local Concentration in the Crystallization of l-Methionine from Aqueous Solution. *Cryst. Growth Des.*, 16(6):3454–3464, 2016.

[15] H.-M. Shim and K.-K. Koo. Molecular Approach to the Effect of Interfacial Energy on Growth Habit of ϵ-HNIW. *Cryst. Growth Des.*, 16(11):6506–6513, 2016.

[16] J. Housty and M. Hospital. Localisation des atomes d'hydrogène dans l'acide adipique $COOH[CH_2]_4COOH$. *Acta Crystallogr.*, 1965.

[17] D. Eilerman and R. Rudman. Refinement of pentaerythritol. *Acta Crystallogr., Sect. B: Struct. Crystallogr. Cryst. Chem.*, 1979.

[18] C. F. Macrae, P. R. Edgington, P. McCabe, E. Pidcock, G. P. Shields, R. Taylor, M. Towler, and J. van de Streek. Mercury: visualization and analysis of crystal structures. *Journal of Applied Crystallography*, 39(3):453–457, 2006.

[19] P. Dandekar and M. F. Doherty. A mechanistic growth model for inorganic crystals: Solid-state interactions. *AIChE J*, 60(11):3707–3719, 2014.

[20] W. K. Burton, N. Cabrera, and F. C. Frank. The growth of crystals and the equilibrium structure of their surfaces. *Philos. Trans. R. Soc., A*, 243:299–358, 1951.

[21] J. Frenkel. On the surface motion of particles in crystals and the natural roughness of crystalline faces. *J. Phys. (Moscow)*, 9:392–398, 1945.

[22] M. A. Lovette and M. F. Doherty. Multisite models to determine the distribution of kink sites adjacent to low-energy edges. *Phys. Rev. E*, 2012.

[23] H. Cuppen, H. Meekes, E. van Veenendaal, W. van Enckevort, P. Bennema, M. Reedijk, J. Arsic, and E. Vlieg. Kink density and propagation velocity of the [0 1 0] step on the kossel (1 0 0) surface. *Surf. Sci.*, 506(3):183 – 195, 2002.

[24] M. A. Lovette and M. F. Doherty. Predictive Modeling of Supersaturation-Dependent Crystal Shapes. *Cryst. Growth Des.*, 12(2):656–669, 2012.

[25] J. P. Sizemore and M. F. Doherty. A stochastic model for the critical length of a spiral edge. *J Cryst Growth*, 312(6):785–792, 2010.

[26] D. Elwell and H. J. Scheel. *Crystal Growth from High-Temperature Solutions*. London: Academic Press,, 1975.

[27] J. A. Dirksen and T. A. Ring. Fundamentals of crystallization: Kinetic effects on particle size distributions and morphology. *Chem Eng Sci*, 46(10):2389–2427, 1991.

[28] H. Cuppen, H. Meekes, W. van Enckevort, and E. Vlieg. Kink incorporation and step propagation in a non-Kossel model. *Surf. Sci.*, 571(13):41 – 62, 2004.

[29] M. Haisa, S. Kashino, R. Kawai, and H. Maeda. The Monoclinic Form of *p*-Hydroxyacetanilide. *Acta Crystallographica Section B*, 1976.

[30] M. Leetmaa and N. V. Skorodumova. KMCLib: A General Framework for Lattice Kinetic Monte Carlo (KMC) Simulations. *Comput. Phys. Commun.*, 185:2340–2349, 2014.

[31] C. J. Tilbury, M. N. Joswiak, B. Peters, and M. F. Doherty. Modeling step velocities and edge surface structures during growth of non-centrosymmetric crystals. *Crystal Growth & Design*, 17(4):2066–2080, 2017.

Chapter 6

Implementation and Automation Strategy

Reproduced in part with permission from:

Jinjin Li, Carl J. Tilbury, Seung Ha Kim and Michael F. Doherty, "A design aid for crystal growth engineering," *Progress in Materials Science*, **2016**, *82*, 1-38.

DOI: 10.1016/j.pmatsci.2016.03.003. Copyright 2016 Elsevier.

Carl J. Tilbury, Mark N. Joswiak, Baron Peters and Michael F. Doherty, "Modeling Step Velocities and Edge Surface Structures during Growth of Non-Centrosymmetric Crystals," *Crystal Growth & Design*, **2017**, *17*, 2066-2080.

DOI: 10.1021/acs.cgd.7b00058. Copyright 2017 American Chemical Society.

6.1 Introduction

The mechanistic models presented thus far offer the ability to accurately predict shapes of crystalline products, according to the choice of growth conditions. Coupled with the theoretical understanding developed, these models can be implemented to en-

able rational design of crystalline products and engineer crystal shapes, tailoring them to specific applications. However, the utilization of these mechanistic models requires significant investment, both in developing the required expertise and building codes to execute the overall framework and underlying calculations at each stage.

To address this drawback and facilitate adoption of these methods, we have developed proof-of-concept software called ADDICT (Advanced Design and Development of Industrial Crystallization Technology). This program demonstrates the feasibility of automating mechanistic models, motivating their continued development, and is acting to transfer these techniques to industrial researchers in the pharmaceutical industry. ADDICT aims to be a visual and convenient prototype tool, useful for both theorists and experimentalists, that is simple enough for novice users to obtain rapid predictions, while enabling more experienced users extra functionality to cater for advanced design. This chapter provides an overview of ADDICT and strategies for model execution.

6.2 ADDICT: A Design Aid for Spiral Crystal Growth from Solution

ADDICT is designed to act both as a 'black box', for non-experts, and a transparent vehicle, for users proficient in mechanistic models. Thus, the base operation requires only three inputs:

1. The crystallography (ADDICT predictions are made for a specific polymorph)
2. A partial charge calculation (e.g., using Gaussian [1]/Antechamber [2])
3. Growth conditions: solvent, supersaturation, temperature

With these inputs, a shape prediction is produced (taking on the order of seconds or

minutes for a standard desktop PC). Thus, the main development of ADDICT has been to organize and execute the framework automatically for a general, non-centrosymmetric molecule. Beyond this fundamental execution, additional features include an automatic sweep of solvents to predict multiple habits, evaluation and visualization of possible shapes given the crystallography and provision of mechanistic data and parameters (i.e., insight into the calculations) to guide shape engineering. ADDICT is currently optimized for small organic molecules, however, future modifications are planned to broaden the applicability to organic salts, via inclusion of recent developments for ionic crystal systems [3–10]. This section provides a structural blueprint that describes the process of obtaining a crystal growth shape prediction for a real (i.e., complex, non-centrosymmetric) system.

The primary goal of ADDICT is to calculate relative growth rates of the predicted crystal faces for a specific solute polymorph and growth environment. Relative growth rates are sufficient to determine the crystal habit using the Frank-Chernov condition (see Section 6.2.5).

Since MATLAB is an ideal language to build a graphical user interface tool, most codes of ADDICT are written in MATLAB, with some compiled C codes integrated into the program to improve computational efficiency. To deal with ADDICT's complexity and manage different types of information, object-oriented program design is applied, where classes are created for various types of information (e.g. lattice symmetry, growth unit/kink/edge/plane properties). A full account of ADDICT's internal operation is beyond the scope of this chapter, which will instead provide an overview of its function without addressing finer computational details. The main structure of ADDICT can be divided into 5 modules:

(1) *Input parameter preparation.* This generates the input panel, which reads the crystallography input alongside all growth conditions and program operation specifications. Partial charges are obtained using external electron density calculation software.

(2) *Solid-state interactions.* A lattice supercell is generated along with all solid-state interactions using the Generalized Amber Force Field (GAFF) [11], which is applied internally within ADDICT.

(3) *Plane and periodic bond chain (PBC) determination.* The relevant crystal planes and their corresponding PBCs are determined.

(4) *Energetic and mechanistic calculations.* The important quantities for the crystal growth model are evaluated (e.g., kink densities, net attachment rates, step velocities etc.) and used to calculate relative growth rates of the crystal faces.

(5) *Outputs.* ADDICT's results are generated and displayed.

This blueprint is presented in Figure 6.1. The segments are colored according to functionality, each of which will now be discussed in more detail.

6.2.1 Input Parameter Preparation (Yellow)

The input panel in ADDICT reads specifications of the crystal system, growth conditions (temperature, solvent, supersaturation) and desired program functionality. One can browse for the crystallography input file and select a directory to save the results. Crystallography data can be provided by a CIF (Crystallographic Information File) or PDB (Protein Data Bank) file format and ADDICT is currently compatible with 194 out of 230 space groups. The user may select either a monomer or dimer growth unit; when a dimer is selected ADDICT treats interactions between the constituent dimer growth units as intramolecular and ignores them, while all the relevant intermolecular interactions between separate dimer pairs are used to calculate inter-dimer interactions.

Cell lengths and angles, atoms types and positions, and symmetry operations are read, stored and used to generate a Gaussian 09 input file (.com), which must be used to perform an electron density calculation with the commercial software [1]. The default

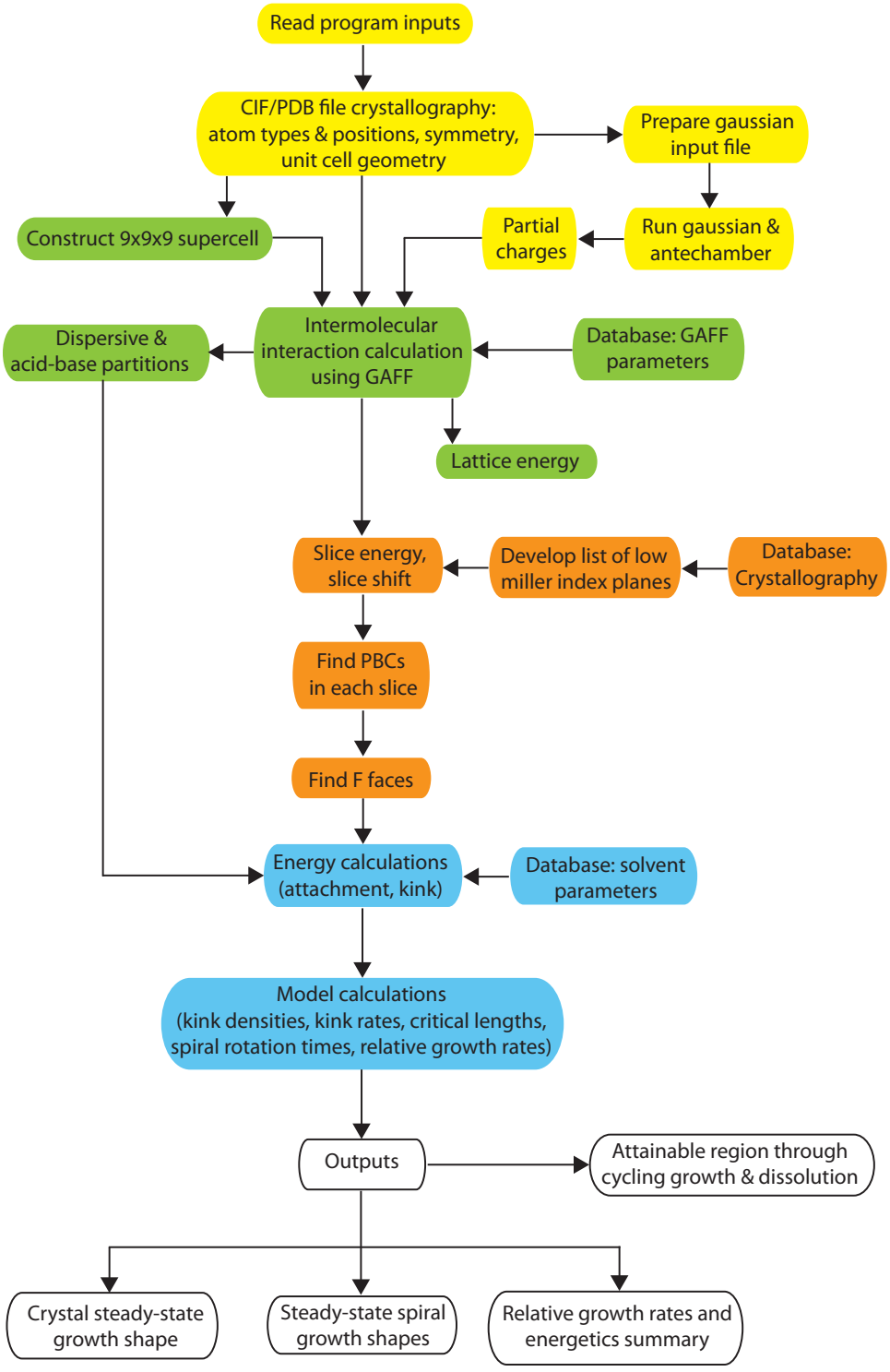

Figure 6.1: Schematic diagram for the structure of ADDICT.

functional and basis set in the .com file are B3LYP/6-31G*, which could be adjusted by an expert user. Antechamber from AmberTools (open source software) [2] must then be run, using the Gaussian output to calculate restrained electrostatic potential (RESP) charges, for a more accurate description of the electron density than the Mulliken point charges calculated using Gaussian. The output from Antechamber is a .mol2 file which should be added to the same directory as the CIF/PDB file before continuing to run ADDICT.

6.2.2 Solid-State Interactions (Green)

From the crystallography, symmetry operations are applied to the asymmetric unit to generate the unit cell, which is translated in the crystallographic directions to form a $9 \times 9 \times 9$ supercell. Intermolecular interactions within the supercell are then calculated using the GAFF parameter database within ADDICT and the obtained RESP point charges; Kirkwood-Slater mixing rules are used to determine atom-atom parameters using polarizabilities [12]. A cutoff distance beyond which interactions are neglected is determined by considering lattice energy convergence. If an intermolecular interaction is included, even interatomic interactions with distances larger than the cutoff must be included to ensure there are no false coulombic artifacts from the atomic partial charges. The total interaction strengths are stored, alongside dispersive (r^{-6}) and coulombic (r^{-1}) portions in order to appropriately modify energetics in accounting for the solvent effect later (see Section 6.3.3).

6.2.3 Plane and PBC Determination (Orange)

As described in Section 6.3.1, a list of low Miller index planes is developed according to the crystal space group, alongside the most stable slice for each; following this, PBCs

are determined for each slice.

The default slice shift setting is 'Auto Slice', where the selected number of displacements (4 by default) are generated to shift the slice incrementally from its initial position up to a single interplanar spacing. If 'No Slice' was selected then no shifting occurs and the 'User-Defined' option allows specification of both the number of slices and the displacement between each slice (removing the constraint of reaching a displacement of one interplanar spacing). The highest slice energy configuration is selected, but this is an advanced technique that is often not required.

6.2.4 Energetic and Mechanistic Calculations (Blue)

This section calculates parameters for, and then executes, the mechanistic growth model on each face. Relevant energies (e.g. kink/edge/terrace energy at each site) are calculated, accounting for the solvent (see Chapter 4; parameters for 31 solvents are presently contained within ADDICT). The identified PBC directions are taken as spiral edges; step velocities are determined, and spiral rotation times are calculated for each face (on a relative basis). Note the current formulation of the spiral model within ADDICT is based on ref. [13], but the program is being steadily upgraded to incorporate the recently developed models described in Chapters 3 and 5.

With the growth rate of a face expressed as $G = h/\tau_S$, the relative growth rates of faces (with reference to the slowest-growing facet) are then calculated, to remove the need to estimate $\Delta G^{\ddagger}$ and ν_0, as discussed in Chapter 3. Absolute growth rates cannot be calculated without estimates for these uncertain parameters, hence our predictions are for the crystal shape, not size.

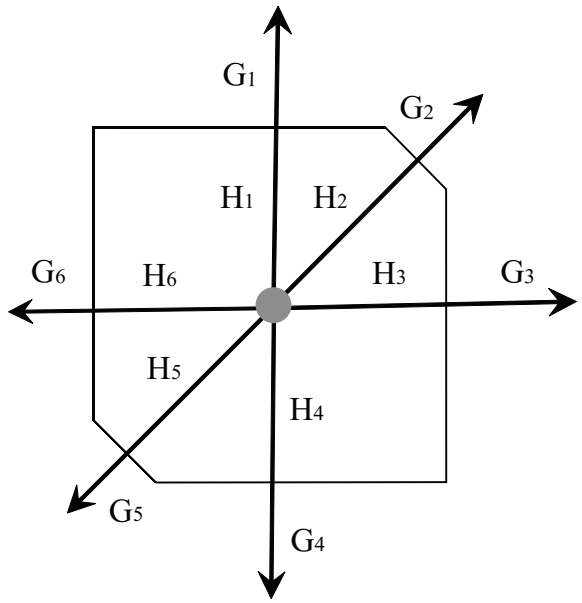

Figure 6.2: The Frank-Chernov condition to predict the steady-state growth morphology, considering a cross-sectional view of the crystal showing 6 faces, where G_i is the growth rate of face i and H_i is the perpendicular distance of face i from the center of the crystal.

6.2.5 Outputs (White)

From the relative growth rates, one can predict the steady-state crystal morphology by re-casting the Frank-Chernov condition [14, 15] (Figure 6.2) to:

$$\frac{R_1}{X_1} = \frac{R_2}{X_2} = \frac{R_3}{X_3} = \frac{R_{n-1}}{X_{n-1}} = 1 \tag{6.1}$$

where $R_i = G_i/G_n$ is the growth rate of face i relative to a reference face n and $X_i = H_i/H_n$ is the perpendicular distance of face i from the crystal center relative to the corresponding distance for face n. The X_i values are used in ADDICT to construct the steady-state growth shape of the crystal.

Upon running ADDICT, outputs appear within the graphical user interface. The

steady-state crystal growth shape is rendered, alongside spiral shapes on each face. Relative growth rates and relevant energetics are also available and saved as data files. The attainable region sub-module allows the user to discover the range of possible shapes through cycles of growth and dissolution [16].

6.3 Practical Considerations for Model Implementation

While Section 6.2 provides an overview of the implementation strategy, there are a variety of subtleties at each stage of the mechanistic shape calculation. These considerations are discussed in the following sections, to provide more detailed insight.

6.3.1 Periodic Bond Chain (PBC) Algorithm

Based on the theory established by Hartman and Perdok (Section 1.2.1), ADDICT calculates relative growth rates of flat 'F' faces (stepped and kinked faces are assumed to grow fast in comparison). If a stepped/kinked face cannot grow out and lead to a closed solid object, a needle-like or plate-like crystal could form, in which case an arbitrarily large relative growth rate is assumed. For each F face, ADDICT identifies a slice, which has a thickness corresponding to the deposited layer for a single elementary growth step.

The Generalized Amber Force Field (GAFF) [11] is used in ADDICT to determine intermolecular interactions; GAFF extended AMBER [17] from proteins to pharmaceutical molecules for use in drug design and should, therefore, be sufficient to accurately describe API molecules. The total interaction is divided into dispersive and coulombic portions using the corresponding GAFF terms, which is required for the solvent effect (see Section 6.3.3).

ADDICT currently works for pure organic molecules, where nearest-neighbor interactions in the crystal dominate the lattice energy due to a lack of significant charges that could result in a larger coulombic term in GAFF (the long-ranged portion of the interaction). In ADDICT, an energy cutoff is used in forming PBCs, which can be modified in the input panel. Typically a cutoff of 1 kT allows the PBCs to represent at least 90% of the lattice energy, while exclusively containing nearest neighbor interactions. From this point on the energetics are assumed to be completely represented by the PBCs.

ADDICT calculates the growth of F faces that are important for a particular space group, based on extinction conditions. To calculate the intermolecular bonds used to form PBCs, all interatomic interactions between a pair of growth units are summed, with the bond vector determined using the center of mass of each growth unit. PBCs are easily determined for centrosymmetric crystal structures, such as naphthalene, since each intermolecular bond corresponds to a PBC: the same bond into a growth unit from one side extends out in the exact opposite direction on the other side (energies are identical). Thus, centrosymmetric growth units produce straight PBCs, and growth units or kink sites along an edge are identical in terms of energy. For non-centrosymmetric structures, such as paracetamol, lovastatin and RDX (1,3,5-Trinitroperhydro-1,3,5-triazine), the determination of PBCs is much more complicated and the constituent bonds of a repeat PBC unit are in general not all aligned with the overall PBC direction (the PBCs can be somewhat jagged along the overall straight direction).

The PBC algorithm for non-centrosymmetric systems in ADDICT uses a combination of hard and "soft" rules in order to optimize the selection of PBCs for each slice. This method could benefit other crystallography researchers, since periodic bond chains are a useful tool in understanding crystal growth and their determination for non-centrosymmetric systems is non-trivial.

Figure 6.3 summarizes the algorithm. Firstly, the slice is defined; the PBC algorithm

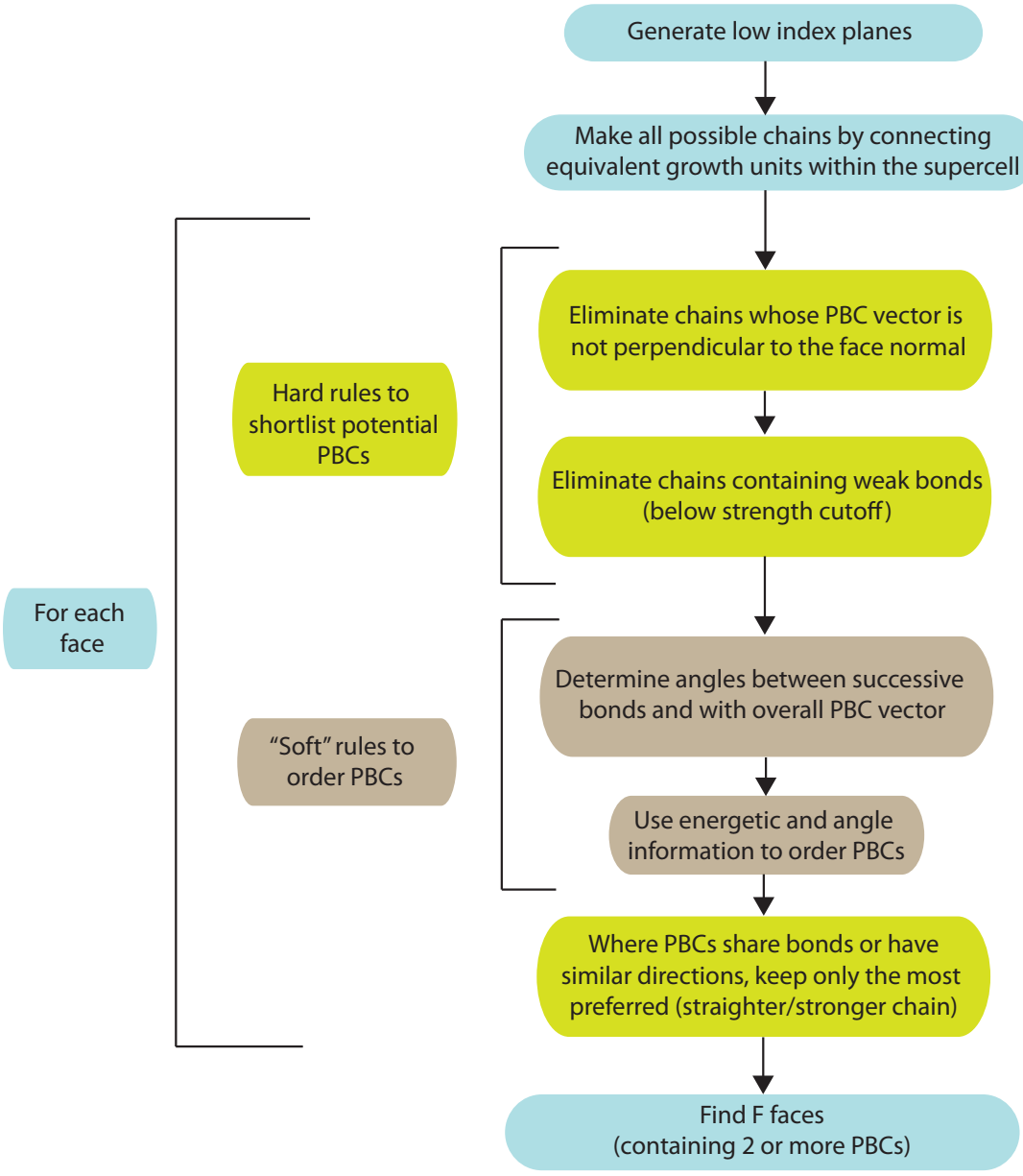

Figure 6.3: Algorithm for finding PBCs and F faces.

is applied on each face individually. A list of the lowest Miller index faces is developed and the unique faces in each direction are selected to investigate, from which the slice thickness is defined based on the interplanar spacing (which can be calculated from the Miller indices). Symmetry (extinction) conditions for the crystal polymorph's space group are applied to determine if a reduced interplanar spacing should be selected in any direction, which corresponds to a set of higher Miller indices and can exist for the special directions in the space group lattice where symmetry dictates repeated slices per unit cell as the face grows.

The second step is to generate a list of all possible periodic bond chains. The core concept is that to be periodic, chains must contain a repeat unit which starts and ends on the same growth unit. Chains can, therefore, be generated by considering each growth unit within the crystal and connecting two such growth units by a path of additional growth units. Single connection chains directly connect growth units, 2-connection chains separate growth units by bonding to a different growth unit and so on. Single connection chains are developed by considering each growth unit within the crystal lattice in turn and finding the intermolecular interactions that connect it to itself. In developing 2-connection chains, for each growth unit considered as the start and end points, one must loop through other growth units (and their different positions within the supercell) that can act as an intermediate connection. This tactic is continued for higher connection chains and does not change except in complexity. While forming these chains, one can apply priority rules to determine whether such a chain is remotely physical and warrants further investigation. Firstly, the PBC vector defining the repeat unit cannot have any component perpendicular to the slice, because upon extending the chain indefinitely it will not remain in the slice. Secondly, chains should not be formed using any intermolecular bonds under the strength cutoff provided in the input panel. This should be of the order 1 kT or lower (corresponding to the roughening transition [18–20]) and if no value

is provided ADDICT uses 0.2 kcal/mol by default. These two rules enable the search for candidate PBCs to be reduced to a practical problem using the above approach based on connecting growth units in a periodic fashion.

With the list of candidate chains, ADDICT ranks PBCs based on soft priorities, in order to select the best PBCs for that slice. The desire is to have PBCs correspond to the most stable step edges on a crystal surface, i.e., those sides naturally emerging from a screw dislocation during spiral growth, which is why the algorithm effectively finds the most physically stable surface structures. ADDICT treats each spiral itself as a faceted object composed exclusively of those in-slice PBCs. Such straight-sided spirals have been experimentally imaged [21, 22] and this picture is essentially exact while the step edges remain below their roughening transition; above this point, step curvature begins to appear. The assumption of straight edges is expected to be valid in the spiral regime and, with relative growth rates being calculated (Section 6.2.5), errors introduced from this approximation should prove inconsequential.

The main priority in ranking PBCs is to consider tradeoffs between straightness and strength. In general, the least jagged chain in the edge direction should be selected; angles between successive bonds or between a bond and the overall PBC vector should be considered. Protrusion in the edge/reverse-edge direction is most important; in contrast, the terrace/reverse-terrace direction is largely irrelevant from the perspective of determining PBCs (it is, however, critically important in predicting fill order of kinks or step rows). Ordering PBCs with respect to this strength and straightness information is necessarily subjective, but providing enough PBCs are considered the subsequent calculations will not be affected (unimportant PBCs will grow out of spirals and not affect the rotation time calculation, see eq 3.22). Nonetheless, when bonds are shared or the PBC vector is very similar between multiple PBCs, the chain with higher priority can be kept and the other eliminated, leaving unique PBCs that offer the 'best use' of interactions

within the slice to form low-edge energy spiral sides with maximum in-chain interactions.

The slice can be shifted, while maintaining its thickness that is defined by the Miller indices, in order to maximize the slice energy (the contained PBCs). This is an advanced technique and often unnecessary, but for complicated non-centrosymmetric cases where the slice is not readily apparent, it can be useful to once again ground the model in an energetically favorable face and edge configuration, which is essential in moving forward for the mechanistic growth calculation to be applicable.

6.3.2 Step Velocity Calculation

Implementing the step velocity model described in Chapter 5 requires some additional considerations. First, sites must be correctly identified. To assist with this, we illustrate the non-centrosymmetric kink density calculation and site identification, by example, in Appendix 6.A. We chose naphthalene to describe the process, since two growth units exist from the perspective of lattice orientation. Thus, Appendix 6.A also demonstrates the appropriate collapse of our non-centrosymmetric formulation to the expected centrosymmetric expressions, when energetics are such to render growth units equivalent. Furthermore, Appendix 6.A describes determination of the fill order along an edge (or as the step advances).

Second, in Section 5.3.3, we indicated that an isotropic x_{sat} (i.e., common to each edge on the crystal) was required for a consistent implementation of our model. The following describes some practical aspects to achieve this under solution growth.

Calculating x_{sat} for Solution Growth

To ensure model consistency, we established that the value of $\overline{\Delta W}_{sat}$, which corresponds to maximal kink cycles, must be the same regardless of edge. This average

detachment work $\overline{\Delta W}_{sat}$ also represents the average growth unit binding energy to the lattice, which includes every crystal interaction for maximal cycles. Under vapor growth the detachment work includes only the solid-state interactions, since there are no solution effects; thus, the vapor-growth $\overline{\Delta W}_{sat}$ is simply the lattice energy of the crystal. When periodic bond chains (PBCs) can be approximated as the only relevant solid-state interactions, the vapor-growth $\overline{\Delta W}_{sat}$ then corresponds to the PBC portion of the lattice energy.

For solution growth, the surface energetics are modified to account for interfacial solvent effect (see Chapter 4); in this case, $\overline{\Delta W}_{sat}$ depends on the surfaces (interfaces) that are created upon growth unit detachment. The energetic-modification process is applied to each site-specific surface, containing some subset of the total interactions; since each individual intermolecular interaction will extend from various surfaces across different edges/faces, the effect of this modification will vary slightly with location. An artifact of this technique is the introduction of minor edge variation in $\overline{\Delta W}_{sat}$. To ensure consistency, one should determine an average value for $\overline{\Delta W}_{sat}$ following the solvent modification and then rescale the solvent-modified surface energies at each site to converge all maximal cycles to this average value of $\overline{\Delta W}_{sat}$ and, therefore, maintain an isotropic value for x_{sat}.

6.3.3 Solvent Effects

Chapter 4 described the process of modifying interfacial energies to account for the solvent, from the perspective of using the CLP force field [23]. Since ADDICT uses the Generalized Amber Force Field (GAFF), we will briefly mention how crystal energies are divided into dispersive and acid-base contributions. First, locations of potential acid-base interactions are found by analyzing PBCs with a large coulombic character (r^{-1}

term in GAFF). The dispersive portion of crystal energy is calculated by multiplying the total PBC interaction strengths by $d/(d+c)$, where d and c correspond to the r^{-6} and r^{-1} terms from GAFF, respectively. The acid-base portion is calculated by multiplying instead by $c/(d+c)$. This fractional treatment is used because partitioned force field terms are less reliable than the total interaction energy [24].

6.4 Conclusions

This chapter demonstrates the automated execution feasibility of mechanistic models and describes their implementation from the perspective of proof-of-concept software, ADDICT. The program has been tested for a variety of organic compounds and predicted shapes are generally in good agreement [25] with experimental reports. Additionally, ADDICT makes it possible to evaluate a wide variety of crystal systems quickly. As a result, it allows us to identify deficiencies in the methodology that are otherwise difficult to uncover and permits rapid testing of alternative approaches. Model augmentations that further improve accuracy or applicability can then be incorporated. Indeed, ADDICT is being continually upgraded based on concurrent research developments.

ADDICT currently implements a model for spiral growth, so supersaturation-dependent shape effects that result from transitioning to different growth mechanisms (i.e. 2D nucleation) are not yet accounted for. Note that the kink rate for non-centrosymmetric molecules has a complex supersaturation-dependence that leads to relative growth rates that do depend on the supersaturation (albeit usually to a minor degree) even with all faces in the spiral regime. For centrosymmetric systems however, there is no dependence on supersaturation for the relative spiral growth rates (see eq 3.73), so shapes are independent of supersaturation. These limitations are likely acceptable for the controlled synthesis of pharmaceuticals, where low supersaturations and a spiral regime are

applicable.

Appendices

6.A Kink Density Example: Naphthalene Face (001)

We demonstrate the non-centrosymmetric kink density calculation for a real crystal by considering the [010] and [110] steps on the (001) face of naphthalene under sublimation growth. This is an example of a centrosymmetric crystal containing two centrosymmetric growth units, which are equivalent in terms of interaction energetics but distinct from the perspective of lattice orientation. This section will demonstrate the collapse of our new non-centrosymmetric formulation to the centrosymmetric case.

Figure 6.4 indicates our growth unit definitions for naphthalene. Tables 6.2a and 6.2b contain the energetic parameters for the [010] and [110] steps, respectively, on face (001). Refer to the subsequent figures for visualization of the relevant in-slice intermolecular interactions responsible for these energetics. Under sublimation, the kink energy is half the total kink-direction periodic bond chain (PBC) strength; edge energies similarly involve half interaction strengths of PBCs extending from that growth unit in the edge direction. For the centrosymmetric case reverse kink/edge/terrace energies are equivalent to their kink/edge/terrace counterparts, which is clearly demonstrated by the symmetry evident in the forthcoming step images. Furthermore, note that the detachment work, ΔW, is the same for each step; as indicated in Chapter 5, symmetry dictates that a centrosymmetric system will show this isotropic nature.

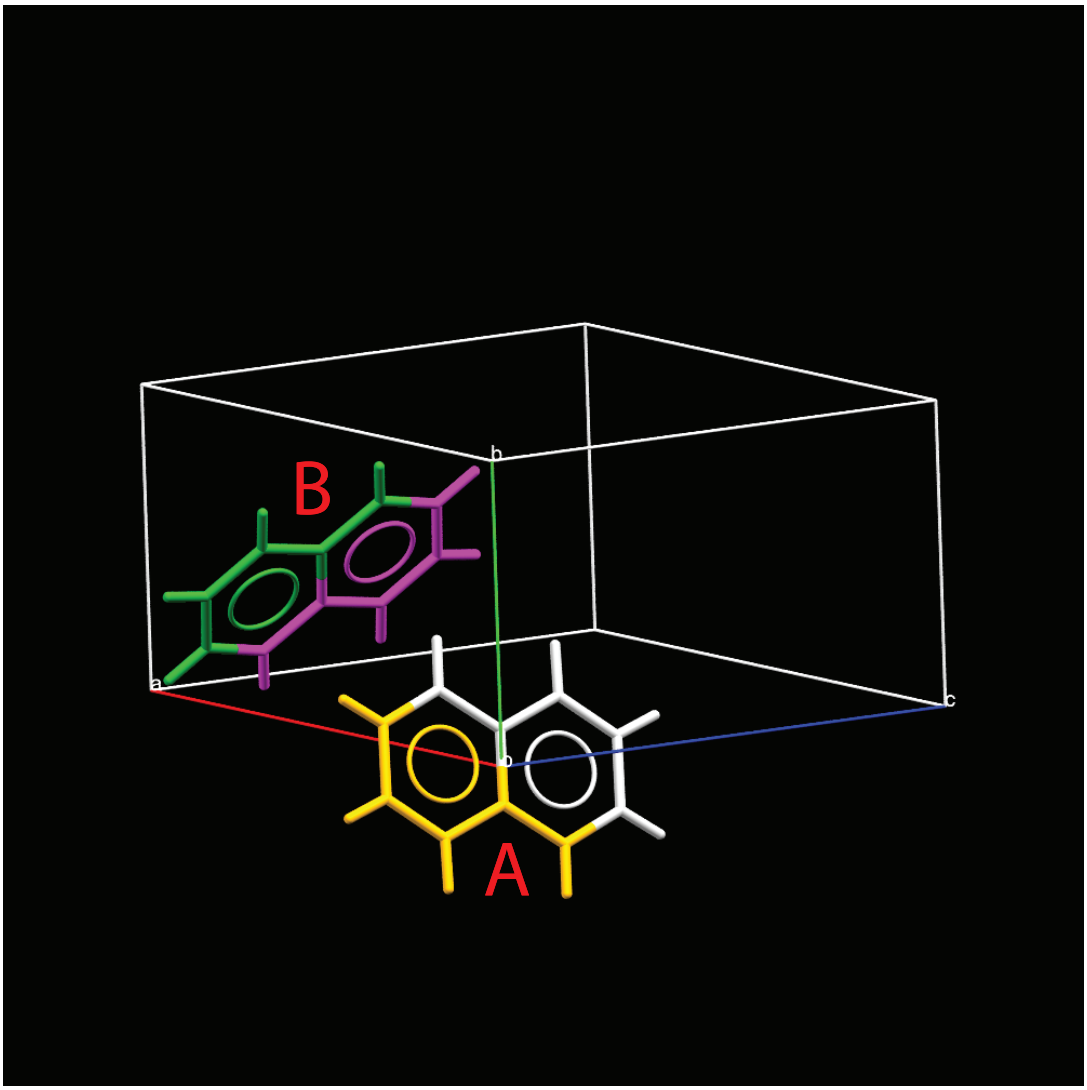

Figure 6.4: A and B growth units for naphthalene.

Table 6.1: Energetic parameters for the (a) [010] and (b) [110] steps on face (001) of naphthalene (sublimation growth at $T = 283K$, calculated using the CLP force field [23]). Note that although 2 growth units exist, A and B parameters are identical due to symmetry. All values are in units of kT.

	A	B
E_{PBC}	6.0	6.0
$\phi^K = \phi^{RK}$	3.0	3.0
$\phi^E = \phi^{RE}$	7.7	7.7
$\phi^T = \phi^{RT}$	3.9	3.9
ΔW	29.2	29.2

(a) Step 010

	A	B
E_{PBC}	7.7	7.7
$\phi^K = \phi^{RK}$	3.9	3.9
$\phi^E = \phi^{RE}$	6.8	6.8
$\phi^T = \phi^{RT}$	3.9	3.9
ΔW	29.2	29.2

(b) Step 110

6.A.1 Step [010]

The [010] step on the (001) face of naphthalene contains two rows, each with a single growth unit. The following sites must be considered:

- A0 (A edge site)
- B0 (B edge site)
- A1W (west A single-kink)
- A1E (east A single-kink)
- B1W (west B single-kink)
- B1E (east B single-kink)
- A2W (west AB double-kink)
- A2E (east AB double-kink)
- B2W (west BA double-kink)
- B2E (east BA double-kink)

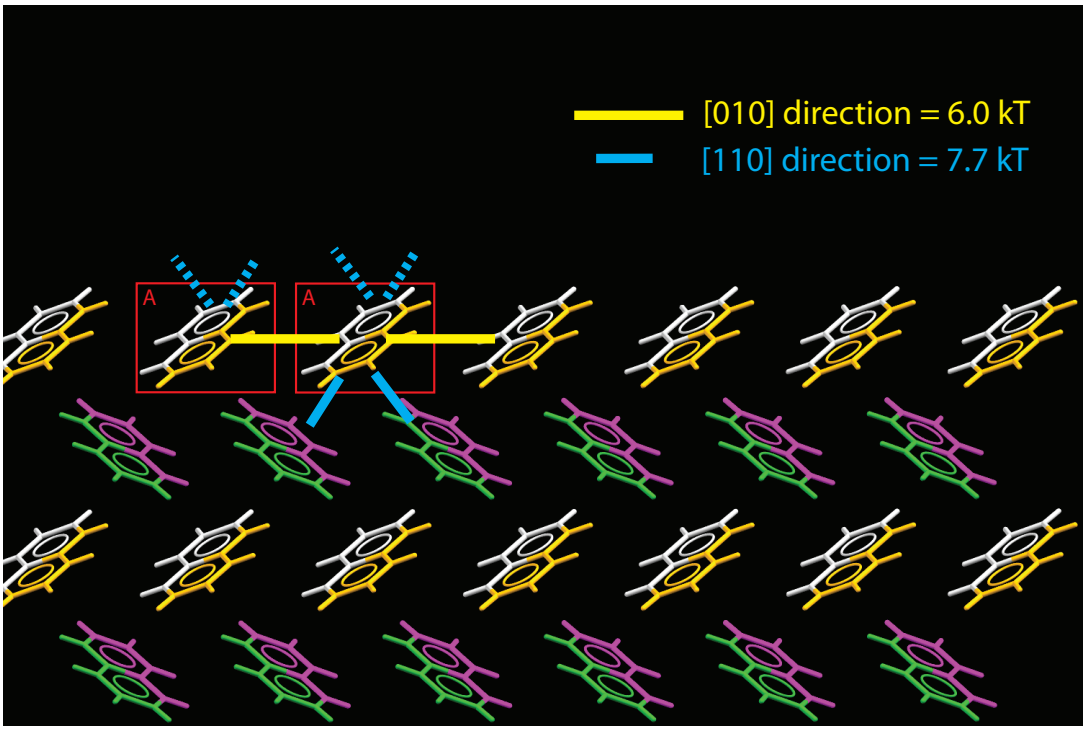

Figure 6.5: A0 edge site. The relevant intermolecular in-slice interactions are also pictured. Edge energy interactions correspond to surface energies, which represent half of the solid-state interaction strength. For our Boltzmann weighting we use a further half of the edge energy for each growth unit either side of the junction. Terrace interactions are not pictured.

Figure 6.5 shows the definition of an A0 edge site. Since there are no kink energy contributions, the Boltzmann weighting (w_{A0}) is half the combined row-averaged edge and terrace energy from each growth unit either side of the junction: $w_{A0} = 1/2(\phi_A^E + \phi_A^T + \phi_A^E + \phi_A^T) = \phi_A^E + \phi_A^T$.

Figure 6.6: B0 edge site indicating edge interactions.

Figure 6.6 shows the definition of an B0 edge site. The Boltzmann weighting (w_{B0}) is: $w_{B0} = 1/2(\phi_B^E + \phi_B^T + \phi_B^E + \phi_B^T) = \phi_B^E + \phi_B^T$.

Figure 6.7 shows the definition of a A1W and A1E single-kink sites (west and east). The Boltzmann weighting is identical for east and west; it accounts for the full kink energy exposed and half the (row-averaged) edge + terrace energy from the growth units either side: $w_{A1W} = w_{A1E} = \phi_A^K + 1/2(\phi_B^E + \phi_B^T + \phi_A^E + \phi_A^T)$. It is clear that for this case the successive rows of growth units are not aligned perfectly on top of each other. Although in Chapter 5 we drew our examples with aligned growth units for convenience, in reality this skewed nature is common. This illustrates the importance of formulating row-averaged edge and terrace energies for the Boltzmann weightings, to avoid the need to decide which growth unit's edge energy should be included. In Figure 6.7, selecting the partially exposed B growth unit below the A growth unit would render a different edge + terrace contribution and not reflect a full growth unit. For step [010], each row has only a single growth unit, so the row-averaging has no effect, but a full growth unit must be used.

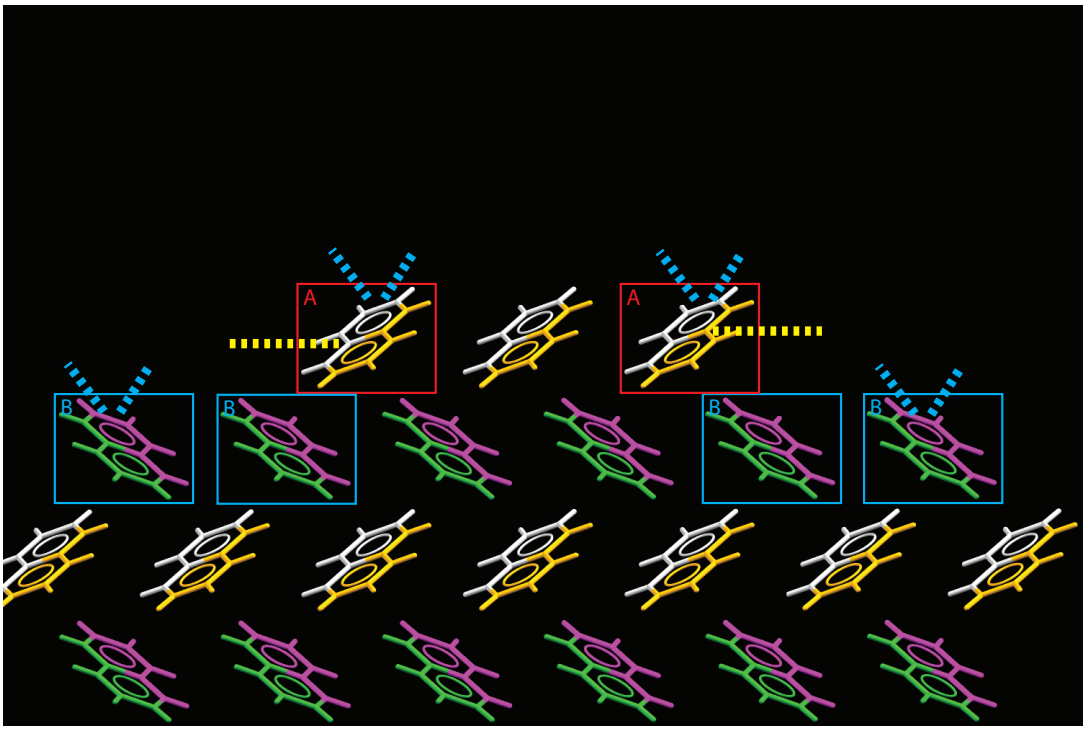

Figure 6.7: A1W and A1E single-kink sites (west=left and east=right), indicating kink and edge-direction interactions.

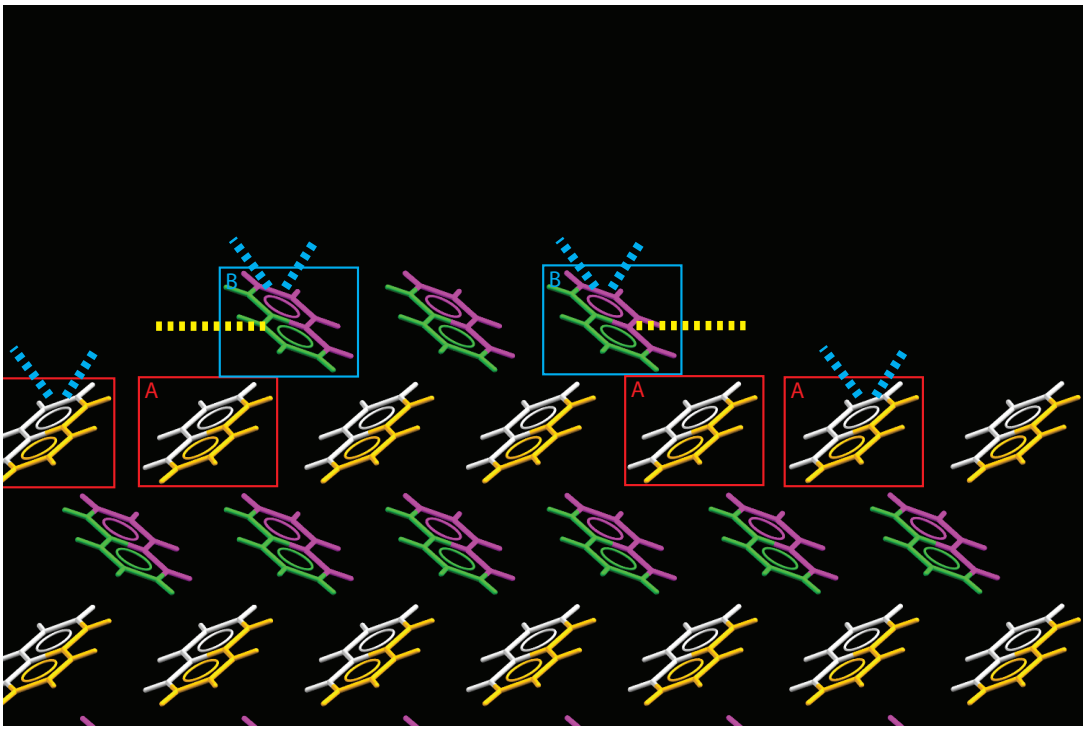

Figure 6.8: B1W and B1E single-kink sites (west and east), indicating kink and edge-direction interactions.

Figure 6.8 shows the definition of B1W and B1E single-kink sites (west and east). Both Boltzmann weightings are $w_{B1W} = w_{B1E} = \phi_B^K + 1/2(\phi_B^E + \phi_B^T + \phi_A^E + \phi_A^T)$.

Figure 6.9 shows the definition of A2W and A2E AB-double-kink sites (west and east). The Boltzmann weightings are: $w_{A2W} = w_{A2E} = \phi_A^K + \phi_B^K + 1/2(\phi_A^E + \phi_A^T + \phi_A^E + \phi_A^T) = \phi_A^K + \phi_B^K + \phi_A^E + \phi_A^T$. Figure 6.9 also indicates another complication: which way is the double kink oriented? Figure 6.10 illustrates an alternative choice of double-kink surface structure. To determine which option is most physically realistic, we need to consider the optimal fill order. If overhangs are not permitted, the structures in Figure 6.9 must be formed regardless of which starting kink is realistic. Thus, we can consider which attachment event is most favorable at this point. We can determine the ΔW that would result from attachment at a position (equivalently, the detachment work of removing a growth unit that was deposited in such a position). In Figure 6.9, the growth unit attachment work to the B row is greater than the A row, due to the completion of an extra [110] interaction. This justifies our selection of Figure 6.9 as the optimal surface structure and indicates that Figure 6.10 is *not* physically realistic. Note for the centrosymmetric case distinguishing between these options is not required, since they produce identical mechanistic results due to symmetry. However, our tactic for fill order determination (maximizing the attachment work at each sequential event) becomes important when non-centrosymmetric skewed double-kinks must be considered. Furthermore, this consideration is equally important in determining the order of step row deposition during edge advance. From this point on, all figures will indicate the double-kink starting structures according to this rule of maximizing ΔW.

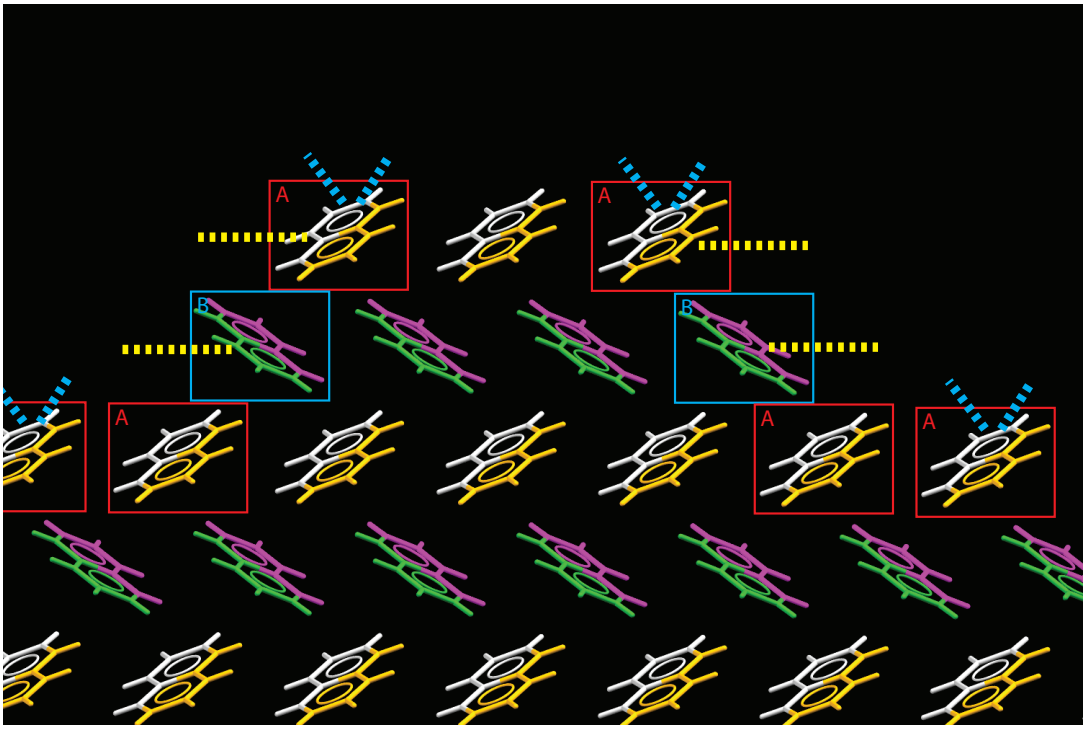

Figure 6.9: A2W and A2E AB-double-kink sites (west and east).

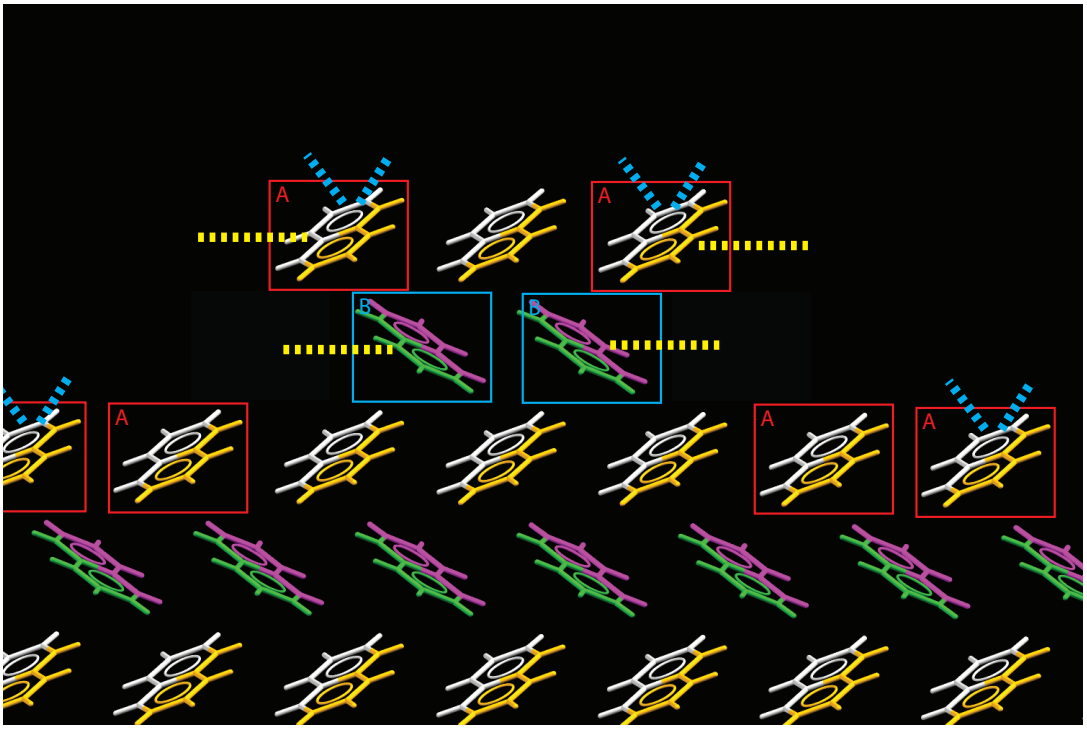

Figure 6.10: Unfavorable AB double-kink sites.

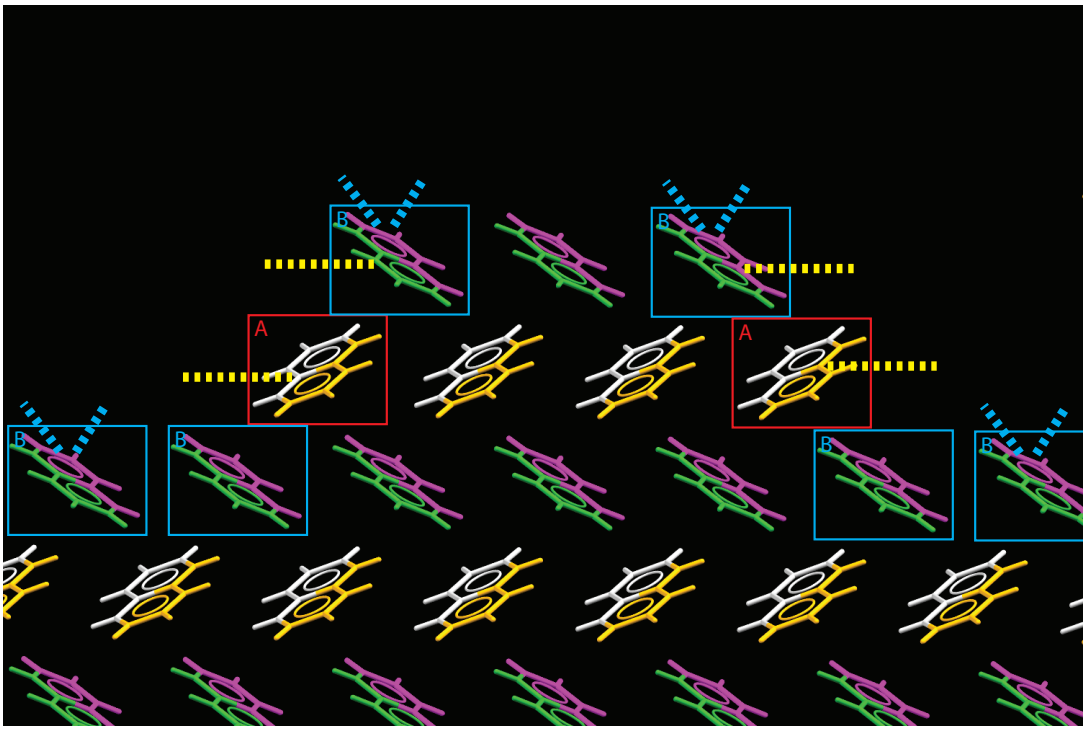

Figure 6.11: B2W and B2E BA-double-kink sites (west and east).

Figure 6.11 shows the definition of B2W and B2E BA-double-kink sites (west and east). The Boltzmann weightings are: $w_{B2W} = w_{B2E} = \phi_A^K + \phi_B^K + 1/2(\phi_B^E + \phi_B^T + \phi_B^E + \phi_B^T) = \phi_A^K + \phi_B^K + \phi_B^E + \phi_B^T$.

The partition function for the Boltzmann distribution, $Q_{[110]}$ accounts for each possible site (note $\beta = 1/kT$):

$$\begin{aligned} Q_{[110]} = &\exp\left(-\beta w_{A0}\right) + \exp\left(-\beta w_{B0}\right) \\ &+ \exp\left(-\beta w_{A1E}\right) + \exp\left(-\beta w_{A1W}\right) + \exp\left(-\beta w_{B1E}\right) + \exp\left(-\beta w_{B1W}\right) \\ &+ \exp\left(-\beta w_{A2E}\right) + \exp\left(-\beta w_{A2W}\right) + \exp\left(-\beta w_{B2E}\right) + \exp\left(-\beta w_{B2W}\right) \end{aligned} \tag{6.2}$$

Since each growth unit has identical interactions (centrosymmetric case, see Table 6.2b), we find $w_{A0} = w_{B0} \equiv w_0$, $w_{A1W} = w_{A1E} = w_{B1W} = w_{B1E} \equiv w_1$ and $w_{A2W} = w_{A2E} = w_{B2W} = w_{B2E} \equiv w_2$, with the following definitions:

$$w_0 = \phi^E + \phi^T \tag{6.3}$$

$$w_1 = \phi^K + \phi^E + \phi^T \tag{6.4}$$

$$w_2 = 2\phi^K + \phi^E + \phi^T \tag{6.5}$$

Our kink densities reduce to

$$\rho_{single} = \frac{4\exp\left(-\beta w_1\right)}{Q_{[110]}} \tag{6.6}$$

$$= \frac{4\exp\left(-\beta w_1\right)}{2\exp\left(-\beta w_0\right) + 4\exp\left(-\beta w_1\right) + 4\exp\left(-\beta w_2\right)} \tag{6.7}$$

$$= \frac{4\exp\left(-\beta(\phi^K + \phi^E + \phi^T)\right)}{2\exp\left(-\beta(\phi^E + \phi^T)\right) + 4\exp\left(-\beta(\phi^K + \phi^E + \phi^T)\right) + 4\exp\left(-\beta(2\phi^K + \phi^E + \phi^T)\right)} \tag{6.8}$$

$$= \frac{2\exp\left(-\beta\phi^K\right)}{1 + 2\exp\left(-\beta\phi^K\right) + 2\exp\left(-2\beta\phi^K\right)} \tag{6.9}$$

and

$$\rho_{double} = \frac{4\exp\left(-\beta w_2\right)}{Q_{[110]}} \tag{6.10}$$

$$= \frac{4\exp\left(-\beta w_2\right)}{2\exp\left(-\beta w_0\right) + 4\exp\left(-\beta w_1\right) + 4\exp\left(-\beta w_2\right)} \tag{6.11}$$

$$= \frac{4\exp\left(-\beta(2\phi^K + \phi^E + \phi^T)\right)}{2\exp\left(-\beta(\phi^E + \phi^T)\right) + 4\exp\left(-\beta(\phi^K + \phi^E + \phi^T)\right) + 4\exp\left(-\beta(2\phi^K + \phi^E + \phi^T)\right)} \tag{6.12}$$

$$= \frac{2\exp\left(-2\beta\phi^K\right)}{1 + 2\exp\left(-\beta\phi^K\right) + 2\exp\left(-2\beta\phi^K\right)} \tag{6.13}$$

Equations 6.9 and 6.13 are identical to eqs 5.46 and 5.47; thus, our non-centrosymmetric treatment of this centrosymmetric edge collapses to the expected centrosymmetric expressions.

Table 6.2a (and 6.2b) further demonstrates that an isotropic ΔW exists for centrosymmetric systems. Thus, each kink cycle produces the same net incorporation rate. As indicated in Chapter 5, transformations are not relevant for this case and the step velocity simply results from the combined kink density multiplied by this isotropic kink rate.

6.A.2 Step [110]

The [110] step on the (001) face of naphthalene contains a single row that contains both A and B growth units. The following sites must be considered:

- A0 (AB edge site)
- B0 (BA edge site)
- A1W (west A single-kink)

- A1E (east A single-kink)
- B1W (west B single-kink)
- B1E (east B single-kink)
- A2W (west AB double-kink)
- A2E (east AA double-kink)
- B2W (west BA double-kink)
- B2E (east BB double-kink)

Figures 6.12 - 6.16 portray these kink structures; Boltzmann weights are provided in the captions. Note that each row is identical and has row-averaged terrace + edge energy equal to $0.5(\phi_A^E + \phi_A^T + \phi_B^E + \phi_B^T)$.

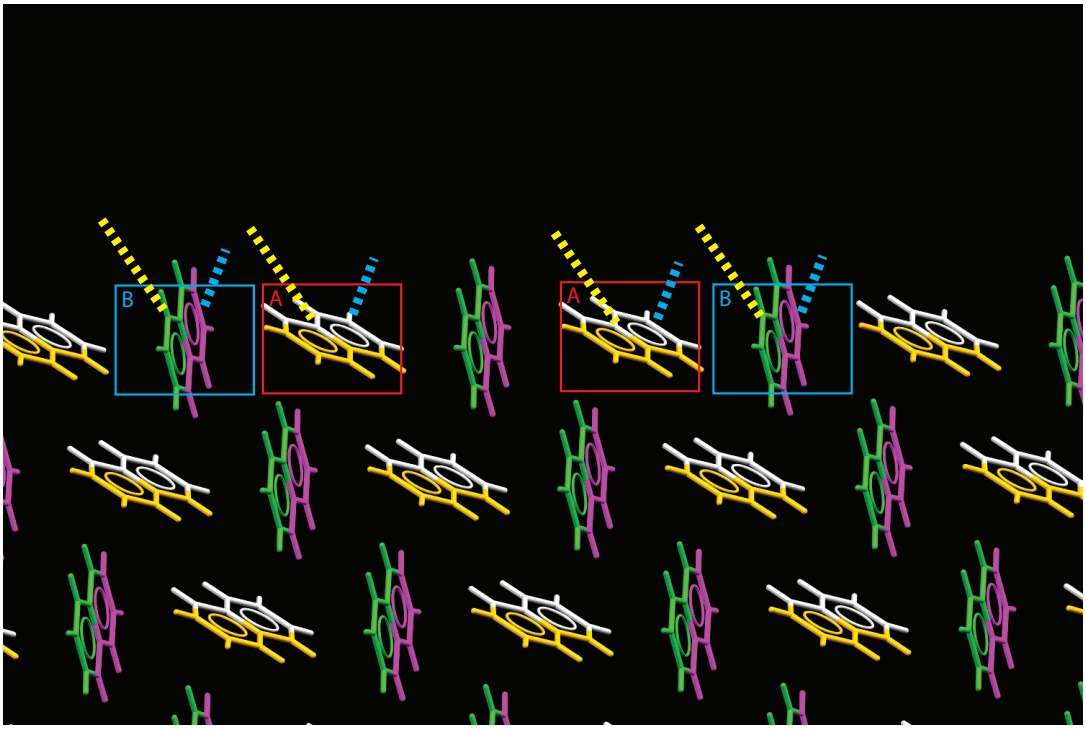

Figure 6.12: A0 AB-edge (right) and B0 BA-edge (left) sites. Boltzmann weights: $w_{A0} = w_{B0} = 0.5(\phi_A^E + \phi_A^T + \phi_B^E + \phi_B^T)$.

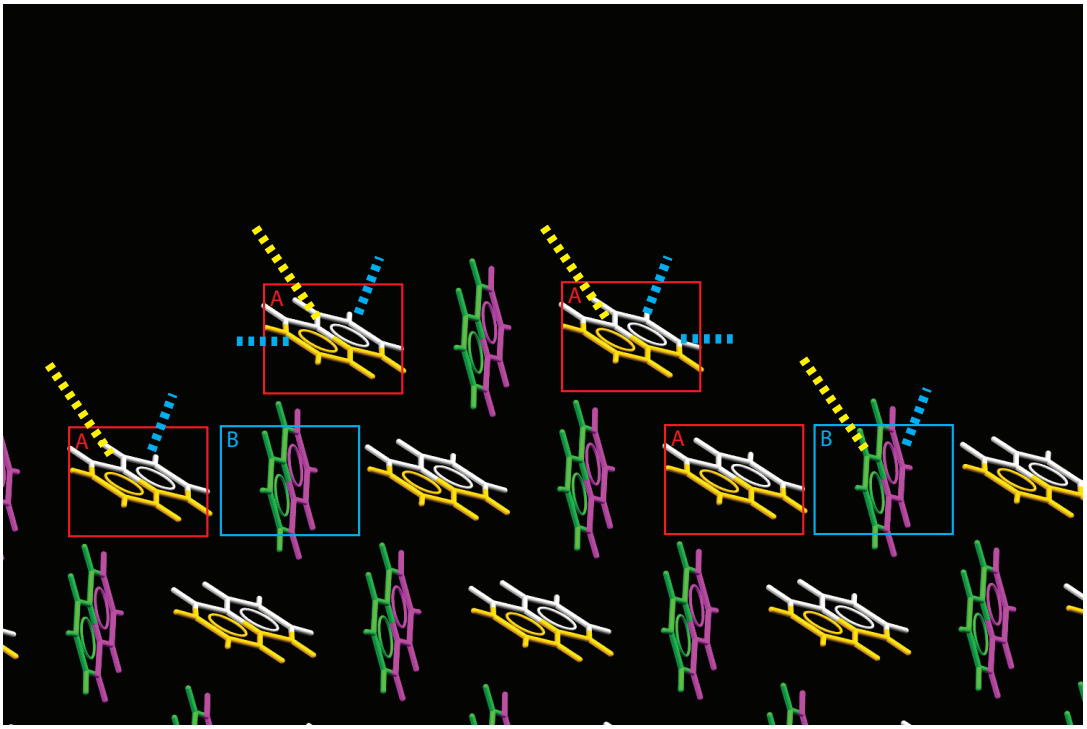

Figure 6.13: A1W and A1E single-kink sites (west and east). Boltzmann weights: $w_{A1W} = w_{A1E} = \phi_A^K + 0.5(\phi_A^E + \phi_A^T + \phi_B^E + \phi_B^T)$.

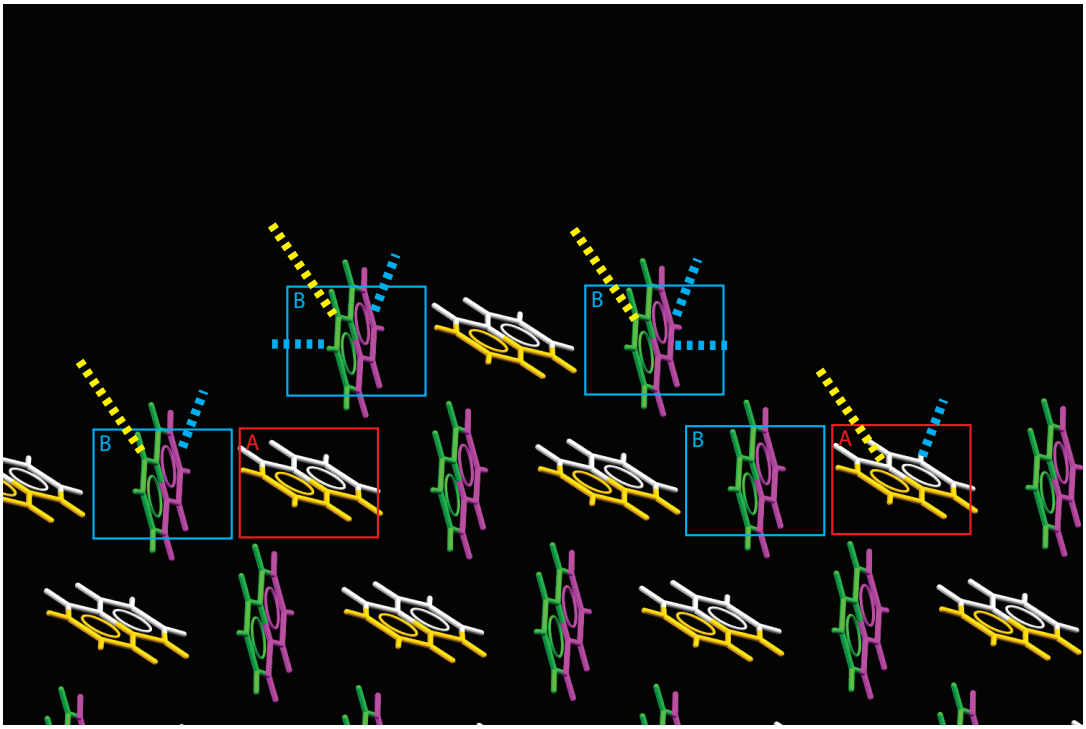

Figure 6.14: B1W and B1E single-kink sites (west and east). Boltzmann weights: $w_{B1W} = w_{B1E} = \phi_B^K + 0.5(\phi_A^E + \phi_A^T + \phi_B^E + \phi_B^T)$.

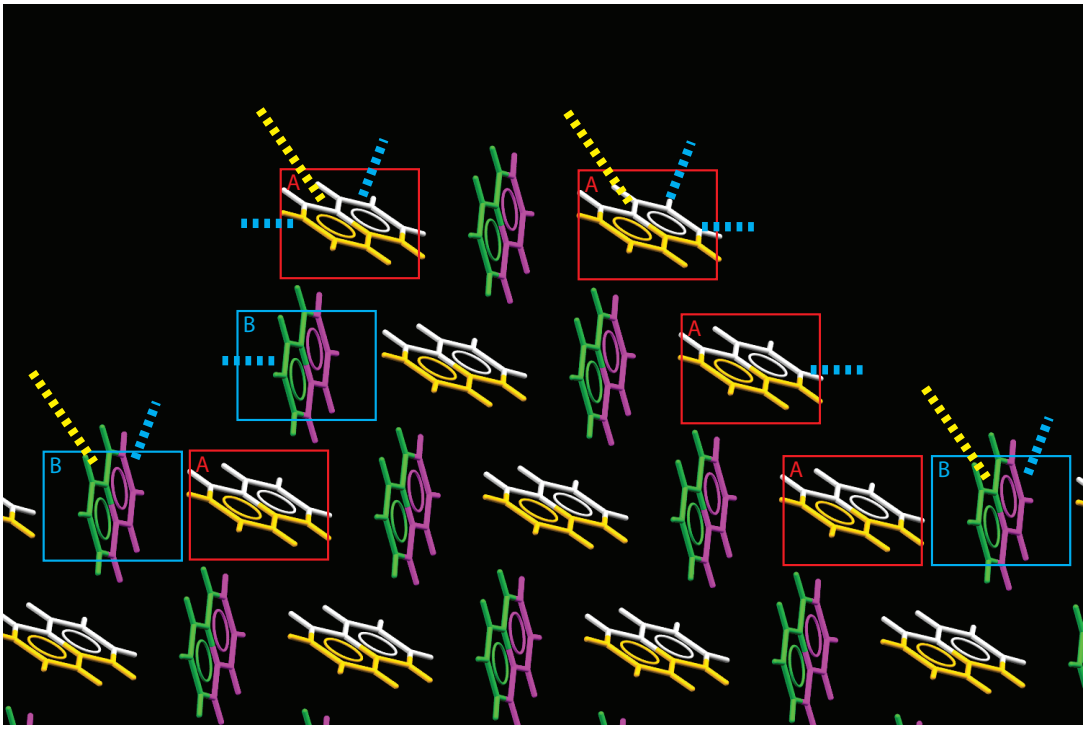

Figure 6.15: A2W (west) and A2E (east) double-kink sites. Boltzmann weights: $w_{A2W} = \phi_A^K + \phi_B^K + 0.5(\phi_A^E + \phi_A^T + \phi_B^E + \phi_B^T)$, $w_{A2E} = 2\phi_A^K + 0.5(\phi_A^E + \phi_A^T + \phi_B^E + \phi_B^T)$.

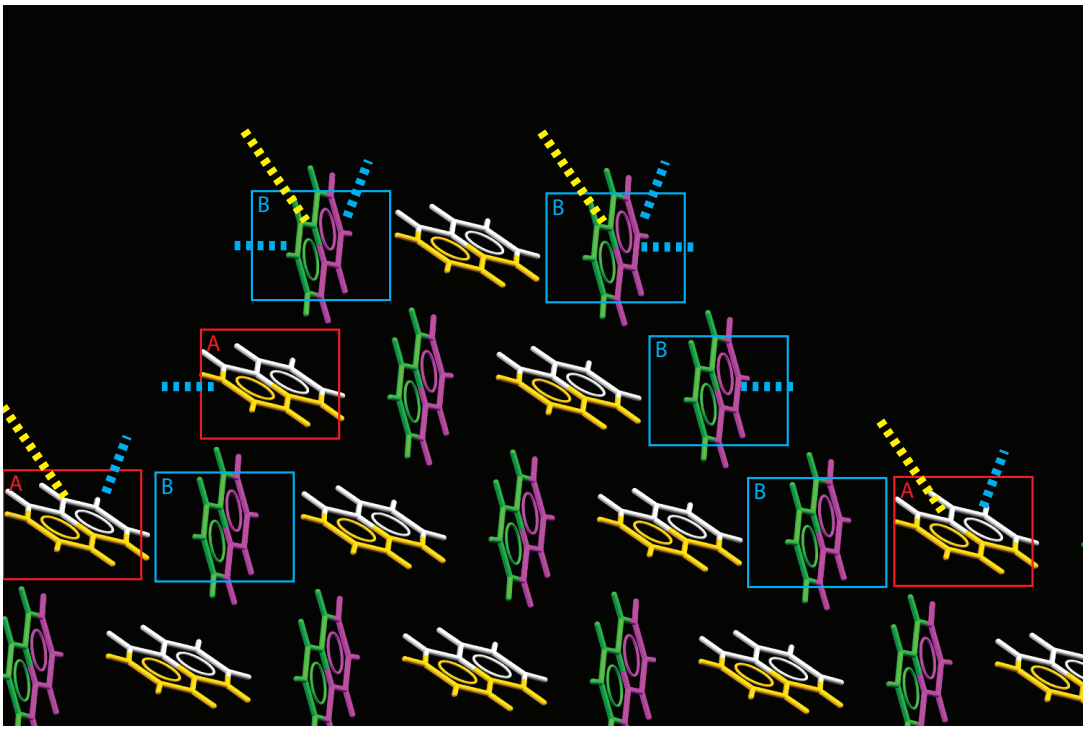

Figure 6.16: B2W (west) and B2E (east) double-kink sites. Boltzmann weights: $w_{B2W} = \phi_A^K + \phi_B^K + 0.5(\phi_A^E + \phi_A^T + \phi_B^E + \phi_B^T)$, $w_{B2E} = 2\phi_B^K + 0.5(\phi_A^E + \phi_A^T + \phi_B^E + \phi_B^T)$.

Since $\phi_A^K = \phi_B^K$, $\phi_A^E = \phi_B^E$ and $\phi_A^T = \phi_B^T$, the resulting kink densities collapse to the centrosymmetric case, in essentially identical fashion to the [010] step. Note, of course, $\phi_{[010]}^K \neq \phi_{[110]}^K$, so the actual kink density values for each step are different.

Bibliography

[1] M. Frisch, G. Trucks, H. Schlegel, G. Scuseria, M. Robb, J. Cheeseman, G. Scalmani, V. Barone, B. Mennucci, G. Petersson, H. Nakatsuji, M. Caricato, X. Li, H. Hratchian, A. Izmaylov, J. Bloino, G. Zheng, J. Sonnenberg, M. Hada, M. Ehara, K. Toyota, R. Fukuda, J. Hasegawa, M. Ishida, T. Nakajima, Y. Honda, O. Kitao, H. Nakai, T. Vreven, J. M. Jr., J. Peralta, F. Ogliaro, M. Bearpark, J. Heyd, E. Brothers, K. Kudin, V. Staroverov, R. Kobayashi, J. Normand, K. Raghavachari, A. Rendell, J. Burant, S. Iyengar, J. Tomasi, M. Cossi, N. Rega, J. Millam, M. Klene, J. Knox, J. Cross, V. Bakken, C. Adamo, J. Jaramillo, R. Gomperts, R. Stratmann, O. Yazyev, A. Austin, R. Cammi, C. Pomelli, J. Ochterski, R. Martin, K. Morokuma, V. Zakrzewski, G. Voth, P. Salvador, J. Dannenberg, S. Dapprich, A. Daniels,

O. Farkas, J. Foresman, J. Ortiz, J. Cioslowski, and D. Fox. Gaussian 09, revision a. 02; gaussian, inc. *Wallingford, CT*, 19:227–238, 2009.

[2] J. Wang, W. Wang, P. A. Kollman, and D. A. Case. Automatic atom type and bond type perception in molecular mechanical calculations. *Journal of Molecular Graphics and Modelling*, 25(2):247 – 260, 2006.

[3] P. Dandekar and M. F. Doherty. A mechanistic growth model for inorganic crystals: Solid-state interactions. *AIChE J*, 60(11):3707–3719, 2014.

[4] P. Dandekar and M. F. Doherty. A mechanistic growth model for inorganic crystals: Growth mechanism. *AIChE J*, 60(11):3720–3731, 2014.

[5] A. G. Stack, P. Raiteri, and J. D. Gale. Accurate rates of the complex mechanisms for growth and dissolution of minerals using a combination of rare-event theories. *J. Am. Chem. Soc.*, 134(1):11–14, 2012. PMID: 21721566.

[6] A. G. Stack and M. C. Grantham. Growth rate of calcite steps as a function of aqueous calcium-to-carbonate ratio: independent attachment and detachment of calcium and carbonate ions. *Crystal Growth & Design*, 10(3):1409–1413, 2010.

[7] P. Fenter, S. Kerisit, P. Raiteri, and J. D. Gale. Is the calcite-water interface understood? direct comparisons of molecular dynamics simulations with specular x-ray reflectivity data. *The Journal of Physical Chemistry C*, 117(10):5028–5042, 2013.

[8] P. Raiteri and J. D. Gale. Water is the key to nonclassical nucleation of amorphous calcium carbonate. *Journal of the American Chemical Society*, 132(49):17623–17634, 2010. PMID: 21090620.

[9] P. Raiteri, J. D. Gale, D. Quigley, and P. M. Rodger. Derivation of an accurate force-field for simulating the growth of calcium carbonate from aqueous solution: A new model for the calcite-water interface. *The Journal of Physical Chemistry C*, 114(13):5997–6010, 2010.

[10] J. N. Bracco, M. C. Grantham, and A. G. Stack. Calcite growth rates as a function of aqueous calcium-to-carbonate ratio, saturation index, and inhibitor concentration: Insight into the mechanism of reaction and poisoning by strontium. *Crystal Growth & Design*, 12(7):3540–3548, 2012.

[11] J. Wang, R. M. Wolf, J. W. Caldwell, P. A. Kollman, and D. A. Case. Development and testing of a general amber force field. *Journal of computational chemistry*, 25(9):1157–1174, 2004.

[12] A. R. Leach. *Molecular modelling: principles and applications*. Pearson Education, 2001.

[13] Z. B. Kuvadia and M. F. Doherty. Spiral growth model for faceted crystals of non-centrosymmetric organic molecules grown from solution. *Cryst. Growth Des.*, 11(7):2780–2802, 2011.

[14] F. C. Frank. On the kinematic theory of crystal growth and dissolution processes. In R. H. Doremus, B. W. Roberts, and D. Turnbull, editors, *Growth and Perfection of Crystals*, pages 411–419. New York: Wiley,, 1958.

[15] A. A. Chernov. Crystal growth forms and their kinetic stability. *Kristallografiya*, 8:87–93, 1963.

[16] M. A. Lovette, M. Muratore, and M. F. Doherty. Crystal shape modification through cycles of dissolution and growth: Attainable regions and experimental validation. *AIChE Journal*, 58(5):1465–1474, 2012.

[17] P. K. Weiner and P. A. Kollman. Amber: Assisted model building with energy refinement. a general program for modeling molecules and their interactions. *Journal of Computational Chemistry*, 2(3):287–303, 1981.

[18] H. Cuppen, H. Meekes, W. van Enckevort, E. Vlieg, and H. Knops. Nonequilibrium free energy and kinetic roughening of steps on the kossel (001) surface. *Phys. Rev. B: Condens. Matter Mater. Phys.*, 69(24):245404, 2004.

[19] P. Bennema and H. Meekes. Two centuries of morphology of crystals: integration of principles of mathematical crystallography, statistical mechanics of surface models and chemistry. In X. Y. Lui and J. J. De Yoreo, editors, *Nanoscale Structure and Assembly at Solid-Fluid Interfaces*, volume Volume I: Interfacial Structures versus Dynamics, pages 177–208. Kluwer Academic, Boston, 2004.

[20] L. Onsager. Crystal statistics. I. A two-dimensional model with an order-disorder transition. *Physical Review*, 65(3-4):117–149, 1944.

[21] I. M. Dawson and V. Vand. The observation of spiral growth-steps in n-paraffin single crystals in the electron microscope. *Proc R Soc A*, 206(1087):555–562, 1951.

[22] G. T. Paloczi, B. L. Smith, P. K. Hansma, D. A. Walters, and M. A. Wendman. Rapid imaging of calcite crystal growth using atomic force microscopy with small cantilevers. *Applied Physics Letters*, 73(12):1658–1660, 1998.

[23] A. Gavezzotti. Efficient computer modeling of organic materials. The atom–atom, Coulomb–London–Pauli (AA-CLP) model for intermolecular electrostatic-polarization, dispersion and repulsion energies. *New J Chem*, 35(7):1360–1368, 2011.

[24] J. D. Dunitz and A. Gavezzotti. How molecules stick together in organic crystals: weak intermolecular interactions. *Chem. Soc. Rev.*, 38(9):2622–2633, 2009.

[25] J. Li, C. J. Tilbury, S. H. Kim, and M. F. Doherty. A design aid for crystal growth engineering. *Prog. Mater Sci.*, 82:1–38, 2016.

Chapter 7

Conclusions and Future Work

Controlling crystal growth shapes to improve product functionality is highly desirable in every industry that manufactures or uses crystalline products. An engineering tool to screen through the available design space and find growth conditions that confer an optimum crystal morphology would, therefore, be extremely valuable. Mechanistic models for crystal growth serve as the foundation upon which such a predictive tool can be realized. This dissertation details various developments to mechanistic models that enhance their accuracy and applicability for general systems. These improvements are summarized below, and then avenues for continued research are suggested.

7.1 Summary of Model Improvements

Figure 7.1 summarizes again how the developments contained in this dissertation fit into the multi-scale modeling structure presented in Chapter 1.

Chapter 2 analyzed various sets of attachment/detachment rate expressions and considered the growth unit incorporation mechanism at kink sites on the step edge. These kinetic processes underpin the entire mechanistic formulation, so it is important to ensure

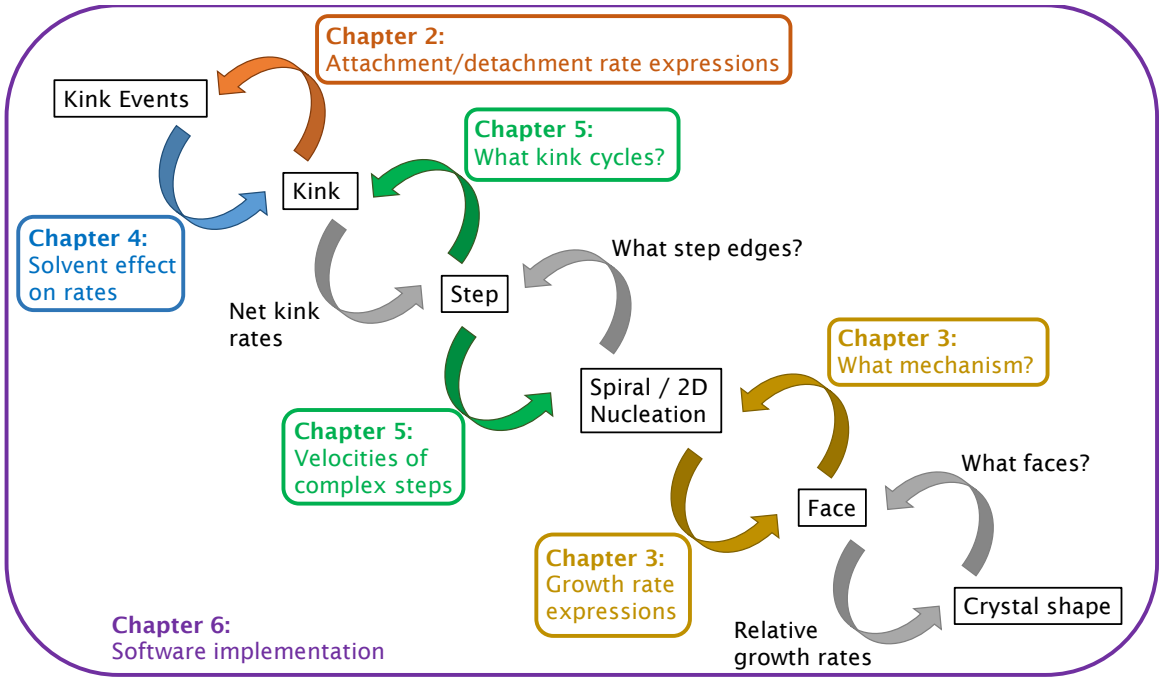

Figure 7.1: An indication of where each modeling development fits into the overall multi-scale mechanistic structure.

an accurate description is contained. Sets of rate expressions used in previous mechanistic models are evaluated with respect to crystallization thermodynamics and kinetics; the most consistent set is then proposed. Interestingly, this preferred set of rate expressions is actually simpler than alternative formulations.

Chapter 3 addresses the critical issue of modeling the correct growth regime on each crystal face. It is essential to model the dominant mechanism, which is potentially different for each face family, and account for the mechanistic parameters that drive regime progressions as supersaturation is increased. The introduction of a mechanistic expression for the 2D nucleation rate prefactor enables us to connect regimes and predict face-specific crossovers; the presented framework, using new mechanistic parameter groupings within growth rate expressions, offers a reliable way to calculate the impact of supersaturation. This is demonstrated via successful predictions for various systems, which confirm the model's accuracy.

Chapter 4 details an investigation into accounting for the effect of solvent by implementing an energetic modification at the crystal–solvent interface. Various practical options for determining the work of adhesion are reviewed, and the model by van Oss, Chaudhury and Good [1] is selected as offering the best balance between predictive power and feasible application into automated shape-prediction models. Sublimation and solution growth shape predictions are compared to experimental determinations, which confirm the predictive capacity of the proposed technique.

Chapter 5 introduces a step velocity model for non-centrosymmetric growth units that, for the first time, accounts for multiple kink cycles and interdependent surface structures on the step. Both thermodynamic and kinetic contributions to step row instability are discussed and accounted for, which are phenomena unique to non-centrosymmetric growth units (such growth units represent most industrially relevant compounds). Critically, this model collapses to the centrosymmetric formulation under appropriate limits, so it offers vastly increased potential for model automation, while simultaneously offering improved description of surface growth physics at the step edge.

Finally, Chapter 6 describes the strategy for implementing mechanistic models to obtain a shape prediction. This strategy is presented from the perspective of proof-of-concept software, called ADDICT, which is serving to transfer these high-fidelity crystal growth models to researchers in the pharmaceutical industry and facilitate methodology adoption. Specific tactics are discussed relating to periodic bond chain determination, amongst other automation details, to offer deeper insight into program operation and how to execute these calculations. Ultimately, this software reinforces that mechanistic models can actually deliver the ability to improve design of crystalline products; their continued development is not just a theoretical exercise.

7.2 Areas for Future Enhancement

A significant advantage of adopting a mechanistic approach is the ability to refine and assimilate future developments to increase model performance and utility. The following sections indicate interesting avenues for further model enhancements, divided according to estimated feasibility.

7.2.1 Shorter Term

The developments detailed in Chapter 5 pave the way to generalize the framework in Chapter 3 to non-centrosymmetric growth units. The base rate expressions for 2D-nucleation regimes do not require modification and can incorporate the non-centrosymmetric step velocity model directly. Furthermore, the average edge energy for each critical nucleus side can be calculated assuming a Boltzmann distribution of edge rows along the step front, adopting a similar methodology to the kink density tactics from Chapter 5. This circumvents the complication of alternating edge energies as the critical nucleus grows, and is more physically realistic for organic molecular crystals, where we expect the step edge to reorganize according to instability effects.

In Chapter 4, we indicated the need to estimate electron accepting/donating ratios using chemical intuition. Although shapes may not prove sensitive to this value, the Hydrogen Bond Propensity (HBP) analysis [2–5] available within the CCDC Mercury software [6] may prove useful for a more systematic determination, where necessary. This has an additional advantage of being a data-driven model based on the wealth of crystal structures contained in the Cambridge Structural Database [7]; it could enable ratios to be tailored to specific functional groups exposed at surface sites.

At various stages, we have mentioned the possibility of obtaining mechanistic parameters, such as kink energies or kinetic rate constants, using molecular simulations.

Such accurately determined parameters can be readily incorporated within the modeling framework; a notable example of this is Dogan and coworkers [8], who applied the spiral growth model under dissolution and used simulated parameters to compute absolute rates. Though we have focused on shape engineering for practicality, the potential convergence of techniques reinforces the intrinsic value of this mechanistic framework.

7.2.2 Longer Term

Obtaining solvent-modified interfacial energies through simulations is largely incompatible with a fast engineering tool, due to the number of surface sites and the need to screen a vast design space (each set of conditions requires new simulations). A middle ground, between computationally expensive methods and the approximate techniques in Chapter 4, might be found using the COSMOlogic suite of programs [9–11]. COSMO-RS theory [12–15] is able to determine thermodynamic properties of mixtures by considering statistics of interacting molecular surface segments, each with defined charge density. A molecule's distribution of surface charges (σ-profile) is the result of a COSMO calculation [16] (taking on the order of hours–days depending on molecular size, theory level and parallelization), which only has to be done once for each molecule. Thus, one could perform a COSMO calculation, overlay the molecular σ-profile onto the CIF file, and propagate this information through the crystal supercell generated during the mechanistic model execution. At each surface site, a subset of the σ-profile could be generated according to the exposed fraction of the molecule. The COSMOlogic software could then calculate interfacial thermodynamics against the solvent for each reduced, site-specific σ-profile. While less automatable than the current formulation, this tactic is much more suitable for design space screening than molecular simulations, since the semi-expensive portion of the calculation is required just once [17]. Alongside potentially increased accu-

racy, this would also facilitate mixed solvent growth shape predictions (using an average solution σ-profile).

Our current strategy to verify force field accuracy for a given crystal is to compare the predicted lattice energy to reported sublimation enthalpies. However, crystal shapes depend on relative growth rates, and so our predictive capability depends primarily on how well our calculated energetics match relative interaction strengths. Thus, while a lattice energy that closely corresponds is reassuring, it would be optimal to instead compare predicted relative interaction strengths for the dominant PBCs against some benchmark.

While the presented models consider single crystal growth in solution, modeling epitaxial growth of thin films could broaden predictive utility to the production of organic electronic devices made from small conjugated molecules, which is an area of rising interest. The techniques for connecting growth regimes established in Chapter 3 might serve as a starting point, but any additional mechanisms and the effect of substrate must be accounted for (e.g., lattice mismatch, presence of dislocations etc.). Nonetheless, evidence exists of steps on inkjet-printed single-crystal thin films [18], and engineering aligned crystalline domains within device active layers could improve product characteristics [19].

Finally, broadening these models beyond crystal shapes is another area of current focus in our research group. Considering appropriate solute and solvent descriptors of the underlying attachment/detachment kinetic processes shows great promise for developing models that could be assimilated within the framework and predict absolute rates. This opens up the connection to predictive population balance modeling of crystal systems.

Bibliography

[1] C. J. van Oss, M. K. Chaudhury, and R. J. Good. Monopolar surfaces. *Adv Colloid Interface Sci*, 28:35–64, 1987.

[2] P. T. A. Galek, L. Fábián, W. D. S. Motherwell, F. H. Allen, and N. Feeder. Knowledge-based model of hydrogen-bonding propensity in organic crystals. *Acta Crystallographica Section B*, 2007.

[3] P. T. A. Galek, F. H. Allen, L. Fabian, and N. Feeder. Knowledge-based h-bond prediction to aid experimental polymorph screening. *CrystEngComm*, 11:2634–2639, 2009.

[4] P. T. A. Galek, L. Fábián, and F. H. Allen. Persistent hydrogen bonding in polymorphic crystal structures. *Acta Crystallographica Section B*, 2009.

[5] P. T. A. Galek, L. Fabian, and F. H. Allen. Truly prospective prediction: inter- and intramolecular hydrogen bonding. *CrystEngComm*, 12:2091–2099, 2010.

[6] C. F. Macrae, P. R. Edgington, P. McCabe, E. Pidcock, G. P. Shields, R. Taylor, M. Towler, and J. van de Streek. Mercury: visualization and analysis of crystal structures. *Journal of Applied Crystallography*, 39(3):453–457, 2006.

[7] F. H. Allen. The Cambridge Structural Database: a quarter of a million crystal structures and rising. *Acta Crystallographica Section B*, 2002.

[8] B. Dogan, J. Schneider, and K. Reuter. In silico dissolution rates of pharmaceutical ingredients. *Chemical Physics Letters*, 662:52 – 55, 2016.

[9] COSMOtherm, Version C3.0, Release 16.01; COSMOlogic GmbH & Co. KG, http://www.cosmologic.de.

[10] F. Eckert and A. Klamt. Fast solvent screening via quantum chemistry: COSMO-RS approach. *AIChE Journal*, 48(2):369–385, 2002.

[11] TURBOMOLE 7.1 2016, a development of University of Karlsruhe and Forschungszentrum Karlsruhe GmbH, 1989-2007, TURBOMOLE GmbH, since 2007; available from http://www.turbomole.com.

[12] A. Klamt. Conductor-like screening model for real solvents: A new approach to the quantitative calculation of solvation phenomena. *The Journal of Physical Chemistry*, 99(7):2224–2235, 1995.

[13] A. Klamt, V. Jonas, T. Brger, and J. C. W. Lohrenz. Refinement and parametrization of COSMO-RS. *The Journal of Physical Chemistry A*, 102(26):5074–5085, 1998.

[14] A. Klamt. *COSMO-RS: From Quantum Chemistry to Fluid PhaseThermodynamics and Drug Design*. Elsevier; Amsterdam, The Netherlands, 2005.

[15] A. Klamt. The cosmo and cosmo-rs solvation models. *Wiley Interdisciplinary Reviews: Computational Molecular Science*, 1(5):699–709, 2011.

[16] A. Klamt and G. Schuurmann. COSMO: a new approach to dielectric screening in solvents with explicit expressions for the screening energy and its gradient. *J. Chem. Soc., Perkin Trans. 2*, pages 799–805, 1993.

[17] J. F. Krzyzaniak, P. A. Meenan, C. L. Doherty, K. Pencheva, S. Luthra, and A. Cruz-Cabeza. Integrating computational materials science tools in form and formulation design. In Y. A. Abramov, editor, *Computational pharmaceutical solid state chemistry*, chapter 6, pages 117–144. John Wiley & Sons; Hoboken, NJ, 2016.

[18] H. Minemawari, T. Yamada, H. Matsui, J. Tsutsumi, S. Haas, R. Chiba, R. Kumai, and T. Hasegawa. Inkjet printing of single-crystal films. *Nature*, 2011.

[19] Y. Diao, B. C.-K. Tee, G. Giri, J. Xu, D. H. Kim, H. A. Becerril, R. M. Stoltenberg, T. H. Lee, G. Xue, S. C. B. Mannsfeld, and Z. Bao. Solution coating of large-area organic semiconductor thin films with aligned single-crystalline domains. *Nat Mater*, 2013.